THE MICROSTRUCTURE AND PROPERTIES OF HIPPED POWDER TI ALLOYS

KUN ZHANG

A thesis submitted to
The UNIVERSITY OF BIRMINGHAM
For the degree of
DOCTOR OF PHILOSOPHY

School of Metallurgy and Materials
College of Engineering and Physical Sciences
The University of Birmingham
April 2009

Abstract

In the present study, the effect of hot isostatic pressing (HIPping) variables such as HIPping temperature, HIPping cycle and powder particle size, on the microstructure and mechanical properties of HIPped samples of two Ti alloys have been assessed. Powders of the most commonly used ($\alpha + \beta$) alloy, Ti-6Al-4V and one specific beta alloy, Ti-25V-15Cr-2Al-0.2C wt% (burn resistant titanium alloy, BuRTi) were studied. The Ti-6Al-4V powder was made by the plasma rotating electrode process (PREP). BuRTi powders, which were made both by gas atomisation and by PREP were HIPped to investigate the influence of the initial structure of the powder on the microstructure and associated mechanical properties of the HIPped alloy.

The PREP Ti-6Al-4V powder was shown to be fully martensitic in the as-atomised condition. The gas-atomised and PREP powders of BuRTi showed very different as-atomised structures, but in both cases the structure was, as expected single phase beta, with the carbon retained in solution. The individual particles of gas-atomised BuRTi powder were always polycrystalline, although there was a significant scatter in grain sizes within different particles. In contrast the individual particles in the PREP powder were either coarse grained polycrystals or single crystals. These differences led to significant differences in the microstructures and properties of HIPped samples.

It was found that HIPping of Ti-6Al-4V samples resulted in the formation of equiaxed regions and lath-like microstructure. The small equiaxed regions are formed by recrystallisation which occurs at original particle boundaries where most of the deformation occurs during HIPping; the lath-like microstructure is formed by simply tempering the (less deformed) original alpha prime martensite within the central part of original particles. Among the three

HIPping temperatures used, samples machined from powder HIPped at 930°C exhibited a better balance of properties than those HIPped at 880°C or 1020°C. The fatigue properties of samples HIPped at 930°C, made using different HIPping procedures were compared. It was found that samples which contain the as-HIPped surface, which were made using a new HIPping procedure, have better fatigue properties than samples with as-HIPped, machined or electro-polished surfaces which were produced by conventional HIPping . The properties of optimally HIPped Ti-6Al-4V samples are as good as or better than ingot-route samples.

In the case of BuRTi the original single crystals or coarse grained polycrystals in the PREP powder are retained after HIPping and limited grain growth occurs in the gas-atomised samples. The tensile strength is comparable for the gas-atomised and PREP samples, but samples tested to failure showed a significant scatter in ductility (a larger scatter in the PREP powder samples) and all fracture surfaces contained large circular fracture initiation sites, with larger sites associated with lower ductility. Initiation occurs in the centre of these circular regions in large grains or in adjacent grains which have similar orientations and the failed region expands symmetrically in powder samples where no texture is expected. The fatigue properties of the PREP samples are much lower whereas the fatigue properties of the gas atomised samples are better than those of samples from ingot route. This behaviour is associated with obvious facetted failure sites in the PREP powder samples where it is suggested that the coarser microstructure has allowed persistent slip to occur leading to localised deformation and to premature failure.

These observations are discussed in terms of the potential of net shape HIPping for the production of engineering components and in this context the fact that a new HIPping schedule has been developed during this study, where the fatigue properties of samples containing an as-HIPped surface are excellent, is very significant.

ACKNOWLEDGMENTS

I wish to express my sincere indebtedness to my supervisors, Prof. Xinhua Wu and Dr. Junfa Mei for their excellent supervision, continuous support, constant encouragement and understanding with respect to both research and domestic issues. Special thanks must go to Prof. M. H. Loretto for many useful discussions. I also wish to thank School of Metallurgy and Materials and ORS Committee for the award, Rolls- Royce plc. for additional financial support.

Thanks to Prof. S. Blackburn and Prof. P. Bowen for the provision of research facilities. I am grateful to Dr. D. Hu and Dr. N. Wain for their help over the Ph.D. years. The involvement of Prof. M. Bache and Dr. P. Hurley from the University of Swansea was particularly beneficial to the project and I would like to express my gratitude for their helpful discussions. I also wish to thank Dr. T. Doel, Dr. H. Li and Dr. Y. Li for helping the mechanical testing. I am greatly obliged to Mr. J. Shurvinton for his help with the powders' HIPping. Also thanks to D. Price, P. Stanley, M. Chu, and J. Singh for their technical assistance and co-operation. I would also like to thank my friends and colleagues, both past and present, for their support and assistance.

Finally, I wish to thank my family especially my parents and parents-in-law for their constant support and understanding. Last but not least, I would like to thank my husband, Aijun for his love, endless support and our lovely little son, Boyan who brings me the cherished experience on motherhood. I could never have completed my study without them.

Table of Contents

Chapter 1 Introduction

The rapid development of low density titanium alloys with high strength, good creep and fatigue-resistant properties continues to play a major role in aero-engine advances. Alloys with improved properties and processing characteristics have been developed to meet the stringent technological and quality requirements for modern aero-engines. Titanium alloys, especially Ti-6Al-4V, are the preferred alloys for both rotating and non-rotating parts as they can withstand high impact stress over a wide range of operating conditions and have good formability. Equally importantly there is a large data base available covering the influence of processing parameters, composition and microstructure on properties so that the users have confidence in this alloy.

Beta or near beta titanium alloys have the highest strength to weight ratio and possess attractive combinations of strength, toughness and fatigue resistance. They are promising materials for fan blades or for engine casings. Ti-25V-15Cr-2Al-0.2C wt% burn-resistant beta titanium alloy (BuRTi) maintains good mechanical properties and offers burn resistance up to 500^{o}C, and is also significantly cheaper and has a lower density (5.1 g/cm^{3}) than other commercially available burn-resistant products.

Titanium and its alloys are amongst the advanced materials which are keys to enhancements in aerospace and terrestrial systems. However, a major concern with titanium-based materials is the high cost compared to competing materials. It is recognised that in the current economic climate, where cost is a major factor to be considered at the design stage, conventional alloy systems will remain an essential

constituent for the foreseeable future. This implies that titanium alloys will have to be employed more efficiently if they are to continue to meet future requirements. This has led to investigation of various lower cost processes. Near net shape HIPping can be utilised with titanium-based materials to obtain cost reduction by reducing the amount of difficult titanium machining and large amount of material loss. HIPping of "near net" and "net" complex shape parts is becoming an industrial technology for several critical high quality components of jet and rocket engines and power units as an alternative to investment casting or machining of wrought materials.

HIPping of two high performance titanium alloys, Ti-6Al-4V and BuRTi are carried out in this study. These HIPped materials have potential application for engine casings. The understanding of the HIPping responses of alloy powders is crucial in order to achieve the optimum powder material/HIPping process/microstructure/ property requirements. A systematic study on the effect of HIPping variables (HIPping temperature, HIPping procedure and powder type) on microstructure, surface condition, tensile properties, fatigue properties and fracture mechanisms has been carried out in the work reported in this thesis.

Chapter 2 presents the literature review which starts with the general introduction and classification of titanium alloys followed by a summary of the mechanical properties and applications of these alloys. Since two titanium alloys, Ti-6Al-4V and BuRTi are focused on in this study, a separate review on their mechanical properties and applications is presented. Processing methods, especially powder HIPping including powder production and details of the HIPping process are described. Following this, a brief review on the findings of other researchers on the microstructural behaviour and

mechanical responses of HIPped titanium alloys is given. Finally, the main aims of the research project are summarised.

Chapter 3 describes the experimental methods used in this investigation, which include descriptions of powder materials used and HIPping procedure. Details on the specimen preparation and microstructural analyses of as-received powders and of as-HIPped samples utilising well-established metallographic and analytical electron microscopy techniques are given. Mechanical testing and fracture analyses methods of the tested HIPped samples are also presented.

The results and discussion are divided into two chapters considering the different HIPping responses of two powder materials- Ti-6Al-4V and BuRTi. In Chapter 4, the microstructure and properties of HIPped samples of Ti-6Al-4V powder are presented. The details of microstructure and morphology of PREP (Plasma Rotating Electrode Process) Ti-6Al-4V powders and of HIPped samples are given. The effects of HIPping temperature, surface finish of as-HIPped samples and powder particle size on mechanical properties are assessed. Moreover, the fracture surface features are analysed in order to understand the fracture mechanisms. Following this, the optimum HIPping conditions were chosen to obtain desired properties for net shape HIPped samples. Chapter 5 presents the HIPping responses of two BuRTi powders, gas-atomised and PREP powders. The microstructures of powder samples HIPped under different conditions are presented. The mechanical properties of these two powder HIPped materials are compared. The observed differences in properties are discussed in terms of observations of the fracture surfaces of samples tested to failure. The

effect of powder particle size on microstructure and properties of HIPped gas atomised BuRTi samples is also described.

A general discussion is presented in Chapter 6 which focuses on the differences between the microstructures of as-atomised powders and HIPped samples of the two materials (Ti-6Al-4V and BuRTi) and between two powders of BuRTi (gas atomised and PREP). The differences in the fracture behaviour of PREP and gas atomised samples of BuRTi tested to failure in tension are also discussed.

Chapter 7 summarises the main findings and conclusions in this study. It also proposes some future work that should be carried out in order to obtain further understanding in this research area.

Chapter 2 Literature Review

2.1 Titanium and its alloys

A brief overview of titanium and its alloys will be given in this section. This includes their general characteristics/ properties, alloy classification and mechanical properties. Some examples of the commonly used alloys in the industry and their main applications will also be mentioned.

2.1.1 Introduction

Titanium is used for many aerospace and non-aerospace applications because of an attractive combination of low density, good mechanical properties, and good corrosion resistance [*Moll 1998*]. Titanium has a relatively low density of about 4.5g/cm^3 and a high tensile strength of about 900MPa. A significant weight saving can often be achieved [*Powell 1995*], without sacrificing strength, when this metal is used as a base material for structural purposes [*Polmear 1995*]. When exposed to air or other oxidising environments such as seawater, hydrocarbon and human body fluids, a stable and adherent oxide surface layer will be formed which contributes to the excellent corrosion resistance at low temperatures. The much higher melting temperature of titanium (1670°C) than that of aluminium, the main competitor in light weight structural applications, gives titanium a definite advantage above application temperatures of about 150°C. On the other hand, despite its high melting point, the high reactivity of titanium with oxygen limits the maximum use temperature of titanium alloys to about 600°C. Above this temperature the diffusion of oxygen through the oxide surface layer becomes too fast resulting in excessive growth of the

oxide layer and embrittlement of the adjacent oxygen-rich layer of the titanium alloy [*Lütjering 2003*].

One of the features that distinguish titanium from other light metals is that it exists in more than one crystallographic form. Pure titanium exhibits an allotropic phase transformation at 882°C, changing from a body-centred cubic crystal structure (β phase) at higher temperatures to a hexagonal close-packed crystal structure (α phase) at lower temperatures. The exact transformation temperature is strongly influenced by interstitial and substitutional elements and therefore depends on the purity of the metal. This allotropic transformation is present in virtually all titanium-based alloys and enables the many different titanium alloys to be processed to produce a range of microstructures consisting of α, β and metastable phases such as martensite (α') and omega (ω).

2.1.2 Alloying elements

Alloying elements in titanium are usually classified into α or β stabilizing additions depending on whether they increase or decrease the α/β transformation temperature of 882°C of pure titanium. The alloying additions alter both the transformation temperature (α/β transus) and the shape of two-phase field in which both α and β phases are present, and different elements can improve specific mechanical properties of titanium alloys [*Tsujimoto 1989*, *Wunderlich 1993*]. The alloying elements for titanium can be generally classified into α stabilisers and β stabilisers.

α stabilisers, such as Al, O, N, C, and Ga dissolve preferentially in the α phase and increase the transformation temperature at which the α phase is stable with increasing

solute content. In other words, the β transus is raised as the α phase field is extended, which can be seen from the schematic phase diagram in Fig. 2-1 (a). Aluminium is the most commonly used α-stabiliser in commercial alloys; it acts as an effective α strengthening element and is also the only common metal raising the transition temperature and having large solubilities in both the α and β phases. Among the interstitial elements, oxygen can be considered as an alloying element in titanium in those cases where the oxygen content is used to obtain the desired strength level. This is especially true for the different grades of CP titanium. Other α stabilisers include Ge, B, and the rare earth elements but their solid solubilities are much lower than aluminium or oxygen and none of these elements is used commonly as an alloying element. When the aluminium content is about 6%, the α/β transformation temperature of 882°C for pure titanium is increased to about 1000°C and the effectiveness of other alpha stabilisers on the transus is usually described in terms of their "aluminium equivalence". This quantity is derived empirically from the summation of the weight percentages of alloying elements in the alloy through the following equation [*Weiss 1999*]:

$$[Al]_{eq.}=[Al]+ 0.17[Zr] +0.33[Sn] +10([O]+[C]+2[N]) \qquad (2.1)$$

The Al equivalent in multi-component titanium alloys, is limited to about 9% because at higher values a brittle Ti_3Al (α_2) phase is formed leading to a decrease in ductility.

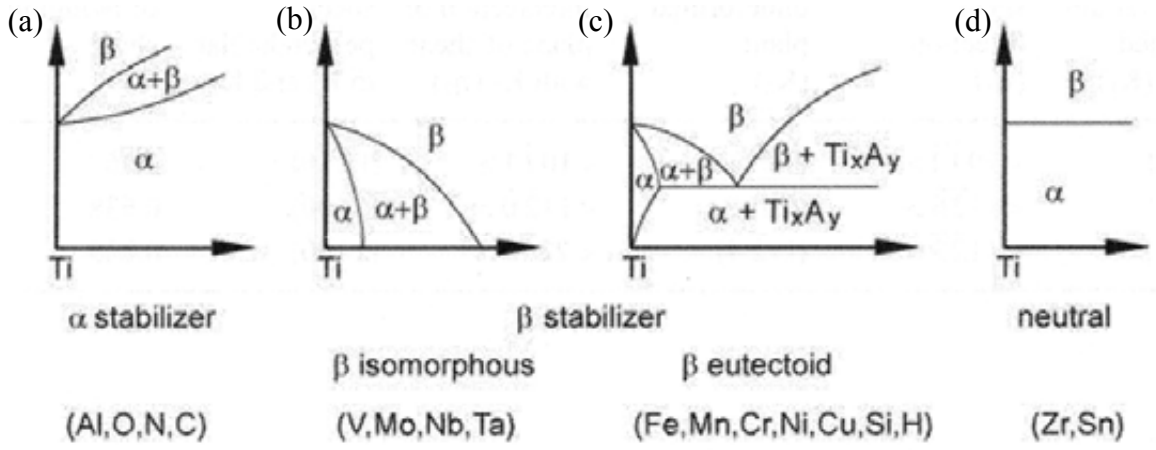

Fig. 2-1 Basic types of phase diagrams for titanium alloys and effect of alloying elements, (a) α stabilisers; (b) β isomorphous elements; (c) β eutectoid elements; (d) neutral elements [*Lütjering 2003*].

β stabilisers, such as V, Mo, Nb, Cr, Fe, Si, Cu, and Mn stabilise and strengthen the β phase and decrease the β transus. These beta-stabilisers are divided into β isomorphous elements and β-eutectoid forming elements, depending on the details of the binary phase diagrams. The most frequently used β-isomorphous elements in titanium alloys are V, Mo, and Nb. Sufficient concentrations of these elements make it possible to stabilise the β phase to room temperature (shown in Fig. 2-1(b)). Addition of 15% Mo lowers the β→ α+β transformation temperature from 882°C for pure titanium to about 750°C. Analogously to the Al equivalence a molybdenum equivalence is used to describe the relative influence of beta stabilisers in multi-component titanium alloys and is given by [*Lütjering 2003*]:

$$[Mo]_{eq.} = [Mo] + 0.2\,[Ta] + 0.28\,[Nb] + 0.4\,[W] + 0.67\,[V] + 1.25\,[Cr] + 1.25\,[Ni] + 1.7\,[Mn] + 1.7[Co] + 2.5\,[Fe] \quad (2.2)$$

β-eutectoid elements such as Cr, Fe, Si, Cu, Ni and Mn have a limited solubility in the β phase and form intermetallic compounds by eutectoid decomposition of the β phase (shown in Fig. 2-1(c)). For some alloy systems such as Ti-Fe, Ti-Cr and Ti-Mn, the eutectoid reactions can be very sluggish, where eutectoid decomposition is very slow and no intermetallic compounds is able to form during normal fabrication and heat treatment practice. In effect, the behaviour of this group of alloys is similar to the β-isomorphous systems. For alloy systems with β-eutectoid elements such as Cu and Si, the β phase decomposes to α+intermetallic compound (γ) during conventional furnace cooling through the eutectoid reaction, $\beta \rightarrow \alpha+\gamma$. It should be mentioned, that hydrogen belongs to eutectoid forming elements and that the low eutectoid temperature of 300°C in combination with the high diffusivity of hydrogen led to a special process of microstructure refinement, the so-called hydrogenation/ dehydrogenation (HDH) process, in which hydrogen is used as a temporary alloying element. Generally, the maximum hydrogen content in CP titanium and titanium alloys is strictly limited to about 125-150ppm because of hydrogen embrittlement [*Lütjering 2003*]. Besides stabilising and strengthening the β phase, β-stabilisers also improve the alloy fabricability, the hardenability and the response to heat treatment.

In addition some elements (Zr, Sn) behave more or less neutrally, because initially they lower the α/β transformation temperature only slightly and then increase the transformation temperature at higher concentrations (Fig. 2-1(d)). In fact, Sn belongs to the β eutectoid forming elements, but has essentially no effect on the α/β transformation temperature. Many commercial multicomponent alloys contain Zr and Sn but in these alloys both elements are considered and counted as α stabilising elements. This is because of the chemical similarity of Zr to titanium and because Sn

can replace aluminium in the hexagonal ordered Ti_3Al phase (α_2). These elements were thus considered in equation (2.1) as α-stabilisers by Rosenberg [*Rosenberg 1970*].

2.1.3 Alloy classification

Commercial titanium alloys are classified conventionally into three different categories (α, α+β, and β alloys) according to the predominant, final room temperature constituents after heat treatment and thermomechanical processing. In the following sections the equilibrium structures formed during processing and cooling to room temperature are discussed before considering the influence of composition on non-equilibrium phases.

2.1.3.1 α alloys

α alloys include the various grades of CP titanium (fully α alloy) and α alloys which, upon annealing well below the β transus, contain only small amounts of β phase (2-5 vol%) typically stabilised by iron (near α alloy). The main alloying elements in these alloys are Al, O, N, Sn and Zr, which all stabilise the α phase. Al, Sn and Zr contribute to solid solution strengthening while addition of O and N results in interstitial hardening. Fully α alloys have relatively low tensile strength and limited formability because of the high stress required to activate non-basal slip systems. These limitations are, however, alleviated by adding up to 2% β stabilisers (eg. Mo, V), which causes the introduction of a small amount of β phase into the microstructure. The β phase is also helpful in controlling the recrystallised α grain size and improves the hydrogen tolerance of these alloys. These commercially pure titanium alloys are not heat treatable, hence they exhibit good weldability [*Boyer 1996*].

Near α alloys are also usually included under alpha alloys; they have high room temperature tensile strength and the best creep resistance of all conventional titanium alloys and are preferred for elevated temperature applications up to about 600°C [*Neal 1985*]. Some of the commercially available α alloys are CP Ti, TIMETAL 230 (Ti-2.5Cu), TIMETAL 3-2.5 (Ti-3Al-2.5V), TIMETAL 685 (Ti-6Al-5Zr-0.5Mo-0.25Si), TIMETAL 834 (Ti-6Al-4Sn-3.5Zr-0.5Mo-0.35Si-0.7Nb-0.06C) and TIMETAL 1100 (Ti-6Al-2.7Sn-4Zr-0.4Mo-0.45Si). They are used primarily as wrought products in the aerospace and chemical industry.

2.1.3.2 (α+β) alloys

(α+β) alloys consist of a mixture of α and β phases and contain α stabilisers to stabilise and strengthen the α phase, together with 4-6% β stabilisers which permit considerable amounts of β phase to be retained on quenching from the β or (α+β) phase fields. The two-phase (α+β) field enables various heat treatment regimes and processing to be done which are commonly annealed in the β or (α+β) phase fields and can be further strengthened by solution treatment and aging, resulting in a variety of microstructure/property combinations. The amount of strengthening which can be achieved is a function of the alloy and section thickness. Alloys with the lower β stabilising contents are highly weldable, and with the β stabiliser content increasing, the hardenability increases but welding becomes more difficult. (α+β) alloys can provide a weight savings in place of the lower strength aerospace type steels and have very superior corrosion resistance to aluminium alloys and low alloy steels.

One of the most important (α+β) alloys is Ti-6Al-4V, the 'workhorse' of the industry [*Boyer 1996*]. Other examples include TIMETAL 550 (Ti-4Al-4Mo-2Sn-0.5Si),

TIMETAL 62S (Ti-6Al-2Fe-0.1Si), TIMETAL 6-6-2 (Ti-6Al-6V-2Sn-0.5Fe-0.5Cu), TIMETAL 6-2-4-2 (Ti-6Al-2Sn-4Zr-2Mo-0.08Si) and TIMETAL 6-2-4-6 (Ti-6Al-2Sn-4Zr-6Mo). These alloys are widely used for airframe and aerospace engine components, automotive parts, medical prostheses and implants and sporting equipment.

2.1.3.3 β alloys

β alloys are by definition those alloys which do not transform martensitically upon quenching to room temperature and form instead a metastable β phase. The α phase can be precipitated from the metastable β phase as very fine, strong particles (platelets) upon aging and cooling to room temperature. β alloys exhibit high strength, which is controlled by the dispersion of α phase in the β matrix and improved forgeability as a result of the simple body-centred cubic (bcc) structure in the as-quenched condition. Beta alloys offer fabrication advantages, particularly for producing sheet, owing to their cold rolling capabilities. Owing to the limitations in reductions which can be achieved in (α+β) alloys they must be hand rolled which is a very labour intensive operation; the β alloys, on the contrary, can be strip rolled. In addition, for hot-die or isothermal precision forgings, some β alloys can be forged at lower temperatures, resulting in lower die costs and forging advantages for some shapes. β alloys can be heat treated over a broad range of strengths in excess of about 1400 MPa, permitting the strength/fracture toughness properties combination to be tailored to those desired.

Some of the commercially available β alloys are Beta C (Ti-3Al-8V-6Cr-4Mo-4Zr), TIMETAL 15-3 (Ti-15V-3Cr-3Sn-3Al), TIMETAL 21S (Ti-15Mo-3Nb-3Al-0.2Si), TIMETAL 10-2-3 (Ti-10V-2Fe-3Al) and Beta-CEZ (Ti-5Al-2Sn-2Cr-4Mo-4Zr-1Fe)

where they find primary usage in the aircraft industry. More recently, a burn resistant fully β alloy was developed separately by Pratt & Whitney [*Hansen 1996*] and Rolls-Royce plc. [*Voice 2004*]/ Birmingham University [*Loretto 2002*] known respectively as Alloy C (Ti-35V-15Cr) and BuRTi (Ti-25V-15Cr-2Al-0.2C wt%). The low cost, high strength BuRTi alloy has been developed for blade applications at elevated temperature to reduce the potential risk of titanium fires [*Bache 2002*].

2.1.3.4 Non equilibrium phases in α, α+β and β alloys

All Ti alloys develop non-equilibrium phases if they are cooled sufficiently rapidly and/or subsequently aged within the two phase region. The influence of the extent of beta stabilisation upon these phase transformations are most conveniently represented on a pseudo phase diagram as illustrated in Fig. 2-2. This diagram shows that as the beta equivalent is increased the temperature at which martensite starts to form (M_s) decreases until at a sufficiently high value of β stabilisation martensite is not formed on quenching to room temperature - as noted above when discussing stable β alloys. As in all martensite transformations [*Otte 1970*, *Williams 1973*] the high temperature phase (in the present case β phase) transforms, mainly by a shear mechanism to produce a different crystal structure. At high M_s temperature and low cooling rate, martensite forms colonies of parallel-sided plates which are related to the β matrix by the Burger's orientation relationship $(0001)_\alpha$ // $\{110\}_\beta$ and $<11\bar{2}0>_\alpha$ // $<111>_\beta$. On the other hand, alloys with a low M_s temperature and high cooling rate will produce individual plates with no apparent orientation relationship with the β matrix. The hexagonal α' martensite is supersaturated in β stabilisers and, upon annealing in the (α+β) phase field, decomposes to α+β by precipitating incoherent β particles at dislocations or β phase layers at plate boundaries. With increasing solute content the

hexagonal structure of the martensite becomes distorted, α' martensite loses its hexagonal symmetry and orthorhombic martensite (α") is formed [*Williams 1973*]. The α" martensite has a similar lattice correspondence with the β phase and is internally twinned on the $\{111\}_{\alpha''}$ planes [*Polmear 1995*]. The martensite in Ti alloys does not confer the high hardness seen in steels but importantly subsequent heat treatment gives rise to a fine microstructure, which is highly relevant to the development of microstructures in powders when they are heat treated (or hot isostatically pressed (HIPped)) in the two phase region.

When alloys which are highly β stabilised are cooled rapidly two other phase transformations may take place. Firstly the alloy may form athermal or isothermal omega (ω) depending on the alloy composition and processing condition or secondly β phase splitting (β') may take place, as shown in Fig. 2-2. The formation of omega does not involve diffusion and is illustrated in Fig. 2-3, where it is shown that effectively the new phase is formed by collapse of the {111} of the β phase. The omega phase is unstable in Ti alloys at higher temperatures but it can act as a precursor for precipitation of alpha during ageing of alloys such as Ti5553 which are heavily beta stabilised [*Boyer 2005*]. Beta phase splitting (β'), which does require some diffusion since two bcc phases of different compositions are formed, may also play a part in precipitation of alpha in quenched and aged alloys which are highly beta stabilised [*Williams 1971, Wang 1988*].

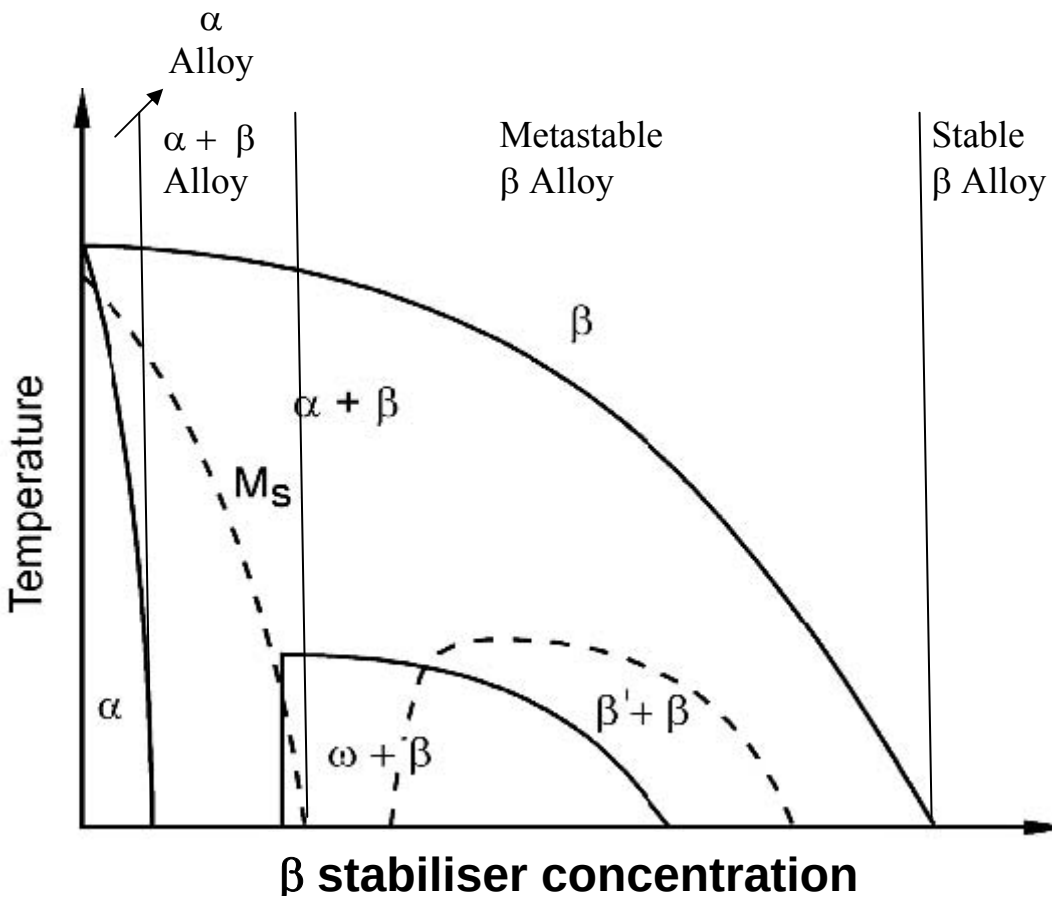

Fig. 2-2 Pseudo-binary section through a β isomorphous phase diagram, M_S-martensite start temperature [*Lütjering 2003*].

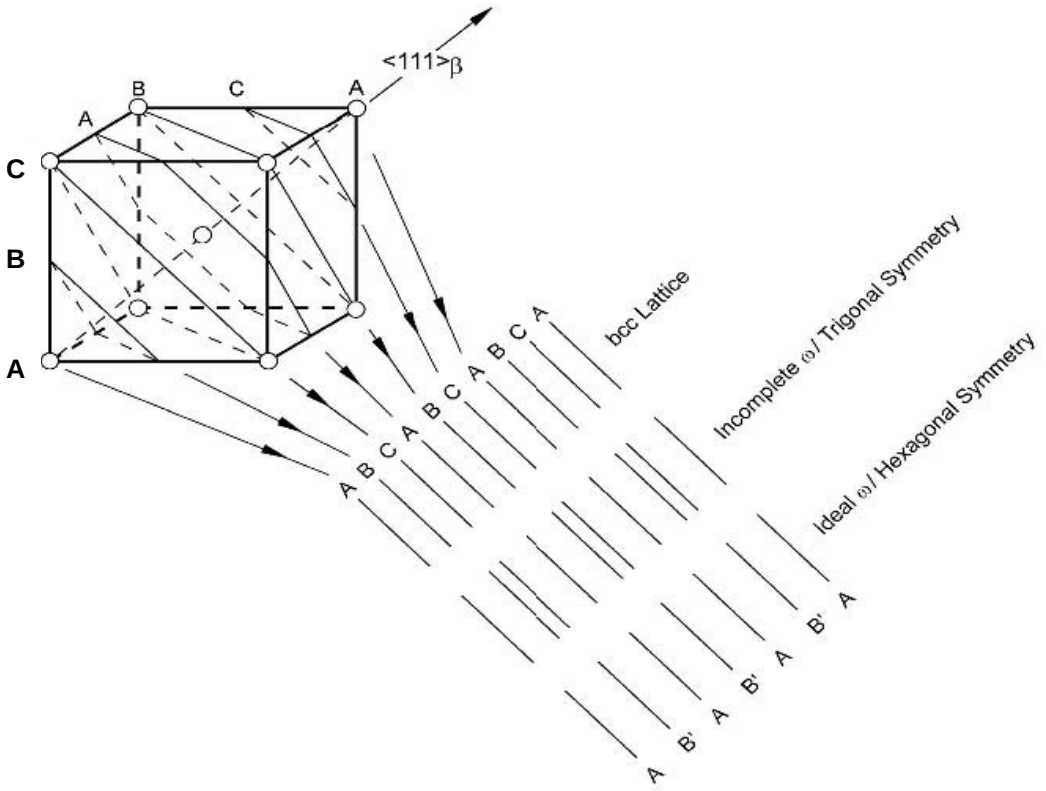

Fig. 2-3 Representation of the β → ω transformation showing the (222) planes of the bcc lattice [*Collings 1994*].

2.1.4 Mechanical properties

2.1.4.1 Deformation mechanism

Hexagonal α titanium (hcp) has an axial ratio of **c**/**a** =1.587 and is elastically and plastically anisotropic. Slip occurs predominantly in the close-packed directions with Burgers vector **a** = $\frac{1}{3}<11\bar{2}0>$ on the basal planes (0001) or prismatic planes $\{1\,\bar{1}\,00\}$ (Fig. 2-4 (a)). This **a**-slip, however, does not provide any dimensional change along the c-axis. In order for hcp metals to exhibit good ductility, an additional deformation mode contributing to the strain in the c-direction is necessary. Secondary slip on the

first order pyramidal planes $\{10\bar{1}1\}$ or second order pyramidal planes $\{\bar{1}\,\bar{1}\,2\,2\}$ with Burgers vector **(c+a)** $=\frac{1}{3}<11\bar{2}3>$, is important in providing the additional slip system for general plastic deformation, has also been reported by various researchers [*Cass 1970*, *Jones 1981*, *Numakura 1986*] (shown in Fig. 2-4 (b)). The combination of **a** and **(c+a)** slips provide sufficient number of slip systems necessary for general deformation resulting in potentially reasonable ductility in titanium. The stress to activate **(c+a)**-dislocations is, however, considerably higher than that required to activate **a**-dislocations so that titanium is not as ductile as most fcc metals. Besides slip, titanium also deforms readily by twinning on the $\{10\bar{1}2\}$, $\{11\bar{2}1\}$ and $\{11\bar{2}2\}$ planes [*Rosi 1953*, *Churchman 1954*, *Kocks 1967*], and twinning is especially important for plastic deformation and ductility at low temperatures if the stress axis is parallel to the c-axis and the dislocations with a basal Burgers vector have no shear stress acting upon them and thus do not move. Increasing concentrations of solute atoms in α titanium, such as oxygen or aluminium, suppress the occurrence of twinning. Therefore, twinning as a deformation mode to allow shape changes parallel to the c-axis plays a major role only in pure titanium or in CP titanium with low oxygen concentrations [*Paton 1973*].

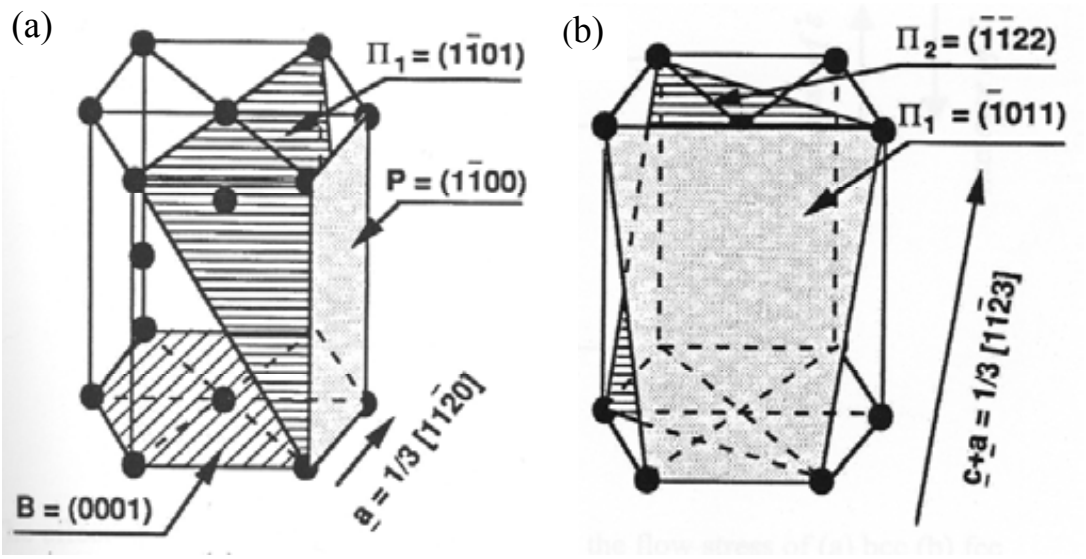

Fig. 2-4 Slip systems in titanium: (a) basal (B), prismatic (P) and first-order pyramidal (Π_1) slip planes containing the Burgers vector a=$\frac{1}{3}<11\bar{2}0>$; (b) first and second-order pyramidal (Π_2) slip planes containing the Burgers vector c + a=$\frac{1}{3}<11\bar{2}3>$ [*Naka 1991*]

Plastic deformation in (α+β) alloys is more complex as deformation occurs in two phases which have different responses to stress. The operative slip system in β phase is the same as those for bcc metals; in Ti-V alloys the slip direction was found to be $<111>$ with {110}, {112} and {123} as possible slip planes [*Breedis 1969*, *Paton 1970*].

2.1.4.2 α alloys

The tensile strengths of commercial titanium alloys range from 345 MPa to more than 1300 MPa [*Polmear 1995*] depending on the type of alloy, alloying elements and the

heat treatment to which the alloys were subjected. In general, α and near α alloys have the lowest strength amongst the titanium groups and they display good ductility especially at low temperature. Near α alloys can have better strength retention with temperature than (α+β) alloys. Their mechanical properties are also comparatively insensitive to microstructure and heat treatment, which is mainly done to increase creep strength. Near α alloys such as Ti-11 (Ti-6Al-2Sn-1.5Zr-1Mo-0.35Bi-0.1Si) and Alloy 829 (Ti-5.5Al-3.5Sn-3Zr-1Nb-0.25Mo-0.3Si) have better creep resistance properties up to temperature above 500°C than (α+β) or β alloys. It is believed that the basketweave microstructure of the alloys and the small addition of Si lead to the improvement in creep properties [*Rhodes 1986*]. An alloy such as TIMETAL 834 heat treated high in the (α+β) phase field, which exhibits primary α plus transformed β microstructures, can be used at operating temperatures of about 600°C [*Polmear 1995*].

2.1.4.3 (α+β) alloys

The mechanical properties of (α+β) alloys are very sensitive to the microstructure; the morphology and distribution of the phases; the grain size and shape; and the texture [*Seshacharyulu 2002*]. The basic correlation between microstructural features and tensile strength, high cycle fatigue (HCF), and fracture toughness properties, are reviewed briefly in this section.

In the (α+β) alloys three distinctly different types of microstructures can be obtained by changing the thermo-mechanical processing route: (1) β transformed lamellar structures; (2) fully equiaxed structures; (3) so-called bi-modal (duplex) microstructures containing equiaxed primary α in a lamellar (α+β) matrix. β

transformed lamellar microstructures (Fig. 2-5 (a)) can be obtained fairly easily in the final steps of the processing route by an annealing treatment in the β phase field (β recrystallisation) followed by slow cooling. The α phase, nucleates preferentially at grain boundaries and has the classical orientation relationship with one of the grains, so that in principle 12 different orientation alpha lamellae can form within one beta grain. The grain boundary α grows into the β grain as parallel plates belonging to the same variant of the Burgers relationship (so-called α colony) and continues to grow into the β grain interior until they meet other α colonies. The individual α plates are separated within the α colonies by the retained β matrix, which are often called α and β lamellae resulting in lamellar microstructure. Each of pre-existing beta grain consists of one or more alpha colonies, depending on cooling rates, within which the alpha laths are parallel and have the same orientation. The size of pre-existing beta grains and the number of colonies in the beta grain determine the size of the alpha colonies. With increasing cooling rate the size of the α colonies as well as the thickness of the individual α plates become smaller. Colonies nucleated at β grain boundaries cannot fill the whole grain interior anymore and colonies start to nucleate also on boundaries of other colonies. To minimise the overall elastic strains, the new α plates nucleating by "point" contact on the broad face of an existing α plate tend to grow nearly perpendicular to that plate. This selective nucleation and growth mechanism in combination with the smaller number of α plates within the colonies leads to a characteristic microstructure called "basket weave" structure or Widmanstätten structure [*Lütjering 2003*].

The process for obtaining the so-called bi-modal (duplex) microstructure (Fig. 2-5 (b)) can be divided into four different steps: (i) homogenization in the β phase field; (ii)

deformation in the (α+β) phase field; (iii) recrystallisation in the (α+β) phase field and (iv) the final aging and/or stress relieving treatment. For a fully equiaxed microstructure (Fig.2-5 (c)), there are two possible process routes. In the first case, the processing route is identical to the route for obtaining a bi-modal microstructure up to the recrystallisation process in step (iii). If now the cooling rate from the recrystallisation annealing temperature is sufficiently low, only the α primary grains will grow during the cooling process and no α lamellae are formed within the β grains, resulting in a fully equiaxed structure with the equilibrium volume fraction of β phase located at the 'triple-points' of the α grains. The second possibility to obtain a fully equiaxed microstructure is to recrystallise in step (iii) of the processing route at such a low temperature that the equilibrium volume fraction of α phase at that temperature is high enough to form the fully equiaxed microstructure directly from the deformed lamellar structure during the recrystallisation process [*Lütjering 2003*].

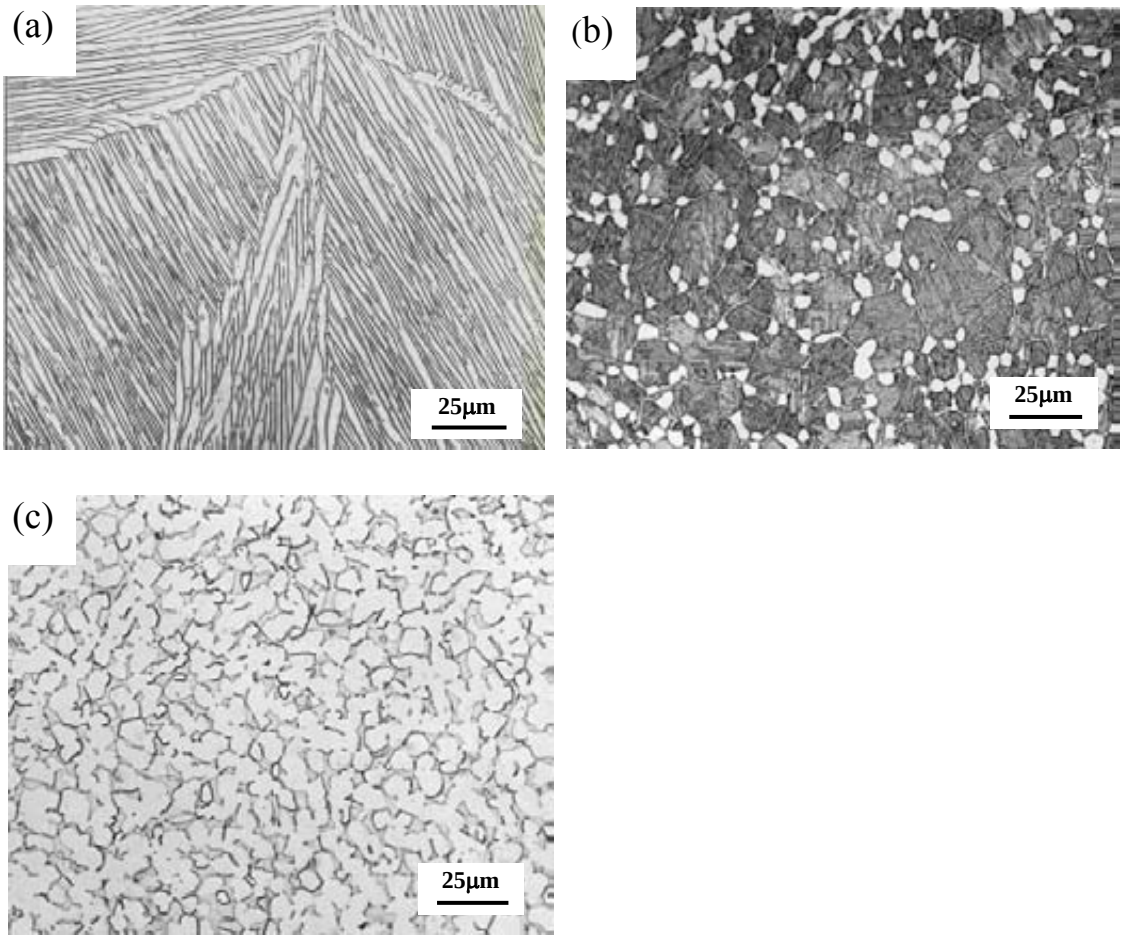

Fig. 2-5 Three distinctly different types of microstructures obtained by different thermo-mechanical processing routes: (a) β transformed lamellar structures; (b) so-called bi-modal (duplex) microstructures; (c) fully equiaxed structures [*Lütjering 2003*]

The most influential microstructural parameter on the mechanical properties of lamellar microstructures is the α colony size, which is controlled by the cooling rate from the β heat treatment temperature, because the α colony size determines the effective slip length in the lamellar microstructures. With increasing cooling rate the α colony size is decreased with a commensurate reduction in effective slip length and a corresponding increase in yield stress. As the cooling rate is increased the ductility

and HCF increase, while the fracture toughness decreases if the cooling rates do not result in the formation of martensite. The most influential microstructural parameter on the mechanical properties of bi-modal microstructures is the β grain size, which is about equal to the distance between primary α (α_p) grains or particles. The β grain size is therefore determined by the volume fraction of α_p, formed at the recrystallisation annealing temperature, and by the α_p size, which is mainly influenced by the amount of deformation during working and the cooling rate from the homogenization temperature in the β phase field. For the whole range of commercial cooling rates (30-600°C/min) the α colony size (slip length) of bi-modal microstructures is about equal to the β grain size, and therefore much smaller than in β transformed lamellar microstructures. Bi-modal structures should therefore exhibit a higher yield stress, a higher ductility, a higher HCF strength and a lower fracture toughness than fully lamellar microstructures, when compared at constant cooling rate. The mechanical properties of fully equiaxed microstructures are primarily influenced by the α grain size. Since the α grain size determines the slip length, the qualitative correlation between slip length and mechanical properties for the α colony size of β transformed lamellar microstructures can also be used here. Fully equiaxed microstructures with small α grain size exhibit a higher yield stress, a higher ductility, a higher HCF strength and a lower fracture toughness.

As mentioned before, the strength and ductility of (α+β) alloys are strongly dependent on microstructure and further enhancement in strength can be achieved by variations in thermomechanical processing. They replace α alloys for medium temperature applications up to 400°C as they offer the prospect of relatively higher tensile strength

but this is generally accompanied by a reduction in ductility. The mechanical behaviour of (α+β) alloys is also strongly influenced by alloying elements which determine the volume fraction of α and β phases. As a rule of thumb, the strengths of (α+β) alloys are the mixture-rule averages of those of their constituent elements. Strengthening is achieved primarily in the α phase by adding elements such as Al, Sn, C, N and O, which are potent solid solution strengtheners and α stabilisers. β stabilisers such as V, Mo and Cr stabilise the β phase but at low concentrations these only confer a weak solid solution strengthening in the alloys. A further increase in strength for (α+β) alloys is normally achieved by solution treatment and elevated temperature ageing which decomposes the β phase that was retained upon quenching. One example is the solution treatment of Ti-6Al-4V high in the (α+β) phase field before being quenched and aged at about 500°C. The resulting microstructure consists of equiaxed α in a fully transformed β matrix, which increases the tensile strength to about 1000 MPa with good creep resistance up to 380°C [*Polmear 1995*].

2.1.4.4 β alloys

The most important factor which influences the strength of β alloys is the fraction and distribution of α and this is strongly influenced by the extent of β stabilisation and hence by composition. There are other factors, such as trace element additions, heat treatment, and exposure, which can affect the mechanical properties of β alloys. In the case of fully stabilised beta alloys such as Alloy C and BuRTi (which are discussed later in this review), α does not precipitate during ageing but may form during exposure at service temperatures.

β alloys can be cold worked and precipitation hardened by low temperature ageing to precipitate α from the β microstructure and as noted earlier precipitation of α can be influenced by omega and/or by beta phase splitting which promote much finer precipitation than is possible with alloys such as Ti-6Al-4V where nucleation is controlled by the beta grain boundaries. Strengthening is achieved from the combination of solid solution hardening of the β phase by elements such as Mo, V, Cr and Fe and by precipitation hardening. In alloys such as Beta III, cold deformation can be carried out at room temperature prior to ageing, where nucleation of finely dispersed α precipitates on dislocations can further increase the tensile strength to as high as 1400MPa [*Polmear 1995*]. Even though the tensile strengths of most β alloys are higher than α or (α+β) alloys, they are less commonly used at present than α or (α+β) alloys.

Two high performance titanium alloys, Ti-6Al-4V and BuRTi (Ti-25V-15Cr-2Al-0.2C) are focused on in this thesis and details of their mechanical properties will be introduced in later sections.

2.1.5 Applications

Titanium alloys were first introduced in the Pratt and Whitney J57 engine in 1952 [*Polmear 1995*]. The main stimulus for the rapid development of titanium alloys over the past 50 years has come from the aerospace industry, where there has been a critical need for new materials capable of accommodating increased engine efficiency and performance, while reducing overall weight. The development of high strength, low density, creep and fatigue-resistant materials continues to play a major role in aero-engine advances. Titanium alloys are generally characterised by excellent

strength-to-weight ratios and corrosion resistance, good elevated temperature properties and an oxidation limit of ~500°C (see Table 2-1). This has resulted in a progressive increase in their use for airframe and aero-engine components (fan blades, compressor blades and discs, stator vanes, inlet and outlet guide vanes and casings), from under 5% (total weight) in the mid 1950s to currently ~30% [*Boyer 1995*]. Fig. 2-6 shows typical materials used in the Rolls-Royce Trent 800 aero-engine and it can be seen that titanium takes a significant share of the materials used.

Table 2-1 Properties for selected titanium alloys, steels and superalloys [*Boyer 1994*]

Property	α–Ti (Ti-5Al-2.5Sn)	Near α–Ti (Ti-6Al-2Sn-4Zr-2Mo)	α/β–Ti (Ti-6Al-4V)	β–Ti (Ti-13V-11Cr-3Al)	Plain carbon steel (AISI 1045)	18-8 Stainless steel (301)	Inconel 718
Density ρ (g/cm^3)	4.8	4.54	4.43	4.84	7.9	7.8	8.4
Yield strength (MPa)	805	895	925-1100	1170	530	215-760	1190
Tensile strength (MPa)	860	980	990-1170	1220	625	540-1450	1430
Ductility at 20°C (%)	16	15	10-14	8	12	10-30	21
Creep limit (°C)	250-350	450-500	350-400	300	450	600	1090-1093

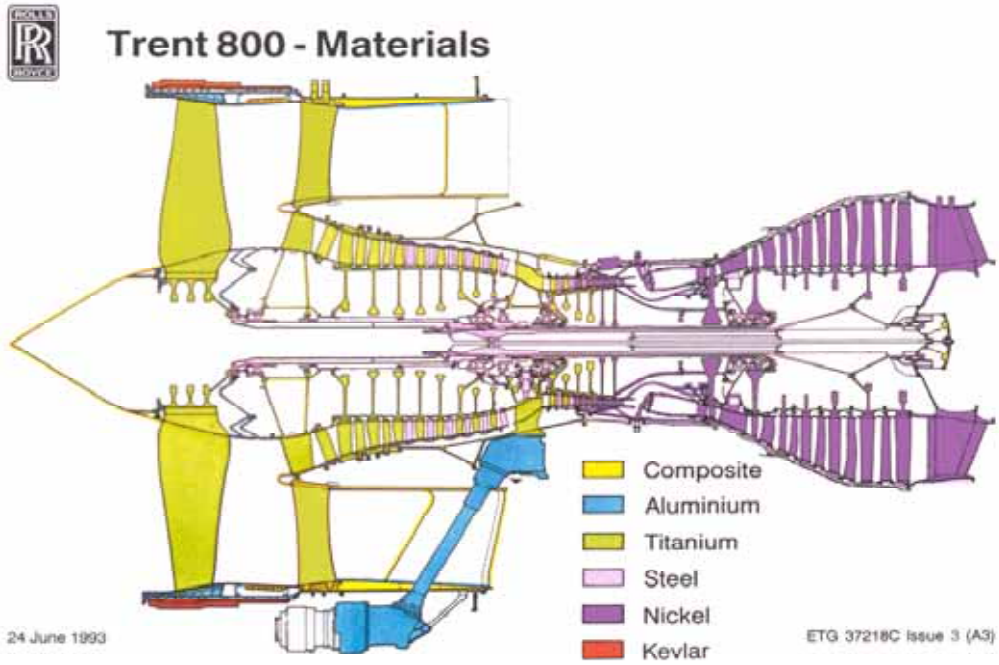

Fig. 2-6 Typical materials used in Trent 800 aero-engine (courtesy of Rolls-Royce Plc)

The good formability and corrosion resistance of α alloys make them a suitable candidate for non-structural applications in an aircraft. They are used for floor support structure in the lavatory system, clips and brackets, and ducting system. Alloys with high creep resistance such as CP Ti and Ti-6-2-4-2S are used for elevated temperature rotating components such as blades, discs and rotors at temperatures up to about 540°C. TIMETAL 834, which has a reported maximum use temperature of 600°C [*Neal 1985*], can be used in the RR Trent 800 for compressor discs in the last two stages of the intermediate pressure compressor, and the first four stages of the high pressure compressor. This alloy is used with an α/β solution treatment and age at a minimum RT tensile strength of 930 MPa.

Ti-6Al-4V is one of the most important titanium alloys, which can be used in all product forms including forgings, bar, castings, foil, sheet, plate, extrusions, tubing and fasteners, and probably 80-90% of the titanium used on airframes has been this alloy. Its application will be discussed in the following section. TIMETAL 6-6-2 can be used at higher strengths than Ti-6Al-4V, up to about 1170 MPa after solution treating and ageing. It was used extensively in the landing gear support structure of the Boeing 747 owing to its superior corrosion resistance to the low alloy steels, and it provided a weight saving, for applications such as drag braces, torsion links, and bell cranks. TIMETAL 6-2-4-6 was developed by Pratt and Whitney to provide a high strength alloy which can be used for moderate temperatures, up to about 315 °C. It is used primarily for military engines, such as the F-100 and F-119, at a yield strength level of 1035 MPa. The damage tolerance characteristics of this alloy are not as good as those of Ti-6Al-4V or TIMETAL 6-2-4-2 so it is not used in commercial engines owing to the shorter inspection intervals which would be required.

One of the earliest β alloys used is the Ti-13-11-3 (Ti-13V-11Cr-3Al) on the SR-71 "Blackbird" plane. It was used for wing and body skins, frames, ribs and landing gears. The primary use of these alloys today is for aircraft springs. TIMETAL 15-3 is another β alloy, which is being extensively used especially for environmental control system (ECS) ducting [*Boyer 1996*].

The second largest application of titanium alloys is in the chemical industry involving the use of CP Ti tubing in heat exchangers of seawater-cooled condensers and hydrocarbon cooling systems [*Polmear 1995*]. Titanium is superior to Cu-Ni, Al-brass and Al-bronze alloys where no corrosion allowance is required for titanium tube

materials. Other chemical process equipment that use titanium as base materials are tanks and vessels, pumps, valves, scrubbers and piping. The excellent corrosion resistance of titanium alloys is the prime factor in choosing them for such applications. Besides chemical engineering applications, titanium alloys are also used in biomaterials where compatibility with both human bones and tissues makes them an excellent choice. Most applications have been with Ti-6Al-4V and CP Ti in prosthetic devices such as aortic heart valve, artificial joint and pins. Dental implants as well as orthodontic devices are increasingly using titanium alloys as base materials.

For the past few years, there has been an increasing market for titanium in the sports industry. Titanium alloys such as Ti-6Al-4V, Ti-3Al-2.5V and SP-700 (Ti-4.5Al-3V-2Mo-2Fe) are extensively used as golf clubs, bicycle frames and high performance automotive and mountain climbing equipment [*Boyer 1994*]. These equipments benefit greatly from a selection of the following properties: the low density and low elastic modulus, high tensile strength and high strength/weight ratio of titanium alloys.

2.2 Properties and applications of Ti -6Al-4V

2.2.1 Introduction

Ti-6Al-4V is a representative of (α+β) titanium alloys which are widely used in commercial and military aero-engines [*Seshacharyulu 2002*], as a blade and disc alloy in the low and intermediate pressure compressor stages of modern gas turbines. In addition to the relatively high specific strength required for rotating discs and blades, the high specific stiffness offered by this alloy is also relevant to non-rotating aerofoils or ‘stator vanes’. Since this alloy is utilised in significant volumes, including a wealth of alternative non-aerospace applications, the material is also recognised as a

cost-effective option for applications where service temperatures do not exceed 350°C [*Bache 2002*]. Depending on the application, the oxygen content may vary from 0.08 to more than 0.2% (by weight), the nitrogen content may be adjusted up to 0.05%, the aluminium content may reach 6.75%, and the vanadium content may reach 4.5%. The higher the level of these elements, particularly oxygen and nitrogen, the higher the strength of the alloy. Conversely, lower additions of oxygen, nitrogen, and aluminium will improve the ductility, fracture toughness, stress-corrosion resistance, and resistance against crack growth [*Boyer 1994*].

2.2.2 Properties of Ti-6Al-4V

The mechanical properties of Ti-6Al-4V are very sensitive to the oxygen content [*Boyer 1994*]. For industrial applications, this alloy is available in two different grades: commercial (or regular) grade with 0.16-0.20 wt% oxygen and extra-low interstitial (ELI) grade with 0.10-0.13 wt% oxygen [*Prasad 2001*]. Oxygen can promote formation of Ti_3Al (α_2) within Ti alloys. These coherent α_2 particles increase the yield stress and result in a reduction of tensile ductility. With increasing oxygen content, high cycle fatigue strength is increased and fracture toughness is decreased. Monolithic α_2 has been investigated for aerospace and gas-turbine applications because of its excellent fatigue strength at high temperatures [*Huang 1999*, *Haanappel 2002*, *Garbacz 2003*] but its poor oxidation resistance and its lack of burn-resistance, were found to limit its potential usefulness in gas turbines. Room temperature tensile properties of Ti-6Al-4V are also affected by heat treatment methods, by which tensile strength can be changed by around 200 MPa. For example, a sample annealed at 700°C and slowly cooled has a yield strength of 925 MPa, and a tensile strength of 990 MPa, whereas a sample solution treated and aged at 500°C has a yield strength of 1100 MPa, tensile strength of 1170 MPa [*Polmear 1995*]. The high

temperature strength decreases significantly as the temperature is increased (see Fig. 2-7) and Ti-6Al-4V was developed for aerospace application with temperatures that did not exceed 350°C.

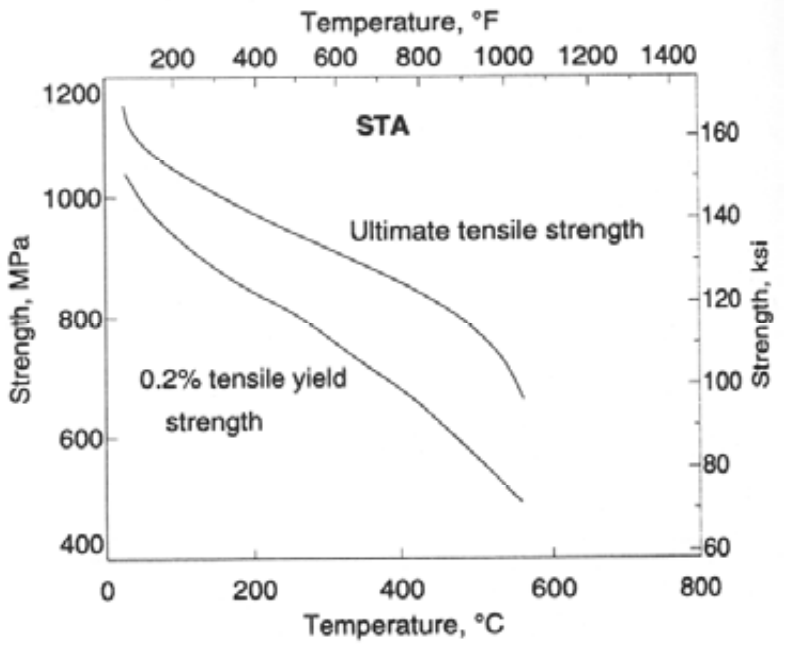

Fig. 2-7 The relationship between tensile strengths and temperature of solution treated and aged (STA) Ti-6Al-4V, STA condition: 955°C/1h/WQ (water quench), ageing 4h at 525°C and AC (air cool) [*Properties 1980*]

The fatigue and fracture behaviour of Ti-6Al-4V is greatly influenced by its microstructure. Three typical microstructures were introduced in section *2.1.4.3*. Fig. 2-8 illustrates the effect of microstructure on high cycle fatigue (HCF) strength, where the grain size of primary α is also shown. There is evidence regarding Ti-6Al-4V which indicates that superior high cycle (10^7 cycles) fatigue properties are obtained when the slip length is small [*Lucas 1973*, *Peters 1981*, *Stubbington 1974*]. Small

slip lengths accompany a fine-grain equiaxed material or fine, acicular α′ (martensite) obtained by quenching from the β phase field. There is general agreement that the Widmanstätten or colony (α+β) microstructure has decidedly poorer fatigue properties. In the coarser, equiaxed microstructure the fatigue strength is significantly lower than the finer microstructure, but it is still better than in the coarser colony microstructure [*Chesnutt 1978*]. Conversely, the fracture toughness of Ti-6Al-4V increases as the amount of transformed β (colony (α+β)) structure increases, i.e. a β–forged alloy with an acicular Widmanstätten structure has a higher fracture toughness and lower fatigue strength than the alloy forged in the (α+β) phase field with equiaxed grains of α and transformed β. This is attributed to the slower rates of crack propagation through the Widmanstätten structure. However, this structure is less resistant to the initiation of fatigue cracks resulting in a lower fatigue strength than that of the (α+β) forged alloys.

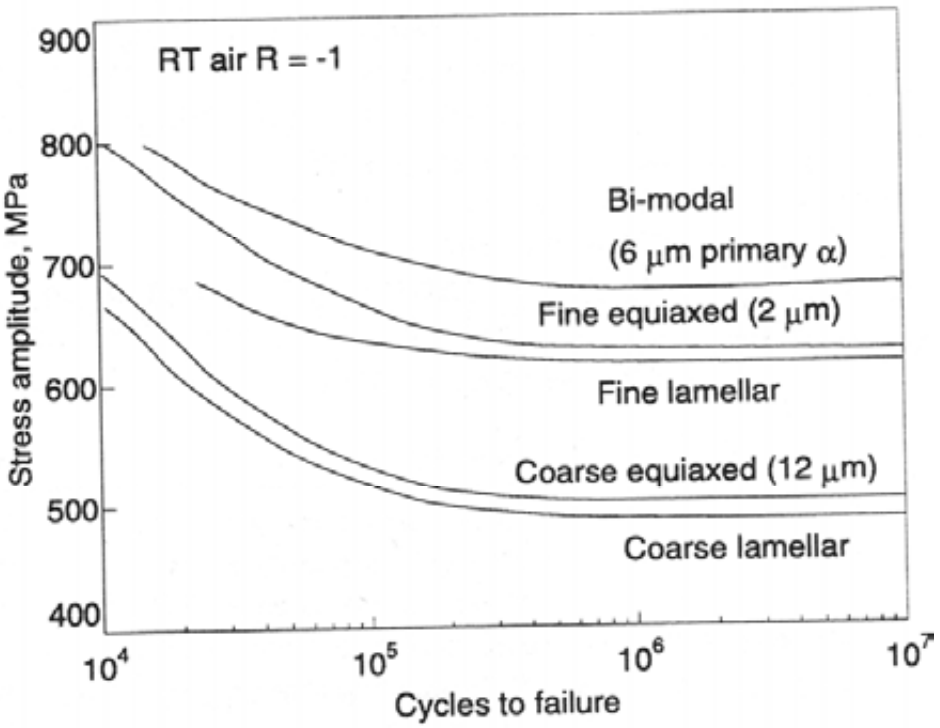

Fig. 2-8 Effect of microstructure on fatigue strength in aged Ti-6Al-4V [*Lütjering 1985*]

2.2.3 Applications of Ti-6Al-4V

Ti-6Al-4V has played a major role in the rapid development of the aerospace industry over the past 50 years. One major application area of Ti-6Al-4V alloy is aircraft structural parts, where this alloy is selected over other competing metallic materials, such as high strength aluminium alloys, because of its higher yield stress and fatigue strength (even on a density normalised basis), better corrosion resistance, higher modulus of elasticity, and higher temperature capability. Ti-6Al-V can be used in all sections of the aircraft such as fuselage, nacelles, landing gear, wing, and empennage, and good fatigue crack growth characteristics are highly desirable for such large structural parts. For example, the β transformed lamellar structure, which can be

produced by β annealing, is selected for safety critical aircraft structural components such as bulkheads because of its excellent fatigue crack growth resistance for macrocracks [*Lütjering 2003*].

Another major application area of Ti-6Al-4V alloy is rotating and non-rotating parts in aero-engines. With the limitation of maximum application temperature of about 350°C, Ti-6Al-4V is restricted in the rotating section of the engine to the fan stage, to the low pressure (LP) compressor, and to the front stages in the intermediate pressure (IP) compressor. Fan and compressor blades can experience large oscillatory stresses and, therefore, require a high fatigue crack nucleation and propagation resistance (HCF strength) in the airfoil section and good LCF strength in the attachment locations. Consequently, (α+β) forged Ti-6Al-4V blades are usually recrystallised to a bi-modal microstructure that exhibits a higher HCF strength than equiaxed or mill-annealed microstructures, as shown in Fig. 2-8. Ti-6Al-4V alloy is also the most common disk material, and the bi-modal microstructure is normally selected because of much better LCF strength and microcrack propagation resistance than the β-transformed lamellar microstructure as well as better and more reproducible properties than fully equiaxed and mill-annealed structures. For non-rotating parts in aero-engines, the good formability of Ti-6Al-4V makes it the main material for this application at temperatures below 350°C. For example, the compressor engine casing (outer-duct), which is made of rolled Ti-6Al-4V plate and fabricated by conventional sheet forming methods, has a fine grained mill-annealed microstructure for good forming properties (high ductility). For manufacture of components with complex shapes, investment casting of Ti-6Al-4V alloy can be used to replace the wrought material.

There is a limitation for the ingot-route processing with high production cost and low fly-to-buy ratio (less than 5%) that limits the extensive use of Ti alloys.

2.3 Burn resistant titanium alloys

2.3.1 Development of burn resistant alloys

Beta titanium alloys, where large amounts of alloying additions such as V, Cr and Mo contributes to their high density and cost, have so far been little used and accounted for only 1% of the total titanium market in the US aerospace industry in 1993 [*Bania 1994*]. However, their excellent cold workability and good combination of strength and fracture resistance continues to drive their development. One of the most fundamental changes in aero-engine design and performance over the last 30 years has been the progressive replacement of compressor blades, stators and discs made from steel by titanium alloys in the cooler parts of the engine [*Li 1996*]. Unfortunately, the use of conventional titanium alloys in the latter stages of the high-pressure compressor (i.e. beyond the "fire line") is prevented due to their high reactivity/propensity to ignite and burn at temperatures above ~450^{o}C, and at present heat-resistant, but heavier nickel and steel alloys are used. Burning occurs when heat extraction from the component is too low to prevent the exothermic reaction of oxidation at the metal/oxide interface from raising the temperature above the alloy's melting point. During the process the protective titanium oxide film dissolves into the metal allowing the exothermic oxidation reaction to be maintained. The oxygen activity is additionally accelerated by the high air-flows and pressures present in turbine engines [*Schutz 1994*]. Titanium ignitions in engine incidents are reported to be primarily caused by friction arising from the ingestion of foreign objects, or a prior

mechanical failure and a Ti fire is usually a secondary effect [*Kneisel 1993*]. To avoid titanium burning in aero-engines and satisfy the demands for lower weight and higher performance of advanced aircraft engines, extensive research was focused on the development of burn resistant alloys.

In the USA, Pratt & Whitney [*Hansen 1996*] developed a burn resistant alloy based on Ti-35V-15Cr, designated Alloy C. Use of a high percentage of vanadium, as the major β stabilising element, ensured that Alloy C had the highest molybdenum equivalency rating (value of 47 wt%) of any commercially available alloy, thereby making it also the most strongly β-stabilised alloy. This alloy was reported to successfully combine very attractive high temperature mechanical properties, especially strength and creep resistance (up to 600°C), together with improved sustained-combustion resistance following ignition [*Hansen 1996*]. Alloy C is being used in several critical applications in the F-119 engine that powers the F-22 advanced tactical fighter for the USA Air Force. However, the large amount of heavy alloying elements has influenced both the density (5.33 g/cm^3) and the costs of Alloy C [*Hansen 1996*]. Additionally, it has been found that if Alloy C is subjected to long time exposure at elevated temperatures, α and/or α_2 may start to precipitate [*Li 1998 a*]. Al has been introduced into the TiVCr system in order to increase the cost-competitiveness of the alloy, since low cost master alloys containing Al, V and Cr can be used. This addition further increases the tendency to precipitate alpha and carbon addition is used to counteract this effect as discussed below. The role of carbon is complex but is now understood [*Wu 2006*].

In the UK a collaborative programme between Rolls-Royce Plc. and the IRC in Materials at the University of Birmingham, resulted in the development of a competitive Ti-25V-15Cr-2Al-0.2C wt% burn resistant β titanium alloy (BuRTi), which has a good balance of room-temperature ductility, strength and high-temperature properties in combination with burn resistance up to 500^{o}C [*Li 1999 a*]. Compared with other commercially available burn resistant products, such as Alloy C and Ti-40 (Ti-25V-15Cr-0.2Si wt%) [*Zhao 2001*], the new alloy is significantly cheaper and has a lower density (5.1 g/cm^{3}). The alloy is designed to displace steels and nickel alloys of almost twice the density (steel stators/compressor blades/turbine casings) in the intermediate and high pressure compressor, operating at ~450-500^{o}C. Ti-25V-15Cr-2Al-0.2C wt% burn resistant alloy (BuRTi) offers an attractive combination of physical properties in comparison with competitive alloys currently employed in Rolls-Royce Plc. aero-engines. The alloy has an elastic modulus at room temperature of 118 GPa, which is significantly higher than for the high-temperature, high-strength creep resistant α/β alloy Ti679 (Ti-11Sn-5Zr-2.25Al-1Mo-0.2Si), which has an elastic modulus of 105 GPa. Thermal conductivity is also higher than for Ti679 at lower temperatures and at operating temperatures the thermal conductivity approaches that of the nickel superalloy IN718 [*Voice 2004*]. This is beneficial, not only with respect to burn resistance, but also from the machining standpoint, as it helps rapid heat extraction from the source. An ignition test was carried out to examine the burn resistance of the alloy under the conditions typically found in the intermediate pressure compressor: air temperature 300^{o}C, 0.965 MPa air pressure and 150 m/s air velocity. BuRTi exhibited a good burn resistance performance, with the ability to quickly extinguish itself after catching fire and repeated attempts to ignite the specimen resulted in its fracture [*Voice 2004*].

Li et al suggested that it is necessary to restrict Al to <3 wt% in BuRTi, since high levels of Al (>3 wt%) were found to cause alloy embrittlement due to the ordering of β phase into B2 in bcc structure [*Li 1998 b*]. Moreover, in other Ti alloys, Al has been reported to give rise to the precipitation of coherent, ordered α_2-Ti_3Al, which leads to intense planar slip bands and reduction in ductility of the alloy, as the dislocation movement is restricted [*Li 1999 b*]. In Ti-25V-15Cr-2Al-0.2C wt%, formation of α_2 phase can be avoided, as the coexistence of α_2 with α was reported to be only possible if the Al content was in the range of ~7-12 wt% [*Li 1998 a*, *Li 1999 a*]. The addition of relatively high levels of carbon (0.2 wt%) was found to be beneficial in terms of reduction of α precipitation, grain growth control and recrystallised grain refinement, through carbide particle formation. α precipitation can be suppressed through gettering of oxygen by Ti_2C to form $Ti(C_xO_y)$ within grains and at grain boundaries and by the C in solution interacting with oxygen [*Wu 2006*]. It was found that high levels of oxygen, which is a strong α stabilising element, promoted α precipitation and reduced ductility. Higher levels of oxygen (above 0.2 wt%) require a higher addition of C in order to limit the influence of this high oxygen content. The formation of an excessively large number of carbides would be detrimental to ductility of the alloy [*Li 1999 a*].

2.3.2 Microstructure and mechanical properties of Ti-25V-15Cr-2Al-0.2C wt% alloy

The microstructure of extruded BuRTi consists of the disordered body centred cubic (bcc) beta matrix phase and uniformly distributed carbide particles of Ti_2C, running along the main extrusion direction (as shown in Fig. 2-9). The size and distribution of the grains and carbides largely depends on the thermomechanical processing route.

The dissolution temperature of carbide particles was found to be ~1200°C [*Broderick 1996*], hence the carbide morphology may be affected by the processing route, such as forging or extrusion at 1100-1500°C. Nevertheless, any subsequent heat treatment below ~1100°C does not affect the carbide size or distribution in any reasonable time.

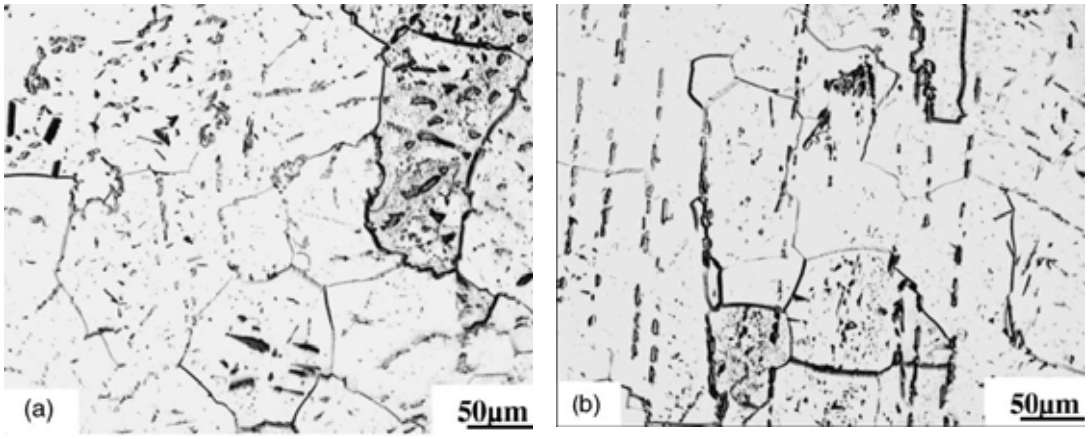

Fig. 2-9 Optical micrographs showing as-extruded microstructures of burn-resistant alloy Ti–25V–15Cr–2Al–0.2C–0.13O: (a) transverse section, (b) longitudinal section [*Li 2001*]

Voice [*Voice 2004*] made a strength comparison at both ambient and elevated temperatures between BuRTi and a conventional high temperature α/β Ti679 alloy, as shown in Fig. 2-10. The ambient temperature strength (ultimate tensile and 0.2% proof) of BuRTi appears to be slightly lower than the Ti679 alloy, however BuRTi retains its strength to beyond 550°C. Unlike metastable β titanium alloys, where α precipitation is desirable and controlled to optimise mechanical properties, the α precipitation in BuRTi alloy is a result of microstructural instability and is not desirable. It can noticeably reduce the ductility and fracture toughness of the material. With the addition of carbon the stability of this alloy is improved significantly [*Li*

1999 a], however, α still precipitates at potential application temperatures after long-term exposure. Pre-exposure heat treatments affect the distribution of α precipitates. Work by Li et al [*Li 2001*] studied the effect of heat treatment and found that pre-exposure annealing at 600, 700 and 800°C affected the distribution of α phase that precipitated following subsequent exposure at temperatures between 450 and 550°C. For a pre-annealing temperature of 600°C for 2h, a significant amount of α precipitation occurs within the grains with generally a very limited amount at grain boundaries during subsequent exposure at 450°C, and samples showed excellent microstructural and property stability. The reduced amount of precipitation of α in grain boundaries was associated with more α nucleation sites (such as dislocations) within grains instead of grain boundaries when annealing at around the β transus temperature (600-650°C for BuRTi).

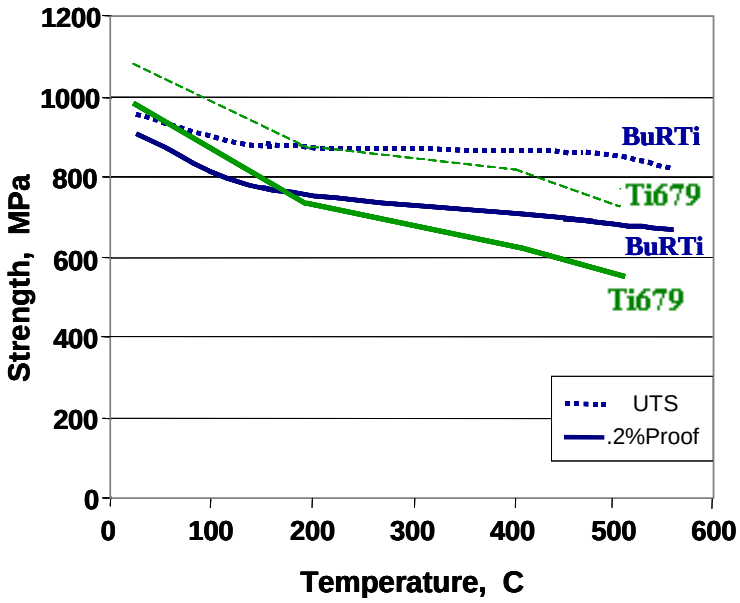

Fig. 2-10 Comparison of strength of BuRTi with α/β Ti679 titanium alloy [*Voice 2004*]

Preliminary work on the fatigue properties of BuRTi samples with polished surface (four point bending tests, R=0.1) at ambient temperature, undertaken by Pollard [*Pollard 2002*], suggested a drop of ~100 MPa in the fatigue run-out strength relative to conventional Ti-6Al-4V samples with hand-ground surface tested under similar conditions. The decrease in fatigue strength is believed to be caused by the combined effect of increased local stress concentration at large carbides and greater slip length. Coarse carbides also acted as cleavage fracture initiation sites [*Novovic 2004*]. Additionally, all fatigue specimens failed from the corners/sides, not from the tested surface, indicating that the mechanism of fatigue initiation may be associated with stress concentration at corners and hence different from being related to the controlled (polished) surface condition. Comparison of the fatigue properties at two temperatures (20 and 450^{o}C respectively, Kt=1) suggested that BuRTi did not exhibit a rapid reduction in fatigue life with increase of temperature, which is characteristic of other Ti alloys [*Voice 2004*]. At ambient temperature BuRTi had slightly inferior fatigue strength relative to the Ti679 alloy, however at 450^{o}C, the fatigue strength of BuRTi was higher than that of Ti679. The improved fatigue resistance was attributed to the change in fracture characteristics (to a fully ductile mode) at around 200^{o}C, depending on grain size.

Work by Novovic [*Novovic 2004*] reported that the differences in crystallography, together with chemistry/metallurgy of the two alloys BuRTi and conventional Ti-6Al-4V resulted in a marked disparity in the fracture properties tested under the same conditions, with lower fracture toughness for BuRTi (~40 MPa√m) than Ti-6Al-4V (~62 MPa√m), and transgranular cleavage fracture at ambient temperature, in contrast to fully ductile fracture in Ti6/4. She suggested that care must be taken when

assessing BuRTi's fracture and fatigue resistance despite the similarity in its machinability to Ti-6Al-4V.

2.4 Processing methods

2.4.1 Conventional methods

One of the disadvantages associated with titanium alloys is high primary and secondary processing costs, which, despite extremely versatile properties, limits their more extensive use [*Boyer 1996*, *Williams 1999*]. Titanium alloy components are traditionally manufactured using casting or thermo-mechanical working (such as forging). The use of titanium components made by casting has grown over the past fifteen to twenty years. This growth has occurred as the cost of castings has decreased and as the quality and capability of titanium castings have improved. This allows castings to be used in a wider range of components with a broader range of requirements. Nevertheless, for large, complex titanium components for critical defence applications, porosity and other casting defects require extensive weld repair and subsequent machining, increasing the cost of the component. In addition, as-cast microstructures may have large grains or dendrites with relatively poor mechanical properties [*Kuhn 1996*].

Forging is the principal thermo-mechanical process used to manufacture titanium components [*Kuhlmann 1988*, *Boyer 1994 b*], which is consistent with thermo-mechanically processed components being the largest percentage of titanium alloy products sold each year. Over the past two decades, titanium forging technology has progressed dramatically, particularly with regards to two aspects. First, the ability to achieve shapes that are close to those of the desired component has greatly improved.

Second, the ability to manipulate and control the microstructure required to meet different properties has become accepted as standard. The cost of forgings always is however a limitation in their use. For example, the ingot-route can result in fly-to-buy values of less than 5%, so that 95% of the original ingot has to be recycled. It is thus important to develop processing routes which lead to a minimal amount of material loss and to keep costs down. Powder metallurgy, which is an appropriate method to achieve a net-shape or near net-shape [*Wu 2003*, *Jovanović 2006*], can offer this possibility. There are several methods of processing powder to net shape and a considerable effort is focused currently on hot isostatic pressing (HIPping).

2.4.2 Powder metallurgy

Powder metallurgy (PM) is an energy efficient technology given its high precision and net shape capability. In recent years, the application of PM parts has enjoyed considerable growth owing to the advantages of the route over conventional methods [*Simchi 2003*]. Among various material processing, PM is the most suitable to produce composite materials due to the large difference in melting points [*Cho 2001*]. Powders can often be the end products in themselves and are used in many industrial applications. Production of porous products such as self-lubricating bearings and filters is made easy because of PM. Refractory metal products and composite structures such as cemented carbides are also produced using this route [*Cahn 1991*]. Increasing application is in the more demanding area of aerospace technology where PM is preferred not only for the attractive high-temperature properties and desirable microstructures, but also for the near net shape of the end products.

In general, PM can be divided into two major categories:

- . Elemental PM, in which a blend of elemental powders, along with master alloy or

other desired additions (a binder), is cold pressed into shape and subsequently sintered to higher density and uniform chemistry.

- Prealloyed PM, which is based on hot consolidation of powder produced from a prealloyed stock.

Processes that use binders produce parts at relatively low cost, and numerous pores remain in the parts [*Minabe 1990*]; this technique is typically used for iron [*Automotive 1984*], copper [*Stevenson 1984*], and heavy-metal [*Penrice 1984*] alloys. Fully dense high-performance components from aerospace alloys, such as nickel [*Ferguson 1984*], titanium [*Froes 1984*], aluminium [*Stevenson 1984*], and beryllium [*Beryllium 1984*] are produced using techniques such as HIPping (with no binders). This thesis is focussed on the development of PM to manufacture potential components in aerospace application, particularly in the gas turbine engine, and therefore prealloyed PM process rather than blended elemental method is described in detail.

Prealloyed PM can broadly be divided into the following processing steps: production of powder; compaction and sintering, or hot compaction process under isostatic pressure conditions which combines compaction and sintering into a single step and is now becoming increasingly popular for fabricating complex shape components and load bearing high temperature parts.

2.4.2.1 Production of powder

The size, shape and purity of the powder are important parameters in determining the quality of a PM product. Considerable effort has gone into developing a variety of techniques to manufacture metal and alloy powders with the required properties. Atomisation is a process of breaking up liquid metal or alloys into fine droplets and

allowing them to solidify as powder, which is a flexible and widely used PM method. This method affords the greatest control over the alloy properties [*Shao 1994*]. Because of the versatility, purity and the control of powder shape inherent in the process, atomisation is becoming increasingly popular as a route for large scale manufacture with attendant reduction in costs of components. Commercial methods of atomisation include: water atomisation, gas atomisation, centrifugal atomisation (e.g. plasma rotating electrode process), vacuum (soluble gas) atomisation and ultrasonic atomisation. Rapid solidification, which is inherent in this process, can affect the processing of the material by increasing its microstructural homogeneity, by extending its solid solubility and/or by supporting the formation of metastable phases [*Greer 1994*]. Each powder particle is considered as a tiny ingot, having the same composition as the melt prior to atomisation [*Lawley 1978*].

Two techniques are introduced in this thesis: gas atomisation and plasma rotating electrode process (PREP). Gas atomisation is a well established rapid solidification processing technique used to produce superalloy, high alloy steels, aluminium alloys, and more recently titanium alloy and aluminide powders [*Rabin 1990*]. A schematic diagram of gas atomisation process is shown in Fig.2-11. Molten metal is poured into a tundish with a ceramic nozzle which controls the shape and size of the falling metal stream. This stream passes through an atomising nozzle system, in which high velocity jets of an atomising gas (argon or helium) strike and disintegrate the stream into fine droplets. These droplets are carried at high velocity with the atomising gas stream inside the chamber and solidify owing to heat loss by convection [*Thummler 1993*].

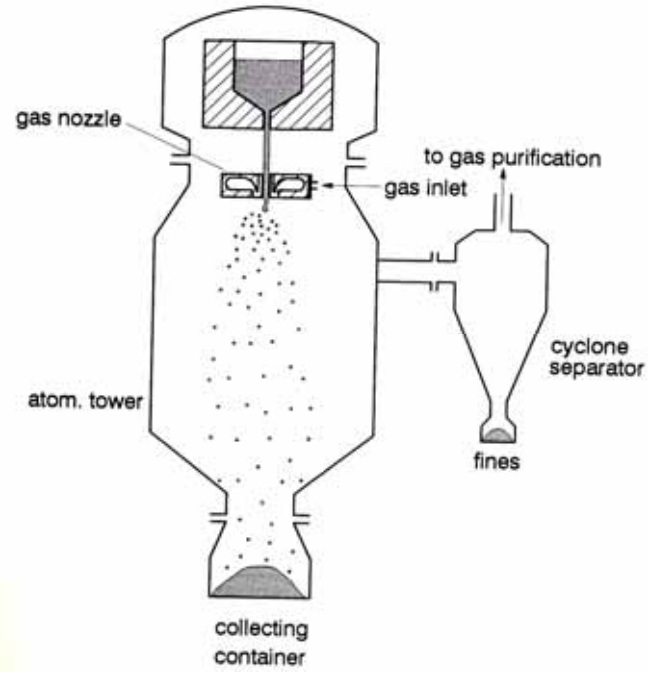

Fig. 2-11 Vertical gas atomisation unit (schematically) [*Thümmler 1993*]

Gas atomisation thus occurs by transferring kinetic energy from the atomising medium (gas) to the liquid metal. The most widely known model of the liquid break-up process and the formation of droplets which solidify as powder particles in this process has been the wave-ligament model (see Fig. 2-12). This model describes the disintegration of a sheet of liquid being swept by a compressible gas phase. It assumes that a wave is formed and is growing at the surface of the sheet causing its tearing into ligaments which subsequently spheroidise (i.e. break down into droplets). The energy of the gas jets is so large that the broken ligaments are further fragmented into droplets which can reach very small sizes [*Lawley 1977; Shinde 1977*]. Gas atomisation produces spherical (or near spherical) powders, as a result of surface tension. Particles with irregular shape are considered to be due to the formation of solid surface layers caused by the reactions between the gas and the melt [*Thümmler 1993*].

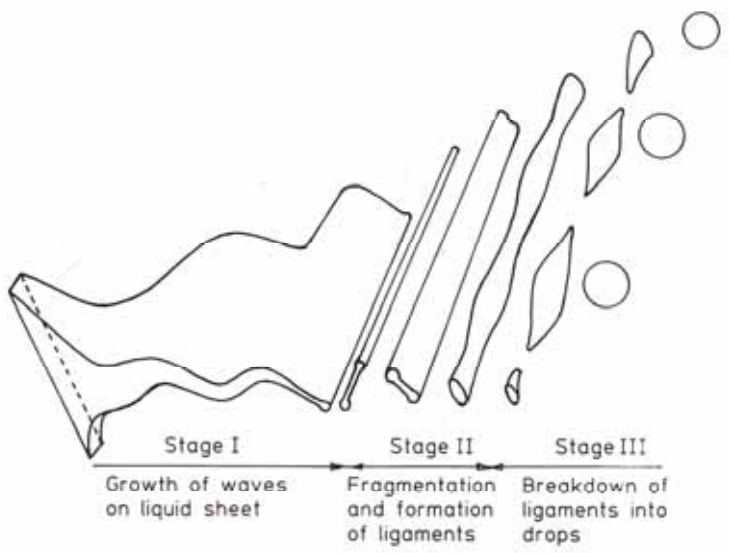

Fig. 2-12 Mechanism of droplet formation in gas atomisation [*Lawley 1981*]

There has been some concern about the production of particles which contain trapped gas in gas atomisation, since after HIP consolidation the argon in these may have deleterious effects on the properties of the material.

(i) Internal porosity of GA powders

All gas atomised powders contain porosity, regardless of the atomising media or melting process. The internal pores have no contact with the particle surface, i.e. they are closed. The amount of internal porosity increases with the particle size [*L'Estrade 1988*]. Several different mechanisms have been suggested for the pore formation:

- *Particle collision* which has not been proved to be the mechanism of pore formation [*L'Estrade 1988*]; it is only known to produce satellite particles.
- *Gas formation in the melt* is the mechanism where the molten metal before the atomisation contains interstitial elements (O, C, H, N). These elements may have

very limited solubility in the solid state, so gas is evolved at the liquid/solid interface and trapped inside the powder particle forming pores during solidification. The formation of bubbles during solidification is an important source of porosity, resulting in smooth, spherical pores.

- *Gas entrapment* is considered to be the most important mechanism. As was discussed previously, in atomisation the molten metal is broken up into ligaments, which subsequently form the metal droplets (particles). It has been suggested that at an intermediate stage of the droplet formation parachute-like membranes are formed. When these fragments of the melt are closing to form particles, gas is easily trapped in them. Although some of this gas is expected to diffuse away, and some might dissolve into the metal, there will be a sufficient amount of gas left to form pores in solid particles. This is also called the bag break-up process [*Rabin 1990*], as shown in Fig. 2-13.
- *Solidification shrinkage* is the mechanism according to which the centre of the liquid droplet solidifies last and often results in pore formation due to the volume change associated with solidification. These pores are not expected to contain gas.

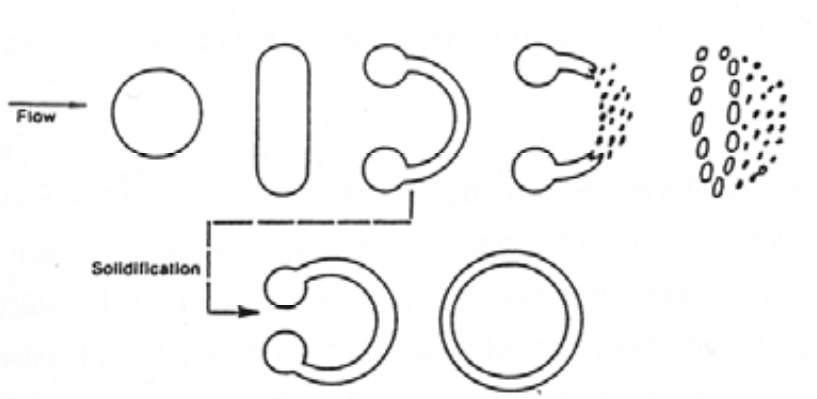

Fig. 2-13 Schematics of the bag break-up process model for the formation of porosity during solidification [*Rabin 1990*]

(ii) Effects of internal porosity

- Hot consolidation will not totally close the pore if the gas is insoluble in the solid material; a quick calculation shows that for typical HIPping conditions the volume of a pore will be reduced by a factor of about 300.
- Another detrimental effect is the thermally induced porosity (TIP) i.e. an increase in the total pore volume during heat treatment. After consolidation when the material appears fully dense, the entrapped gas exists in small pressurised bubbles, as noted above. Upon heating at high temperatures in the absence of pressure, these gas bubbles tend to coarsen (via vacancy diffusion), resulting in density decrease and macroscopic gas porosity [*Rabin 1990*]. Most gas atomised titanium alloy powders are produced using argon as the atomising gas. Therefore the gas entrapped inside the powder particles is usually argon. Coarsening in the absence of vacancies requires diffusion of the trapped argon but this has virtually no

solubility and thus will not easily diffuse. Expansion of the pores will also occur when the strength of the metal at the heat treatment temperature is less than the HIPping pressure used, since gas at this pressure is present in the pore or bubble.

The purity of the powder material produced is of paramount importance, therefore the chemical composition of the powder should be uniform throughout. Because of the high specific surface of a powder, a large amount of the material is exposed to the environment during production and processing, which can pick up chemical impurities. Several types of impurities have been detected in the atomised powders, including:

-dissolved impurities (in the molten metal)

-surface impurities (e.g. oxide films)

-contamination by other metal powders (can be eliminated by clean equipment and a careful operation practice) [*Thümmler 1993*]

-contamination as a result of the interaction between the molten metal and the ceramic spray nozzle, in some cases, ceramic bits from a damaged spray nozzle

The driving force for the development of centrifugal atomisation processes has been the cleanliness of the product. These processes avoid gas jets and atomisation nozzles. Therefore the liquid metal continues to remain pure during the entire process. Thus this method is eminently suited for atomising reactive metals such as titanium and zirconium. Plasma rotating electrode process (PREP) is now commercially well developed, which is a direct energy transfer process, where a rod is rotated at high speed and simultaneously melted at one end. The melting is carried out with a tungsten electrode as in a vacuum plasma furnace or with another electrode of the

same material. The atomised liquid droplets are cooled by convection either in vacuum or through the helium gas present in the vacuum chamber and the powder is collected at the bottom *[Cahn 1991]*. A schematic diagram of a PREP atomisation chamber is shown in Fig. 2-14.

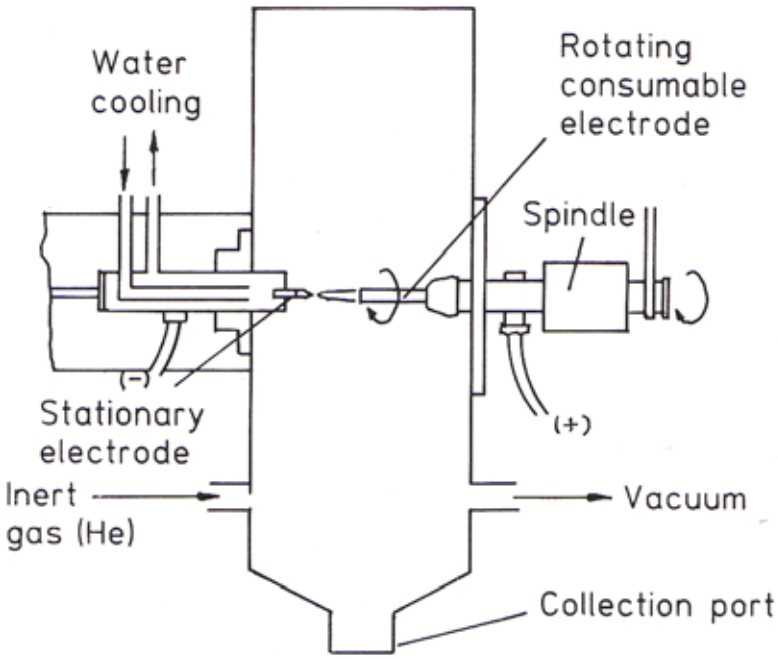

Fig. 2-14 Schematic of plasma rotating electrode process (PREP) [*Lenel 1982*]

In this technique, the molten pool is rotated at high speed till the liquid metal spreads towards its periphery and forms a toroidal rim. Owing to instability at the rim, the sheet of the liquid breaks up into fine threads, which in turn break into droplets. It may also happen that the time of flight of the liquid droplet to hit the chamber walls is smaller than the time required for solidification. In such instances, the particles appear as flat discs solidified on impact with the walls. Compared to gas atomised powder,

PREP powder is relatively coarse [*Moll 1998*]. PREP powder is free from satellites that are commonly seen in gas atomised spherical powder. Various process modifications have been investigated to produce finer powder. The use of a large diameter disk electrode rather than a bar electrode has been reported to decrease the mean particle size by more than 40% and to reduce the cost of input material [*Nachtrab 1993*]. PREP powder is spherical, has good flow characteristics, and a tap density of 65% of theoretical density. The properties of PREP powders depend on the experimental parameters, such as rotational speed, bar diameter, plasma mode, melting rate, and plasma gas composition [*Wosch 1995*].

(i) Powder sizes

Of all parameters the rotational speed has the greatest influence on powder diameter. At the front end of the rotating bar the melt is driven outwards by the centrifugal force. If the centrifugal force exceeds the retaining force due to surface tension, melt droplets are ejected. The powder diameter d can be described by the Eq. (1).

$$d = const \bullet \left(\frac{\sigma}{D \bullet \rho} \right)^{\frac{1}{2}} \bullet \frac{1}{2\pi n} \tag{1}$$

where D bar diameter, σ surface tension, n rotational speed, ρ density.

The constant includes further influences on the powder diameter as melting rate, dynamic viscosity and the chemical composition of the material melted [*Champagne 1984*]. From the equation, it can be seen that the powder diameter decreases approximately in the proportion of l/n with increasing rotational speed. The higher the surface tension, the coarser are the powders produced and the greater the bar diameter, the smaller the powder sizes produced, due to the increased centrifugal force. The

balance between the centrifugal and surface tension forces sets a limit for the decrease of the powder size.

(ii) Melting performance

The influence of melting performance on the powder size depends on the mechanism of pulverisation and tails off at higher melting performance. Proceeding from low to high melting performance three different pulverisation mechanisms can be distinguished:

— direct droplet formation (DDF), (at low melting rates, the melt at the front end of the rotating bar creates a melt ring, which results in protuberances, which disintegrates into bigger primary droplets which are for a short time linked to the edge by fine liquid threads and smaller secondary droplets. The particle size distribution becomes bimodal in this mode);

— ligament disintegration (LD), (at higher melting rates, the protuberances stretch into ligaments, which break down into strings of many particles, the proportion of secondary particles increases steadily with the melting rate);

— film disintegration (FD), (at very high melting rates, a film is formed at the edge of the melt ring which disintegrates at will. This never occurs with the PREP).

Fig. 2-15 shows the different mechanism of droplet formation.

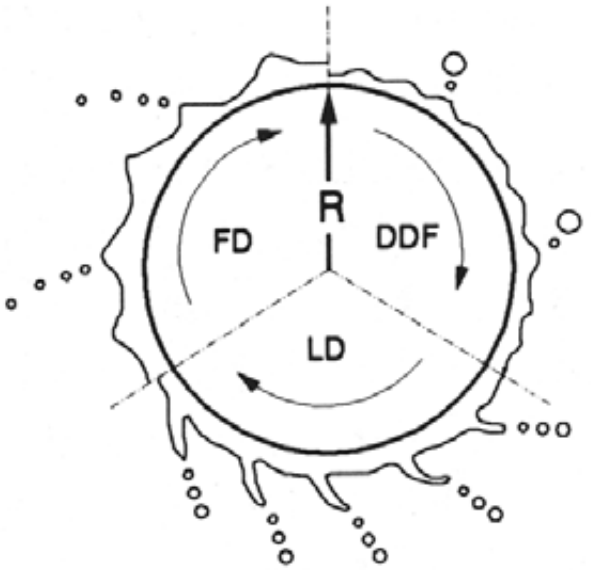

Fig. 2-15 mechanism of droplet formation in PREP [*Thümmler 1993*]

Because PREP prevents contact of the melted alloy with any container material, it provides a decided advantage over other methods of making contamination-free spherical particles. Molten titanium is extremely aggressive and reacts with all container materials; consequently, PREP is ideally suited for production of clean Ti-6Al-4V powder in commercial quantities [*Roberts 1984*]. Table 2-2 shows the composition of PREP Ti-6Al-4V powder.

Table 2-2 Typical characteristics for PREP Ti-6Al-4V powder [*Roberts 1984*]

Composition, wt%	
Aluminum	5.50-6.75
Vanadium	3.50-4.50
Oxygen (standard grade)	0.13-0.20
Oxygen (ELI grade)	0.05-0.13
Iron	0.30 max
Carbon	0.10 max
Nitrogen	0.05 max
Hydrogen	0.0125 max
Other	0.4 max
Titanium	rem

2.4.2.2 Hot isostatic pressing

Hot isostatic pressing (HIPping) was initially developed as a means of closing porosity in castings and diffusion bonding nuclear reactor components and for the removal of porosity in hard materials [*Duszczyk 1998*], but is now widely adapted for powder consolidation to complex shapes in many areas of technology. The advantages of HIPping powder include its capability for forming complex components with near-net or net shape dimensions, for consolidation at a lower temperature and for handling radioactive and toxic materials. In its simplest form, HIPping of powders is a process where the pressure is applied isostatically to the powder which is hermetically sealed inside the HIP vessel. The powder to be compacted is tap filled into a shaped container, degassed under vacuum and sealed. The canned components are loaded into the HIP pressure vessel, and processed through the pressure/temperature/ time cycle for consolidation [*Cahn 1991*]. High-density argon gas is the most common pressurising medium. Fig. 2-16 gives a schematic overview of a HIPping unit. After

HIPping, the can material is stripped off the component by acid leaching or machining. The various sequences in the process of HIPping are shown in Fig.2-17.

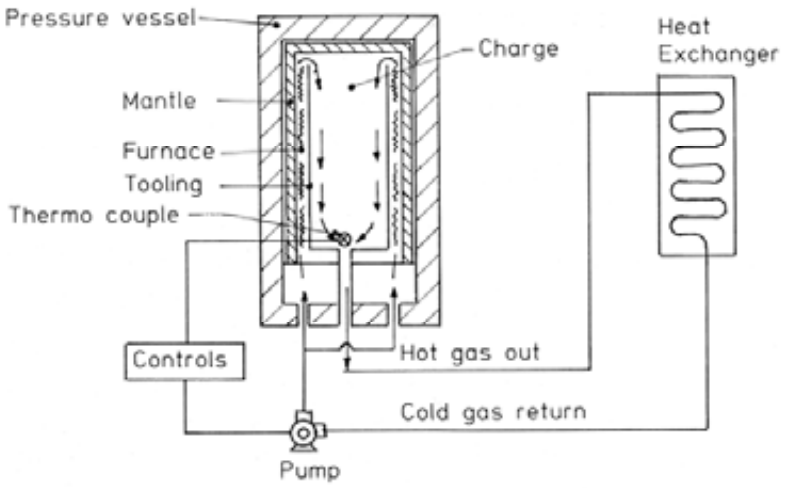

Fig. 2-16 Schematic of a hot isostatic pressing (HIPping) equipment [*Price 1984*]

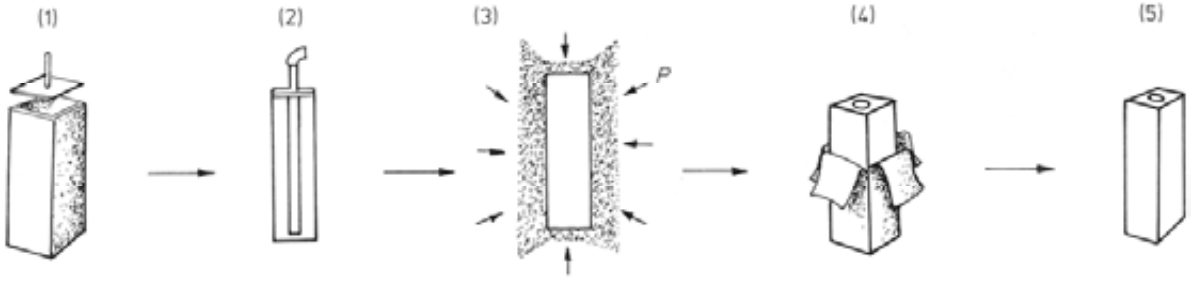

Fig. 2-17 Processing steps in hot isostatic pressing for powder consolidation: (1) fabricate can to fit formed part; (2) fill powder in can, evacuate, degas and seal; (3) HIP; (4) strip can to give (5) consolidated part [*Meiner 1981*]

HIPping involves the transmission of external pressure through the powder, in order to deform the material and close the porosity, giving a compact of full density with uniform distribution in all directions [*Jinka 1996*]. This pressure is "felt" by the powder material as an omni-directional force acting across the particle contacts. Due to the simultaneous effects of pressure and temperature, the HIP process not only "closes" pores, but ideally completely eliminates all trace of powder surfaces by diffusion bonding. At the beginning of the densification process, when a pressure is applied to packed powder particles, it is transmitted through the powder bed as a set of forces acting across the inter-particle contact regions. The deformation at these contacts is at first elastic, but as the pressure rises, the contact forces increase, causing plastic yielding and expanding the points of contact into grown and flattened contact areas. Once these contact areas can support the forces without further yielding, time-dependent deformation processes will, therefore dominate the rate of further densification. Stress-enhanced diffusion processes also play a major role in the consolidation of the material [*Exner 1983*].

There have been detailed studies on the mechanisms that contribute to the densification process during HIPping. Helle et al [*Helle 1985*] and Ashby et al [*Ashby 1991*] proposed the mechanism of plastic flow, i.e. deformation of the powder by plastic yielding upon application of pressure. They also suggested the following mechanisms: *a* diffusional redistribution of matter, i.e. diffusion of material from the contact areas between particles enable the particles to move closer and the pores to fill up; *b* power-law creep, which is creep-deformation at the particle contacts under pressure; *c* inhibition of diffusional densification, when grain growth separates pores

from grain boundaries and isolates them in the mid-grain. In addition, Nabarro-Herring creep (volume diffusion) and Coble creep (grain boundary diffusion), which cause deformation of particles themselves and are considered to be important when the grain size is much smaller than the particle size, also contribute to powder densification [*Duszczyk 1998*]. Delo et al [*Delo 1999*] studied early stage consolidation mechanisms during HIPping of Ti-6Al-4V powder compacts. They carried out a series of experiments on Ti-6Al-4V powder compacts hot isostatically pressed to relative densities ranging from 71% to 100%. Relative particle motion, characterised by small relative movements of particles and clusters of particles, was found to contribute significantly to compaction over a broad range of relative densities. A mechanism was identified by which the preferential deformation of small particles at large-small particle contacts enable rigid body motion of larger particles which, in turn, increases the relative density of the compact.

HIPping, which enables the achievement of 100% theoretical density, ensures improved mechanical properties coupled with a reduced scatter band of properties as compared with those achieved through other processing routes [*Duszczyk 1998*]. HIPping of powders offers both economic and metallurgical advantages. Near-net shape technology results in more efficient material utilisation, which is important for high-cost materials such as titanium-based alloys [*Froes 1999*]. Additionally, the metallurgical benefits include improved homogeneity and control of microstructure to achieve enhanced mechanical properties. Although the potential advantage of near-net shape parts produced by HIPping prealloyed powders was already recognised in the 1970's, with attempts to industrialise the process in the 1980's, by Crucible Research for ceramic moulds and by PCC for metallic moulds, it was not until the early 1990's

that the process was applied to the manufacture of highly loaded components. Russian manufacturers played a pioneering role in this respect, with the production of net shape components for rocket engines [*Raisson 1999*].

When the powder composition, conditioning, HIP cycle and final heat treatment have been optimised, it is possible to achieve functional properties equivalent to or even better than those obtained by a casting and forging route. Such high performance is due to the ability to closely control the microstructure and the possibility of using alloy chemistries inaccessible to conventional processing [*Raisson 1999*]. Wu et al (unpublished work 2005) and Di Iorio et al [*Di Iorio 2007*] reported the unique microstructure of HIPped Ti-6Al-4V, which contains approximately 10% of the body-centred cubic phase (β) and 90% of the hexagonal close packed phase (α). The α grains are the combination of equiaxed grains (nodular) and basket weave (lamellar colonies), and different from the thermomechanically processed microstructure, as shown in Fig.2-18. The α lamellar grains are gathered in colonies of about 10 laths, with the same crystallographic orientation. The nodular grains are located mainly in between previous powder grains.

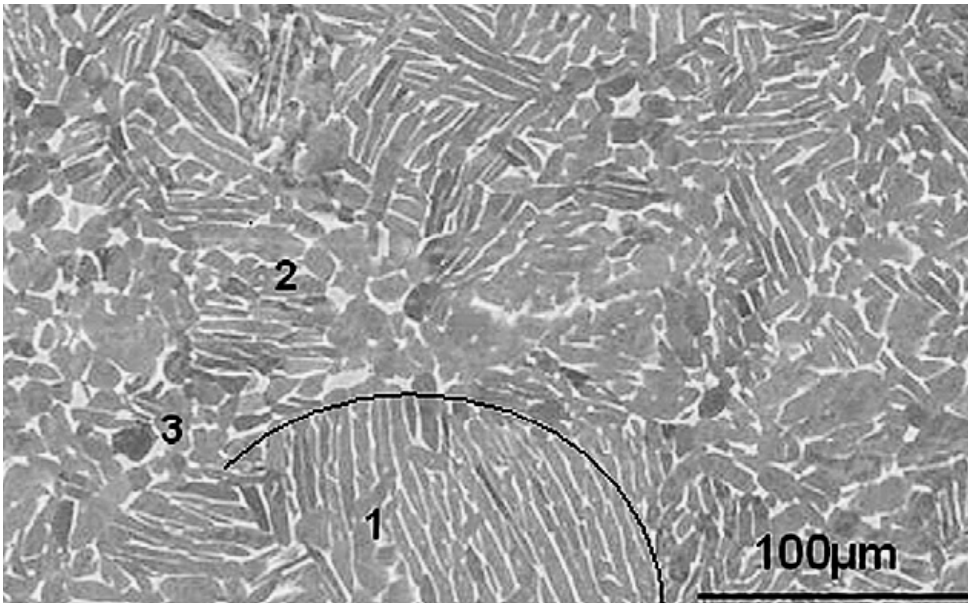

Fig. 2-18 HIPped Ti–6Al–4V ELI microstructure, (1) lamellar α grain gathered in colonies; (2) nodular α grain; (3) boundary of a former powder particle [*Di Iorio 2007*]

Titanium PM alloys are usually consolidated below the beta transus, and superior material properties can be achieved. Typical HIPping processing conditions for Ti-6Al-4V include pressing at 950°C at 100 MPa for 4h [*Penrice 1984*]. Comparative tensile properties for Ti-6Al-4V product processed by various fabrication techniques are given in Table 2-3, which show competitive strength and ductility of HIPped product. Fig. 2-19 shows the comparison of fatigue behaviour of Ti-6Al-4V made using prealloyed PM-HIPping with ingot metallurgy material, which are comparable or superior to those for cast and wrought materials.

Table 2-3 Typical room temperature tensile properties of Ti-6Al-4V product processed by various fabrication techniques [*Kelto 1980*]

Process	**Tensile strength (MPa)**	**Yield strength (MPa)**	**Elongation (%)**	**Reduction in area (%)**
Cast	930	841	7	15
Isothermally forged	965	875	15	40
Diffusion bonded	924	855	11	23
Blended elemental PM	917	834	11	18
Prealloyed PM-HIPping	979	882	14	26

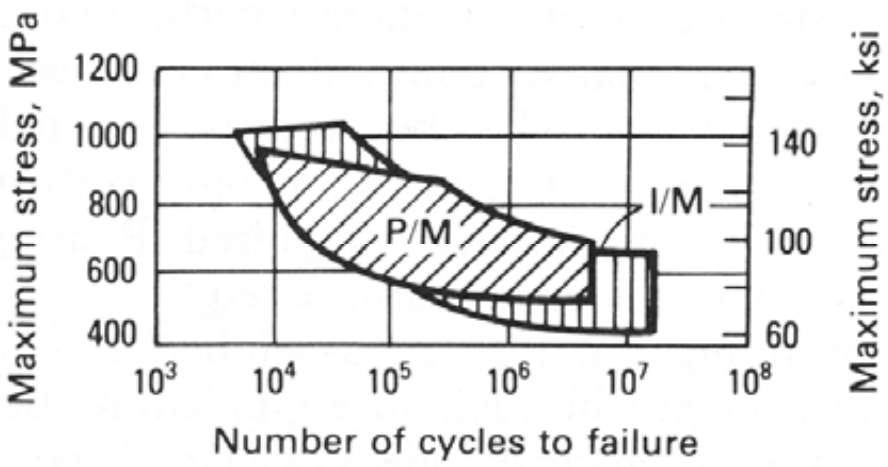

Fig. 2-19 Comparision of fatigue behaviour of prealloyed PM-HIPped Ti-6Al-4V with ingot metallurgy material [*Roberts 1984*]

2.5 Aim of the project

After several decades of study and development, thermo-mechanically processed titanium alloys have been widely applied in the aero-industry due to their balance of properties. As mentioned in the previous sections, some complicated components which require specific properties can be manufactured by casting but these require significant machining or post casting weld-repair operations thus leading to low fly-to-buy ratios and excessive manufacturing costs. Manufacturing those components through near net shape powder metallurgy of Ti alloys will effectively reduce the cost and obtain superior mechanical properties through PM routes, as shown by several previous studies.

Although a significant number of studies have been carried out world wide on powder metallurgy of Ti alloys, most of them focused on how to obtain 100% density by optimising the HIPping parameters and on mechanical tests of the resultant samples. Few studies, if any, reported the relationship between the type/size of powder/HIPping condition, microstructures and associated mechanical properties. Little work was done on understanding of the physical metallurgy of the powder HIPping process.

In this thesis, two typical titanium alloys, one most commonly used ($\alpha + \beta$) alloy, Ti-6Al-4V and one specific beta alloy Ti-25V-15Cr-2Al-0.2C (BuRTi), both of which have potential application on gas turbine engines, were chosen to understand the effects of powder condition and HIPping parameters on microstructures and resultant

mechanical properties. Of particular significance to net shape HIPping, work will be carried out to assess the influence of the as-HIPped surface on fatigue properties.

References

Automotive 1984: Automotive Applications, *Metals Handbook,* Vol **7**, *Powder Metallurgy,* 9th ed., American Society for Metals, 1984, p.617.

Ashby 1991: Ashby, M. F., in *Powder Metallurgy: An Overview*, eds. Jenkins, I., Wood, J. V., The Institute of Meterials, 1991, p.144.

Bache 2002: Bache, M. R., Evans, W. J., and Voice, W., *Mat. Sci. Eng.*, **A333**, 2002, p.287.

Bania 1994: Bania, P. J., *JOM*, **46**(7), 1994, p.12.

Beryllium 1984: Beryllium P/M Technology, *Metals Handbook,* Vol **7**, *Powder Metallurgy,* 9th ed., American Society for Metals, 1984, p.755.

Boyer 1994: Boyer, R., Welsch, G., Collings, E. W., Eds.: *Materials Properties Handbook: Titanium Alloys,* ASM International, Materials Park, USA, 1994, p.483.

Boyer 1995: Boyer, R. R., in *Proceedings of the 8th World Conference on Titanium - Titanium'95: Science and Technology*, eds. Blenkinsop, P. A., Evans, W.,J. and Flower, H. M., The Institute of Materials, 1995, p.41.

Boyer 1996: Boyer, R. R., *Mat. Sci. Eng.*, **A213**, 1996, p.103.

Boyer 2005: Boyer, R. R., Briggs, R. D., *J. Mater. Eng. Perform.*, **14**, 2005, p. 681.

Broderick 1996: Broderick, T. F., Reshad, J., Ward, C. H. and Scheltens, F. J., in: *Proceedings of the 8th World Conference on Titanium - Titanium'95: Science and*

Technology, Eds.: Blenkinsop, P. A., Evans, W. J., and Flower, H. M., The Institute of Materials, 1996, p. 2385.

Cahn 1991: Cahn, R.W., Haasen, P., and Kramer, E. J., *Materials Science and Technology,* Vol 15*, Processing of Metals and Alloys*, VCH Verlagsgesellschaft, Weinheim, Germany, 1991, p143.

Cass 1970: Cass, T. R., in: *The Science, Technology and Application of Titanium*, eds. Jaffee, R. T. and Promisel, N. E., Oxford, 1970, p. 459.

Champagne 1984: Champagne, B., Angers, R. and Fiset, M., *Metal Powder Report,* **39**, 1984, p.267.

Chesnutt 1978: Chesnutt, J. C., Thompson, A. W., and Williams, J. C., AFML-TR-78-68, 1978.

Cho 2001: Cho, J. H., Kim, K. T., *Int. J. of Mec. Sci.*, **43**, 2001, p.921.

Churchman 1954: Churchman, A. T., *Proc. Roy. Soc (London) A*, **226**, 1954, p.216.

Collings 1994: Collings, E. W., *Materials Properties Handbook: Titanium Alloys*, ASM, Materials Park,USA, p.1.

Delo 1999: Delo, D. P. and Piehler, H. R., *Acta mater*., **47**(9), 1999, p.2841.

Dunkley 1991: Dunkley, J. J., in *Powder Metallurgy: An Overview*, eds.: Jenkins, I., Wood, J. V., The Institute of Materials, 1991, p.2.

Duszczyk 1998: Duszczyk, J., Zhuang, L. Z., and Buekenhout, L., *J. of Mat. Sci.,* **33**, 1998, p.2735.

Exner 1983: Exner, H. E. and Arzt, E., in *Physical Metallurgy, 3rd* eds.: Cahn, R. W., Hassen, P., North-Holland Physics Publishing, Amsterdam, 1983, p.1885.

Ferguson 1984: Ferguson, B. L., *Metals Handbook,* Vol **7**, *Powder Metallurgy,* 9th ed., American Society for Metals, 1984, p.646.
Froes 1984: Froes, F.H., Eylon, D., Titanium Powder Metallurgy--A Review, in *PM Aerospace Materials,* Vol **1**, MPR Publishing, 1984, p.39-1.

Froes 1999: Froes, F. H. and Hebeisen, J., *in: Hot Isostatic Pressing International Conference 1999,* International Academic Publishing, Beijing, China, 1999, p.1.

Garbacz 2003: Garbacz, H., Lewandowska, M., *Mater. Chem. and Phys.*, **81**, 2003, p.542.

Greer 1994**:** Greer, A. L., *Mat. Sci. Eng.,* **A178**, 1994, p113.

Haanappel 2002: Haanappel, V.A.C., Clemens, H., and Stroosnijder, M. F., *Intermetallics.*, **10**, 2002, p.293.

Hansen 1996: Hansen, J. G., Novotnak, D., Welter, M. F. and Wood, J. R., in *Ti'95: Science and Technology, Proceedings of the 8th World Conference on Titanium*, eds. Blenkinsop, P. A., Evans, E. J., and Flower, H. M., Institute of Materials, London, 1996, p.675.

Helle 1985: Helle, A. S., Easterling, K. E. and Ashby, M.F., *Acta metall. metal.*, **33**, 1985, p.2163.

Huang 1999: Huang, B. Y., He, Y. H., and Wang, I. N., *Intermetalics.*, **7**, 1999, p.881.
Huang 2006: Huang, Y. Z., Blackwood, D. J., *Electrochimica Acta.*, **51**, 2006, p3521.
Di Iorio 2007: Di Iorio, S., Briottet, L., Rauch, E. F., and Guichard, D., *Acta Materialia,* **55**, 2007, p.105.

Jinka 1996: Jinka, A., G.K., *J. of Mater. Proc. Tech.*, **57**, 1996, p.382.

Jones 1981: Jones, I. P., and Hutchison, W. B., *Acta Metall.*, **29**, 1981, p. 951.

Jovanović 2006: Jovanović, M. T., Tadić, S., Zec, S., Mišković, Z. and Bobić, I.,

Mater. and Design., **27**, 2006, p.192.

Kelto 1980: Kelto, C., in: *Powder Metallurgy of Titanium alloys*, Eds., Froes, F., and Smugersky, J., American Institute of Mechanical Engineers, Warrendale, PA, 1980, p.5.

Kneisel 1993: Kneisel, G., *Advanced Materials and Processes*, **9**, 1993, p.7.

Kocks 1967: Kocks, W. F. and Westlake, D. G., *Trans. of the Metall. Soc. of AIME.*, **239**, 1967, p.1107.

Kuhlmann 1988: Kuhlmann, G. W., in *Forging Titanium Alloys,* Metals Handbook, 9th ed, Vol. 14, ASM, Materials Park, USA, 1988, p.267.

Kuhn 1996: Kuhn, H. A., Dax, F. R., *The Int. J. of Powder Metall.,* **32**, 1996, p.229.

Lawley 1977: Lawley, A., *Int. J. Powder Metall. & Powder Technol.*, **14**, 1977, p259.

Lawley 1978: Lawley, A., *Powder Metallurgy Processing: New Techniques and Analyses*, London, Academic Press, 1978.

Lawley 1981: Lawley, A., *J. Metals*, **33 (1)**, 1981, p13.

Lenel 1982: Lenel, F. V., and Ansell, G. S., *J. Metals*, **34(2)**, 1982, p17.

L'Estrade 1988: L'Estrade, L., Hallen, H., and Ljunggren, R., *Modern Development in Powder Metallurgy*, **20**, 1988, p187.

Li 1996: Li, Y. G., Zhang, X. D., Blenkinsop, P. A., Saunders, N., Walker, N. A., Spilling, S. and Small, C., *in: Proceedings of the 8th World Conference on Titanium - Titanium'95: Science and Technology*, Eds. Blenkinsop, P. A., Evans, W. J. and Flower, H. M., The Institute of Materials, 1996, p.2317.

Li 1998 a: Li, Y. G., Blenkinsop, P. A., Loretto, M. H. and Walker, N. A., *Acta Mater.*, **46**, 1998, p.5777.
Li 1998 b: Li, Y. G., Blenkinsop, P. A., Loretto, M. H. and Walker, N. A., *Materials Science and Technology*, **14**, 1998, p.732.

Li 1999 a: Li, Y. G., Blenkinsop, P. A., Loretto, M. H., Rugg, D. and Voice, W., *Acta Mater.*, **47**, 1999, p.2889.

Li 1999b: Li, Y. G., Blenkinsop, P. A., Loretto, M. H., and Walker, N. A., *Materials Science and Technology*, **15**, 1999, p.151.

Li 2001: Li, Y. G., Loretto, M. H., Rugg, D., and Voice, W., *Acta Mater.*, **49**, 2001, p.3011.

Loretto 2002: Loretto, M. H., Horspool, D., Botten, R., Hu, D., Li, Y. G., Srivastava, D., Sharman, R. and Wu, X., *Materials Science and Engineering: Structural Material Properties, Microstructure and Processing*, **A329-331**, 2002, p.1.

Lucas 1973: Lucas, J. J., in *Titanium Science and Technology*, Eds.: Jaffee, R. I., Burte, H. M., Plenum Press, 1973, p. 2081.

Lütjering 1985: Lütjering, G., Gysler, A., *Titanium Science and Technology*, Vol **4**, Deutsche Gesellschaft für Metallkunde e.V., 1985, p.2068.

Lütjering 2003: Lütjering, G., Willians, J. C., *Engineering Materials and Processes*: *Titanium*, Springer, Germany, 2003, p90.

Meiner 1981: Meiner, K. E., and McCall, J. C., *Metal Powder Report,* **36**, 1981, p.437.

Minabe 1990: Minabe, M. and Endoh, H., *Metal Powder Report*, 1990, p673.

Moll 1998: Moll, J. H., Yolton, C. F., *Metals Handbook,* Vol **7**, *Powder Metal Technologies and Applications,* American Society for Metals, 1998, p381.

Nachtrab 1993: Nachtrab, W. T., Roberts, P. R. and Newborn, H. A., Powder Metallurgy of Advanced Titanium Alloys, *Key Eng. Mate.,* **77-78**, 1993, p115-140.

Naka 1991: Naka, S., Kubin, L. P., Perrier, C., *Philosophical Magazine A*, 1991, **63A**, P.1035.

Neal 1985: Neal, D.F., in *Titanium Science and Technology*, eds.: Lütjering, G., Zwicker, U., and Bunk, W., Deutsche Gesellschaft fur Metallkunde e.V., Oberursel, Germany, 1985, p.2419.

Novovic 2004: Novovic, D., *Ph.D Thesis.*, The University of Birmingham, Birmingham, UK, 2004.

Numakura 1986: Numakura, H., Minonishi, Y., and Koiwa, M., *Script. Metall.,* **20**, 1986, p. 1581.

Otte 1970: Otte, H. M., *The Science, Technology and Application of Titanium,* Pergamon Press, Oxford, UK, 1970, p. 645.

Paton 1973: Paton, N. E., Williams, J. C., and Rauscher, G. P., *Titanium Science and Technology*, Plenum Press, New York, USA, 1973, p.1049.

Penrice 1984: Penrice, T. W., *Metals Handbook,* Vol **7**, *Powder Metallurgy,* 9th ed., American Society for Metals, 1984, p.688.

Peters 1981: Peters, M., Gysler, A., and Lütjering, G., in *Titanium'80, Science and Technology,* Eds.: Kimura, H., Izumi, O., Vol **1**, TMS-AIME, 1981, P.1777.

Pollard 2002: Pollard, S., *Final Year Report*, University of Birmingham, Birmingham, UK, 2002.

Polmear 1995: Polmear, I. J., *Light Alloys: Metallurgy of the Light Metals*, Third Edition, Edward Arnold, London, 1995.

Powell 1995: Powell, B. E., *Int. J. Fatigue*, **170**, 1995, p221.

Prasad 2001: Prasad, Y. V. R. K., Seshacharyulu, T., Medeiros, S. C. and Frazier, W. G., *J. of Mater. Proc. Tech.*, **108**, 2001, p.320.

Price 1984: Price, P. E., *Metal Powder Report,* **39**, 1984, p.28.

Rabin 1990: Rabin, B. H., Smilok, G. R., and Korth, G. E., *Mat. Sci. Eng.,* **A124**, 1990, p1.

Raisson 1999: Raisson, G., in: *Hot Isostatic Pressing International Conference 1999,* International Academic Publishing, Beijing, China, 1999, p.390.

Rhodes 1986: Rhodes, C. G., in: *Applied Metallography*, eds.: Vander Voort, G. F., Van Nostrand Reinhold Inc., 1986, p. 237.

Roberts 1984**:** Roberts, P. R., *Metals Handbook,* Vol **7**, *Powder Metallurgy,* 9th ed., American Society for Metals, 1984, p39.

Rosenberg 1970: Rosenberg, H. W., *The Science, Technology and Application of Titanium*, Pergamon Press, Oxford, UK, 1970, p851.

Rosi 1953: Rosi, F. D., Dube, C. A., and Alexander, B. H., *JOM*, **5**, 1953, p. 257.

Schutz 1994: Schutz, R. W., *JOM*, **46**(7), 1994, p.24.

Seshacharyulu 2002: Seshacharyulu, T., Dutta, B., *Scripta Mater.*, **46**, 2002, p.673.

Shao 1994: Shao, G., and Tsakiropoulos, P., *Acta Metall.*, **42(9)**, 1994, p2937.

Shinde 1977: Shinde, S. L., Tendulkar, G. S., *Powder Metall. Int.* **9**, 1977, p.180.

Simchi 2003: Simchi, A., *Materials and Design*, **24,** 2003, p.585.

Stevenson 1984: Stevenson, R.W., *Metals Handbook,* Vol **7**, *Powder Metallurgy,* 9th ed., American Society for Metals, 1984, p733.

Stubbington 1974: Stubbington, C. A., Bowen, A. W., *J. Mater. Sci.*, Vol **9**, 1974, p.941.

Thümmler 1993: Thümmler, F., Oberacker, R., *Introduction to Powder Metallurgy,* The Institute of Materials, London, 1993, p23.

Tsujimoto 1989: Tsujimoto, T., Hashimoto, K., *Proc. Mat. Res. Soc. Symp.*, **133**, 1989, p391.

Voice 2004: Voice, W., in: *Proceedings of the 10th World Titanium Conference Ti-2003*, Hamburg, Germany, 2004, p.2915.

Wang 1988: Wang, J., Duan, X., *Proc. 6th World Conference on Titanium,* France, 1988, p.1607.

Weiss 1999: Weiss, I., Semiatin, S. L., *Materials Science and Engineering,* **A263**, 1999, p.243.

Williams 1971: Williams, J. C., Hickman, B. S., Leslie, D. H., *Met. Trans.*, **2**, 1971, p.477.

Williams 1973: Williams, J. C., *Titanium Science and Technology,* Plenum Press, New York, USA, p. 1433.

Williams 1999: Williams, J. C., *Mat. Sci. Eng.*, **A263**, 1999, p.107.

Wosch 1995: Wosch, E., Feldhaus, S. and Gammal, T. E., *ISIJ International,* **35(6)**, 1995, p.764.

Wu 2003: Wu, X. and Mei, J., *J. of Mater. Proc. Tech.*, **135**, 2003, p.266.

Wu 2006: Wu, X., Prado, J., Li, Q., Huang, A., Hu, D., Loretto, M. H., *Acta Mater.*, **54**, 2006, p.5433.

Wunderlich 1993: Wunderlich, W., Kremser, T. H., and Frommeyer, G., *Acta Metell.*, **41**, 1993, p1791.

Zhao 2001: Zhao, Y., Zhou, L., Zhu, K., Qu, H. and Wu, H., *J. of Mater. Sci. and Tech.*, **17**(6), 2001, p.677.

Chapter 3 Experimental Methods

This chapter details experimental work in terms of the materials that have been used for the purpose of this study, the processing techniques followed for the preparation of these materials, equipment used, types of mechanical tests, and the methodology and analysis techniques for the understanding of microstructural characterisation and fracture mechanism.

3.1 Materials and their processing

3.1.1 PREP Ti-6Al-4V (wt%) powder

The PREP Ti-6Al-4V powder used in this research work was produced by StarMet, USA, using the plasma rotating electrode process. The as-received powder used for the complete size HIPping (hot isostatic pressing) is in the size range of 50~400μm. For the assessment of the effect of powder particle size on microstructure and properties of HIPped samples, the powder was sieved and classified into different size fractions.

Sieves were used to divide the powder into 3 sets according to different particle diameters: 50~150μm, 150~250μm and 250~400μm respectively. The size distribution of sieved powder in different sets was measured using Coulter LS 230, and median powder sizes of 3 sets were obtained as 110 μm, 190 μm and 260 μm.

3.1.2 Burn resistant titanium (BuRTi, Ti-25V-15Cr-2Al-0.2C wt%) powder

The BuRTi powder used in this research work was produced by two production methods: gas atomisation (supplied by Crucible Research) and PREP (supplied by StarMet). The as-received powder is in the size range of 50~400μm. Gas atomised powder was sieved using the sieving unit into two size fractions: 50~150μm and 250~400μm to investigate the effect of powder particle size on microstructure and properties.

3.1.3 Hot Isostatic Pressing

Consolidation of the powders was achieved by hot isostatic pressing (HIPping). This method involves the application of high temperature and high pressure of Ar gas. The powder needs to be encapsulated in a sealing medium that is deformable at the HIPping conditions to be used, and has good weldability. Mild steel was used as a capsule for all HIPping work and after HIPping the steel was either pickled away using acid or machined off. Rectangular section mild steel tubes were used as the capsules for the production of samples to be used for 4-point bending fatigue tests so that suitable test samples could be produced which retained the as-HIPped surface after the capsule was pickled away. For other experiments, where samples were to be machined before testing, cylindrical mild steel cans were used as the capsules. Before being filled with powders, these capsules were checked by the leak detector with a detectable leak rate of $< 5\times10^{-12}$ mbar l/s, as shown in Fig. 3-1. A vacuum furnace (Fig. 3-2) was used to anneal the mild steel cans at 1100°C, 1h, furnace cooling (FC), in order to get rid of impurities inside the cans which could contaminate the powders. A vibration table was used to increase the flow rate during the process of filling

powder into the mild steel can and also to achieve a consistent tap density. The cans filled with powder were then outgassed at 10^{-5} mbar for 20 h using an outgassing system and crimp-closed before being welded to ensure vacuum-tightness. The sealed cans are then placed in the HIP furnace. The pressure and temperature are increased until the final hold conditions are reached. The cooling rate used after the HIP cycle is complete is about 5°C/min. The density of the powder in the can increases as consolidation proceeds during the HIP cycle [*Thümmler 1993*].

Fig. 3-1 A photograph of leak detector for the checking of capsule's sealing quality.

Fig. 3-2 Vacuum furnace for annealing mild steel cans which are used for powder HIPping to get rid of impurities inside.

The EPSI Lab HIP facility (shown in Fig. 3-3) contains a HIP unit with maximum operating temperature up to 1450 °C and pressures up to 200 MPa. This unit consists of a furnace with molybdenum heating elements, a heat shield, a water-cooled pressure vessel and a gas compressor system. The two zone molybdenum furnace (see Fig. 3-4) is used to provide the heating, and thermocouples are positioned at the top and bottom of the two hot zones. A computer system is used to monitor the temperature and pressure continuously inside the HIP furnace. Temperature control is within ±3 °C throughout the working zone.

Fig. 3-3 EPSI Lab HIP facility.

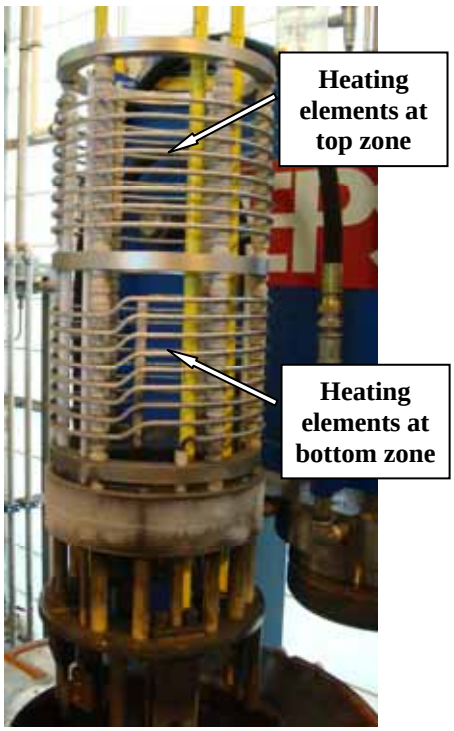

Fig. 3-4 The two zone molybdenum furnace used for HIPping.

3.2 Microstructural characterisation

3.2.1 Specimen preparation

As-received loose powder particles were used directly for surface examination. With respect to the examination of powders' cross sections, individual powder particles were hot mounted in edge protective and conductive bakelite in an OPAL 400 mounting press. For the microstructural examination of HIPped materials, samples were cut by using electro discharge machine (EDM) from the HIPped bars or plates. The cross sections were cut by a Struers Accutom-5 cutting unit using SiC cutting wheel and mounted in conductive bakelite ready for subsequent metallographic

preparation. When powder particles were polished, two-stage grinding procedure using SiC abrasive grinding paper with low force and short operating times were involved. When HIPped samples were polished, an added grinding procedure was used in order to remove any damage caused during specimen sectioning, and higher forces and longer times were selected. All of the grinding and final polishing was carried out in a Struers DAP-7 polishing unit fitted with a pedemin-s automatic polishing head. Tables 3-1 and 3-2 give the details of grinding and polishing routes for Ti-6Al-4V powder particle and HIPped samples, respectively. After final polishing, some of the specimens were chemically etched with Kroll's reagent of 2 %vol hydrogen fluoride (HF), 10%vol nitric acid (HNO_3) and balance water for ~20s, in order to reveal microstructural features for subsequent optical microscopy and scanning electron microscopy (SEM) evaluation.

Table 3-1 Grinding/polishing routes for Ti-6Al-4V powder particles.

Cloth / abrasive	**Rotational speed (rpm)**	**Force (N)**	**Time (min)**
SiC-paper grit 1200 with water	125	8	~3
SiC-paper grit 2400 with water	125	5	~3
MD-Chem cloth with 0.05 μm OP-S colloidal silica + 5% hydrogen peroxide	125	5	~7

Table 3-2 Grinding/polishing routes for Ti-6Al-4V HIPped samples.

Cloth / abrasive	Rotational speed (rpm)	Force (N)	Time (min)
MD-Primo 220 with water	250	15	until plane
SiC-paper grit 800 with water	125	10	~7
SiC-paper grit 1200 with water	125	10	~7
SiC-paper grit 2400 with water	125	10	~7
MD-Chem cloth with 0.05 μm OP-S colloidal silica + 5% hydrogen peroxide	125	5	~9

Note: MD-Primo, SiC-papers and MD-Chem are trademarks of Struers.

For metallographic preparation of BuRTi powder particles and HIPped samples, the same operating parameters were used, although the time for each stage was slightly increased. Additionally, etching was performed in a stronger solution (7 %vol HF, 10 % vol HNO_3 and balance water) for ~1 min.

3.2.2 Microscopy techniques

A Leica DMRX digitised optical microscope, in conjunction with image analysis software KS300-3.0 was used to examine etched samples. Secondary electron (SE) imaging of the surface of loose powder particles and back-scattered electron (BSE) imaging of powder particles' and solid specimens' cross sections were taken using a JEOL 7000. Energy dispersive x-ray (EDX) analyses can be done using Oxford Inca EDX system in this instrument to evaluate the chemical composition of the samples. EDX spectra were acquired using an accelerating voltage of 20 kV, a working distance of 10 mm, an acquisition time of 60s and zero sample tilt. For all the quantified results the collected counts were always greater than 2×10^6 to minimise the

statistical error. Electron back scatter diffraction (EBSD) was performed to provide information about the crystallographic orientation in original powders and HIPped samples. The misorientation angles between grains in the two phase alloy (Ti-6Al-4V) and in the single phase alloy (BuRTi) can be measured by this system, and the grain size distribution can also be illustrated. The EBSD system was an integral part of the JEOL 7000 SEM. The operating parameters were: specimen tilt angle of 70^{o}, accelerating voltage of 20 kV, and a working distance of 12~16 mm.

3.2.3 Chemical composition analysis of HIPped samples

Chemical composition analyses of HIPped samples were performed by IncoTest (Special Metals Wiggin Limited), Hereford, UK. A small solid slice of HIPped sample with a weight of ~5 g was needed to analyse interstitial elements (such as O, C) by the method of LEC (LECO inert gas fusion analyser) and other elements (such as Ti, Al, V) by the method of ICPOES (Inductively Coupled Plasma Optical Emission Spectrometry).

3.3 Mechanical testing

3.3.1 Tensile testing

Cylindrical tensile samples were machined from HIPped compacts. The 9mmϕ cylinders were cut out using EDM and sent out for finish-machining to the final shape shown in Fig. 3-5 (a) and (b). Tensile tests were carried out using a Zwick at a strain rate of $10^{-3}s^{-1}$ in air at room temperature to assess the behaviour of the HIPped materials. The load/displacement curves obtained are converted to nominal stress/nominal strain curves which give tensile strength, yield stress and elongation.

The fracture surfaces of tensile failed samples were studied using a Philips XL30 SEM or JOEL 6060 SEM to understand the fracture mechanism.

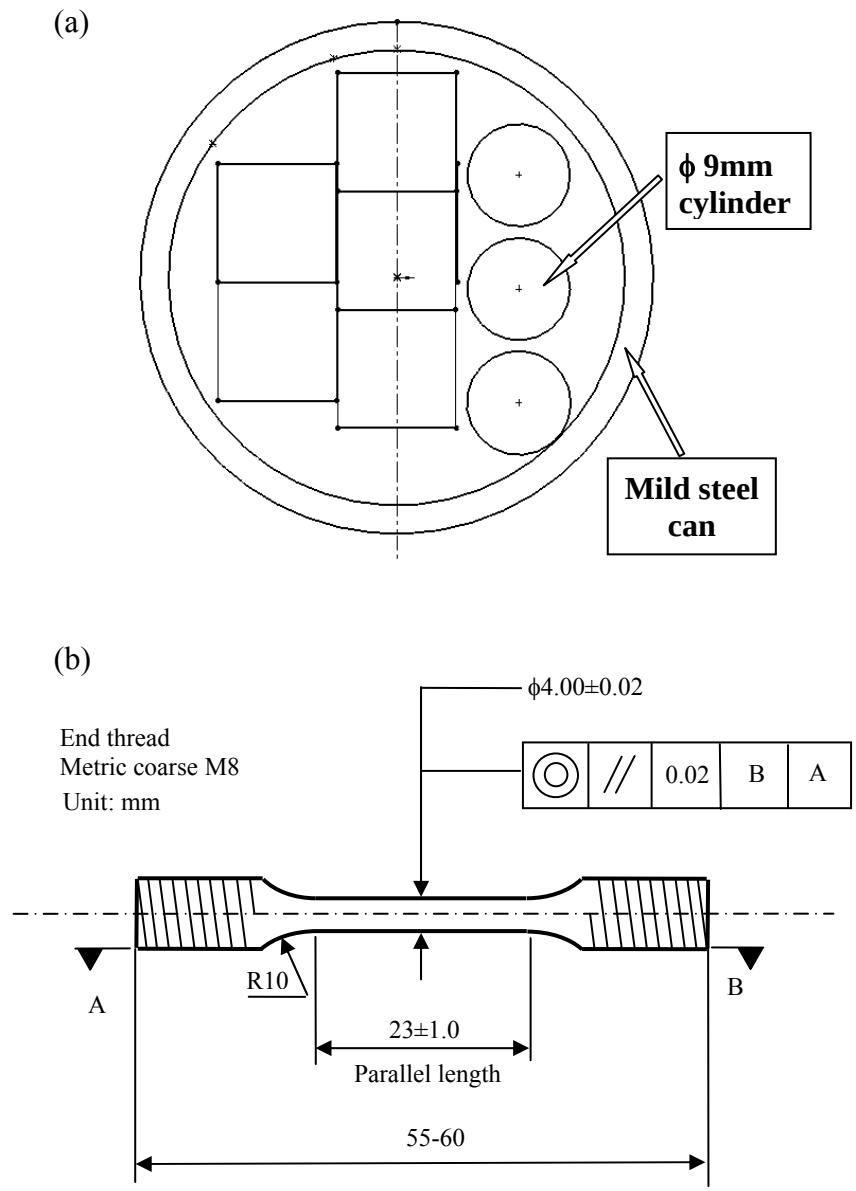

Note: Roughness value for machined surfaces to be 1.6 micrometers unless otherwise stated; all dimensions and tolerances are in mm unless otherwise stated

Fig. 3-5 Schematics of (a) 9mmϕ cylinders cut from the HIPped bar; (b) dimensions for round RT tensile test pieces.

3.3.2 4-point bending fatigue testing

3.3.2.1 Specimen preparation

Flat HIPped plates with the length of 120mm, width of 60mm, and thickness of 10mm were cut by EDM along the length after removing the mild steel can by acid pickling in 20% nitric acid. The EDM cut surfaces were final machined to generate the side surfaces of the samples, and the original plate surfaces, which had been in contact with the mild steel can during HIPping, became the top and bottom surfaces of the testpieces (see Fig. 3-6 (a)). 4-point fatigue specimens (10x10x60mm^3) with as-HIPped surfaces were produced by this way.

Some of the specimens with rough as-HIPped surfaces were electro-polished for 15~20 min to remove the HIPped surface. The solution used was 60%vol Methanol, 35%vol 1-Butanol and 5%vol $HClO_4$, which was kept in a bath of Methanol and liquid nitrogen with a temperature of -35°C, and the current of 0.8~1A was used.

Cylindrical HIPped bars were machined by EDM to produce rectangular blanks of ~10.2x10.2x62 mm^3 which were sent out for machining to produce the samples with the dimension of 10x10x60 mm^3 (see Fig. 3-6 (b)). The machining method is reciprocating surface grinding (RSG) by which the fatigue samples with as-machined surfaces were produced.

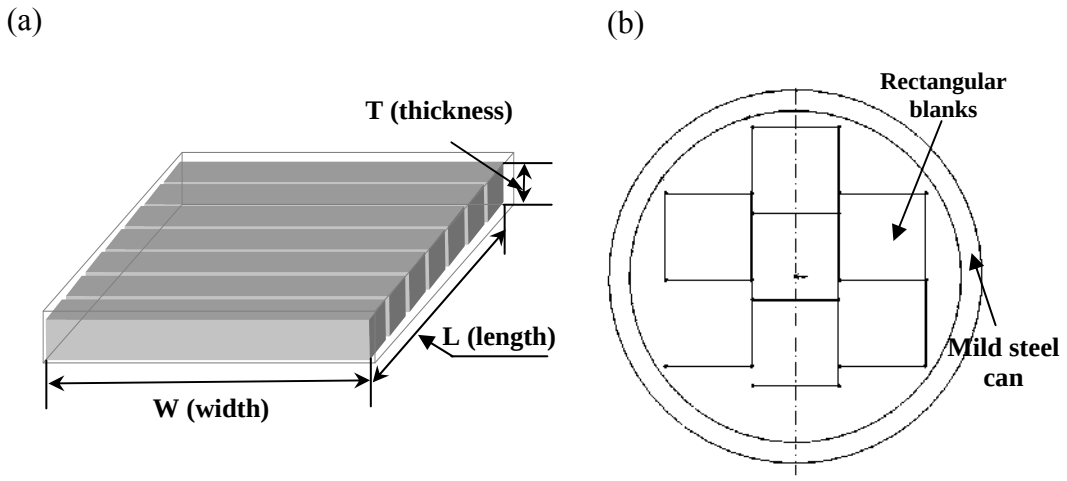

Fig. 3-6 Schematics of machining rectangular blanks for 4-point bending fatigue testing by EDM from (a) flat HIPped plate along the length direction to keep original plate surfaces; (b) cylindrical HIPped bars to produce samples with machined surfaces.

3.3.2.2 Analysis techniques

The 2D surface topography of samples with different surface conditions was characterised with the values of R_a (Arithmetic mean deviation of the assessed profile) and R_{max} (Maximum height of the profile and the distance between the line of peaks and the line of valleys of the profile within the evaluation length) using a Surfcorder SE 1700 (see Fig. 3-7), with a stylus tip radius of 2 μm and a stylus drive speed of 0.5 mm/min. Since the as-HIPped surface is non-directional, each measurement was taken in the transverse direction of each specimen, repeated 6 times at different positions, and an average value was recorded. One of the limitations of using stylus-based equipment for the study of surface topography is the inability to record minor defects/irregularities such as inclusions. In order to compensate for this limitation, the cross sections of fatigue specimens with different surface conditions were further

assessed by using JOEL 7000 for the presence of deviations/defects and evaluation of surface quality.

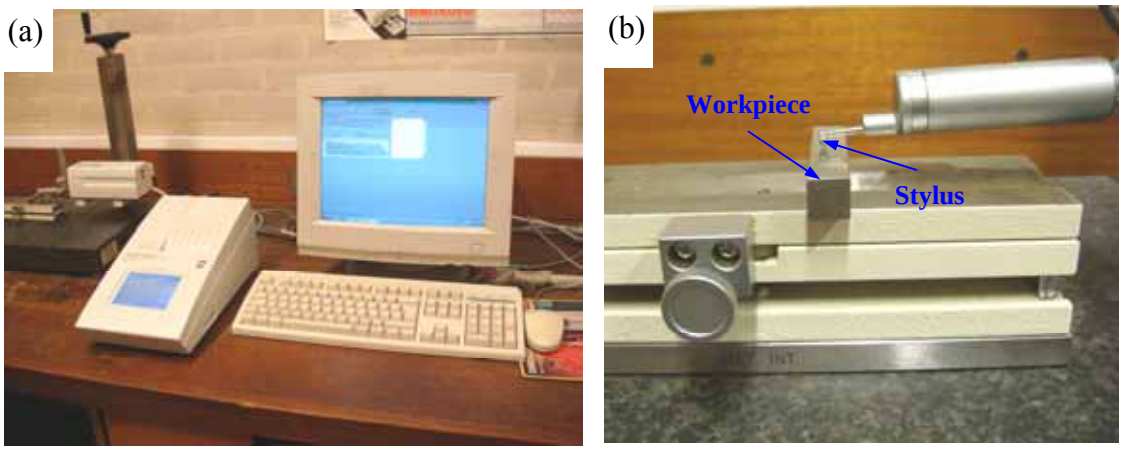

Fig. 3-7 (a) Surfcorder SE 1700 for measuring the surface roughness; (b) the stylus and workpiece set-up.

3.3.2.3 Fatigue life evaluation

4-point bending fatigue tests were carried out using an Amsler Vibrophore electro-magnetic resonance testing machine (see Fig.3-8 (a)) for fatigue life evaluation. Tests were conducted at room temperature, at a stress ratio R of 0.1 and a frequency of ~95 Hz, and 1.0×10^7 cycles were defined as the run-out life. The applied elastic maximum stresses at the control surface σ_{max} was calculated using the elastic bending theory according to the following equations [*Dowling 1999*]:

$$\sigma_{max} = \frac{3P_{max} \cdot S}{b \cdot t^2} \qquad (3.1)$$

where P_{max} is the maximum applied load, S is the span between inner and outer rollers (S=10 mm in this study since the span between inner rollers is 20mm and that between outer rollers is 40mm), b is the specimen width, t is the specimen height,

$R=\sigma_{min}/\sigma_{max}$ is the ratio of minimum stress to maximum stress applied over the fatigue cycle. Fig.3-8 (b) shows 4-point bend arrangement and the position of sample's test surface during fatigue test.

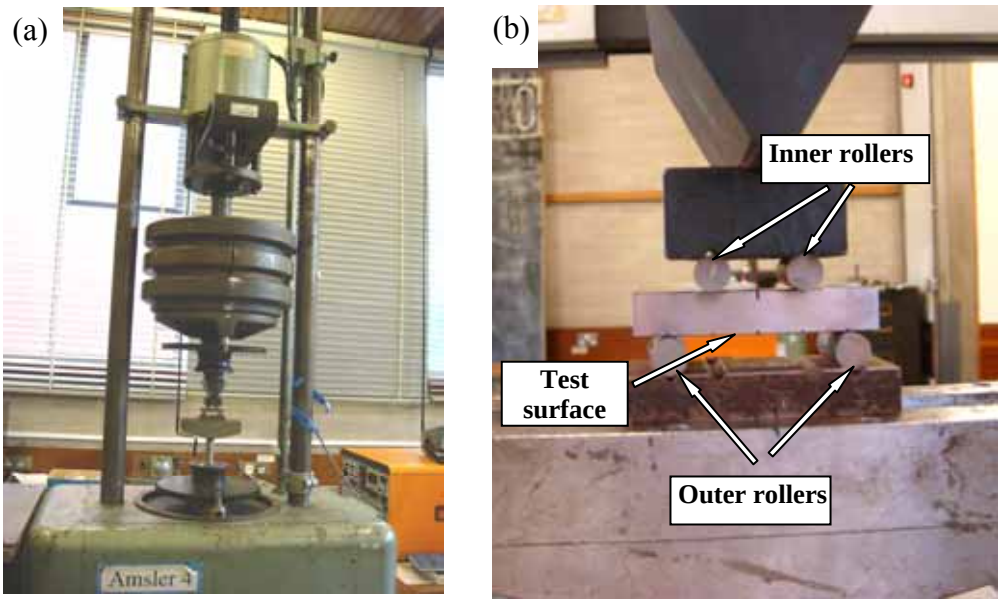

Fig.3-8 (a) Amsler Vibrophore electro-magnetic resonance testing machine for fatigue property assessment; (b) four point bend arrangement and the position of sample's test surface during fatigue test.

Following fatigue tests, fractographic observation of failed samples was carried out using a JOEL 6060, or a Philips XL30 SEM. Both halves of the fracture surfaces were assessed for the majority of failed samples. Fatigue initiation sites were identified and studied in detail. The chemical composition of the rough fracture surface near to the crack initiation site was studied using the EDX system. The crack paths of fracture surface cross sections of failed specimens were examined by SEM BSE and EBSD in a JOEL 7000 to assess the crack propagation resistance and fracture mechanism.

3.3.3 Fracture toughness testing

Fracture toughness testing of ingot-route and HIPped Ti-6Al-4V samples was conducted according to the relevant British Standard [*British Standard 1991*]. Compact tension (CT) specimens were machined from forged billets and HIPped bars, and the dimensions are shown in Fig.3-9. Specimens were pre-cracked at room temperature, using an Amsler Vibrophore testing machine, via fatigue to give starter crack lengths within the range set out in the standard. The maximum applied loads were reduced from 8 kN to 2 kN, together with a stress ratio of 0.1 and a frequency of 60~70 Hz. The final fracture toughness testing was carried out on the servo hydraulic testing machine manufactured by ESH Ltd. with a ramp rate of 0.5 mm/min to obtain load *v.* COD (crack opening displacement) curves, and the value is calculated from the following equation [*British Standard 1991*]:

$$K_Q = \frac{F_Q}{BW^{0.5}} \times f'(\frac{a_o}{W}) \qquad (3.2)$$

Where K_Q is the provisional value of plane strain fracture toughness K_{Ic}; F_Q is the particular value of applied load; B is the thickness; W is the width; a_o is the average original crack length; $f'(\frac{a_o}{W})$ is given by specific value of $\frac{a_o}{W}$. Confirmation that the validity criteria for quoting K_{IC} as defined in the standard was confirmed following each test.

(a)

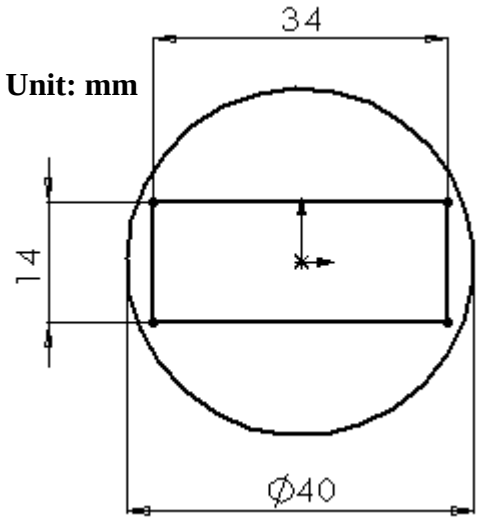

(b)

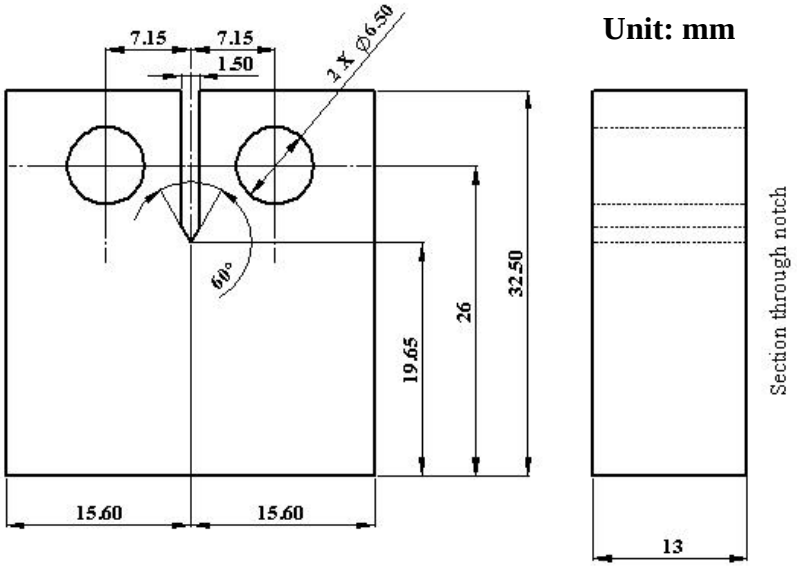

Fig.3-9 (a) Schematics of machining rectangular blanks (14x34x34mm^3) by EDM from cylindrical forged billets or HIPped bars; (b) dimensions of final shape fracture toughness specimens.

An AxioCamMRc5 optical microscope, in conjunction with software AxioVision 4.1 was used to examine fracture surfaces of CT specimens. Detailed fractographic investigations were performed along the plane of fracture in selected CT specimens

for both fatigue pre-crack and tensile overload regions by SEM BSE in JOEL 7000 to understand the relationship between microstructure and fracture toughness property on forged and HIPped Ti-6Al-4V.

References

***British Standard 1991*:** British Standard, "Fracture mechanics toughness tests — Part 1: Method for determination of K_{Ic}, critical CTOD and critical *J* values of metallic materials", *BSI*, BS7448-1: 1991.

***Dowling 1999**:* Dowling, N.E., Mechanical behaviour of metals, Engineering methods for deformation, fracture and fatigue, Ed. 2, *Prentice-Hall Inc.*, New Jersey, USA, 1999.

Thümmler 1993: Thümmler, F., and Oberacker, R., *Introduction to Powder Metallurgy*, Series Editors: Jenkins, I., Wood, J. V., the Institute of Materials, 1993.

Chapter 4 Microstructure and properties of HIPped samples of powder Ti-6Al-4V

Net Shape HIPping (Hot Isostatic Pressing) is becoming an accepted technology for the manufacture of a range of engineering components [*Seliverstov 1994*, *Li 1987*, *Dellis 1996*, *Raisson 1999*] and it is thus essential that the factors which influence the properties of such components are understood and that the HIPping process parameters are optimised according to specific application requirements. In the first part of this chapter work is reported where specimens of the complete size fraction of PREP Ti-6Al-4V powder were HIPped using a variety of conditions and the microstructures examined and properties assessed so that improved HIPping conditions could be defined. The second part of the chapter investigates the influence of the powder characteristics on the properties by using individual powder size fractions of the powder and HIPping using a fixed set of conditions, with microstructures and mechanical properties of resultant samples being compared.

4.1 HIPping of the complete size fraction of PREP Ti-6Al-4V powder

4.1.1 Microstructural examination of original powder

PREP Ti-6Al-4V powder was selected for the study because of its cleanliness [*Cahn 1991*], freedom from satellites, commonly seen in gas-atomised spherical powder, and because it could be used for high performance applications [*Delo 1999*]. The morphology of as-received powder is shown in Fig. 4-1. Spherical clean PREP

powder can be seen in Fig. 4-1 (a, b), but some powder particles appear as flat discs (see Fig. 4-1 (c, d)); these are formed when the liquid metal droplets hit the chamber walls before their solidification into powder [*Cahn 1991*]. The microstructure of powder particles' cross section (Figs. 4-2 (a, b)) shows that it is composed entirely of martensitic alpha-prime phase, a result of the rapid cooling during powder production. The powders are mostly polycrystal, the β/β grain boundaries are visible in high magnification BSE image (see Fig. 4-2 (b)) and EBSD misorientation map (see Fig. 4-2 (c)). Misorientation angle graph (see Fig. 4-2 (d)) between the martensite plates shows they have certain misorientation angles which are in agreement with Burger's relationship [*Lütjering 2003*].

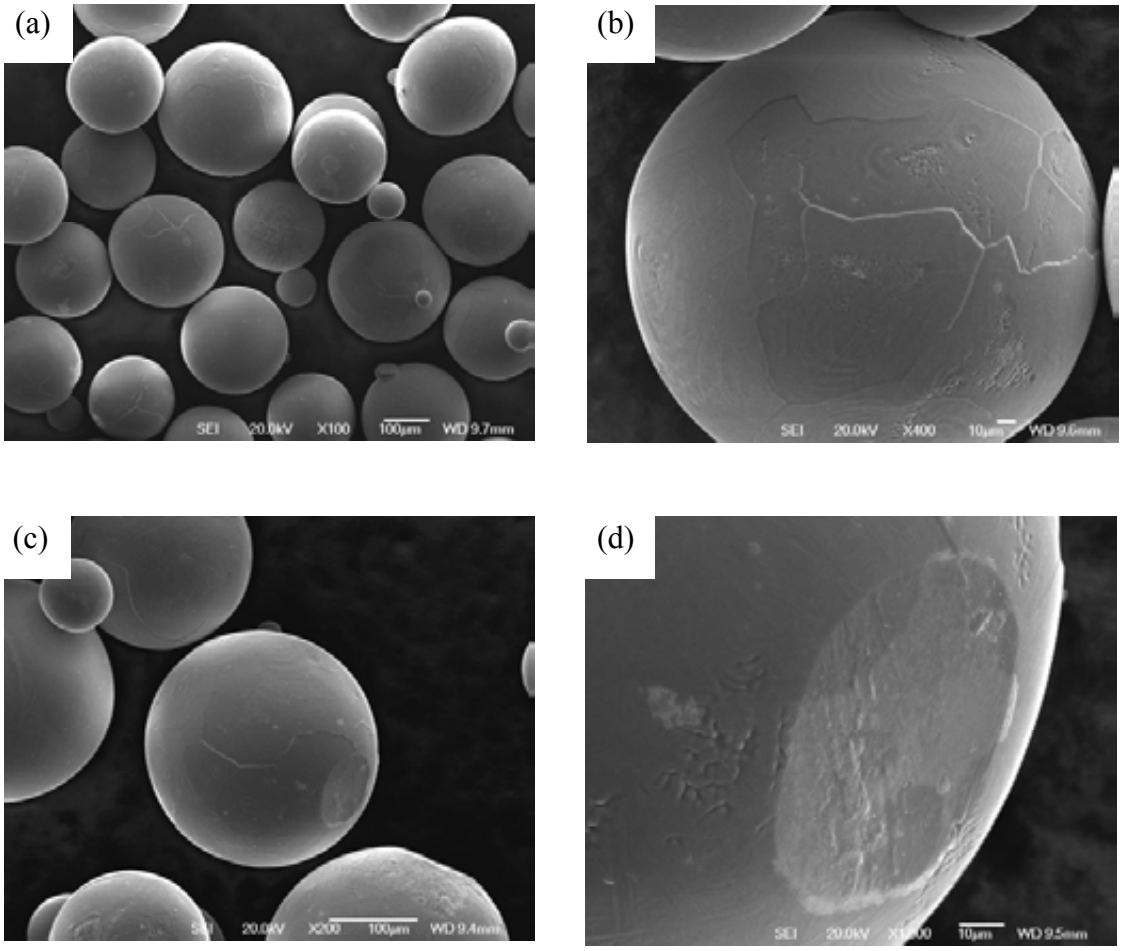

Fig. 4-1 SEM secondary electron micrographs showing the morphology of as-received PREP Ti-6Al-4V powder surfaces at different magnifications: (a, b) spherical clean PREP powder; (c, d) powder with flat disc.

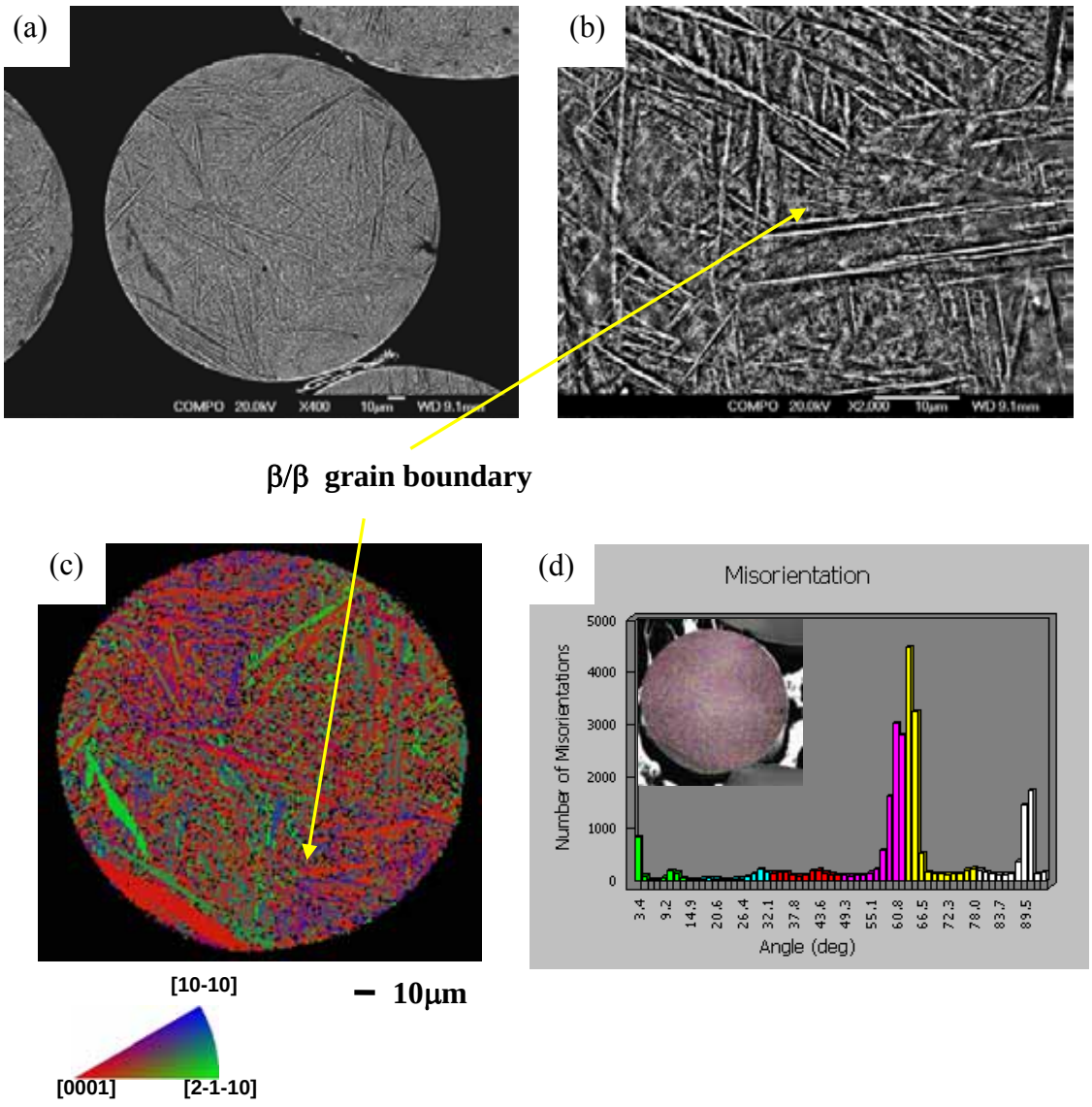

Fig. 4-2 (a) SEM backscattered electron micrograph of cross section of as-received PREP Ti-6Al-4V powder showing martensitic alpha-prime phase; (b) EBSD misorientation map and (c) EBSD misorientation angle graph of the martensite plates showing high misorientation angles among the martensite grain boundaries (shown in (d) as purple and yellow lines).

4.1.2 Effect of HIPping temperature on mechanical properties

4.1.2.1 Microstructure of HIPped samples using different temperature

The complete size fraction (50~400μm) of PREP Ti-6Al-4V powder was HIPped by simultaneously ramping up to the HIPping temperature and pressure, holding the material there for a period, followed by reducing the pressure and the temperature in phase in the HIP. The cooling rate used was about 5°C/min. The effect of HIPping temperature was investigated using a range of temperatures, including both sub-transus and super-transus temperatures (beta transus: about 990°C): 880°C, 930°C and 1020°C. A standard HIPping pressure of 100 MPa and holding time of 4h were used throughout. Chemical analyses of HIPped Ti-6Al-4V samples were conducted to measure the overall composition of elements. Table 4-1 gives the composition of a sample HIPped at one of the chosen HIPping temperatures (930°C).

Table 4-1 Chemical composition of Ti-6Al-4V sample HIPped at one of the chosen HIPping temperatures (930°C) (unit: wt%)

	O	**Fe**	**Al**	**V**	**Ti**
HIPped Ti-6Al-4V	0.20	0.17	6.42	3.88	balance

Individual powder particles were simply heat treated (i.e. not HIPped) at 930°C for 2h followed by slowly furnace cooling, and their microstructure was compared with that in as-HIPped samples (produced by HIPping at 930°C) in order to understand the microstructural changes during the HIPping process, as shown in Fig. 4-3. It is found that simply heat treated powders exhibit lath-like or basket weave structure with high

misorientation angles (see Figs. 4-3 (a, c, e, g)). The as-HIPped microstructure (see Figs. 4-3 (b, d)) is composed of α (the bright phase in optical and the dark phase in BSE) and β (the dark phase in optical and the bright phase in BSE). The beta phase shows two different morphologies in the HIPped sample; equiaxed and lath-like. The alpha phase within these two regions is also equiaxed and lath-like. EBSD misorientation map and angle graph (see Figs. 4-3 (e, g)) show that the lath-like structures within the central part of the original particles in as-HIPped sample still have high misorientation angles, but the small equiaxed grains formed at original particle boundaries have low misorientation angles (mainly shown by green lines in Fig. 4-3 (h)) which are not seen in the misorientation angle graph obtained from simply heat treated particles (see Fig. 4-3 (e, g)). Some of the lamellar laths and equiaxed grains with similar orientations can form clusters acting as larger grains (indicated by arrows in Fig. 4-3 (f)).

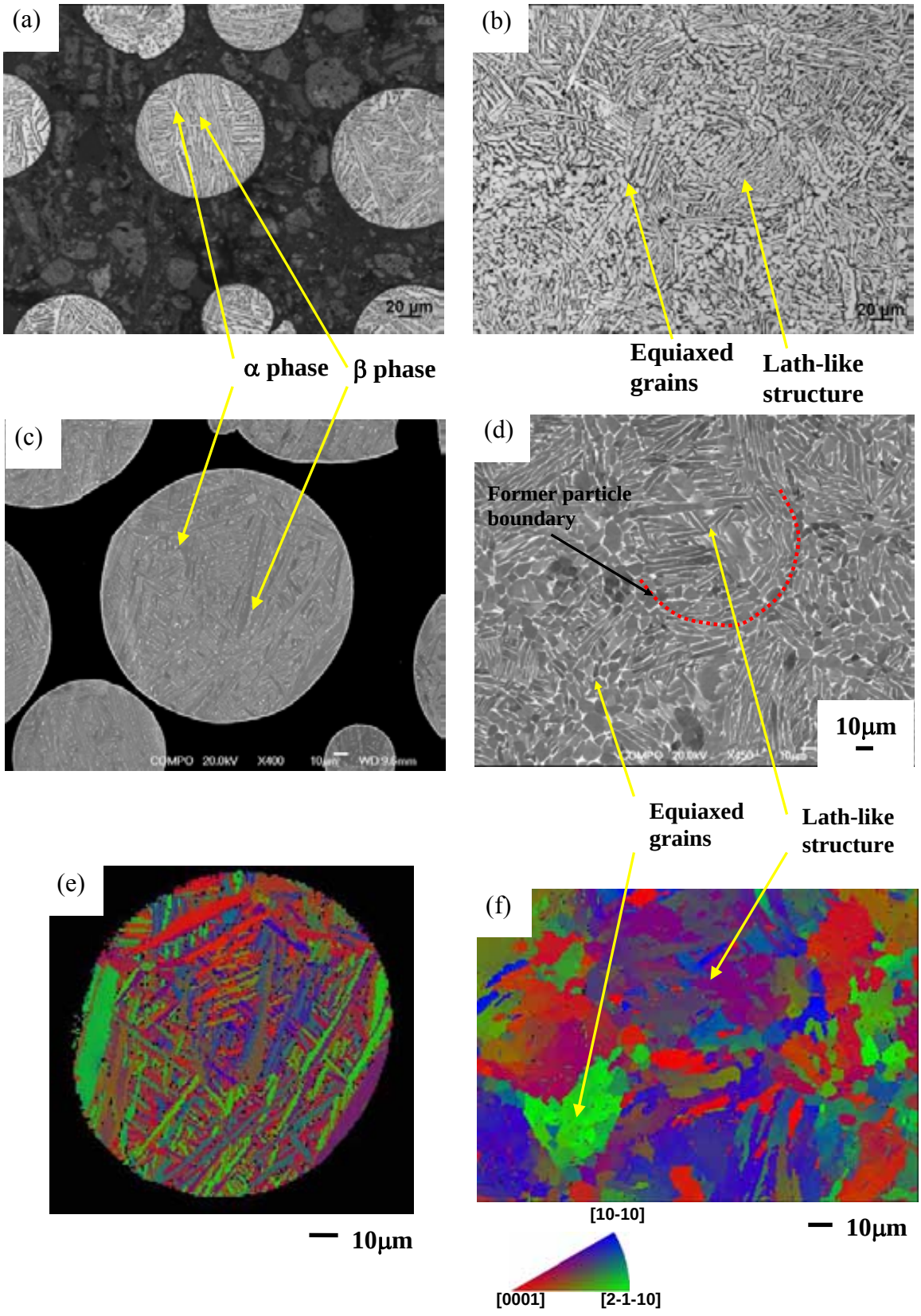
(a)
20 μm
α phase
β phase
(b)
20 μm
Equiaxed grains
Lath-like structure
(c)
(d)
Former particle boundary
10μm
Equiaxed grains
Lath-like structure
(e)
10μm
(f)
[10-10]
10μm
[0001]
[2-1-10]

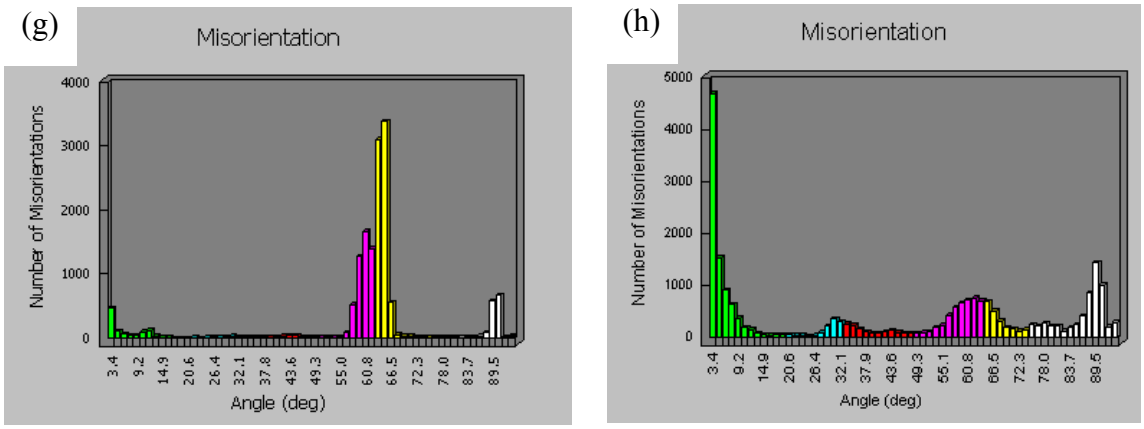

Fig. 4-3 (a, c, e, g) PREP Ti-6Al-4V powders heat treated at 930°C for 2 hours and slowly furnace cooled; (b, d, f, h) Ti-6Al-4V sample HIPped at 930°C, 100MPa, 4h. (a, b) optical image (the bright phase is alpha); (c, d) SEM backscattered electron micrograph (the dark phase is alpha); (e, f) EBSD misorientation map; (g, h) EBSD misorientation angle graph. It shows that simply heat treated powders have lath-like or basket weave structure with high misorientation angles. The as-HIPped microstructure is composed of equiaxed grains formed at the former particle boundaries and similar lath-like structure to (a). The equiaxed grains have low misorientation angles (mainly shown in green lines in Fig. (h)) and some of them can form clusters with similar orientations (shown in Fig. (f)).

Fig. 4-4 shows the microstructure and EBSD maps of Ti-6Al-4V samples HIPped at 880°C. In lower magnification images, such as that shown in Fig. 4-4 (a), it can be seen that the equiaxed beta is distributed mainly, but not exclusively, along the initial particle boundaries and the lath-like or basket-weave structure is present throughout the main body of each original powder particle. Some lamellar colonies with similar orientations can be observed, as indicated by arrows in Figs. 4-4 (b, d). The sizes of

the equiaxed α grains and the widths of the α lamellae were measured to be 2~8 μm and 3~7μm, respectively. Measurements of the beta phase showed that the equiaxed beta was about 0.3~2.6μm and the width of the laths was very fine, about 0.05~0.67 μm. The overall volume fraction of alpha phase was measured to be about 92%, and that of beta phase was measured to be about 8%.

When samples were HIPped at 930°C, the main change was that the microstructure coarsened (see Fig 4-5); the equiaxed α grain size was found to increase to 6~12 μm and the widths of the alpha laths also increased slightly and were measured to be between 5~10μm. The equiaxed beta and the lath-like beta only coarsened by a small amount. It was about 0.6~5.7 μm for the equiaxed beta and about 0.10~0.76 μm for the width of the beta laths. The volume fraction of beta phase increased to 10% after HIPping at 930°C. Since the HIPping temperature is closer to the beta transus than that of 880°C, a much higher beta content at the HIPping temperature is expected [*Lütjering 2003*] but the slow cooling in the HIP would tend to reduce this difference. Fig. 4-6 shows the pseudo binary phase diagram for Ti-6Al-xV, where the beta volume fraction in equilibrium at 880°C is approximately 17% whereas at 930°C it is about 30% and it is thus clear that as expected slow cooling does allow significant formation of alpha during cooling from these temperatures.

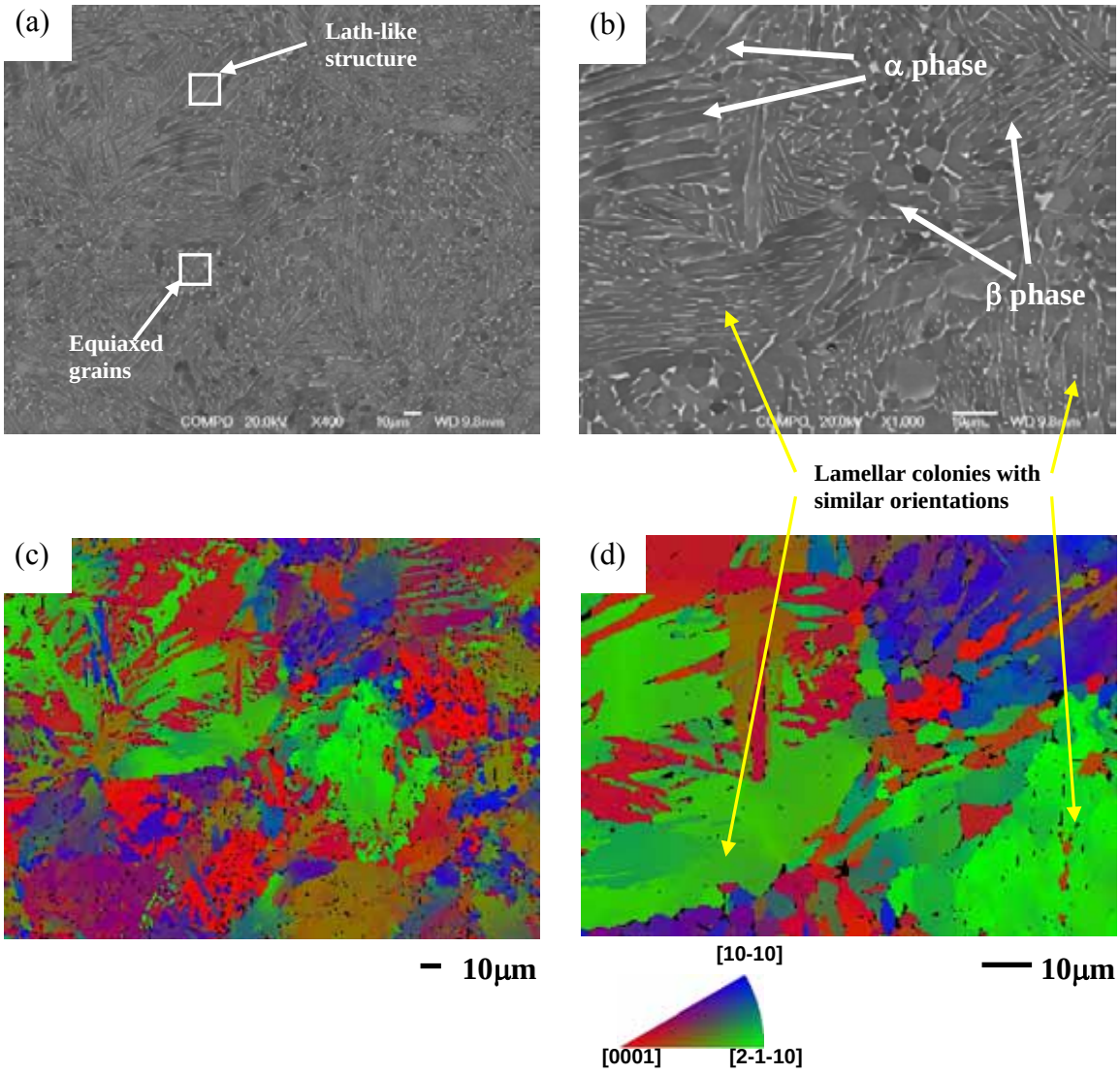

Fig. 4-4 (a, b) SEM backscattered electron micrographs showing the microstructure of Ti-6Al-4V sample HIPped at 880°C, 100MPa, 4h at different magnifications; (c, d) matching EBSD misorientations maps showing that there exist some lamellar colonies with similar orientations (indicated by the arrows).

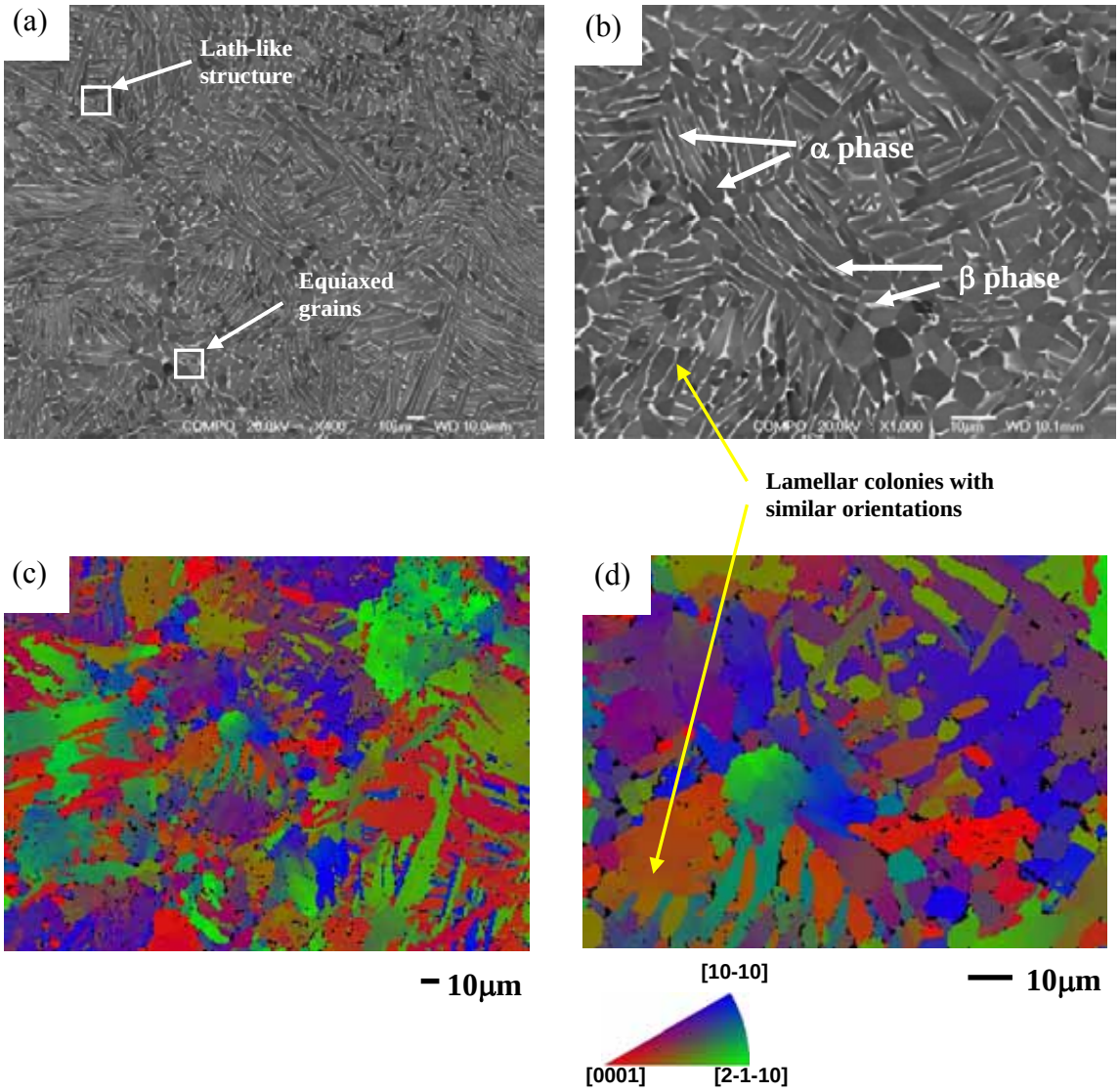

Fig. 4-5 (a, b) SEM backscattered electron micrographs showing the microstructure of Ti-6Al-4V sample HIPped at 930°C, 100MPa, 4h at different magnifications; (c, d) matching EBSD misorientations maps. The microstructure is coarser than that in the sample HIPped at 880°C.

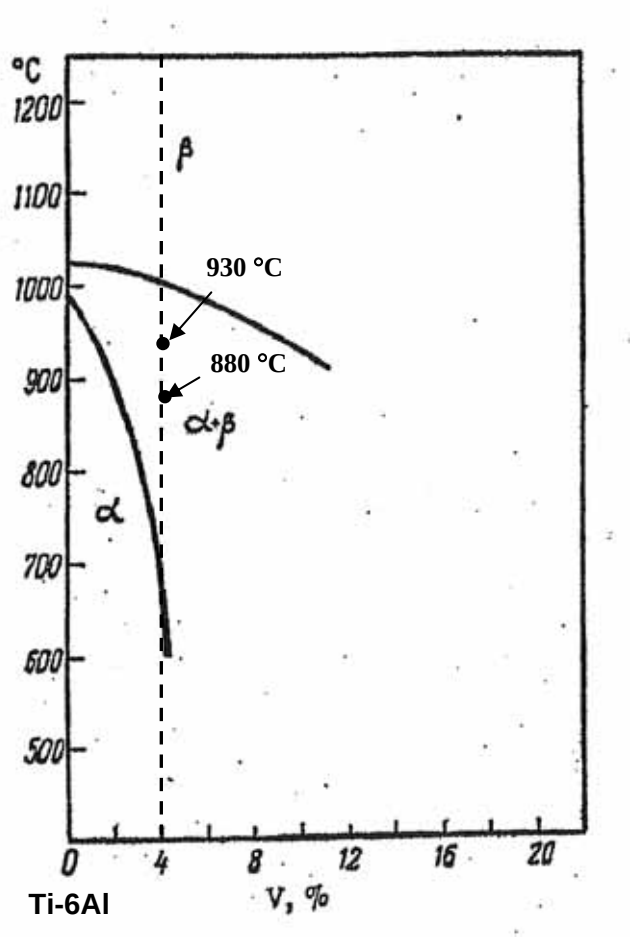

Fig. 4-6 Pseudo binary phase diagram for Ti-6Al-xV from which the beta volume fractions in equilibrium at different temperatures (below beta transus) can be estimated for the alloy containing 4% V. The beta volume fraction in equilibrium at 880°C is approximately 17%, and it is about 30% at 930°C.

When the HIPping temperature was increased to 1020°C i.e. to above the β transus (about 990°C), the microstructure coarsened significantly, as shown in Fig. 4-7. The sizes of equiaxed α grains are up to about 40μm in diameter and the widths of the α lamellae are about 10~20μm. The equiaxed beta grains were measured to be about 0.7~11.8μm and the beta laths about 0.20~2.20μm. The volume fraction of β phase

was about 12%. Fig. 4-8 shows the diameter distribution of equiaxed beta grains and width distribution of beta laths in powder Ti-6Al-4V samples HIPped at different temperatures. It is clear that the beta phase become coarser as the HIPping temperature increases. A summary of the size ranges of alpha and beta phases and phase distribution is given in Table 4-2. Fig. 4-9 shows the misorientation angle graphs of the three sets of HIPped samples' microstructure. It was found that the proportion of low angle misorientations was reduced as the HIPping temperature increased.

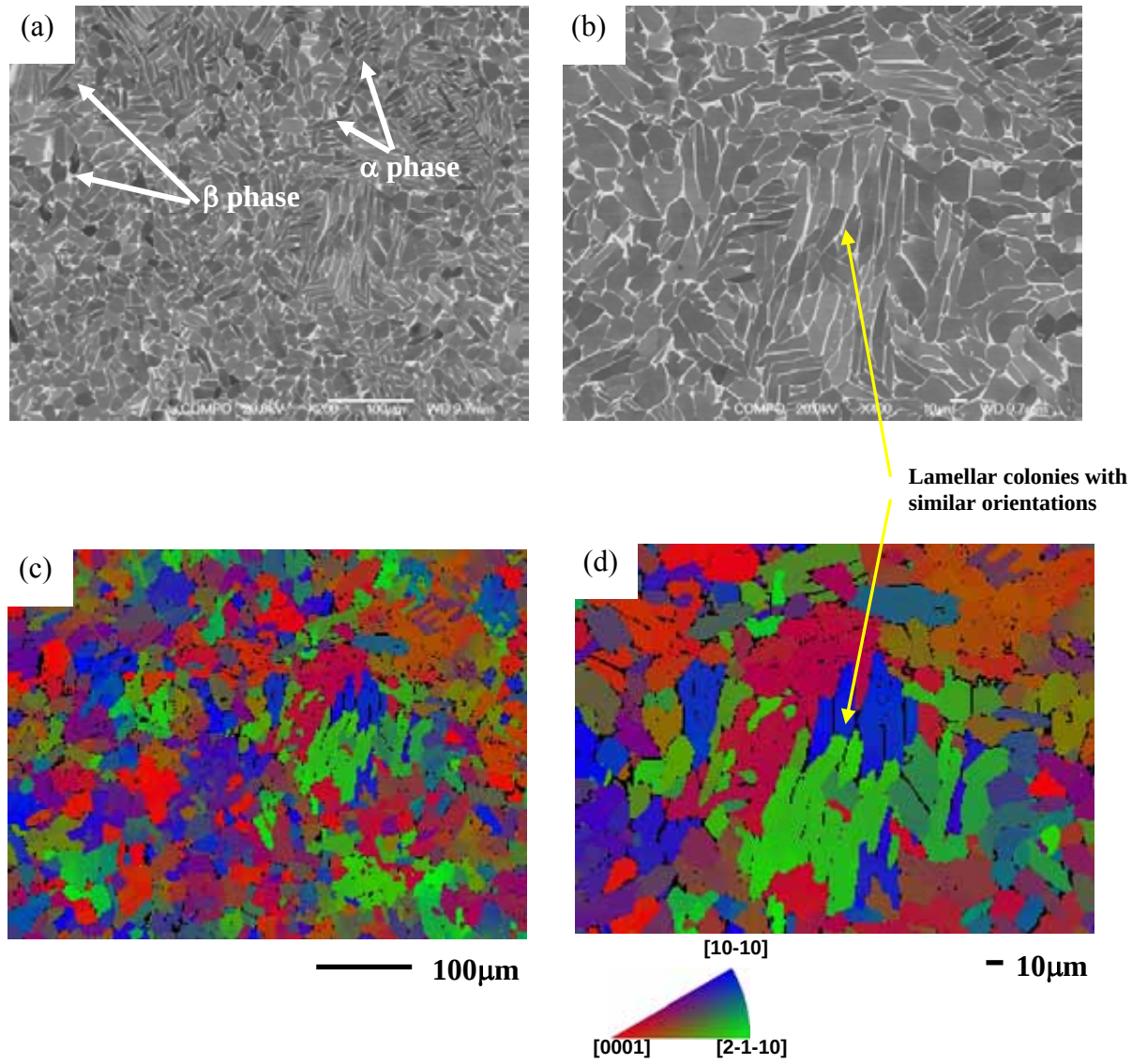

Fig. 4-7 (a, b) SEM backscattered electron micrographs showing the microstructure of Ti-6Al-4V sample HIPped at 1020°C, 100MPa, 4h at different magnifications; (c, d) matching EBSD misorientations maps showing that there exist some lamellar colonies with similar orientations (indicated by the arrows). These sizes of lamellar colonies are up to 60 μm. The microstructure is coarsened significantly compared to that in samples HIPped below beta transus (i.e. 880°C, 930°C).

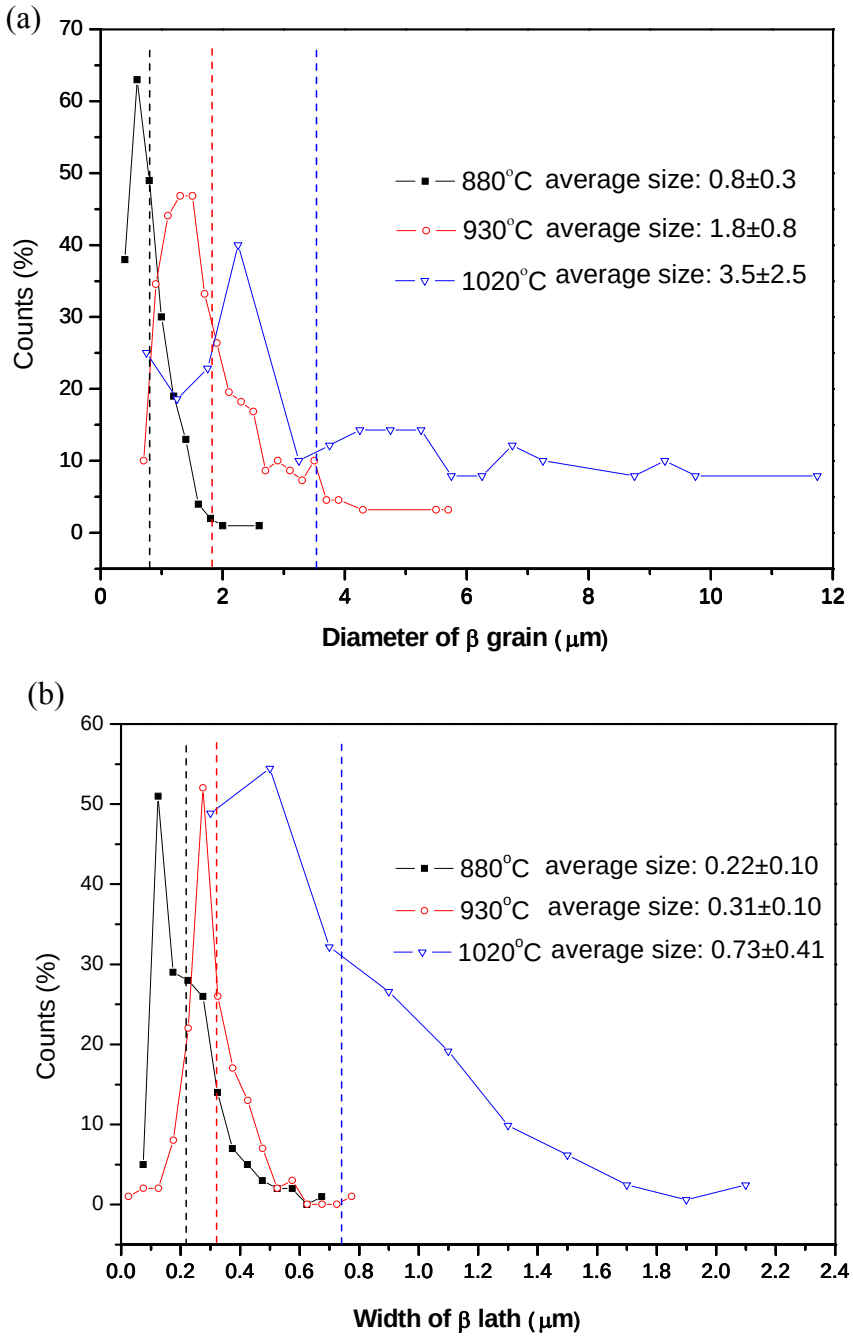

Fig. 4-8 (a) The diameter distribution of equiaxed beta grains; (b) the width distribution of beta laths in powder Ti64 samples HIPped at different temperatures.

Table 4-2 The sizes of alpha and beta phases and phase distribution of powder Ti-6Al-4V HIPped at different temperatures

	Size of α phase(μm)		Size of β phase(μm)		Volume fraction of β phase (%)
	Equiaxed α grain size	Width of α lamellae	Equiaxed β grain size	Width of β lamellae	
880°C/100MPa/4h	2~8	3~7	0.3~2.6	0.05~0.67	8
930°C/100MPa/4h	6~12	5~10	0.6~5.7	0.10~0.76	10
1020°C/100MPa/4h	10~40	10~20	0.7~11.8	0.20~2.20	12

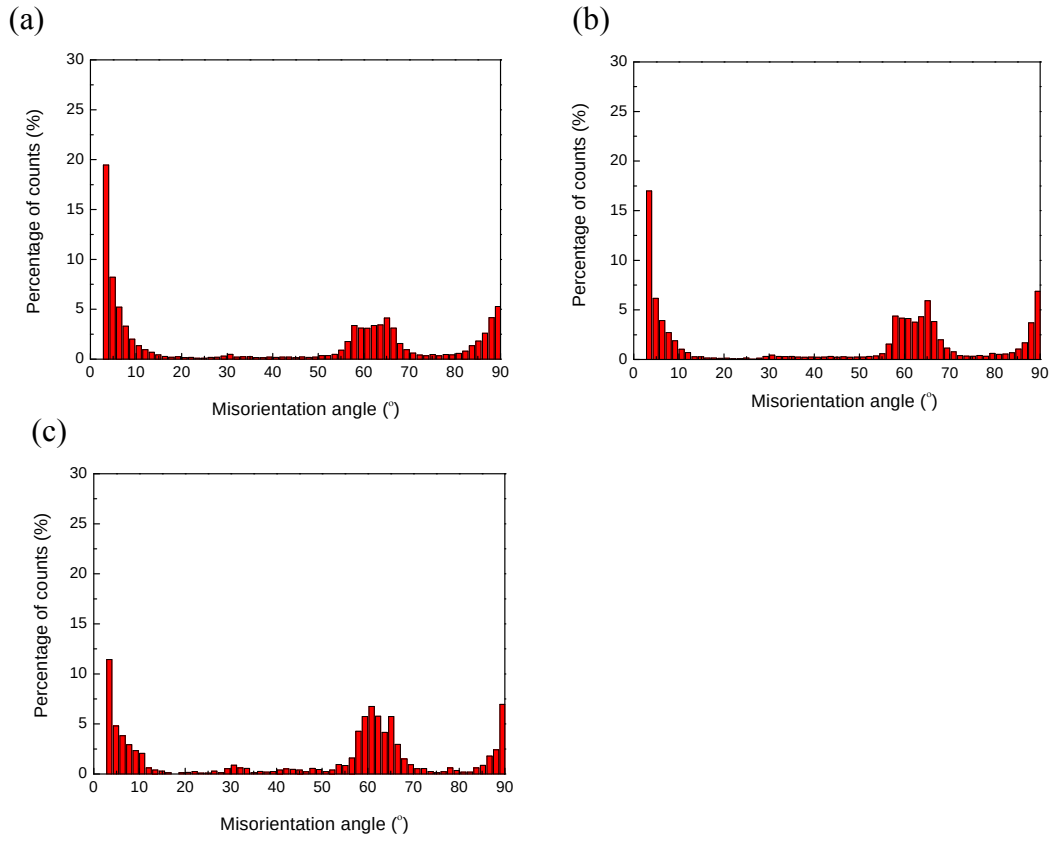

Fig. 4-9 Misorientation angle graphs of (a) Ti-6Al-4V sample HIPped at 880°C, 100MPa, 4h; (b) Ti-6Al-4V sample HIPped at 930°C, 100MPa, 4h; (c) Ti-6Al-4V sample HIPped at 1020°C, 100MPa, 4h showing that the proportion of low angle misorientations is reduced as HIPping temperature increases.

It is noticed that the as-HIPped microstructure is obviously different from the three typical microstructure found in ingot-route samples (see Fig. 2-5). Comparison was made between samples HIPped at 930°C, 1020°C and ingot-rout samples isothermally forged at 910°C, 1050°C and commercially forged at 920~940°C, respectively, as shown in Figs. 4-10, 4-11. It is found that the microstructures of ($\alpha + \beta$)-forged samples (isothermally forged at 910°C (see Fig. 10 (c)) and commercially forged at 920~940°C (see Fig. 10 (e)) are finer than that of ($\alpha + \beta$)-HIPped sample (at 930°C) (see Fig. 10(a)). The microstructure of sample commercially forged at 920~940°C is coarser than that of sample isothermally forged at 910°C. However, in the isothermally forged sample clusters are found which have similar orientations and such a cluster (indicated by the arrow in Fig. 10 (d)) is much larger than the structures in the as-HIPped material. As shown in Figs. 10(g) and (h) there is a higher fraction of low angle boundaries in the isothermally forged sample than in the HIPped sample. The misorientation distribution of commercially forged sample (see Fig. 10 (i)) shows similar fractions of low angle and high angle boundaries to the HIPped sample.

As for the microstructure of samples HIPped at 1020°C, it is simply a coarser version of that found in samples HIPped below the transus, which is very different from the beta-forged ingot-route sample (at 1050°C) (see Fig. 4-11). For the beta-forged ingot-route sample, after cooling from the transus the grain boundaries of the coarsened beta act as the site for alpha nucleation during cooling and the basket weave or Widmanstätten structure is formed. This microstructure is typical of 100% transformed β microstructure. It is interesting to note that HIPped sample has some sort of memory as its microstructure did not change completely even when it is HIPped at 1020ºC which is above β transus (990°C) (see Figs. 4-11(a, c)). This

implies that the α phase may not completely disappear at 1020°C as would be expected and further work is needed to understand the reason behind this.

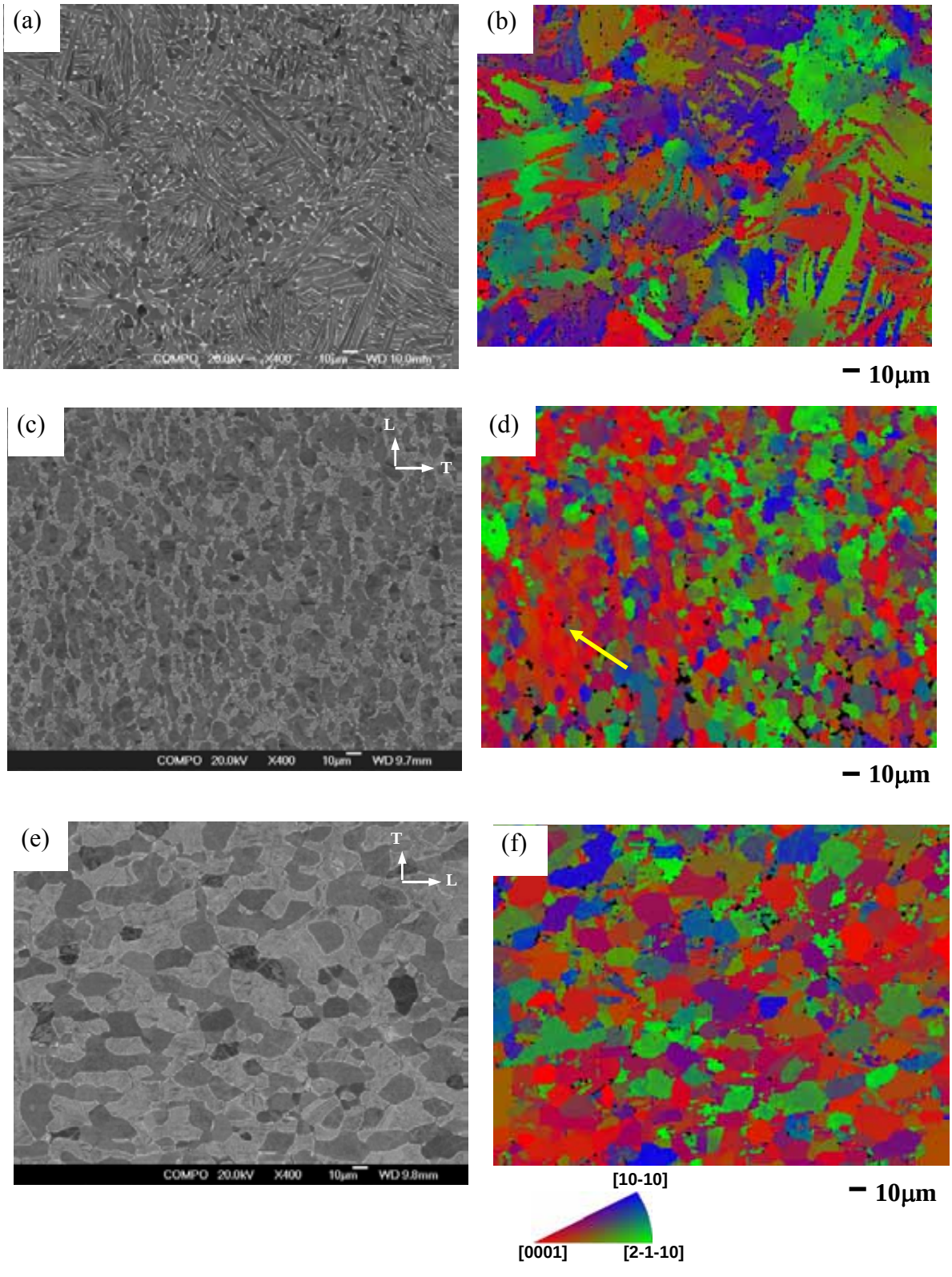

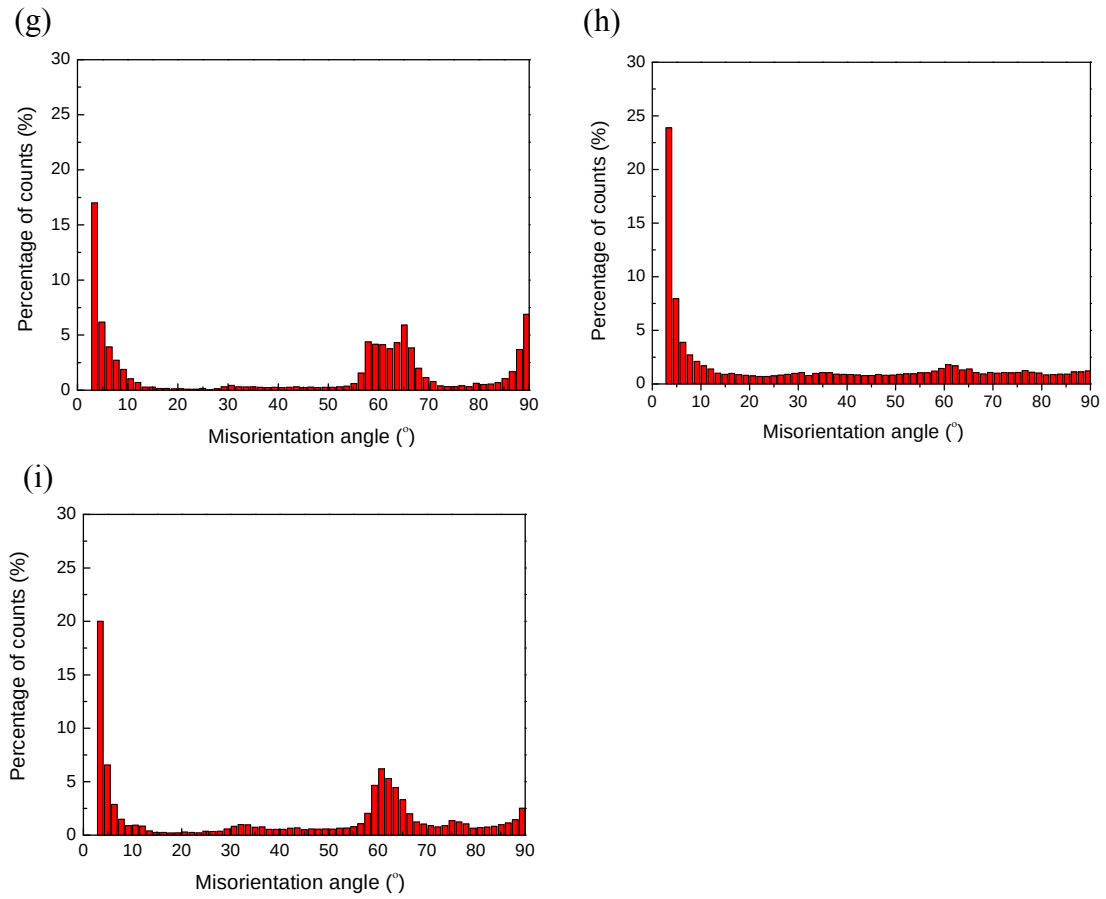

Fig. 4-10 SEM BSE micrographs and EBSD maps of Ti-6Al-4V samples (a, b) HIPped at 930°C; (c, d) isothermally forged at 910°C (microstructure is in the *L-T* plane); (e, f) commercially forged at 920~940°C (microstructure is in the *L-T* plane). A cluster showing similar orientation is indicated by the arrow in (d). Misorientations between grains are shown in samples (g) HIPped at 930°C; (h) isothermally forged at 910°C and (i) commercially forged at 920~940°C (Condition of commercial forging: forged at 920~940°C+HTed at 950°C/1h/WQ+Ageing at 550°C/2h/AC).

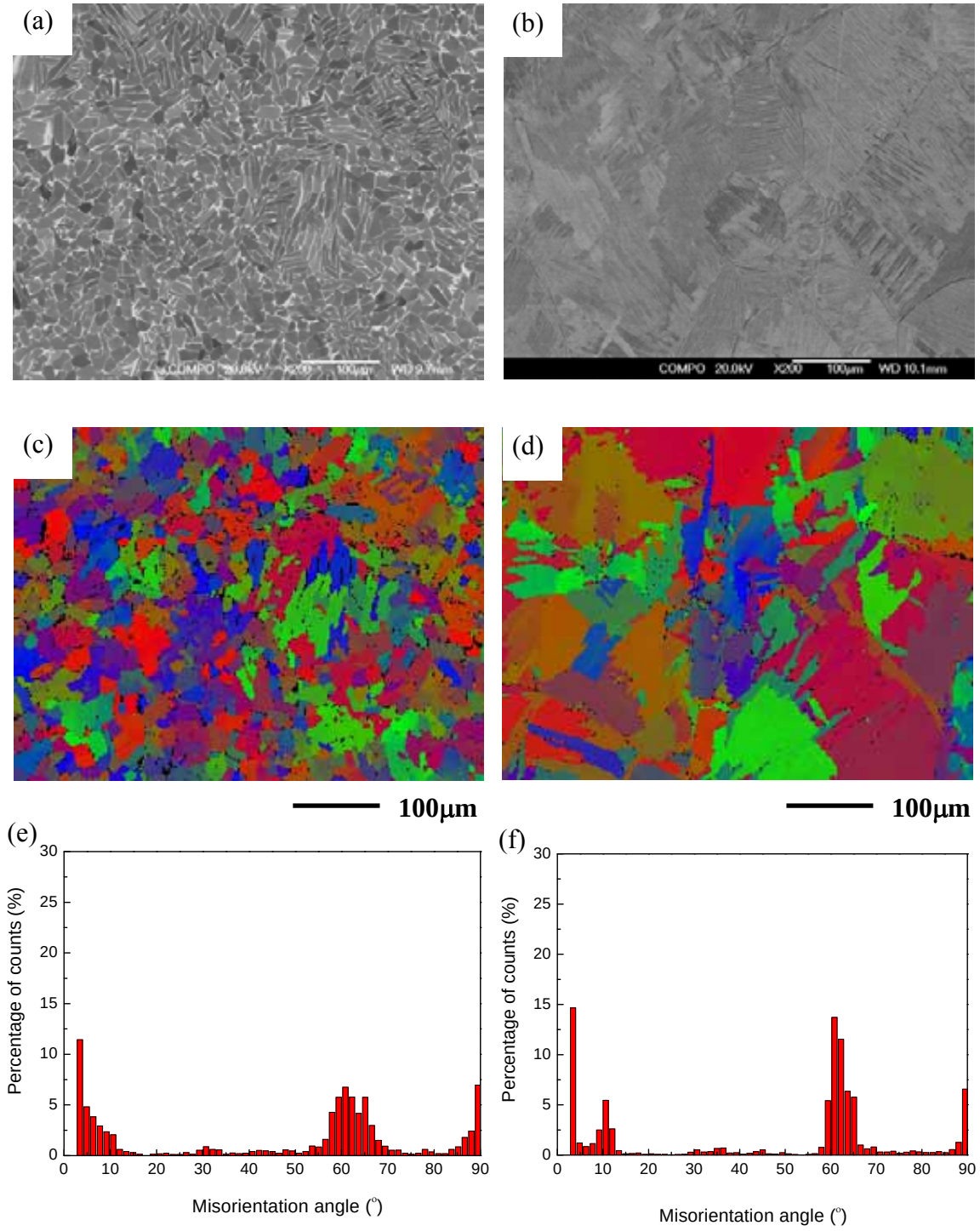

Fig. 4-11 (a, c, e) HIPped Ti-6Al-4V sample at 1020°C; (b, d, f) forged Ti-6Al-4V sample at 1050°C. (a,b) SEM backscattered electron micrographs; (c,d) EBSD misorientation maps; (e,f) misorientation distribution graphs. the microstructure in HIPped sample is different from the beta transformed microstructure in forged sample.

The compositions of two phases in the samples HIPped at different temperatures were measured by EDX, as shown in Fig. 4-12. The fraction of Al, an α-stabiliser, was found to be higher in the α phase (see Fig.4-12 (a)) as would be expected and the V which is a β-stabiliser had a higher concentration in the β phase (Fig.4-12 (b)). The compositions of these two elements in these two phases show no obvious differences for samples HIPped at different temperatures as shown in Table 4-3, again implying that some diffusion occurs during cooling.

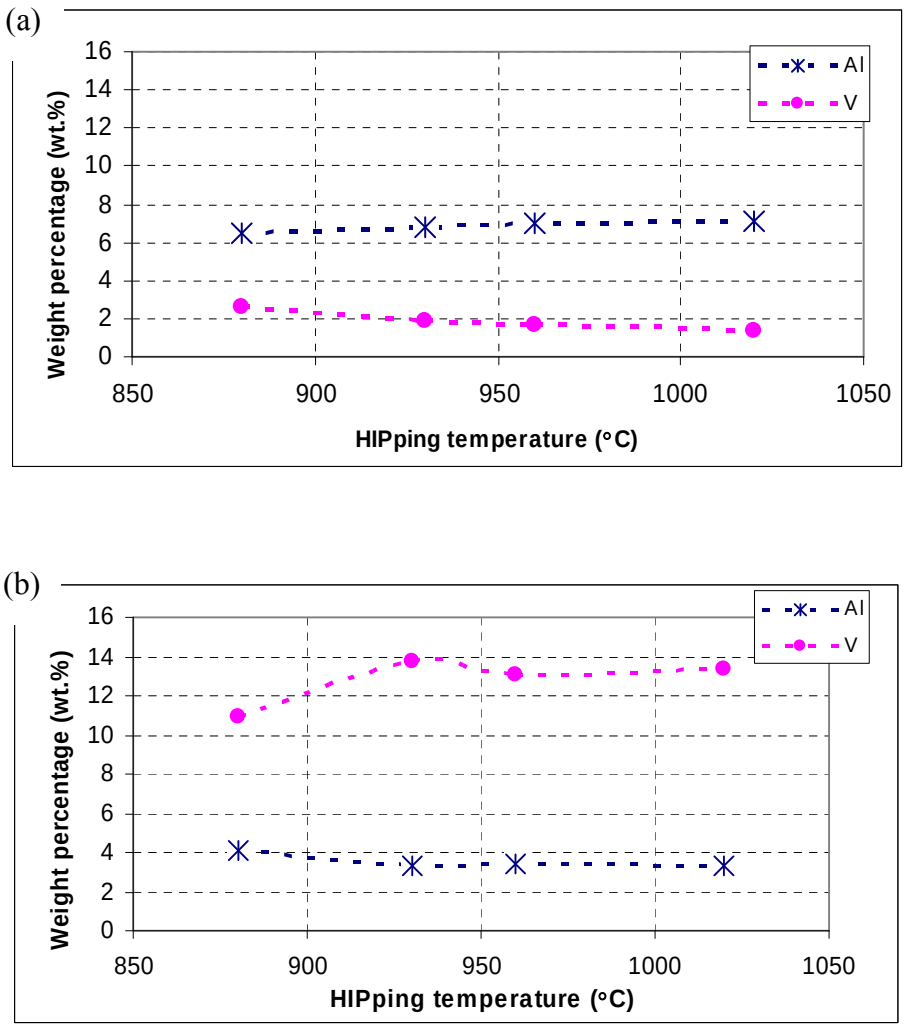

Fig. 4-12 The compositions of two phases in the samples HIPped at different temperatures: (a) concentration of Al and V in α phase showing higher fraction of Al; (b) concentration of Al and V in β phase showing higher fraction of V.

Table 4-3 Chemical compositions of two phases of powder Ti-6Al-4V HIPped at different temperatures

Composition	α phase		β phase	
	Al (wt%)	V (wt%)	Al (wt%)	V (wt%)
880°C/100MPa/4h	6.5 ± 0.1	2.6 ± 0.2	4.1 ± 0.7	10.9 ± 3
930°C/100MPa/4h	6.8 ± 0.1	1.9 ± 0.2	3.3 ± 0.3	13.8 ± 1.5
1020°C/100MPa/4h	7.1 ± 0.1	1.4 ± 0.2	3.3 ± 0.3	13.4 ± 1.2

4.1.2.2 Tensile properties and examination of fracture surfaces in samples tested to failure

Room temperature tensile tests were carried out to assess the tensile behaviour of the samples which were HIPped at different temperatures. Three specimens were used for each HIPping condition in order to obtain some indication of the repeatability of the properties. The yield stress, tensile strength and total elongation to failure are illustrated in Fig. 4-13. Samples HIPped at 880°C had the highest yield stress of 927 MPa and tensile strength of 994 MPa and a relatively low ductility of 10%. The samples HIPped at 930°C had a lower yield stress of 901 MPa and a lower tensile strength of 971 MPa with ductility up to 21%. Samples HIPped at 1020°C were shown to have the lowest yield stress and tensile strength, and a ductility of 11%; similar to that of samples HIPped at 880°C. A summary of the mechanical property

data relating to these tests is given in Table 4-4, where excellent consistency was noted for each set of samples.

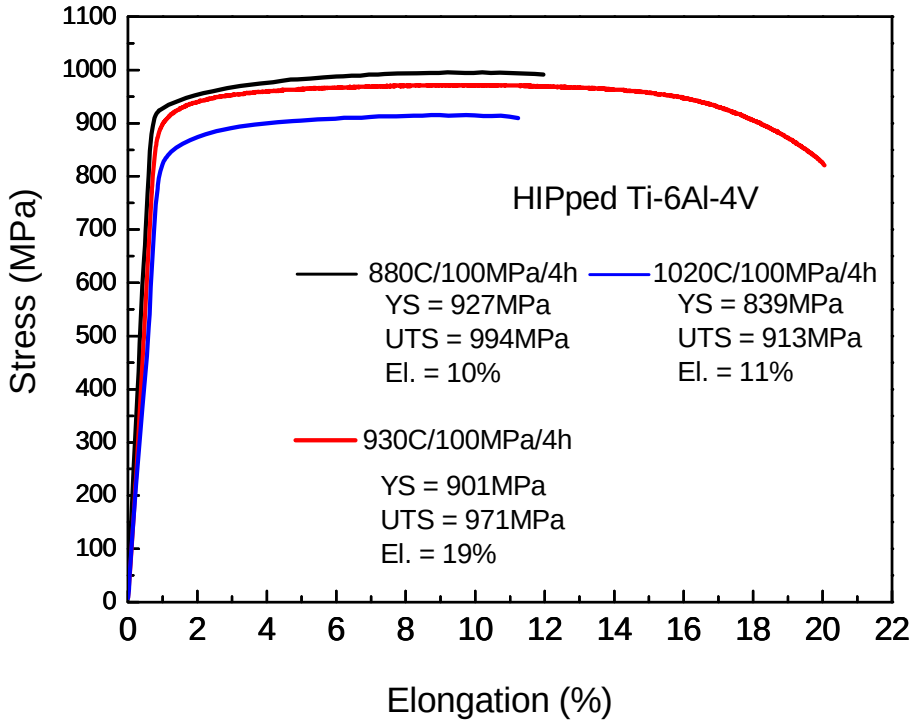

Fig. 4-13 Room temperature tensile properties of powder Ti-6Al-4V samples HIPped at different temperatures.

Table 4-4 Room temperature tensile properties for powder Ti-6Al-4V HIPped at different temperatures

	YS (MPa)	UTS (MPa)	El. (%)
HIPping at 880°C/100MPa/4h	**927**± 4 2	**994** ± 4 5	**10** ± 1 1
HIPping at 930°C/100MPa/4h	**901** ± 3 2	**971** ± 1 1	**19** ± 2 1
HIPping at 1020°C/100MPa/4h	**839** ± 1 2	**913** ± 0	**11** ± 1 1

Fracture surfaces of the tensile specimens were examined and these revealed that there were no obvious crack initiation sites in samples HIPped at 930°C; a typical fracture surface is shown in Fig. 4-14. However at the lower and higher HIPping temperatures some sources of failure were observed. Fig. 4-15 shows the fracture surface in a specimen HIPped at 880°C, where groups of transgranular facets can be seen in the crack initiation site (Figs. 4-15 (a, b)). The crack appears to have propagated along a prior particle boundary (PPB) as shown in Fig. 4-15 (b), which indicates an imperfect degree of bonding at the HIPping temperature of 880°C which probably contributed to the low ductility. In the specimens HIPped at 1020°C, crack initiation was characterised by flat transgranular facets (see Figs. 4-16 (a, b)), which were on the scale of the coarser lamellar colonies in this sample (see Fig. 4-7). Facets along the lamellar interface can also be detected as shown in Fig. 4-16 (b).

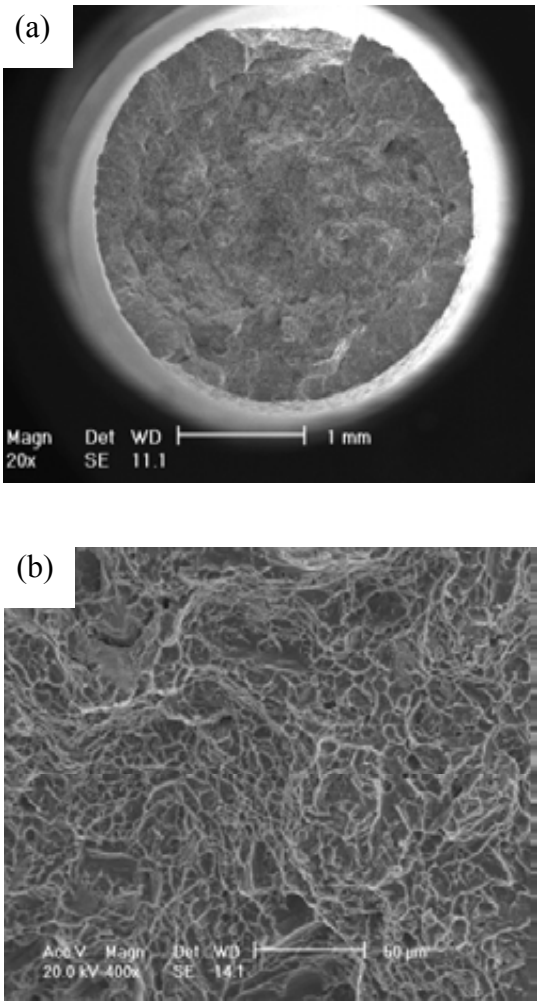

Fig. 4-14 SEM secondary electron micrographs showing the fracture surface of failed tensile samples HIPped at 930°C at different magnifications. No obvious crack initiation site can be seen.

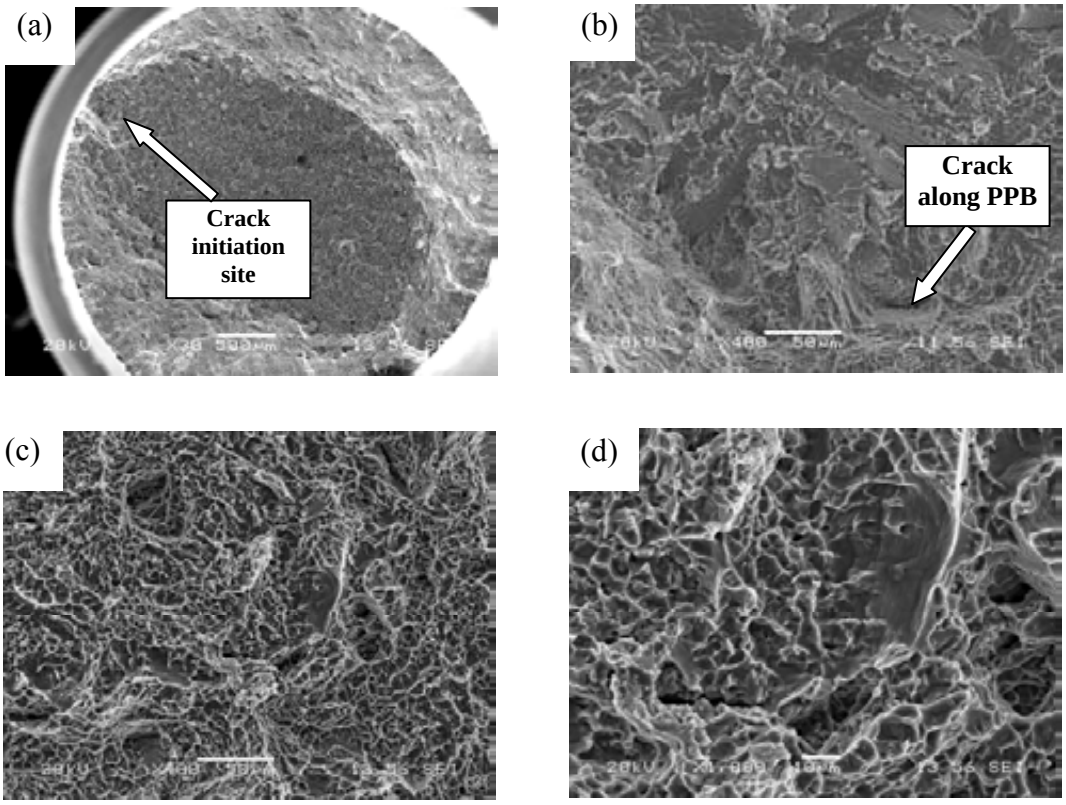

Fig. 4-15 SEM secondary electron micrographs showing the fracture surface of failed tensile samples HIPped at 880°C: (a, b) groups of transgranular facets can be seen in the crack initiation site; (c, d) ductile mode of fracture can be seen in other area. Crack propagating along a prior particle boundary (PPB) is indicated by the arrow in (b).

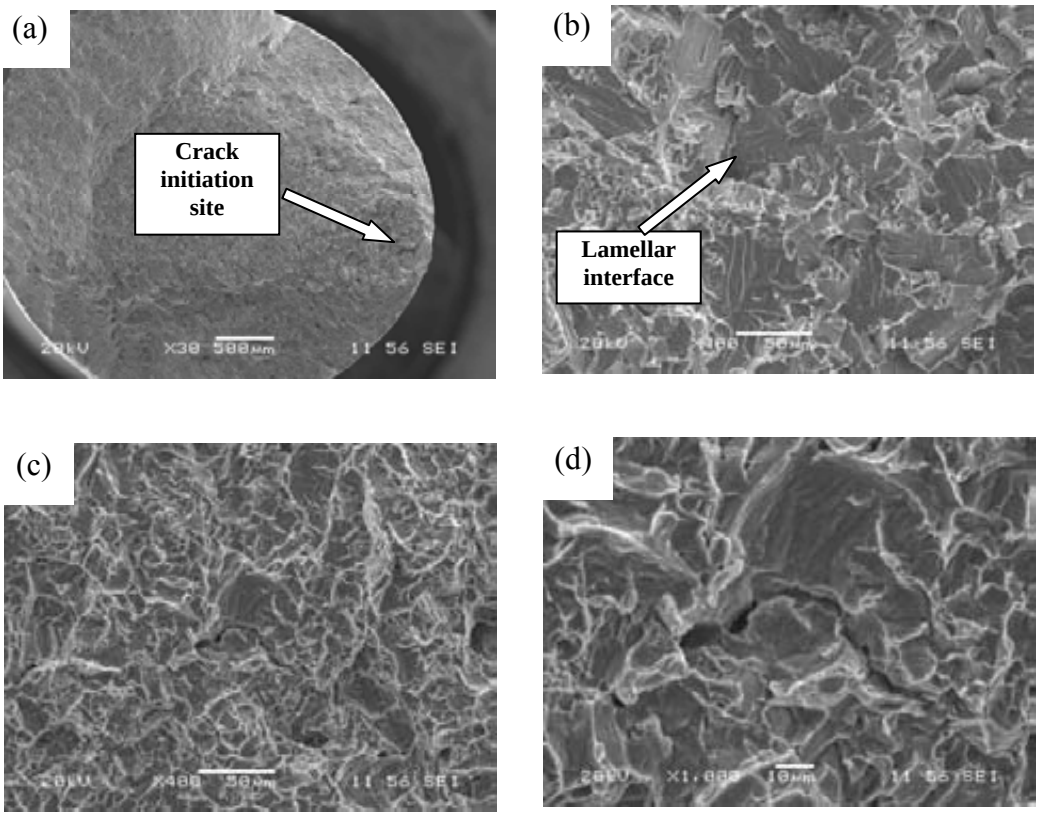

Fig. 4-16 SEM secondary electron micrographs showing the fracture surface of failed tensile samples HIPped at 1020°C: (a, b) flat transgranular facets can be seen in the crack initiation site; (c, d) ductile mode of fracture can be seen in other area. The facets along the lamellar interface are indicated by the arrow in (b).

The fracture surfaces for all the tested specimens showed generally ductile mode of failure and were dominated by microvoid coalescence (see Figs. 4-14 (b), 4-15 (c, d), 4-16 (c, d)), which is in agreement with published work on ingot-route Ti-6Al-4V e.g. by Novovic who suggested that in Ti-6Al-4V, microvoids were eventually formed at some stress concentration sites like grain boundaries or certain types of dislocation tangles [*Novovic 2004*]. However, in sample HIPped at 1020°C (see Figs. 4-16 (c, d)),

the microvoids are relatively shallower than those in sample HIPped at 930°C (see Fig. 4-14 (b)), indicating a reduced ductility.

Some cross sections of failed tensile samples HIPped at different temperatures were examined, as shown in Fig. 4-17. No obvious voids or severe secondary cracks were observed in the samples, indicating the ductile mode of fracture for HIPped Ti-6Al-4V samples.

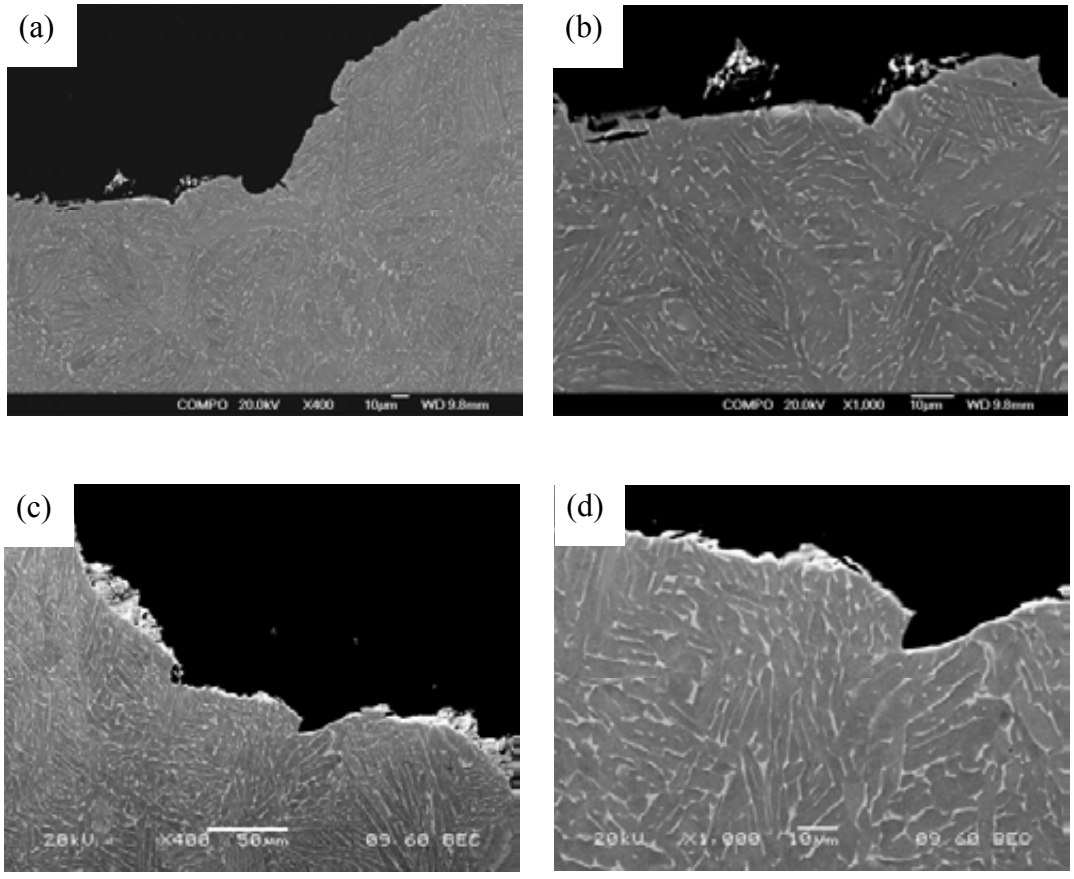

Fig. 4-17 SEM BSE micrographs of the cross sections of failed tensile Ti-6Al-4V samples HIPped at (a, b) 880°C; (c, d) 930°C showing that no obvious voids or severe secondary cracks were observed.

4.1.2.3 Fatigue properties and observations of fracture surfaces of fatigued samples

Fig. 4-18 shows a plot of stress amplitude vs. number of cycles to failure (SN curve) for the samples HIPped at different temperatures. These were machined from HIPped bars and had as-machined surfaces. The samples HIPped at 930°C exhibited the highest run-out strength of 500MPa (at 1.5 x10^7 cycles). The run-out strength of specimens HIPped at 880°C was 400MPa, which decreased further to 300MPa for samples HIPped at 1020°C.

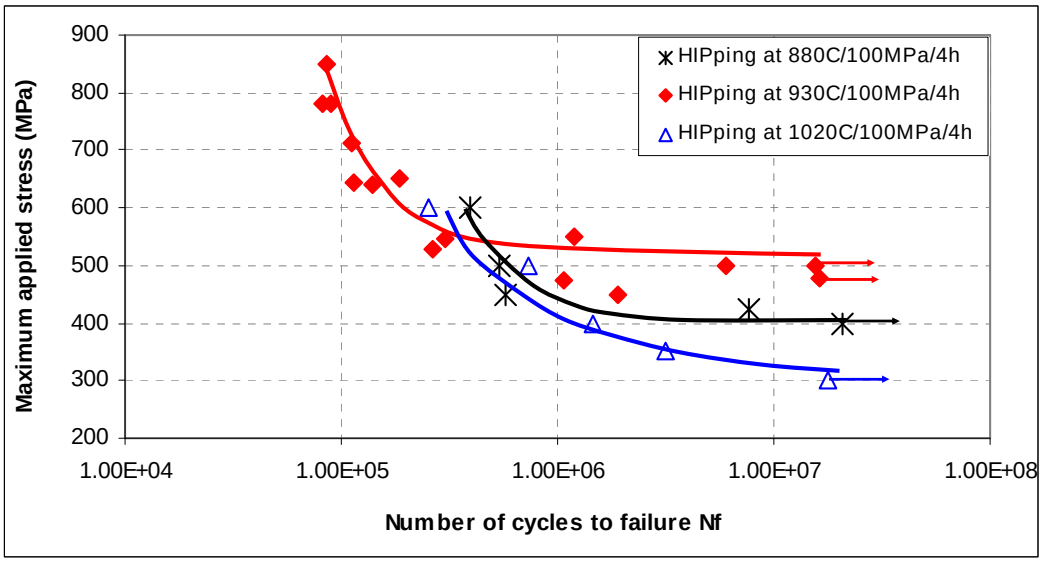

Fig. 4-18 SN fatigue curves for powder Ti-6Al-4V samples with as-machined surface HIPped at different temperatures showing the highest endurance limit of samples HIPped at 930°C.

SEM micrographs of fracture surfaces near crack initiation sites are shown in Figs. 4-19, 4-20, 4-21. It can be seen that fatigue cracks originated from the surface in all

specimens. The main mode of failure of the samples is transgranular. In the fractured surfaces river patterns were seen, which represent steps between different local cleavage facets at slightly different heights but along the same general cleavage plane [*Hertzberg 1989*]. Figs. 4-19 (a, b) illustrate a crack initiation site of a failed fatigue sample HIPped at 930°C, which was characterised by groups of facets. This form of faceting is typical of the early stages of fatigue fractures generated in wrought forms of Ti-6Al-4V, in other α/β alloys and in near α titanium alloys in general [*Bache 2003*].

For samples HIPped at 880°C, transgranular facets can also be identified as the fatigue crack initiation sites (see Fig. 4-20). For samples HIPped at 1020°C large facets are seen as shown in Fig. 4-21. These large facets can be formed when the crack extends through a packet of aligned alpha laths (indicated by arrows in Fig. 4-7) which have similar orientations.

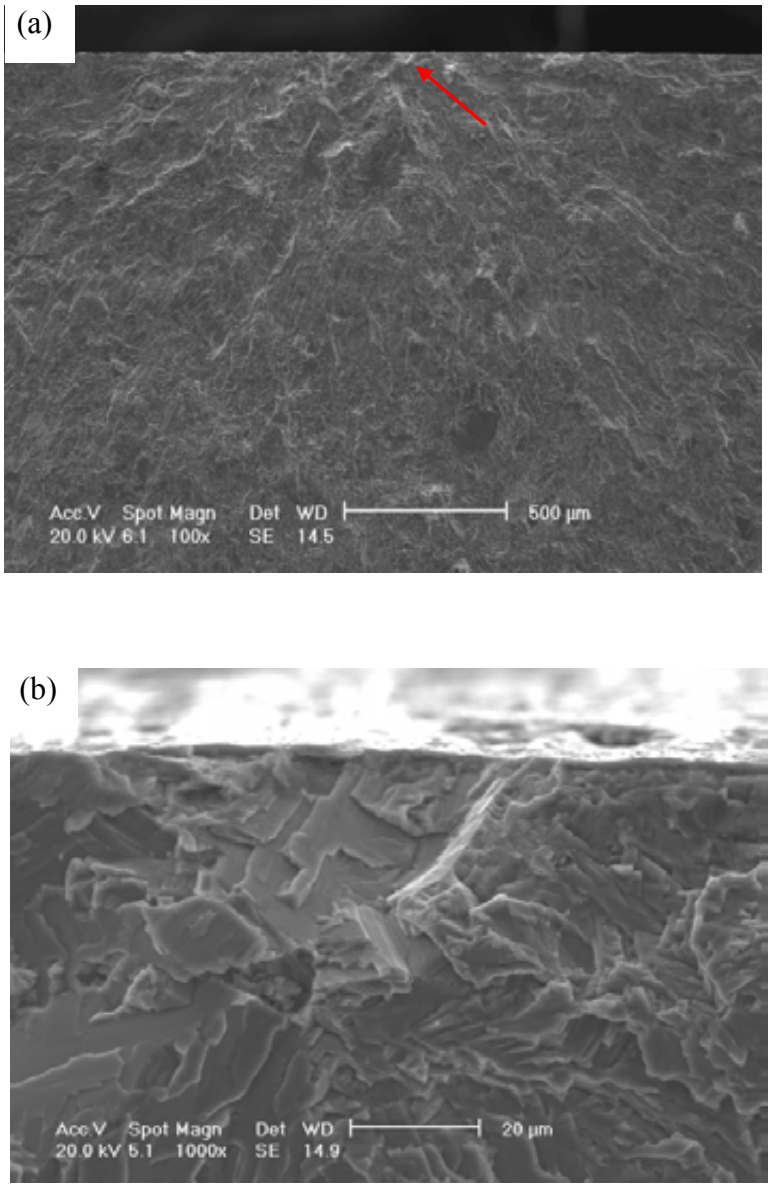

Fig. 4-19 SEM secondary electron micrographs of fracture surface for failed fatigue sample HIPped at 930°C showing crack initiation site (indicated by the arrow) at different magnifications.

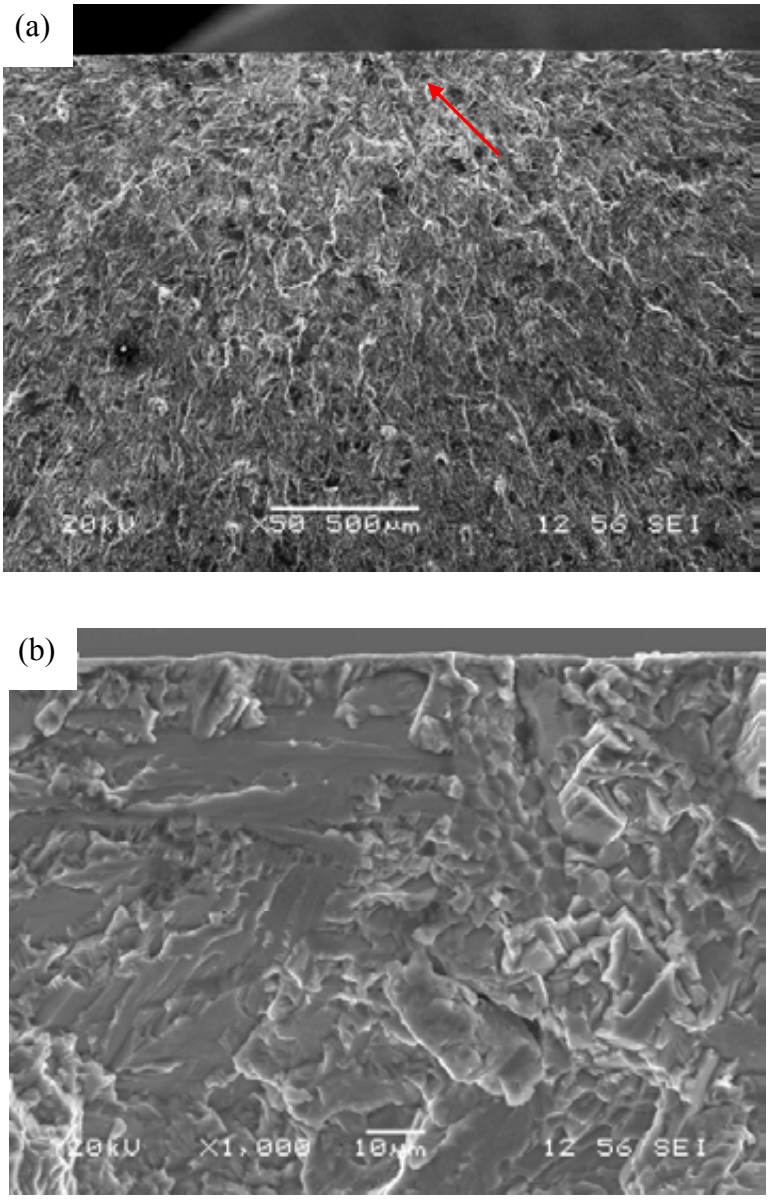

Fig. 4-20 SEM secondary electron micrographs of the fracture surface of fatigue failed sample HIPped at 880°C showing crack initiation site (indicated by the arrow) at different magnifications.

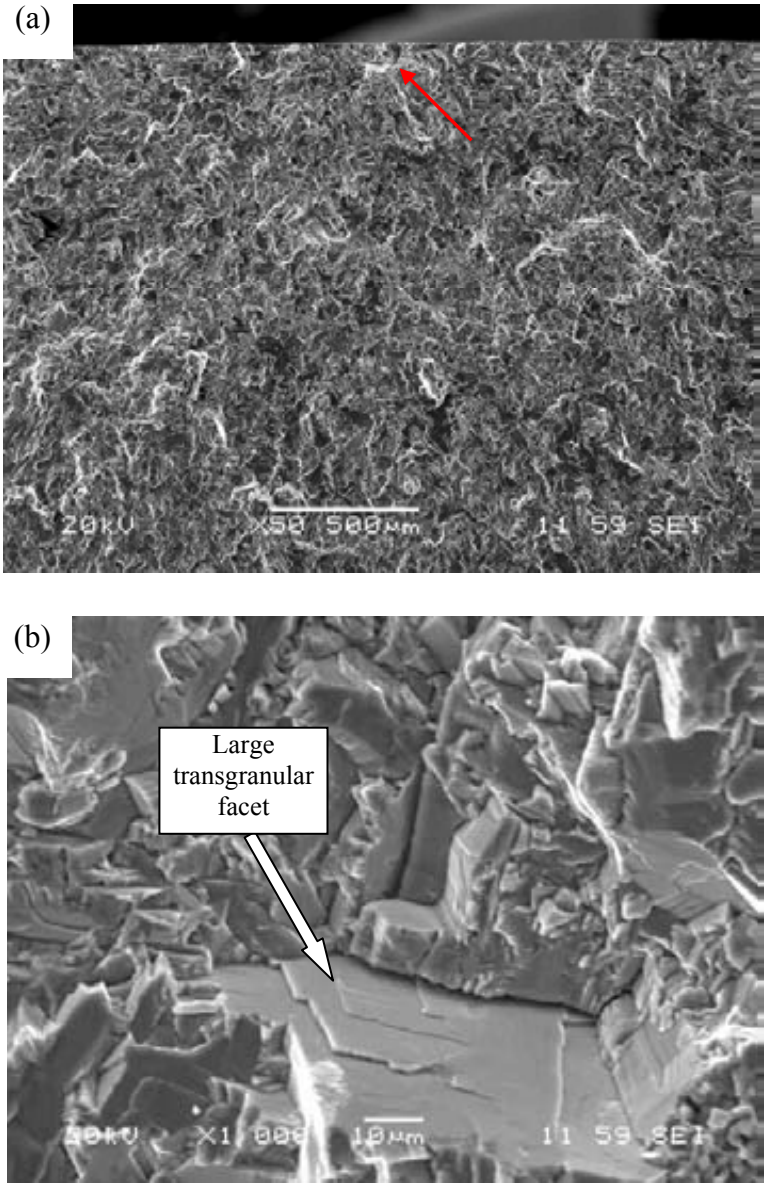

Fig. 4-21 SEM secondary electron micrographs showing the fracture surface of fatigue failed sample HIPped at 1020°C: (a) crack initiation site (indicated by the arrow); (b) large transgranular facet associated with the coarsening of the microstructure.

4.1.2.4 Fracture toughness properties and fractographic investigation

Room temperature fracture toughness testing was conducted to further assess the properties of powder Ti-6Al-4V samples HIPped at 930°C (below the transus) and 1020°C (above the transus). Comparison was made with properties of ingot-route Ti-6Al-4V samples forged at similar temperatures. Values of fracture toughness for the materials are set out in Table 4-5. Samples HIPped at 930°C have slightly higher fracture toughness values than those of samples isothermally forged at 910°C. For the samples HIPped at 1020°C, a slight increase in fracture toughness is found over that of samples HIPped at 930°C. This increase is likely to be associated with the coarsened beta laths in the HIPped microstructure which can lead to more deflection of cracks. Samples forged at 1050°C showing the beta transformed microstructure have the highest fracture toughness values. When compared with those of commercially forged samples, the HIPped samples have a significantly higher fracture toughness values.

Table 4-5 Room temperature fracture toughness values obtained from powder Ti-6Al-4V samples HIPped at different temperatures and ingot-route samples forged at similar temperatures.

Specimen	**Fracture toughness, K_Q ($MPa.m^{1/2}$)**
HIPped Ti-6Al-4V at 930°C	71/74/76/77
HIPped Ti-6Al-4Vat 1020°C	77/80
Forged Ti-6Al-4Vat 910°C	70/72
Forged Ti-6Al-4V at 1050°C	81/81
Commercially forged Ti-6Al-4V (forged at 920~940°C+HTed at 950°C/1h/WQ+Ageing at 550°C/2h/AC)	60/61

Table 4-6 gives a comparison between mechanical properties of HIPped and forged samples processed at similar temperatures. The HIPped samples have better ductility than that of forged samples. Comparable fatigue properties are shown between two samples.

Table 4-6 Typical room temperature mechanical properties of Ti-6Al-4V samples processed by HIPping and forging

	Sample HIPped at 930°C	Sample forged at 920~940°C
Yield stress (MPa)	901	875 [*Kelto 1980*]
Tensile stress (MPa)	971	965 [*Kelto 1980*]
Elongation (%)	19	15 [*Kelto 1980*]
Fatigue run-out strength (MPa)	500	~530 [*Novovic 2004*]
Fracture toughness K_Q ($MPa.m^{1/2}$)	74	60

Fig. 4-22 shows the optical images of fracture surfaces taken from five sets of samples after fracture toughness testing. The transitions between fatigue pre-cracked and tensile overload regions in the samples produced below β transus (~990°C) are obvious (see Figs. 4-22 (a, b, c)) and flow lines can be seen in the overload regions. Samples HIPped and forged at higher temperatures (1020°C and 1050°C) show less obvious transitions. Detailed fractographic investigations were performed along the plane of fracture in selected compact tension (CT) specimens for both fatigue pre-cracked and tensile overload regions, as shown in Figs. 4-23, 4-24. From assessment of the curvature, the crack path of the sample commercially forged at 920~940°C (see Fig. 4-23 (c)) is smoother than those of samples HIPped at 930 °C (see Fig. 4-23 (a)) and isothermally forged at 910 °C (see Fig. 4-23 (b)), which indicates the lowest fracture toughness value for commercially forged sample. Samples isothermally

forged at 1050°C have the highest fracture toughness values, which is associated with the roughest crack path (see Fig. 4-24 (b)). As mentioned above, the microstructure of the sample HIPped at 1020°C is different from that of the sample forged at 1050°C (beta transformed structure), which is a coarsened version of the microstructure observed in samples HIPped below the transus, but the fracture toughness values are quite close to those of ingot-route samples forged above the beta transus. Transgranular mode of failure was dominant along both the fatigue pre-cracked and overload region of these samples, and an intergranular mode was occasionally evident along the crack paths.

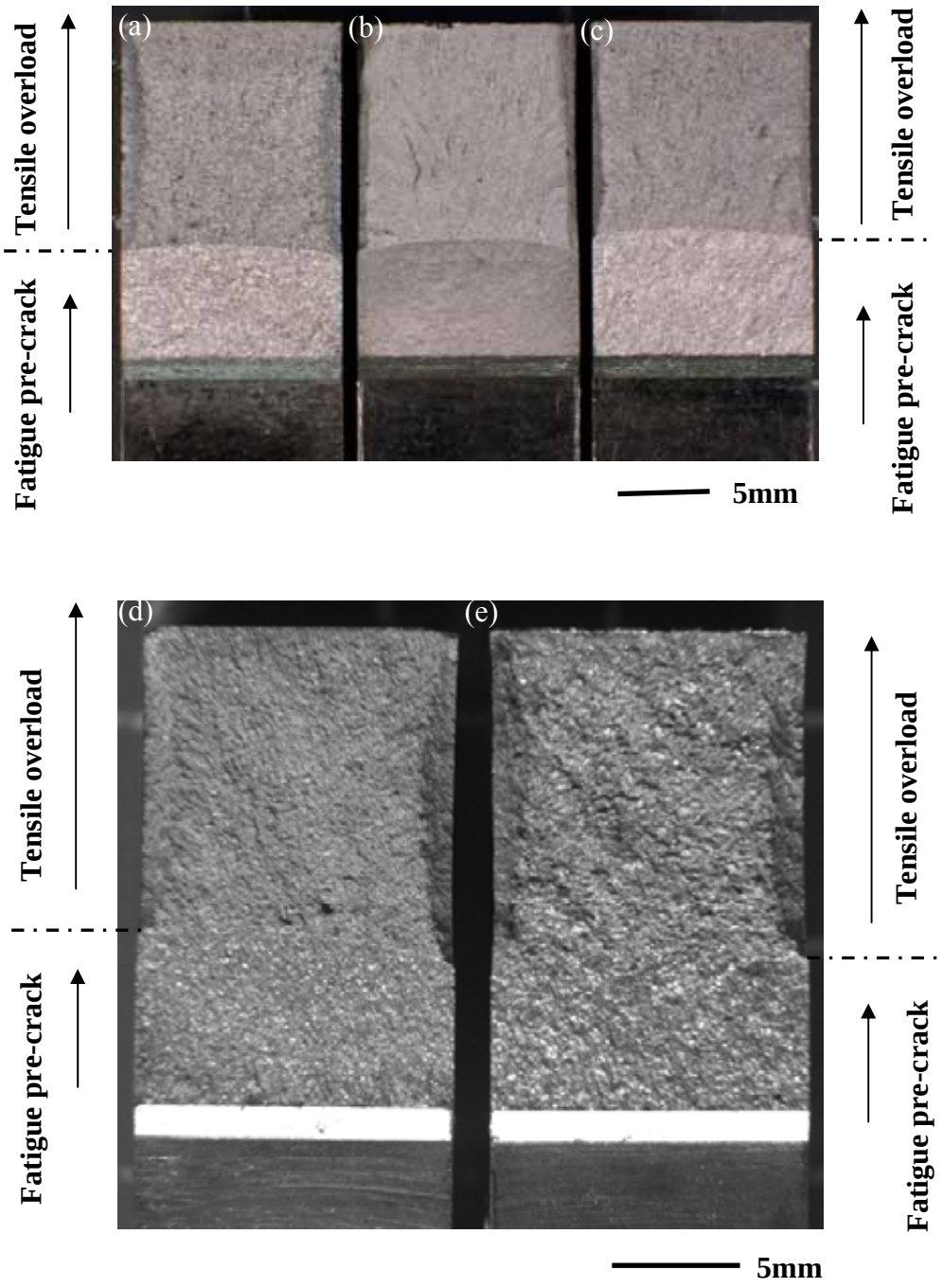

Fig. 4-22 Optical micrographs of fracture surfaces of fracture toughness samples showing fatigue pre-crack and tensile overload regions in (a) HIPped Ti-6Al-4V at 930°C; (b) isothermally forged Ti-6Al-4V at 910°C; (c) commercially Ti-6Al-4V forged at 920~940°C; (d) HIPped Ti-6Al-4V at 1020°C; (e) isothermally forged Ti-6Al-4V at 1050°C.

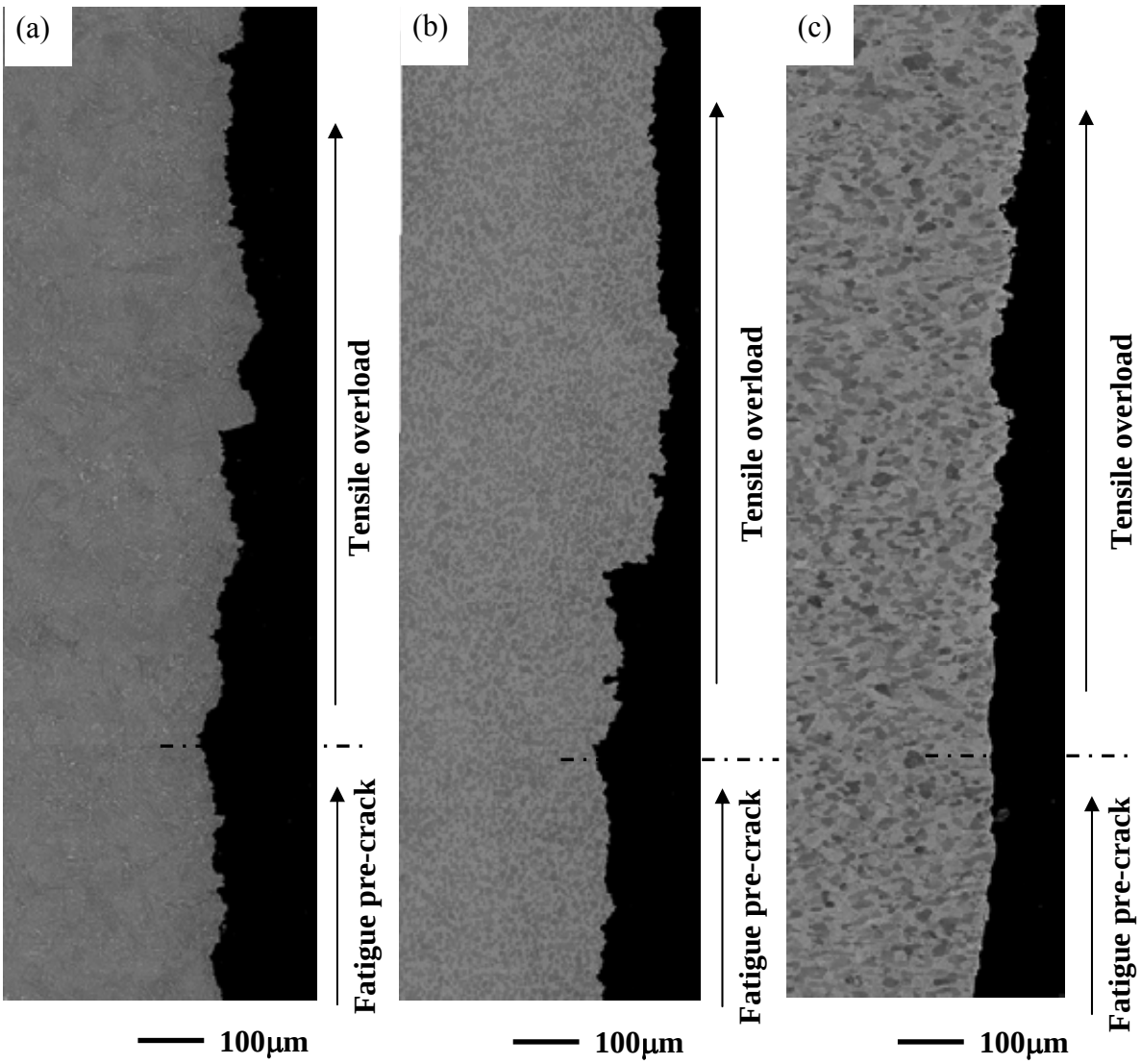

Fig. 4-23 SEM BSE micrographs showing the fatigue pre-crack and fracture toughness crack paths of (a) powder Ti-6Al-4V sample HIPped at 930 °C; (b) ingot-route Ti-6Al-4V sample isothermally forged at 910 °C; (c) ingot-route Ti-6Al-4V sample commercially forged at 920~940°C. The commercially forged sample shows a smoother crack path than the two other samples.

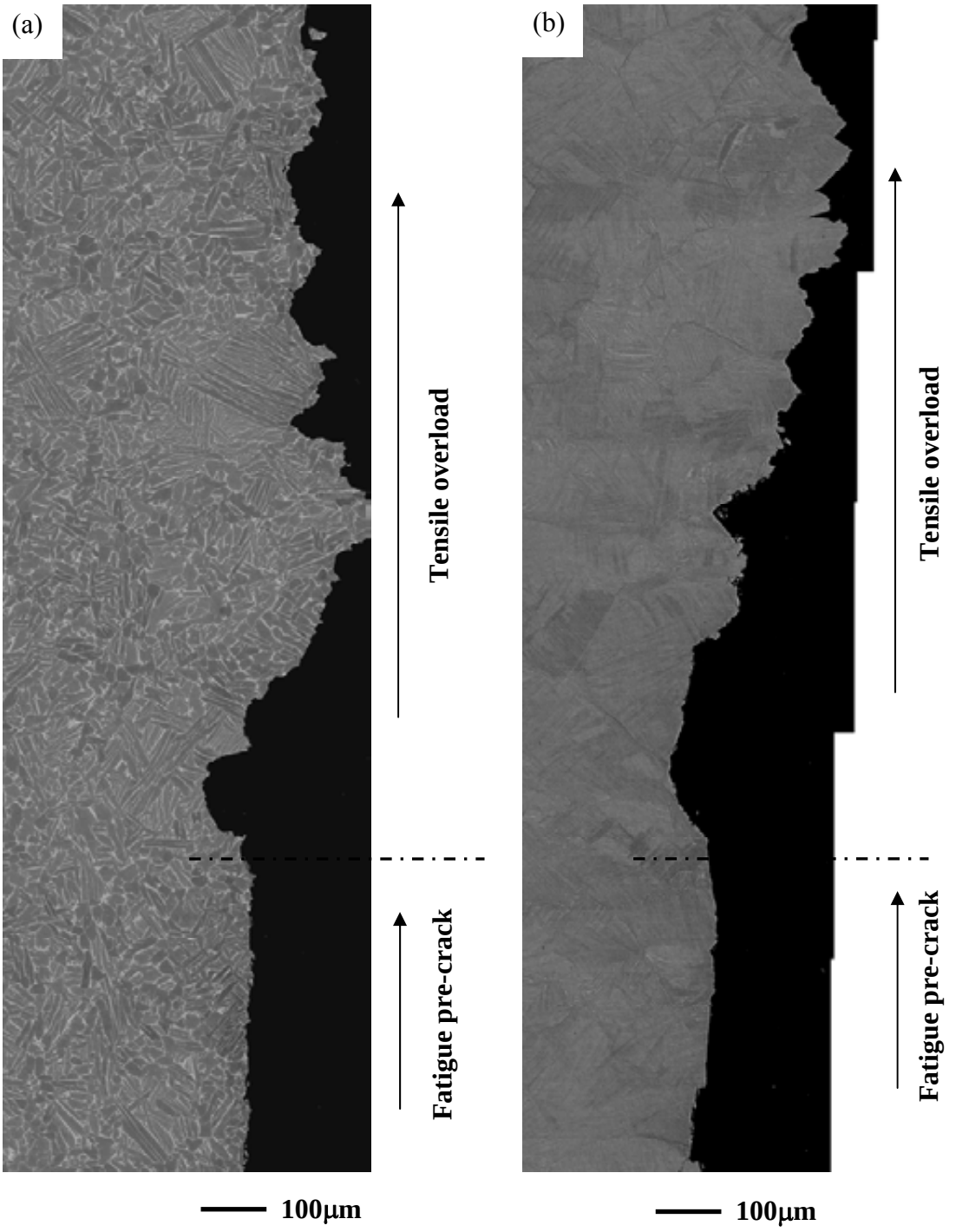

Fig. 4-24 SEM BSE micrographs showing the fatigue pre-crack and fracture toughness crack paths of (a) powder Ti-6Al-4V sample HIPped at 1020 °C; (b) ingot-route Ti-6Al-4V sample isothermally forged at 1050 °C.

4.1.2.5 Discussion

The martensitic microstructure of powder particles in the as-received condition and its transformation to α phase during consolidation underlies the fine microstructure which occurs during HIPping of powder Ti-6Al-4V. Diffusion bonding occurs along the boundaries of powder particles under temperature/pressure/time and hot working deformation to produce recrystallised α and β equiaxed grains at the former powder particle boundaries. Thus this type of microstructure implies that the deformation is essential for the densification of the material. Clearly deformation occurs predominantly (but of course not totally) at the prior particle boundaries under the application of pressure during HIPping and local recrystallisation has occurred to form equiaxed alpha and beta grains. Inside the powder particles, martensite transforms into α laths with different orientation to form lath-like or "basket weave" structure. The lath-like structure in as-HIPped microstructure is formed directly by tempering of the martensitic structure in the original powder (see Fig. 4-3).

With respect to consolidation by HIPping, it is well known that temperature is the most important factor to achieve good bonding [*Pérez 1995*]. Pressure contributes mainly to densification, but a high final density with good bonding is achieved by thermal processes. Elongation/ductility measurements are very useful for evaluating the quality of particle bonding, but elongation/ductility is also influenced by the microstructure formed during HIPping within the original particles. The highest values of elongation to failure which is obtained for samples HIPped at 930°C indicates that this temperature is a suitable HIPping temperature to achieve a good degree of bonding. The lower yield stress and UTS of samples HIPped at 930°C than those of samples HIPped at 880°C are associated with the slightly coarser

microstructure resulting from the increased HIPping temperature which contributes to a commensurate increase in effective slip length. The finest microstructure which is formed in samples HIPped at 880°C generated the highest tensile strength, but it appears that perfect bonding is not achieved at this temperature and failure seems to have initiated at prior particle boundaries (as shown in Fig. 4-15).

In HIPped Ti-6Al-4V samples, the sizes of alpha and beta phases were also considered to affect the ductility, fatigue properties and fracture toughness values significantly. When a crack meets a beta phase, the crack will normally be deflected. Bridging and blunting occur when beta laths are large [*Wu 1996*]. For samples HIPped at 880 °C, beta grains and laths are fine (see Table 4-2, Fig. 4-8) which can not deflect or blunt a crack, so the crack will cut through the beta laths and propagate continuously. For samples HIPped at 1020 °C, a cluster of coarser alpha laths which have similar crystallographic orientations (see Fig. 4-7) is formed, with fine beta laths between the coarse alpha laths. Such a large size cluster can result in earlier crack initiation and rapid crack propagation due to the lack of bridging effect from the fine beta laths between coarser alpha laths (see Table 4-2, Fig. 4-8). The highest values of ductility obtained for samples HIPped at 930°C indicates that this temperature is an appropriate HIPping temperature to achieve not only a good degree of bonding but also a balanced size of alpha and beta laths.

In all tested Ti-6Al-4V specimens HIPped at different temperature, crack initiation sites were characterised by transgranular facets, which corresponded to the average grain size, and in earlier work they were reported to be basal planes of the primary α phase [*Bache 1999a*, *Bache 2001*]. During high cycle fatigue (HCF) crack initiation is

typically associated with the generation of persistent slip bands (PSBs), which generally develop along certain crystallographic orientations and provide the primary route for dislocation movement in cyclic straining. Development of PSBs is directly responsible for cyclic strain localisation, both at the surface and in the interior of crystals. In the HCF regime, total fatigue life depends principally on fatigue crack initiation and early growth behaviour. With respect to the reduced fatigue strength for samples HIPped at 880°C (as shown in Fig. 4-18), the worse resistance for crack growth along PSBs resulting from the relatively fine beta laths is considered to contribute to the reduction of properties, since no obvious differences in crack initiation sites were observed from those in samples HIPped at 930°C (as shown in Figs. 4-19, 4-20).

For samples HIPped at 1020°C, coarsened lamellar colonies with similar orientations, act as crack initiation sites (see Figs. 4-16, 4-21) which degraded the tensile strength, elongation and fatigue properties. Although the two phases in lamellar colonies, the α plates and the β matrix, have to deform independently, shear can occur across the beta lath width if the β lath is fine [*Lütjering 2003*], because as can be seen from Fig. 4-25 two of the slip systems in each phase are exactly parallel, $(110)\,[1\bar{1}1]_\beta \parallel (0002)\,[11\bar{2}0]_\alpha$ and $(\bar{1}12)\,[1\bar{1}1]_\beta \parallel (\bar{1}100)\,[11\bar{2}0]_\alpha$, and two others are off by only 10°, $(110)\,[1\bar{1}2]_\beta$ and $(0002)\,[1\bar{2}10]_\alpha$ as well as $(1\bar{1}2)\,[\bar{1}11]_\beta$ and $(10\bar{1}0)\,[1\bar{2}10]_\alpha$. Hence, lamellar colonies up to 70 μm width can be seen on the crack initiation sites (e.g. see Fig. 4-16), which resulted in early fracture and then to failure during mechanical testing.

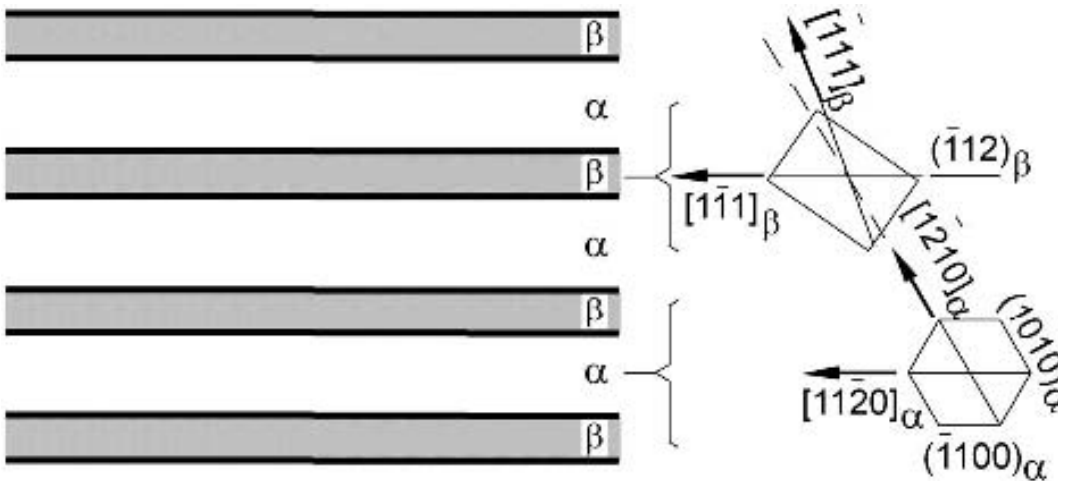

Fig. 4-25 Schematic representation of the crystallographic relationship between α plates and β matrix in α colonies showing that two of the slip systems in each phase are parallel [*Lütjering 2003*].

The misorientation distribution between grains was also considered to be a factor which affected the properties. When samples were HIPped below the beta transus (i.e. 880°C, 930°C), the effect of low angle misorientations on the properties accentuates that of microstructure. Samples HIPped at 1020°C have a smaller volume fraction of low angle misorientations than other HIPped samples (see Fig. 4-9), but the significantly coarsened microstructure overshadowed the positive effect of this decrease of the volume fraction of low angle misorientation.

.

The ratio of HCF strength to yield stress of samples HIPped at 930°C gave a value of ~0.56 which is comparable with the typical value of 0.5 for (α+β) alloy [*Lütjering 2003*]. The best balance of ductility and fatigue properties was obtained for samples

HIPped at 930°C and this temperature was therefore chosen as the HIPping temperature for subsequent tests where the effects of other variables were investigated. It is promising that powder samples HIPped below the beta transus not only have comparable tensile and fatigue strengths to commercially forged sample, but also exhibit better ductility and higher fracture toughness values (see Table 4-6), which means that the HIPped materials have potential for structural applications.

4.1.3 Effect of surface finish on mechanical properties

4.1.3.1 Nature of as-HIPped surfaces

In the case of surface finish it is clear that in some parts of net shape HIPped components the surface, which is in direct contact with the tooling, will remain on the finished component and thus the influence on properties of this surface must be defined. A conventional HIPping procedure, which simultaneously ramped the temperature (up to 930°C by 5°C/min) and the pressure (up to 100MPa by 0.5 MPa/min), was used in order to assess the nature of the as-HIPped surface and its influence on properties. The sample was held for 4h at temperature and pressure and then slowly cooled (see Fig. 4-26).

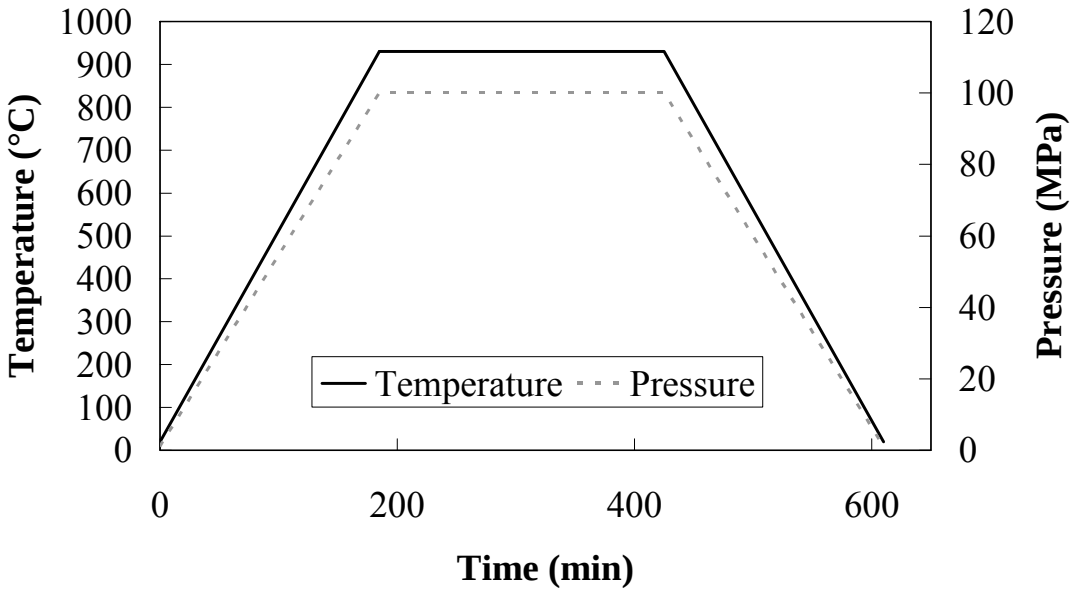

Fig. 4-26 Schematic representation of conventional HIPping procedure showing temperature and pressure were applied simultaneously during HIPping.

Fig.4-27 (a) shows a cross section of the resulting interface between the mild steel can and the HIPped Ti-6Al-4V and Fig.4-27 (b) shows the as-HIPped surface after the mild steel can was pickled off. It is clear that the surface of the Ti-6Al-4V sample is irregular on the scale of the original powder particle size and that the acid pickling which was used to remove the mild steel can in which the powder was HIPped has retained this surface structure. The origin of this surface dimpling can be understood by considering Fig.4-28 where the strengths of Ti-6Al-4V and mild steel as a function of temperature are shown. This figure shows that the strength of Ti-6Al-4V is higher than that of mild steel at low temperatures but is less than that of steel at higher temperatures. Because the temperature and pressure were ramped in phase the individual powder particles indented the weaker mild steel during the heating cycle to produce the undulations seen in Fig.4-27 (b).

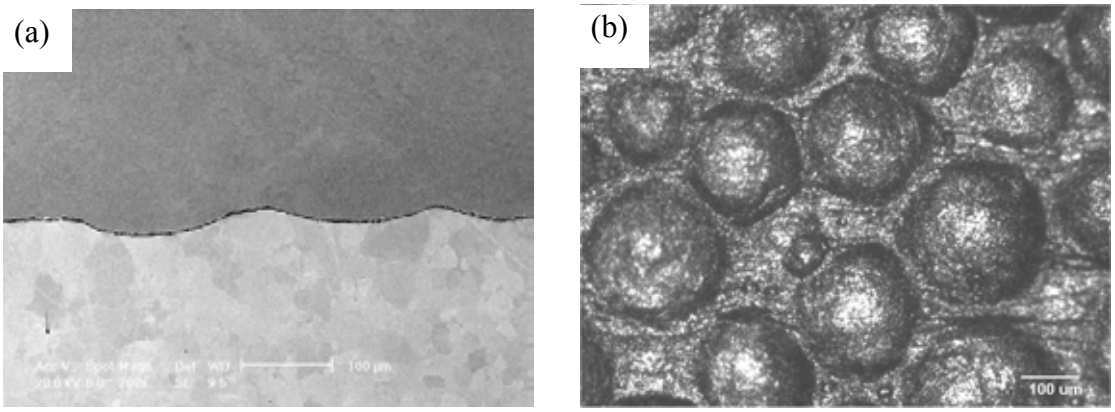

Fig. 4-27 (a) SEM secondary electron micrographs showing the cross section of the interface between mild steel can and conventionally HIPped Ti-6Al-4V sample; (b) optical micrographs of samples' surface topography showing irregularities in as-HIPped surface.

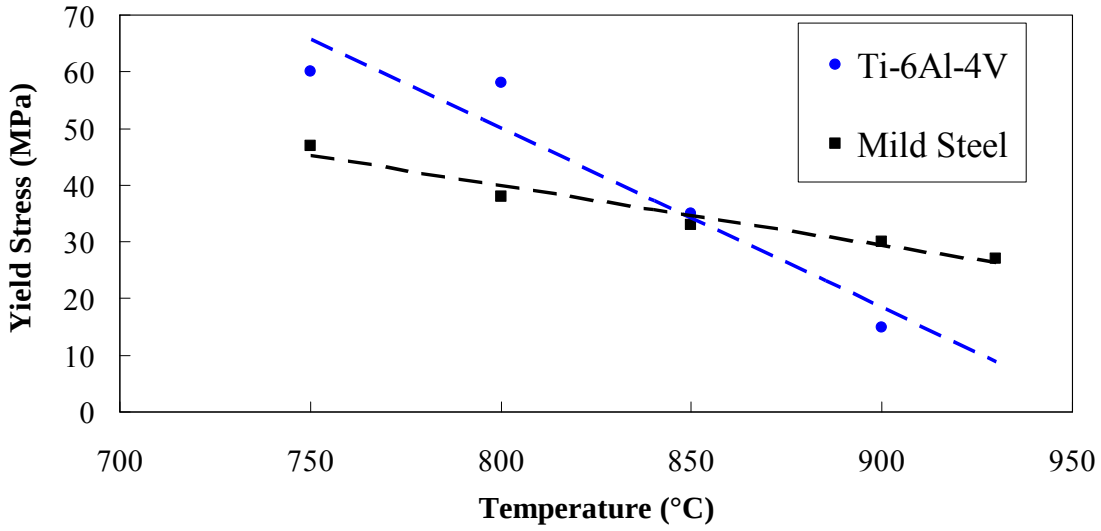

Fig. 4-28 Schematic representation of yield stress vs. temperature for Ti-6Al-4V and mild steel showing the strength of Ti-6Al-4V is higher than that of mild steel at low temperatures but is lower than that of steel at higher temperatures.

A new HIPping procedure, in which the HIPping temperature and pressure were ramped up out of phase, was therefore used in which the temperature was increased to 930°C (at which temperature the mild steel is now harder than the Ti alloy) and only then was the HIPping pressure applied (see Fig. 4-29). So the total holding time at 930°C is 5h (2h during pressure increasing to 100MPa plus 3h under constant pressure). Fig.4-30 (a) shows the cross section of the interface between the mild steel can and the HIPped Ti-6Al-4V sample, and Fig.4-30 (b) shows the surface of the HIPped sample obtained when this HIPping procedure was used. Clearly a much smoother surface was obtained. The importance of using this type of HIP procedure in net shape HIPped samples, where the as-HIPped surface will be part of a component is made clear in the following section where the fatigue properties are reported for samples with different surfaces.

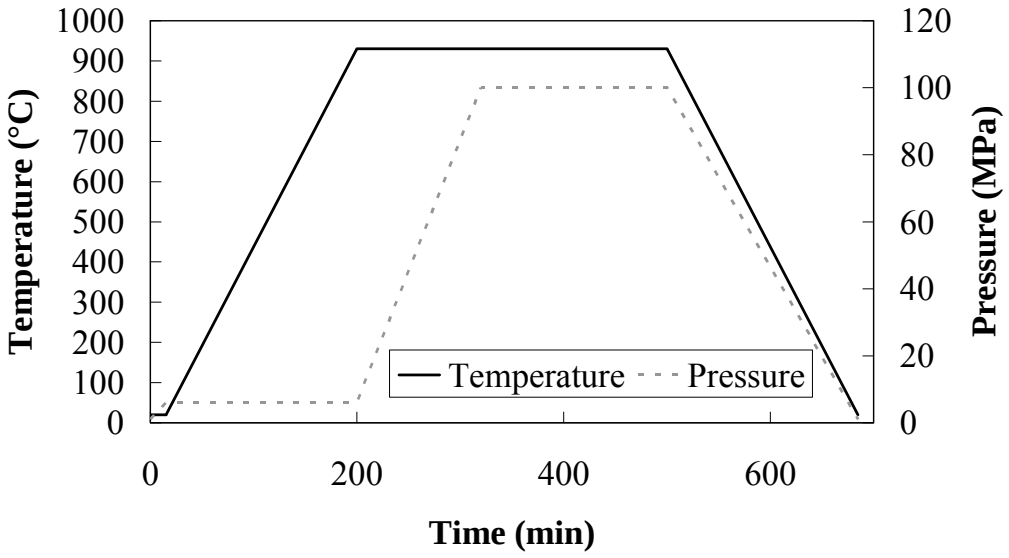

Fig. 4-29 Schematic representation of new HIPping procedure showing temperature and pressure were applied out of phase during HIPping.

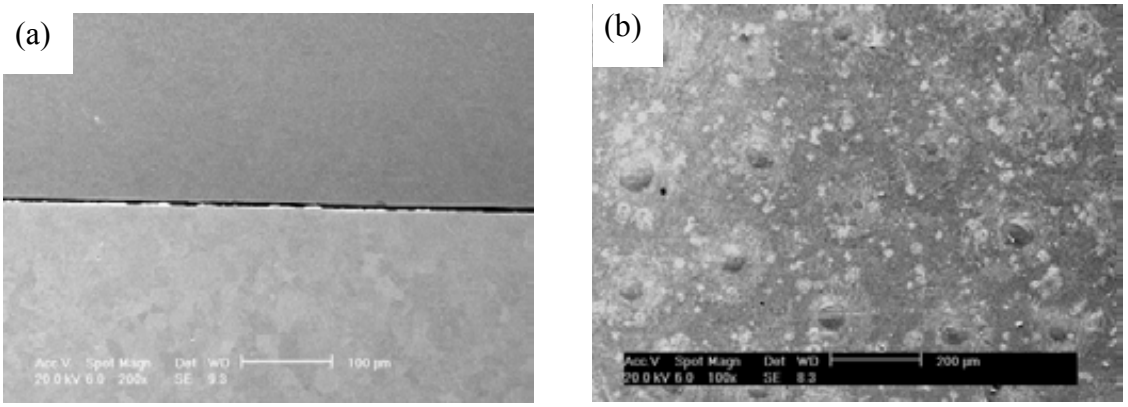

Fig. 4-30 (a) SEM secondary electron micrographs showing the cross section of the interface between mild steel can and Ti-6Al-4V sample made using new HIPping procedure; (b) optical micrographs of samples' surface topography showing very few undulations in the improved as-HIPped surface.

4.1.3.2 Influence of surface finish on the fatigue strength of HIPped samples

4-point bending fatigue tests were used to investigate the influence of sample surface finish, and four sets of HIPped samples with different surface finish were examined. Flat plates were HIPped to generate the samples with as-HIPped surfaces. The testpieces were spark machined along the length of the flat plate and microstructures from different positions were examined to investigate the integrity of HIPped plate. Fig. 4-31 (a) shows the sparking direction and the positions chosen for microstructural assessment. The surface cut in position 1 is the longitudinal cross-section at the corner of the plate, and that cut in position 2 is the transverse cross-section, both of which exhibit typical as-HIPped Ti-6Al-4V (below the β transus) microstructure, as shown in Fig. 4-31 (b, c). Position 3 is in the longitudinal cross-section in the middle of the plate edge, which shows similar microstructure to that of position 4 (see Fig. 4-31 (d, e)), in the transverse cross-section of the middle of the flat plate.

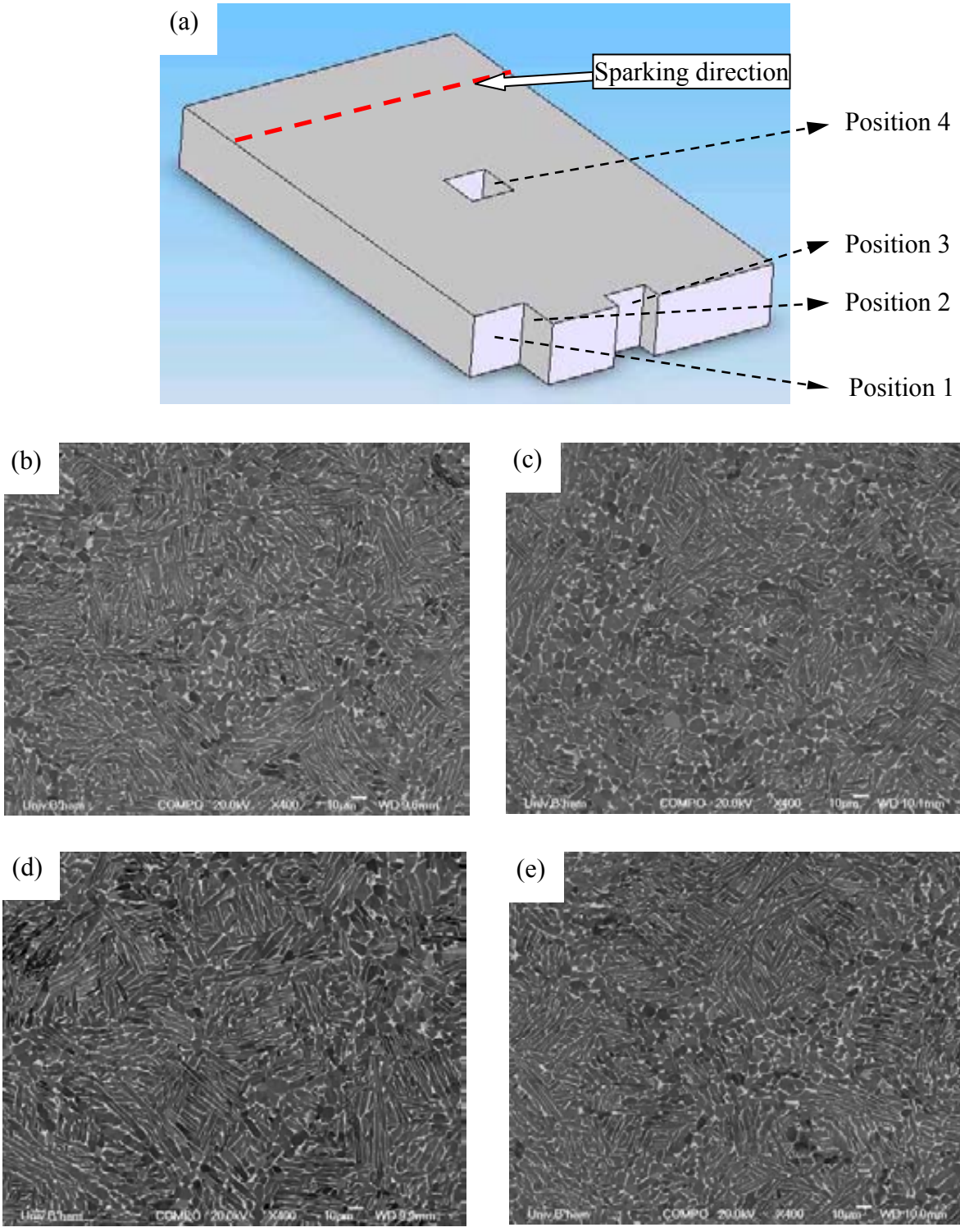

Fig. 4-31 (a) Schematic of the positions chosen for microstructure assessment of the HIPped flat plate which was cut for fatigue testpieces, sparking direction is shown by red dotted line; (b, c, d, e) SEM backscattered electron micrographs showing the microstructure of samples in position 1, 2, 3, 4, respectively.

The first set of samples was prepared from a flat plate HIPped using the conventional HIPping cycle, i.e., temperature and pressure were ramped up together. Machining was carried out on the two side surfaces but the as-HIPped surfaces of the original plate were retained as the top and bottom surfaces of the testpieces. A second set of samples, containing the original HIPped surface (also HIPped using the conventional procedure), were electro-polished for 20 minutes to remove 15~20 microns from the surface. A third set of samples was HIPped using the conventional procedure and machined on all four surfaces so that the surface layer was removed and the machined surface was used for testing. The fourth set of samples was obtained from a flat plate HIPped using the new HIPping procedure, i.e., ramping up the temperature first, then pressurised the HIPping vessel, to produce the flat dimple-free surface (Fig. 4-30) by retaining the as-HIPped surface. Thus, the fatigue properties of specimens containing four surface finishes, as-HIPped, electro-polished, machined surfaces which were made using conventional HIPping procedure, and as-HIPped surfaces made using the new HIPping procedure, were compared.

EBSD analyses were carried out on the samples HIPped using conventional and new procedures. The results are illustrated in Fig. 4-32. EBSD grain size distribution maps and graphs (Figs. 4-32 (g, h, i, j)) were used to characterise the equivalent grain size (or unit size) instead of the conventional linear intercept method which cannot give accurate results when adjacent grains have "low-angle" grain boundaries (misorientation<20°) [*Long 1999*]. It shows that sample HIPped using new procedure has a smaller volume fraction of low angle misorientations than that in conventionally HIPped sample. The unit structure in sample HIPped using new procedure is coarser because of the longer holding time (5h) than that (4h) of conventional procedure.

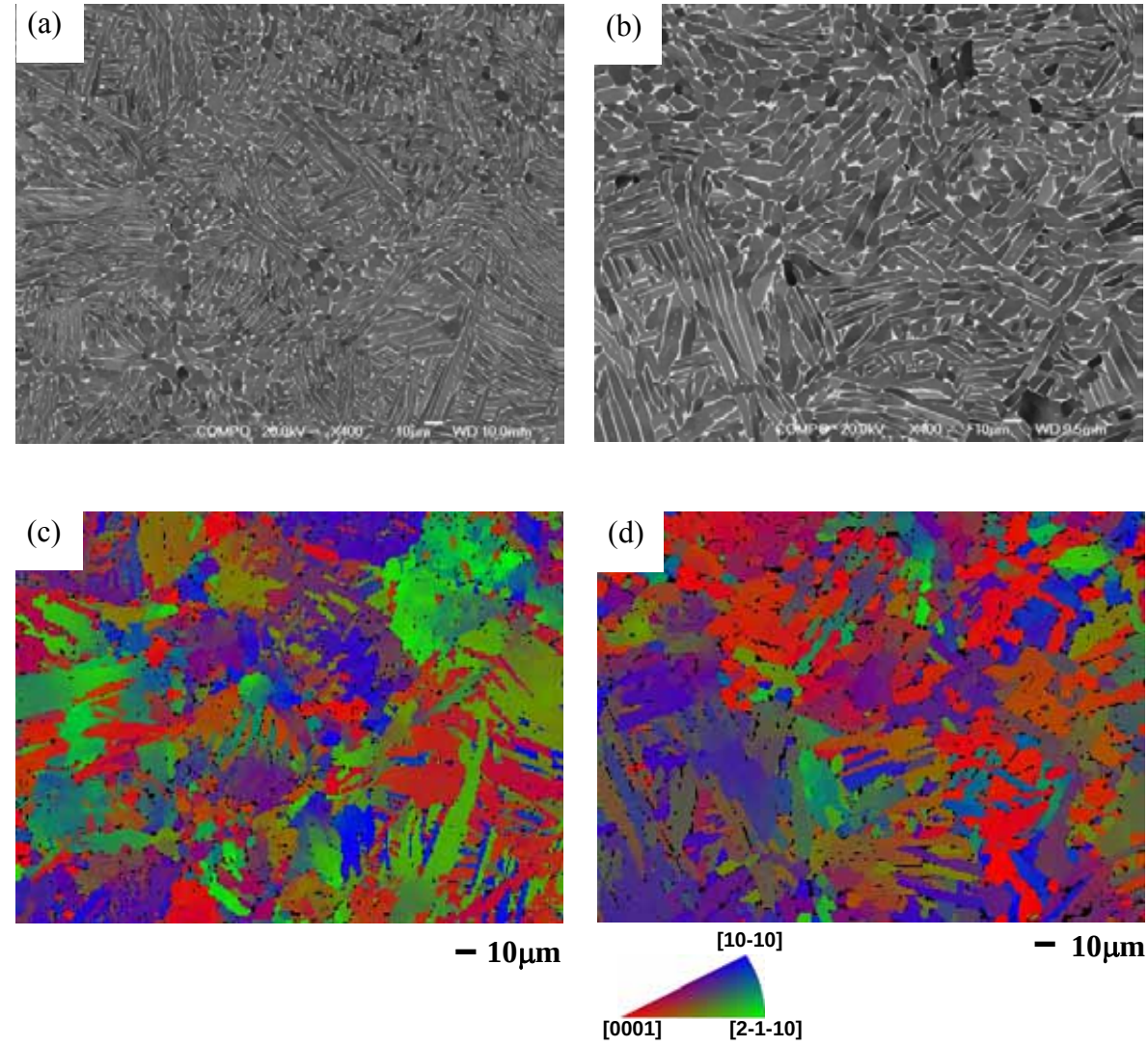
(a)
(b)
(c)
(d)
10μm
10μm
[10-10]
[0001]
[2-1-10]
(e)
(f)
Percentage of counts (%)
Misorientation angle (°)
Percentage of counts (%)
Misorientation angle (°)

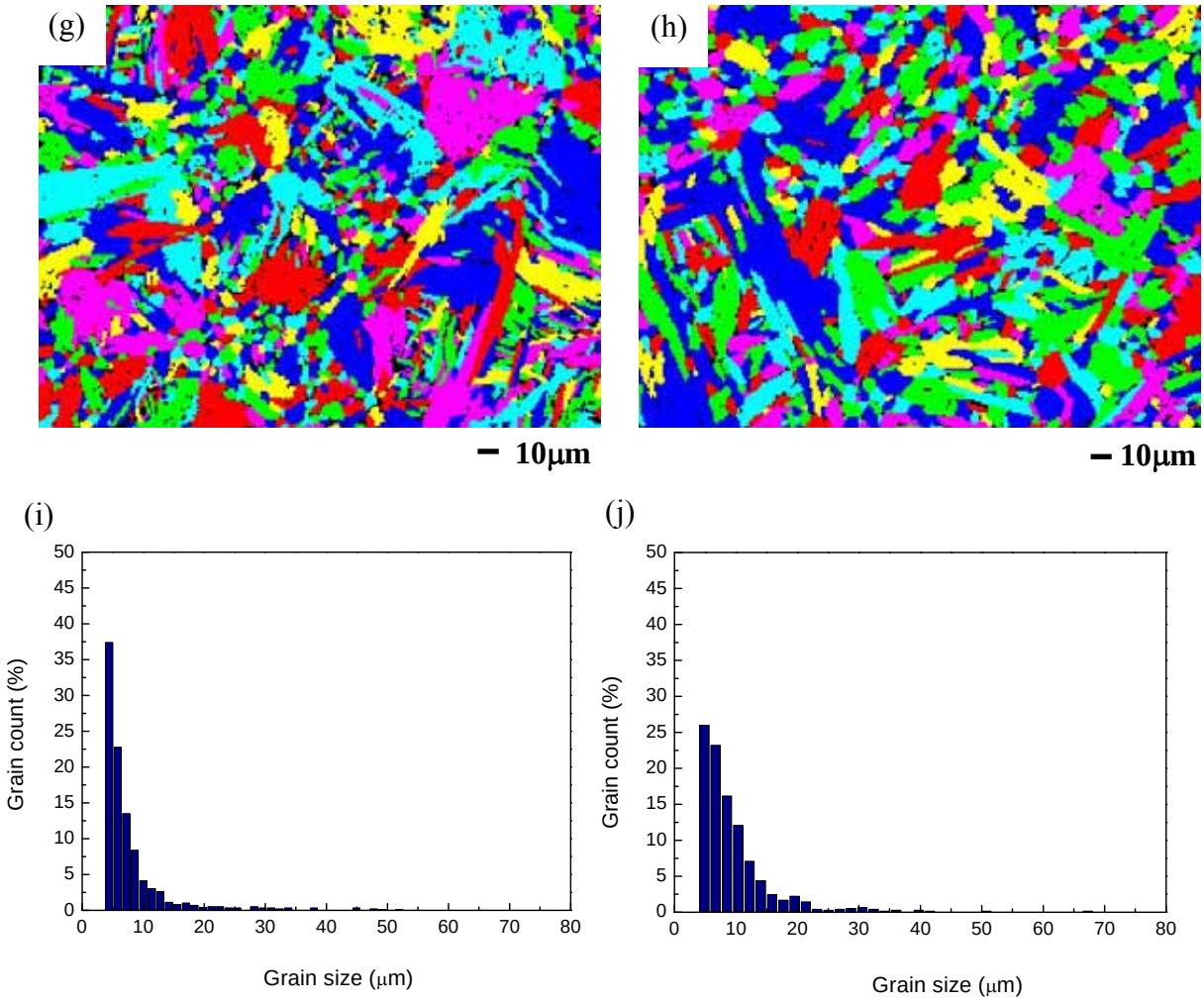

Fig. 4-32 (a, c, e, g, i) HIPped Ti-6Al-4V sample at 930°C using conventional procedures; (b, d, f, h, j) HIPped Ti-6Al-4V sample at 930°C using new procedures. (a,b) SEM backscattered electron micrographs; (c,d) EBSD misorientation maps; (e,f) misorientation distribution graphs; (g,h) EBSD grain size distribution maps; (i,j) grain size distribution maps. It shows that sample HIPped using the new procedure has smaller volume fraction of low angle misorientations than in conventionally HIPped sample. The unit structure in the sample HIPped using the new procedure is coarser.

- Microstructure of HIPped samples with different surface finishes

The microstructure and surface topography of cross sections of samples with four different surface finishes are shown in Fig. 4-33. It is clear that sharp grooves were formed between original powder particles on the as-HIPped surface made using the conventional HIPping procedure, as seen in Fig. 4-33 (a). Electro-polishing removes these grooves as does machining (see Fig. 4-33 (b, c)), but blunt grooves still can be seen in the electro-polished surface. Fig. 4-33 (d) shows that very few undulations can be seen in the as-HIPped surface made using the improved HIPping procedure, which is consistent with the surface topography shown in Fig. 4-30.

Further examinations showed that there are irregularities/defects in the grooves of the as-HIPped surface made using conventional HIPping procedure, as shown in Fig. 4-34 (a). In Fig. 4-34 (b) it can be seen that surface damage has been introduced during machining; the other two surface conditions show much smoother surfaces.

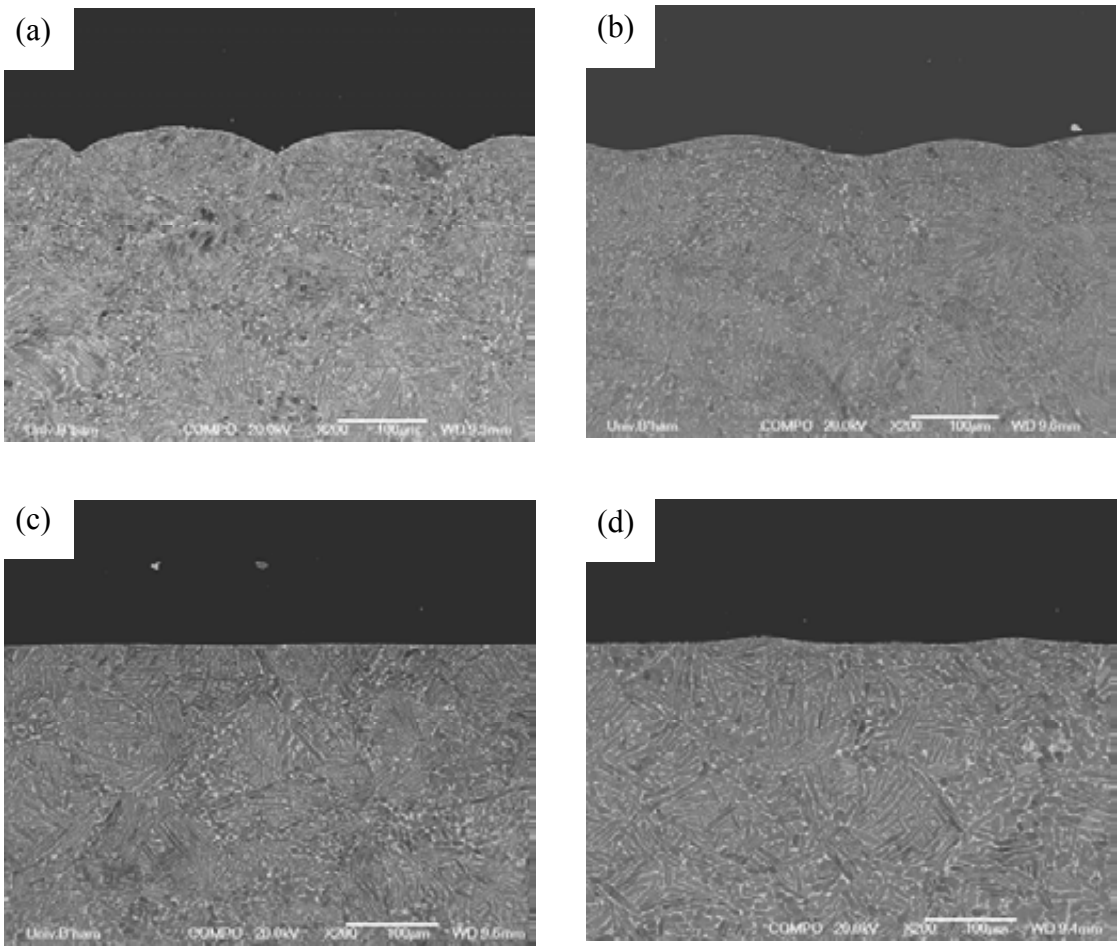

Fig. 4-33 SEM backscattered electron micrographs of cross sections of HIPped samples with: (a) as-HIPped conventional surface showing sharp grooves formed between original powder particles; (b) electro-polished surface showing blunt grooves; (c) machined surface; (d) as-HIPped improved surface showing very few undulations. These surfaces were at the top and bottom during four point bending fatigue property assessment.

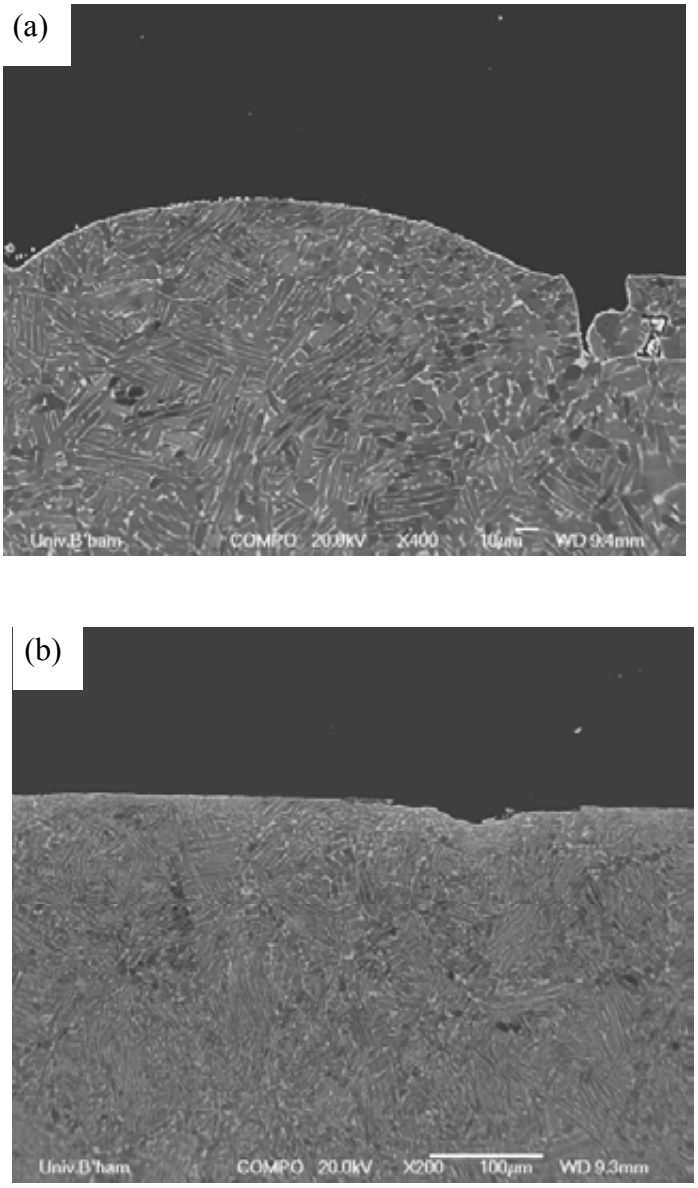

Fig. 4-34 SEM backscattered electron micrographs of cross sections showing some defects on the testing surfaces: (a) irregularities in the grooves on the as-HIPped conventional surface; (b) surface damage on the machined surface.

Table 4-6 shows the surface roughness of the four surface conditions. It is obvious that the as-HIPped surface made using the conventional HIPping procedure had the highest roughness with R_a=9.1μm and the machined surface had the lowest with R_a=0.4μm. The roughness values of the electro-polished surface and as-HIPped surface made using the new HIPping procedure were between these two extremes and the latter shows lower roughness.

Table 4-6 Surface roughness of HIPped four point bending fatigue samples with different surface conditions

	Conventional as-HIPped surface	Electro-polished surface	Machined surface	Improved as-HIPped surface
$\mathbf{R_a}$ (μm)	9.08	4.69	0.4	1.05
$\mathbf{R_{max}}$ (μm)	41.4	28.24	3.75	9.85

- Fatigue properties and observations of fracture surfaces of fatigued samples

SN curves for HIPped Ti-6Al-4Vsamples with the four different surface finishes are shown in Fig. 4-35. Samples with as-HIPped surfaces made using the new HIPping procedure had the highest fatigue limit (at N>10^7 cycles) of 620 MPa (at 1.6x10^7 cycles). The run-out strength of samples with as-HIPped surfaces made using the conventional HIPping procedure was much lower, at 350 MPa, which is consistent with the highest surface roughness shown in Table 4-6. Samples which were machined or electro-polished after conventional HIPping showed better fatigue properties than the as-HIPped sample with run-out strengths of 500 and 550 MPa respectively. The fatigue limit of samples with improved as-HIPped surfaces (620

MPa) is very similar to, but slightly better than that of wrought forms of Ti-6Al-4V samples with as-polished surfaces (610 MPa) [e.g. *Novovic 2004*] tested by other researchers.

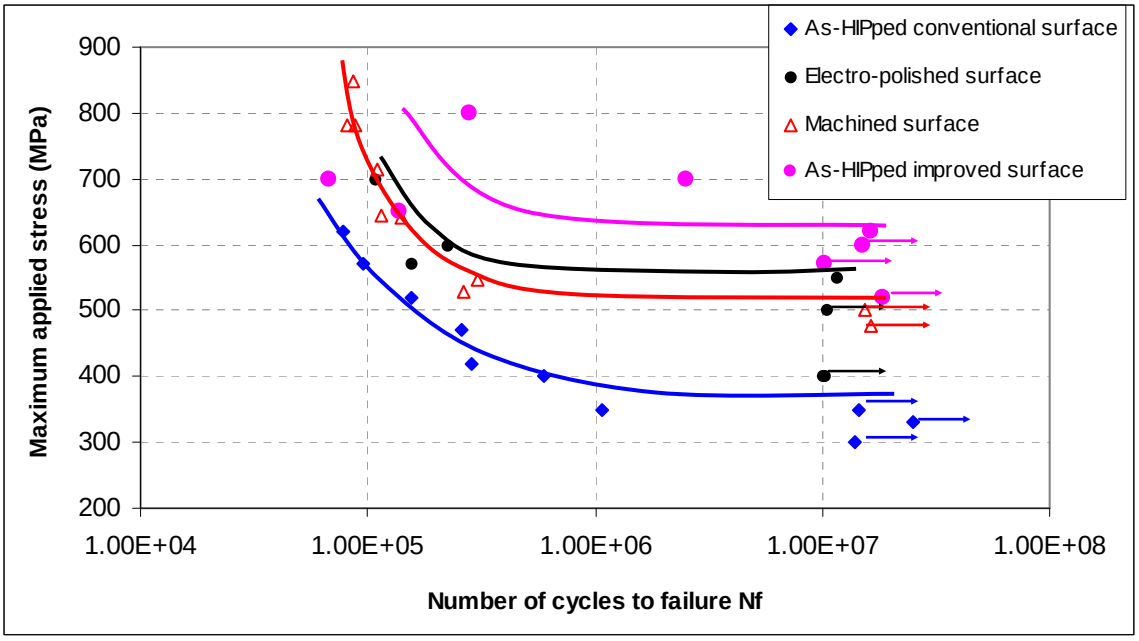

Fig. 4-35 SN fatigue curves for HIPped Ti-6Al-4Vsamples with four different surface finishes. Samples with as-HIPped improved surfaces had the highest fatigue run out limit.

Fracture surfaces of fatigue failed samples with the four surface conditions were examined to investigate the crack initiation characteristics, as shown in Fig.4-36. Fatigue crack initiation occurred at mid-section sites in all of the tests. Figs. 4-36 (a, b) show examples of samples with as-HIPped surfaces made using the conventional HIPping procedure, where crack initiation is associated with transgranular facet, coincidentally a shallow notch of ~20 μm deep can be seen. It is likely to have been formed by the sharp grooves seen in Fig. 4-31 (a) between the original powder

particles on the surface (caused by their penetration into the mild steel capsule in Fig. 4-27), and a similar notch can affect the crack initiation and lead to earlier failure of the material. Figs. 4-36 (c, d) show examples of conventionally HIPped samples with electro-polished surfaces. A facet appears to have initiated the crack which then propagated via a cluster of α and β laths with similar orientation to a blunted notch ~15 μm deep. The micrographs in Figs. 4-36 (e, f) illustrate crack initiation of a conventionally HIPped sample with a machined surface. In Figs. 4-36 (g, h), crack initiation of the sample with as-HIPped surface made using the new HIPping procedure is shown. Since very few undulations and no obvious surface damage can be seen (as shown in Fig. 4-30), there were no evident features except facets influencing the initiation site.

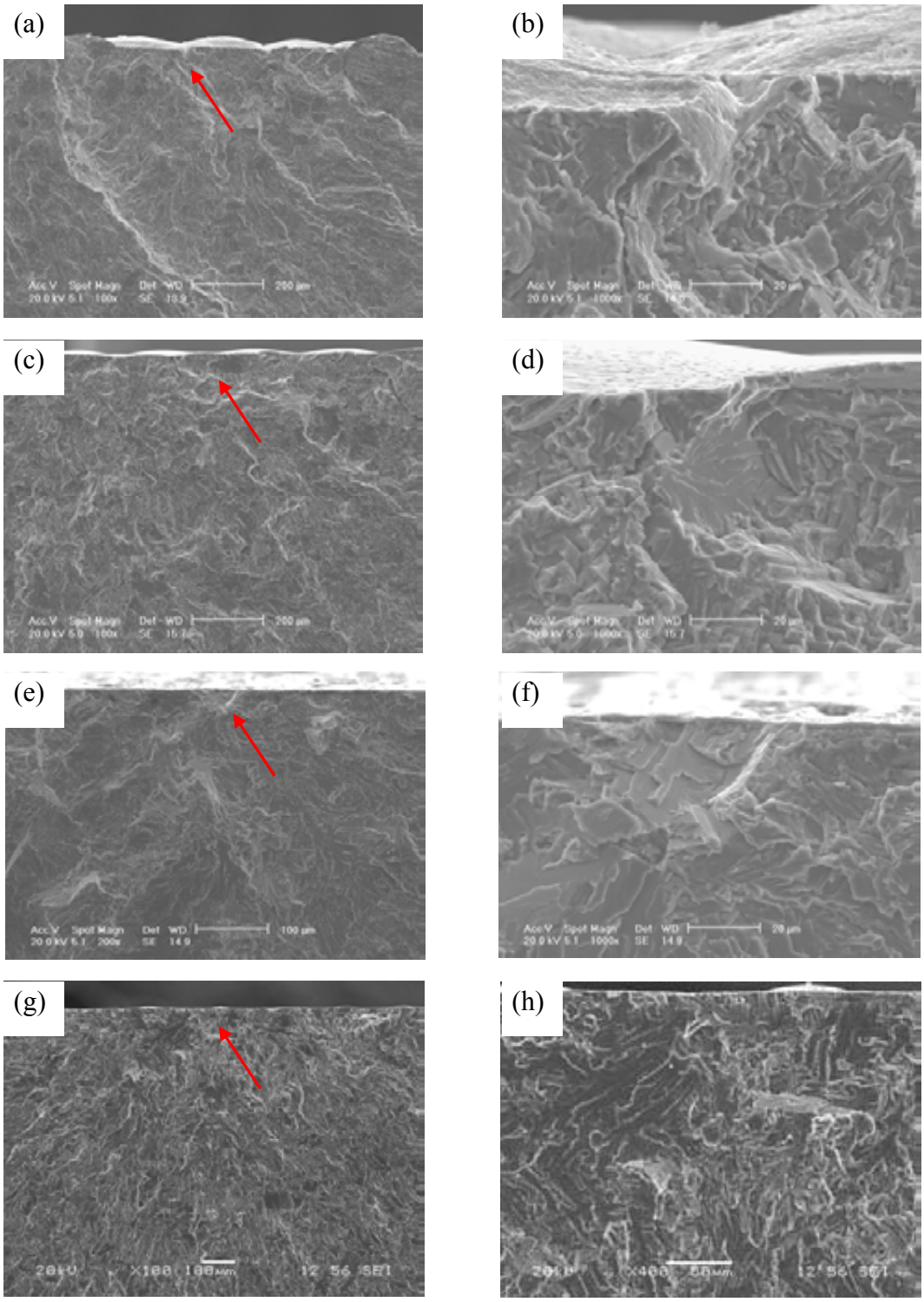

Fig. 4-36 SEM secondary electron micrographs showing fracture surfaces of failed fatigue HIPped Ti-6Al-4V samples with four surface conditions at different magnifications: (a, b) as-HIPped conventional surface; (c, d) electro-polished surface; (e, f) machined surface; (g, h) as-HIPped improved surface.

4.1.3.3 Discussion

In the HCF regime, where total fatigue life depends principally on fatigue crack initiation and early growth behaviour, a very low surface roughness and the absence of any severe surface/subsurface damage, probably contributed to superior fatigue strength. It has been reported that there is no effect of surface roughness on crack propagation, and surface roughness can accelerate crack initiation [*Wagner 1994*]. Hence, crack initiation sites were examined to assess the influence of surface finish on fatigue strength of HIPped samples which have similar crack propagation resistance. It is likely the sharp grooves formed by powder particles on the conventional as-HIPped surface can serve as sites of stress concentration and promote crack initiation under cyclic loading. Electro-polishing removed a surface layer of 15~20 μm and thus sharp grooves were turned into blunt undulations and a lower stress concentration as crack initiation site.

When the surface of a conventionally HIPped sample was removed by machining, examination has shown that fatigue cracks initiate from clusters of α laths which have similar grain orientation. Such clusters fail since they effectively behave as a large individual grain. Nevertheless, the fatigue limit of the current HIPped Ti-6Al-4V with a machined surface was only slightly lower than that of conventionally processed Ti-6Al-4V wrought product, since clusters of grains with similar orientations also occur in the latter material. Despite the fact that electro-polishing produced a surface roughness greater than that of the machining operation, it offered an improved fatigue endurance strength by 50 MPa. This appears to emphasise that crack initiation is sensitive not only to the surface finish but also to the local surface damage/residual

stress state. As-machined specimens, which were machined by reciprocating surface grinding (RSG), contain tensile residual stress on the surface that is responsible for the reduced fatigue endurance strength [*Novovic 2004*]. Some local surface damages (as shown in Fig. 4-33 (b)) resulting from machining can aggravate the initial crack growth stage.

The combined effect of low surface roughness and the absence of any significant surface damage are believed to be responsible for enhanced HCF performance of Ti-6Al-4V specimens with as-HIPped improved surface. Even though the unit structure in the as-HIPped improved sample is coarser (Fig. 4-32), which can result in more facets in the fracture surface (Figs. 4-36 (g, h)), the smaller volume fraction of low angle misorientations also contributes to the higher fatigue property.

4.2 HIPping of individual size fractions of PREP Ti-6Al-4V powder

The results reported in section 4.1.2.1 show that the samples made by HIPping of PREP Ti-6Al-4V powder contain two distinct microstructural regions; those associated with the original particle boundaries, where equiaxed alpha and beta are formed and those associated with the interior of the original particles where a lath-like microstructure dominates. In this section the microstructural characteristics of powder compacts made from individual size fractions have been characterised and the resultant mechanical properties assessed since the observed differences in microstructures at prior particle boundaries and in particle centres would be expected to vary for different size fractions. Three different powder particle size fractions (small size fraction: 50~150μm, intermediate size fraction: 150~250μm, large size fraction: 250~400μm) were used in this experiment and HIPped at 930 °C, 100MPa for 4h.

4.2.1 Microstructural characterisation

Fig. 4-37 shows the morphology of different size fractions of PREP Ti-6Al-4V powders after sieving. Typical scanning electron micrographs were obtained from polished cross sections of powder particles. Because cross sections can underestimate particle size a large number of particles were examined from the different powder size ranges. Thus although there will always be some uncertainty in the original particle size of any cross section, the largest diameter particle found was selected; this uncertainty is therefore minimised. In fact no obvious difference in microstructure of cross-sections of the powders, the structure of martensitic alpha-prime phase (see Fig. 4-2), was found

despite the fact that the cross sections differed in size by over a factor of more than 5. This is not surprising since once a critical cooling rate (about 200°C/s) is exceeded martensite will be formed and particles produced by PREP process cooled extremely rapidly.

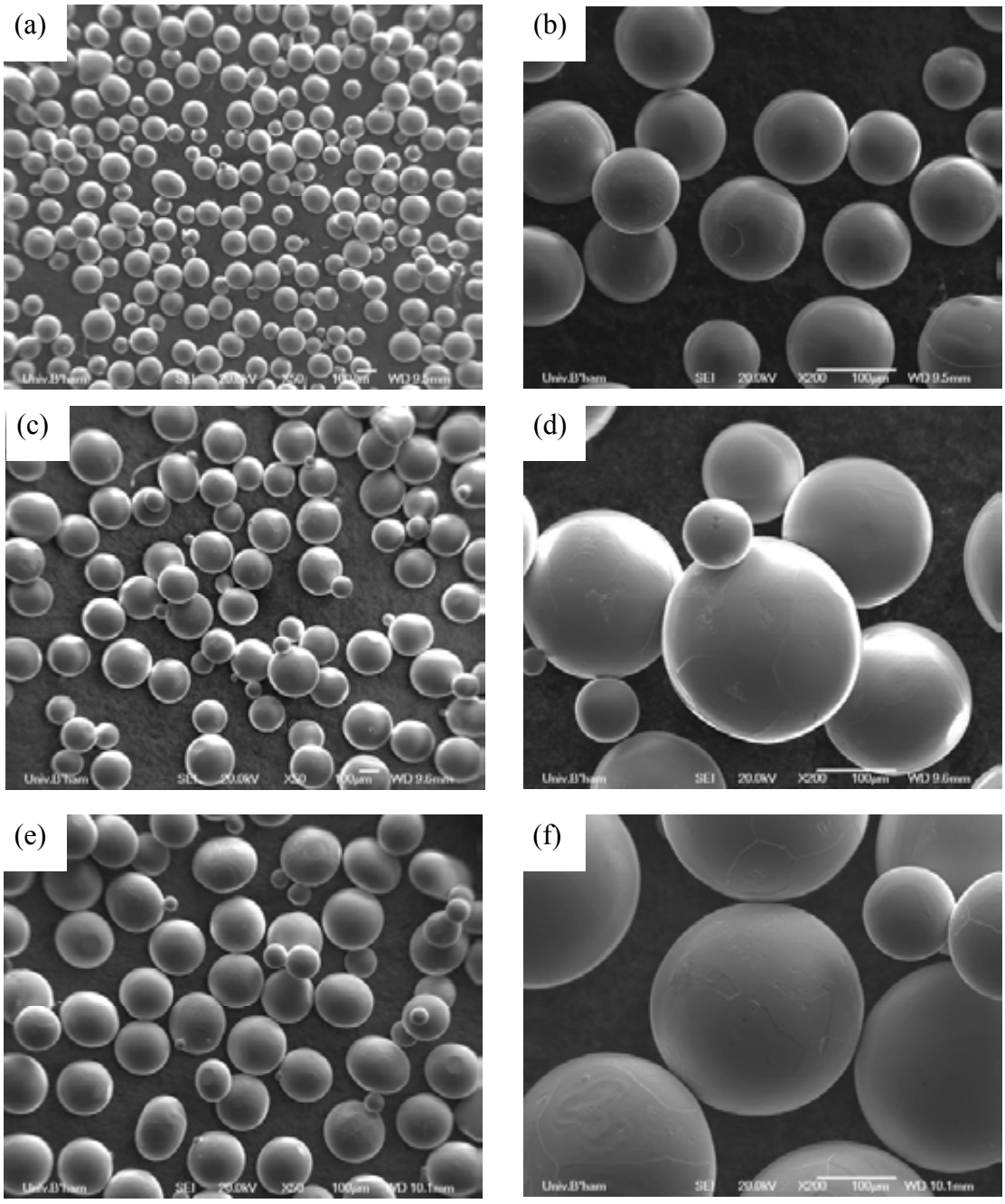

Fig. 4-37 SEM secondary electron micrographs showing the morphology of different size fractions of PREP Ti-6Al-4V powders after sieving: (a, b) small size fraction (50~150μm range); (c, d) intermediate size fraction (150~250μm range); (e, f) large size fraction (250~400μm range).

Small particles may have higher oxygen contents by virtue of their larger surface area per unit volume. Interstitial levels of HIPped samples made using various powder size fractions were analysed, as illustrated in Table 4-7. The values do not show evident difference among these three particle size fractions.

Table 4-7 Interstitial levels of PREP Ti-6Al-4V samples HIPped using various powder size fractions

	C content (ppmwt%)	**H** content (ppmwt%)	**N** content (ppmwt.%)	**O** content (ppmwt%)
Small size fraction (50~150 μm)	340	48	60	2000
Intermediate size fraction (150~250) μm	340	31	60	2100
Large size fraction (250~400) μm	330	37	50	1900

The typical microstructural characteristics of these different particle size fractions of compacts were similar to those of the complete size fraction powder HIPped produced under the same conditions (see Fig. 4-5). They all consisted of α and β phases, and both phases are combinations of lath-like structure and varying amounts of equiaxed grains at the former powder particle boundaries. However, it is evident from the micrographs shown in Fig. 4-38 that the overall distribution of lath-like structures and equiaxed grains is different since it is associated with powder particle size and former powder boundaries (as indicated by red dotted lines). The smaller the particle size, the higher the volume fraction of equiaxed grains for the as-HIPped microstructure.

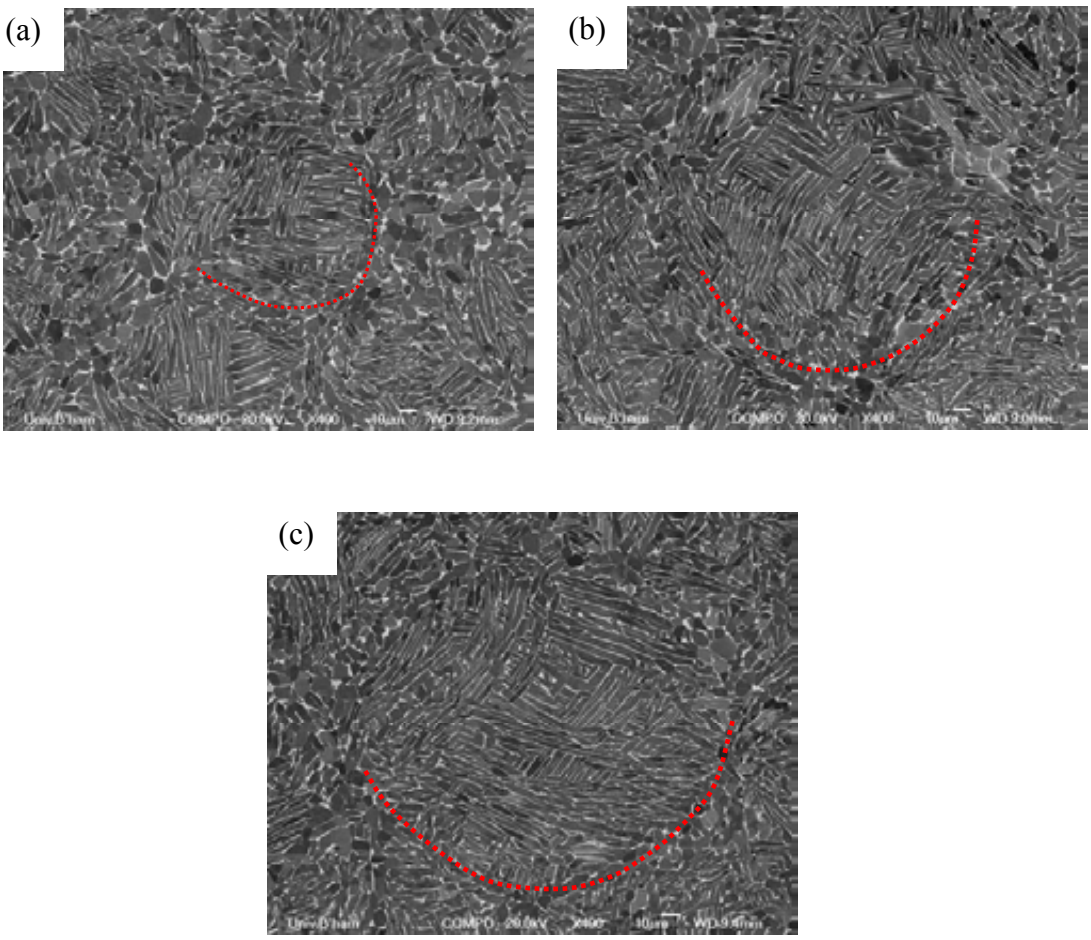

Fig. 4-38 SEM backscattered electron micrographs showing the typical microstructures of HIPped PREP Ti-6Al-4V samples made using: (a) particle size fraction of 50~150μm; (b) particle size fraction 150~250μm; (c) particle size fraction of 250~400μm (red dotted lines indicate original powder boundaries).

EBSD analyses were carried out mainly on the samples HIPped using small and large particle size fractions, as illustrated in Fig. 4-39. It is found that the two samples have similar misorientation distribution, but the size of the unit structure (formed by grains or lamellae with low misorientation angles) is different. The unit structure in the

sample HIPped using a particle size fraction of 250~400μm is coarser than that in the sample HIPped using a particle size fraction of 50~150μm.

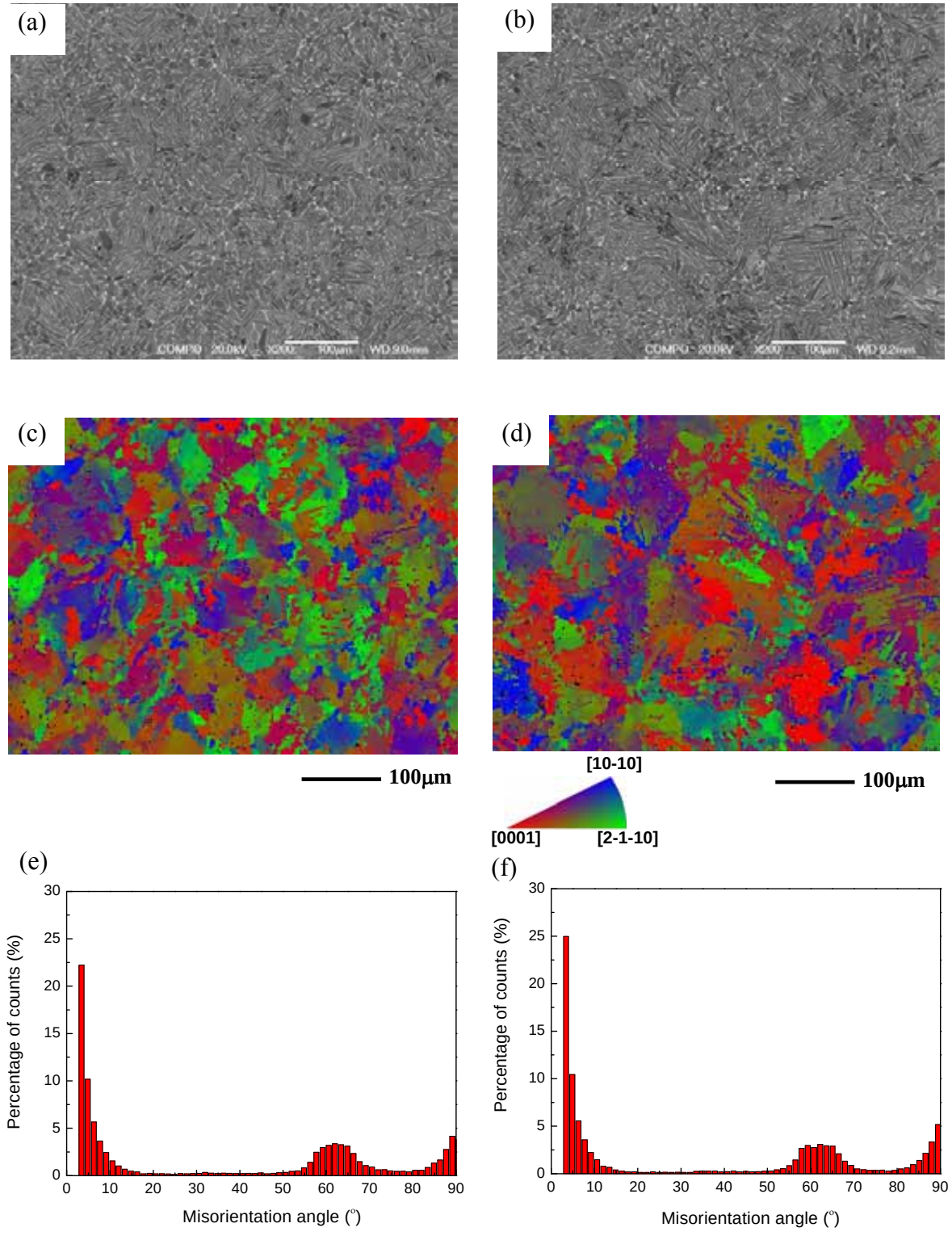

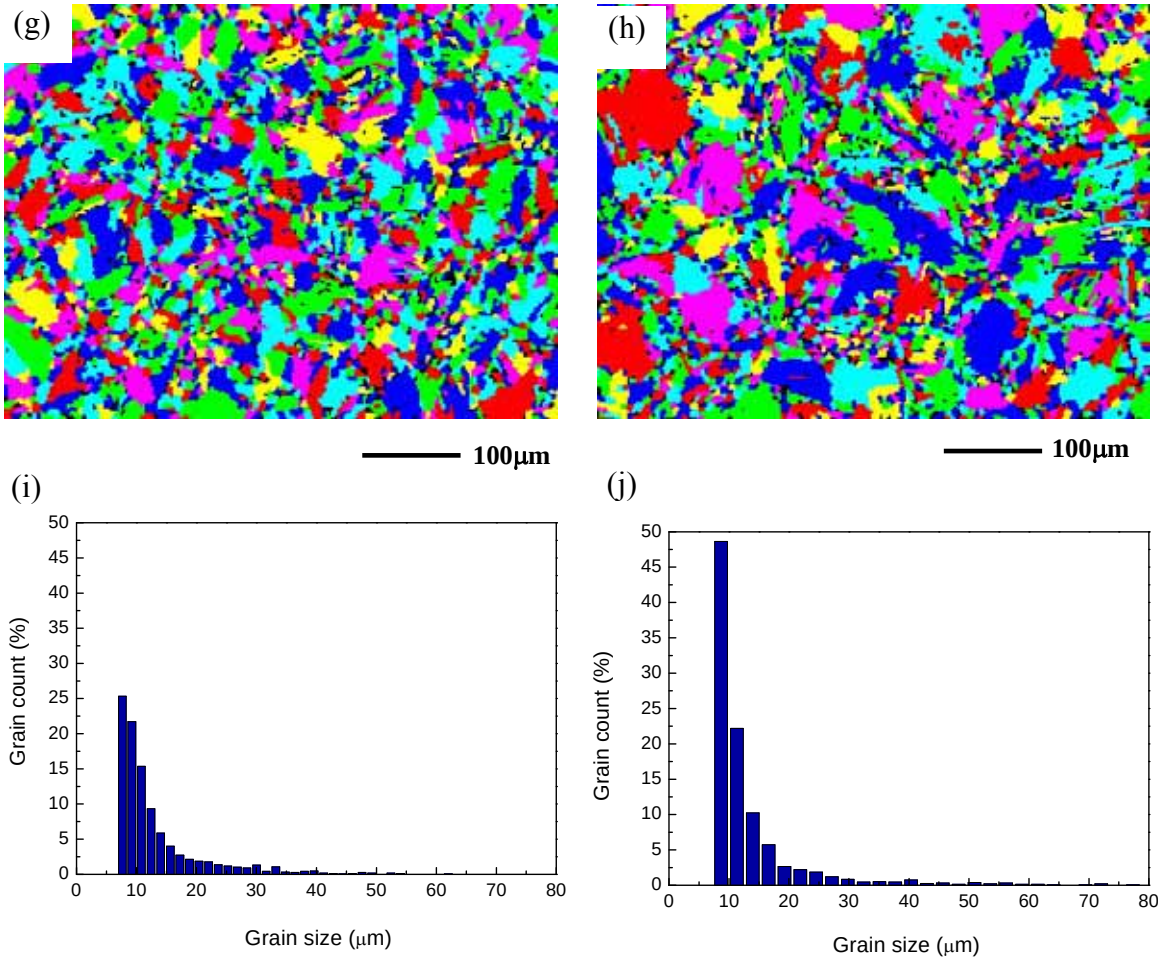

Fig. 4-39 (a, c, e, g, i)HIPped Ti-6Al-4V sample at 930°C using particle size fraction of 50~150μm; (b, d, f, h, j) HIPped Ti-6Al-4V sample at 930°C using particle size fraction of 250~400μm. (a,b) SEM backscattered electron micrographs; (c,d) EBSD misorientation maps; (e,f) misorientation distribution graphs; (g,h) EBSD grain size distribution maps; (i,j) grain size distribution graphs. It shows that the two samples have similar misorientation distribution, but the unit structure in the sample HIPped using a particle size fraction of 250~400μm is coarser than that in the sample HIPped using a particle size fraction of 50~150μm.

4.2.2 Influence of particle size on the properties of machined HIPped samples

4.2.2.1 Tensile property and examination of fracture surfaces in samples tested to failure

Tensile properties of HIPped samples made using different particle size fractions have been measured at room temperature, as illustrated in Fig. 4-40 (a). It can be seen that the yield stress and tensile strength are not influenced significantly by the different original powder particle size, only a small reduction can be detected for samples made using the intermediate particle size fraction (150~250 μm). However the ductility of samples made using the small particle size fraction (50~150 μm) is obviously lower at about 10% than those of samples with other size fractions, which have elongations around 16% (large particle size fraction) and 17% (intermediate particle size fraction), respectively, as shown in Table 4-8 in details. Fig. 4-40 (b) gives a comparison between the tensile properties of HIPped samples using sieved powders and complete size fraction. It is clear that they have similar strengths, but the complete size powder samples exhibit slightly better ductility with an elongation of 19%. Details can be seen from Table 4-4 (for samples HIPped at 930°C) and Table 4-8.

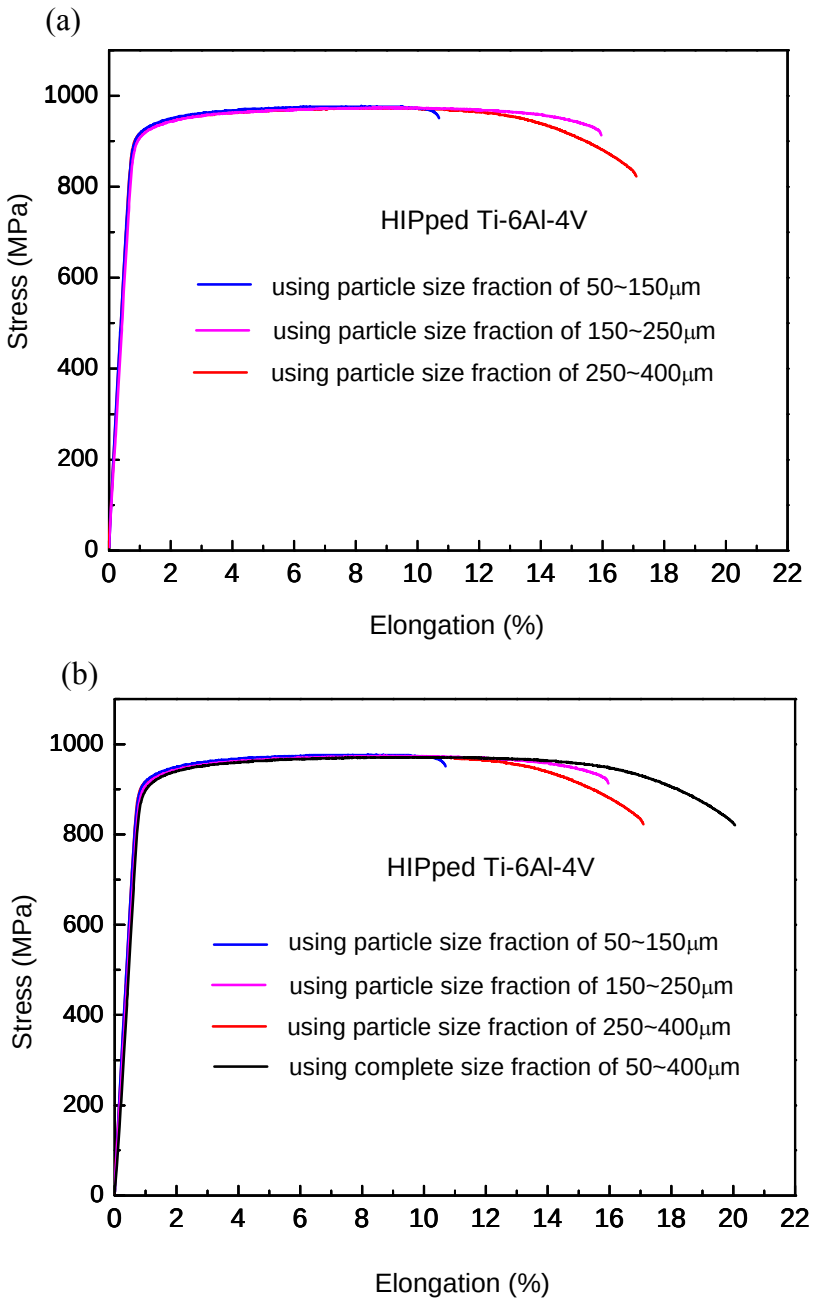

Fig. 4-40 Room temperature tensile properties of HIPped Ti-6Al-4V samples using (a) sieved powders with different size fractions showing similar tensile strengths for the three sets of samples and highest ductility for samples HIPped using the particle size fraction of 250~400μm; (b) sieved powders and complete size fraction with the sample made from the complete size fraction showing slightly better ductility.

Table 4-8 Room temperature tensile properties of HIPped Ti-6Al-4V samples with different powder particle size fractions

	YS (MPa)	UTS (MPa)	El. (%)
Small size fraction (50~150 μm)	**912** $\pm^{7}_{8}$	**979** $\pm^{4}_{2}$	**10** $\pm^{1}_{1}$
Intermediate size fraction (150~250) μm	**903** $\pm^{4}_{4}$	**971** $\pm^{3}_{2}$	**17** $\pm^{2}_{2}$
Large size fraction (250~400) μm	**914** $\pm^{13}_{6}$	**975** $\pm^{5}_{2}$	**16** $\pm^{1}_{0}$

Fracture surfaces of three sets of tensile specimens are shown in Fig. 4-41, where generally ductile mode of failure was showed for all the tested specimens indicating good bonding for HIPped samples and plastic deformation during tensile tests. With respect to the difference, in Figs. 4-41 (a, b), the fracture surface of the sample HIPped using particle size fraction of 50~150μm with an elongation of 9% contains multiple crack initiation sites (indicated by the arrows in (a)) and the crack initiation sites were characterised by groups of transgranular facets (see Fig. (b)). In the case of sample HIPped using particle size fraction of 150~250μm with an elongation of 15%, the crack initiation site formed by transgranular facets was also observed, as shown in Figs. 4-41 (c, d). There were no obvious crack initiation sites in samples HIPped using particle size fraction of 250~400μm with a higher elongation of 17%; a typical ductile fracture surface can be seen in Figs. 4-41 (e, f).

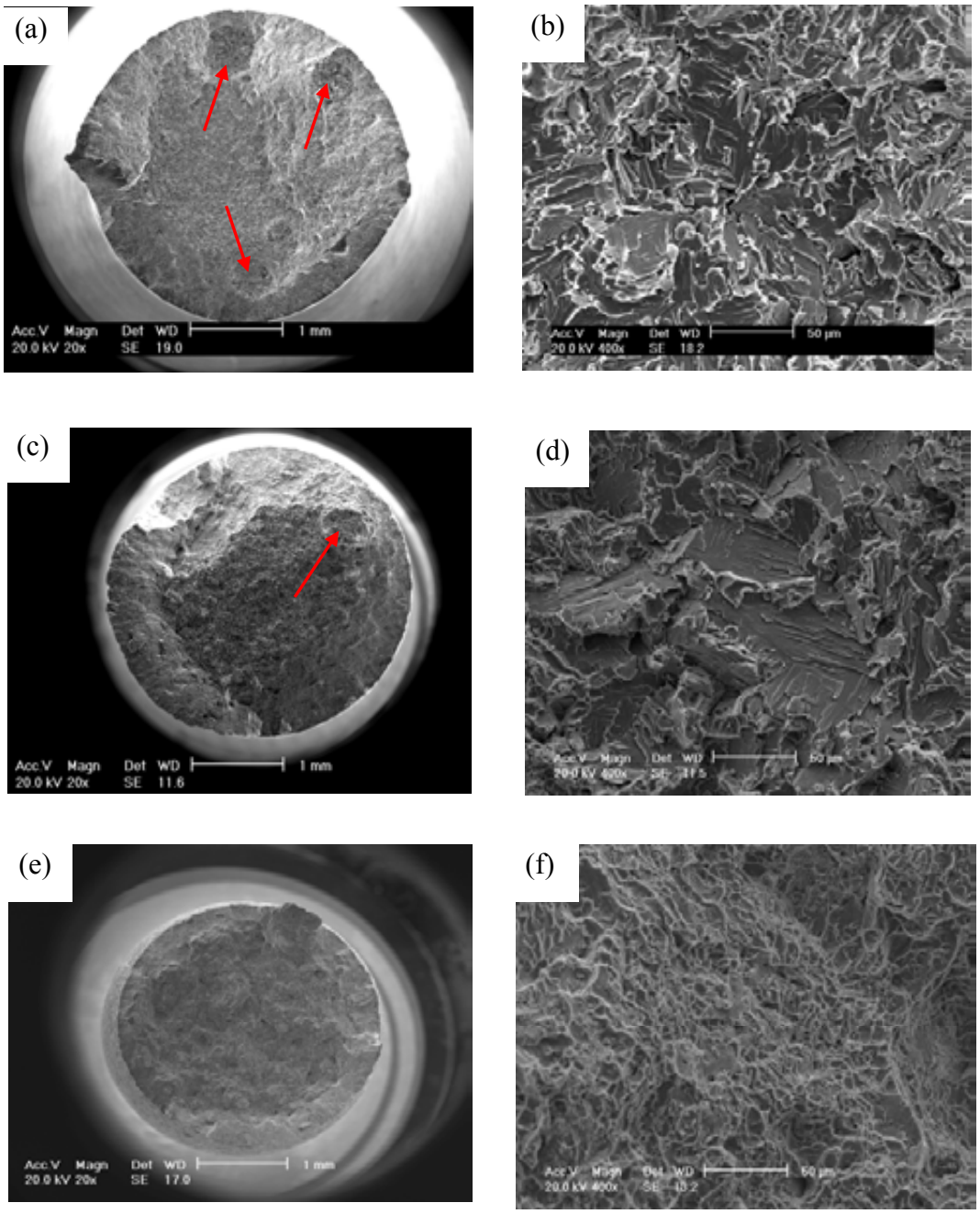

Fig. 4-41 SEM SE micrographs of the fracture surfaces of failed tensile samples HIPped using particle size fraction of: (a, b) 50~150μm with an elongation of 9% showing multiple crack initiation sites formed by groups of transgranular facets; (c, d) 150~250μm with an elongation of 15% showing crack initiation site formed by transgranular facets; (e, f) 250~400μm with an elongation of 17% showing no obvious crack initiation sites. Crack initiation sites are indicated by arrows.

4.2.2.2 Fatigue properties and observations of fracture surfaces of fatigued samples

SN curves for the machined HIPped samples made using different powder particle size fractions of 50~150 μm (small), 150~250 μm (intermediate) and 250~400 μm (large) are shown in Fig. 4-42 (a). The fatigue limit of the samples HIPped using the small powder size fraction lies below those of the two larger size fraction samples. Samples obtained with powder of the large size fraction had the highest run-out strength of 450MPa (at $1.0x10^7$ cycles). The endurance limit of samples made of small powder size (50~150 μm) was lower, at 370 MPa. SN curves for samples made using intermediate powder size range shows some overlap and similarity in the number of cycles to failure at similar stress levels in comparison to those of samples made using other powder size fractions, and a fatigue run-out value of 400 MPa was found. Fig. 4-42 (b) shows a comparison between the fatigue properties of HIPped samples using sieved powders and complete size fraction. It is found that the complete size powder samples exhibit better fatigue property with a run-out strength of 500 MPa.

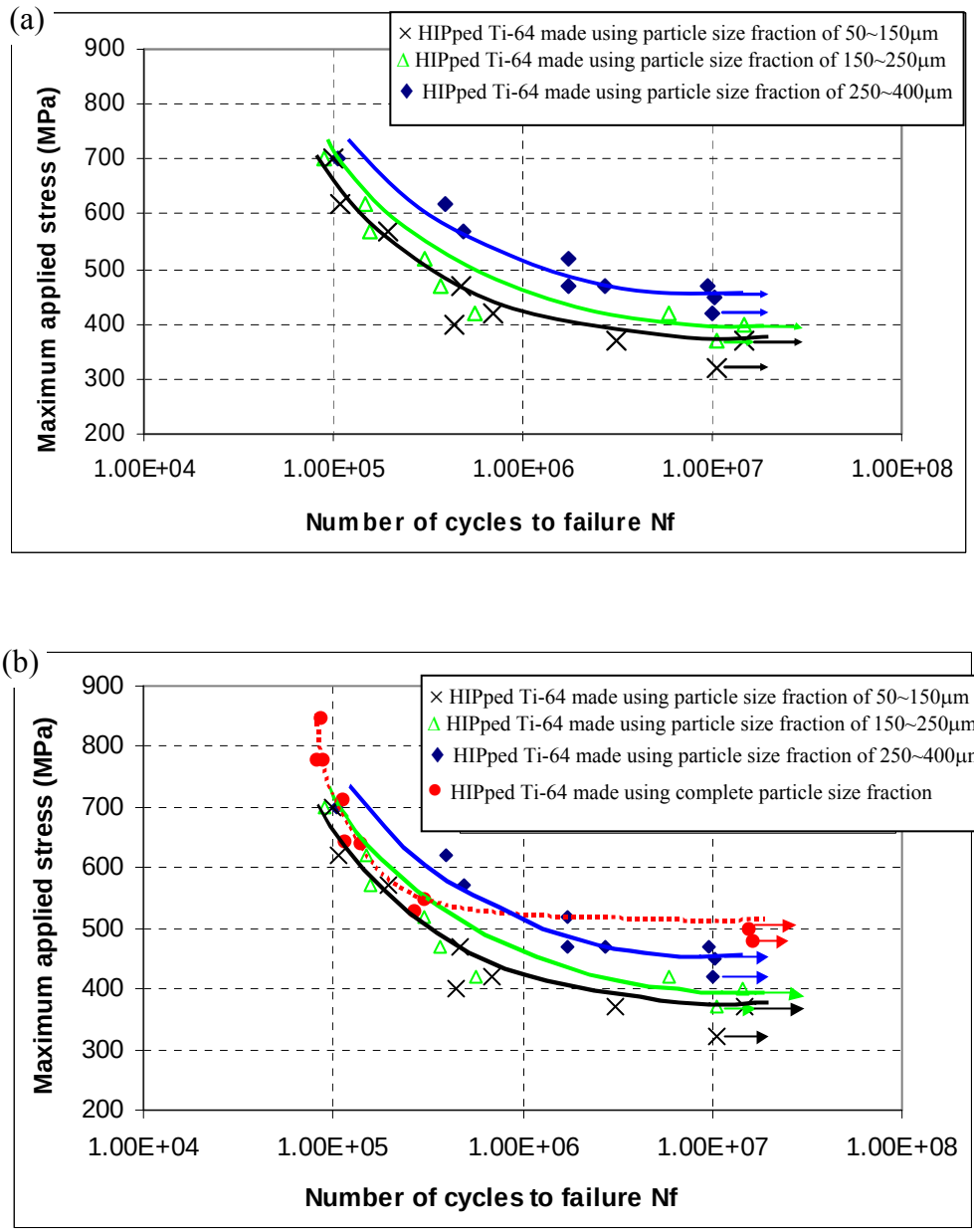

Fig. 4-42 SN fatigue curves for HIPped Ti-6Al-4V samples with machined surface made using (a) sieved powders with different size fractions showing that samples HIPped using the particle size fraction of 250~400μm have highest fatigue endurance limit; (b) sieved powders and the complete size fraction showing that the complete size fraction has the higher endurance limit.

Fractographic comparison between the smallest size fraction and largest size fraction was carried out in order to understand the effect of powder size on the fatigue properties. A detailed fractographic evaluation revealed that fatigue cracks initiated from the machined surface in samples made using both large and small particle size fractions. Fig. 4-43 shows some representative fracture surfaces in failed fatigue specimens made using both of the particle size fractions, where transgranular facets formed by cyclic slip are observed to act as crack initiation sites for the fatigue initiation and cleavage failure. No distinct difference in crack initiation sites between the various size fraction samples is observed. However examination of crack propagation close to the initiation site on fracture surface shows the crack path of the sample made using the small particle size range is much smoother than that of the sample made using the large particle size range, as shown in Fig. 4-44. Matching EBSD misorientation maps and distribution graphs for the crack paths are shown in Fig. 4-45. The two samples show similar misorientation distribution.

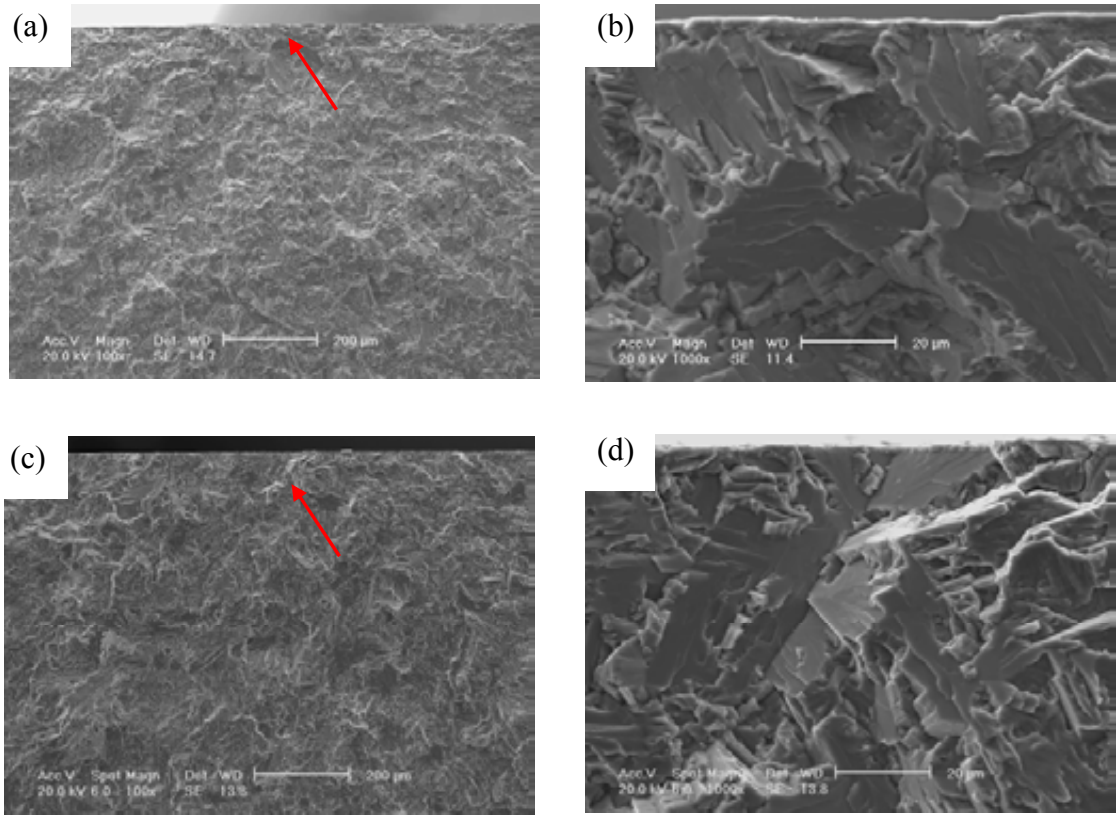

Fig. 4-43 SEM secondary electron micrographs at different magnifications of fracture surfaces of fatigue failed samples HIPped using: (a, b) particle size fraction of 50~150μm (maximum stress=400MPa / number of cycles=439800); (c, d) particle size fraction of 250~400μm (maximum stress=470MPa / number of cycles=2702100) showing no distinct difference in crack initiation sites between the various size fraction samples. Crack initiation sites are indicated by arrows.

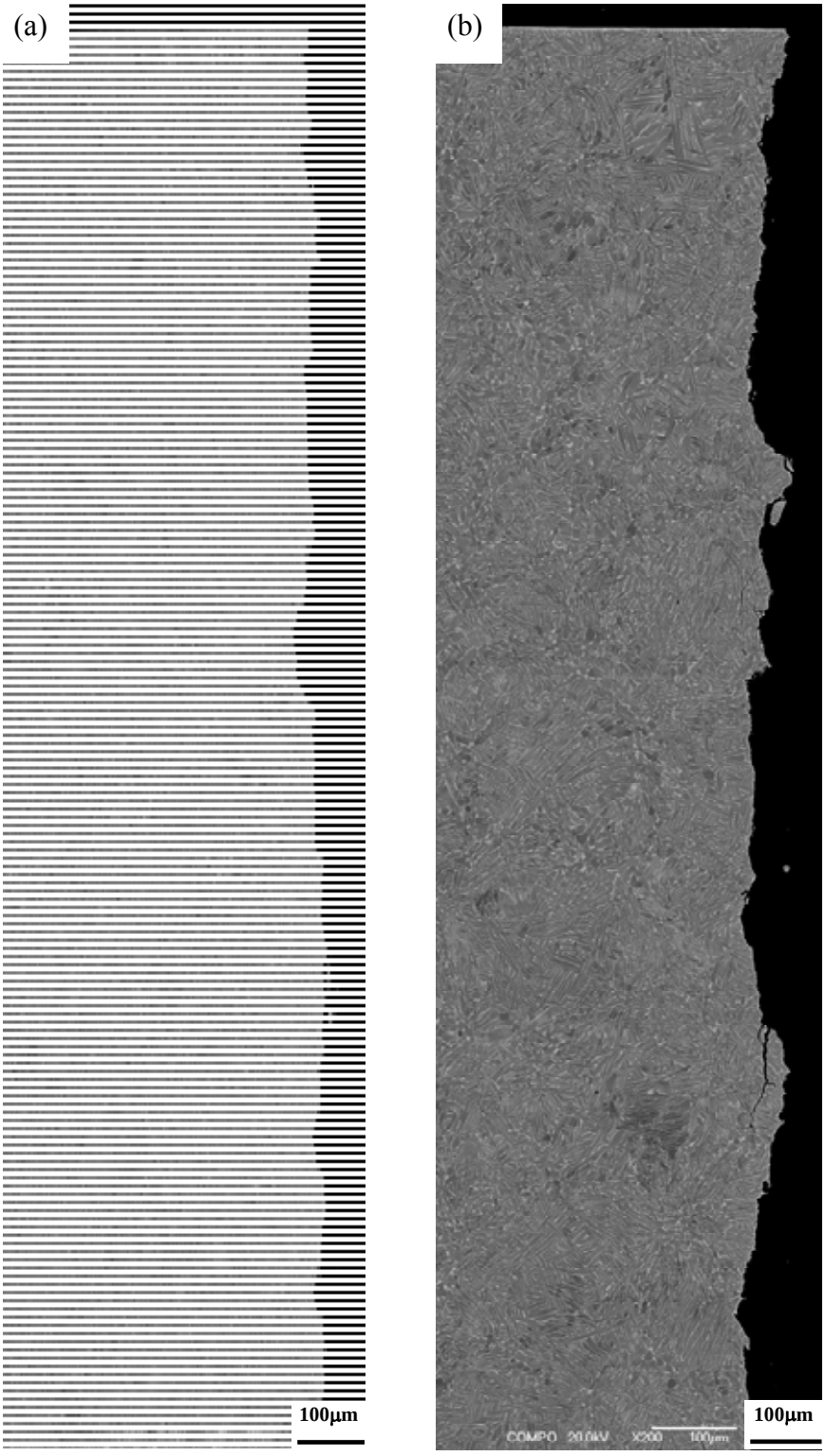

Fig. 4-44 SEM BSE images showing the crack paths of fracture surface cross sections of fatigue failed HIPped Ti-6Al-4V samples made using (a) particle size fraction of 50~150μm; (b) particle size fraction of 250~400μm. The crack path of large size fraction sample is rougher than that of small size fraction.

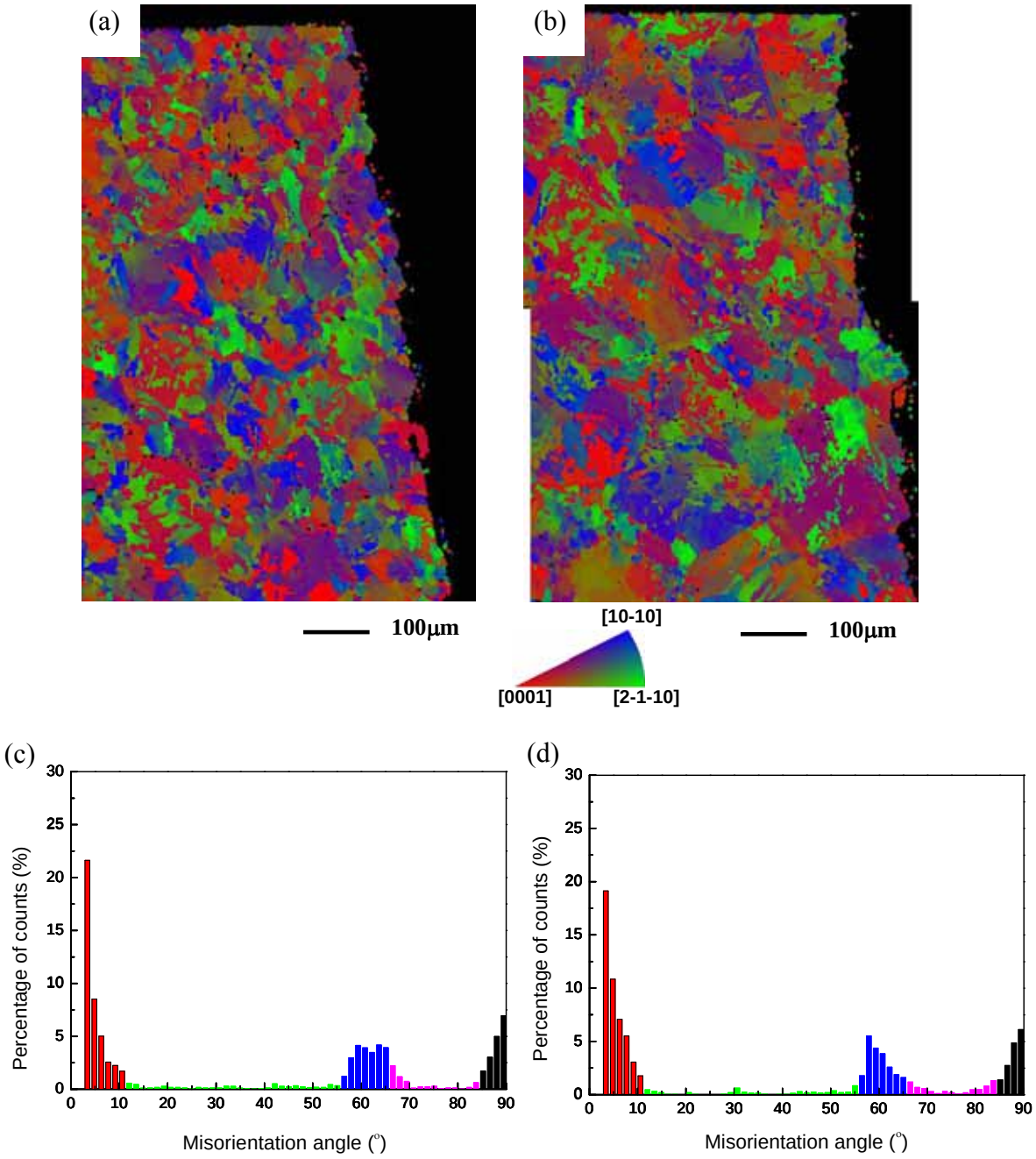

Fig. 4-45 (a, c)HIPped Ti-6Al-4V sample at 930°C using particle size fraction of 50~150μm; (b, d, f, h, j) HIPped Ti-6Al-4V sample at 930°C using particle size fraction of 250~400μm. (a, b) EBSD misorientation maps; (c, d) misorientation distribution graphs for the crack paths of fracture surface cross sections of fatigue failed samples. The two samples show similar misorientation distribution.

4.2.3 Discussion

It is surprising that the samples HIPped using smallest powder size fraction of 50~150 μm show the lowest ductility and fatigue run-out strength. The obvious factor which could lead to differences as a function of particle size is the increase in surface area which could lead to an increase in oxygen pick-up. However the analyses reported in Table 4-7 show that there is no detectable difference between the oxygen levels in the different size fractions and furthermore the yield stress, which is dependent upon oxygen concentration, is not a function of particle size. It thus appears that changes in the oxygen content are not responsible for the differences in fatigue properties and ductilities observed.

There are two main differences between the microstructures which may affect the properties. One is the volume fractions of lath-like structure and of equiaxed grains (see Fig.4-38) with a higher proportion of equiaxed grains in the finer size fraction. The other is the unit structure which is coarser in samples HIPped using the large particle size fraction of 250~400μm. The first difference is clearly associated with the fact that these equiaxed grains are distributed along the original particle boundaries. As a consequence there is a corresponding larger fraction of equiaxed grains in the samples made using the small size fractions. The fracture observations show however that failure occurs through the equiaxed and lamellae regions so that there is no preference for the crack to go through the equiaxed regions. The fact that the fine particle size samples have a lower ductility is not associated with a higher fraction of equiaxed grains.

The second difference - the size of unit structure - could result in different resistance to crack initiation. From the examination of fracture surfaces of failed tensile specimens made using different particle size fractions, it is clear that obvious crack initiation sites are associated with low ductility (see Fig. 4-41). On the other hand, the fracture surfaces and crack paths in samples made from the large size fractions are rougher than those in the samples made using the small size fraction (see Figs. 4-41, 4-44*)*, which is associated with coarser unit structure in large size fraction samples. This could possibly contribute to the better fatigue property since the coarser unit structure leads to more crack-deviation than do fine structures due to tortuous crack path requiring more energy for the crack growth [*Lütjering 2003, Gregory 1994*]. "In-situ" tests would be required to observe the behaviour of crack initiation and growth in different size fraction samples to understand the effect on properties.

HIPped Ti-6Al-4V samples (at 930°C) made using the complete size fraction of the powders have a smaller volume fraction of low angle misorientation than those HIPped (at 930°C) using sieved powders (see Fig. 4-9 (b) and Fig. 4-39), which could partly contribute to better ductility and fatigue property than found in the sieved powder samples.

4.3 Summary

The microstructure of the original PREP powder particles has been assessed and changes in the microstructure occurring during HIPping related to the tensile and fatigue properties of HIPped samples were investigated. The effect of different HIPping conditions (HIPping temperature, surface finish) and the materials

characteristics (particle size distribution) on mechanical properties was analysed. The results obtained can be summarised as follows:

- The microstructure of the original PREP Ti-6Al-4V powder was shown to be martensitic plates for all powder sizes (from 50 - 400μm).
- All HIPped samples show that small equiaxed grains are formed at original particle boundaries where local recrystallisation occurs. Within the central part of original particles HIPping gave rise to a lath-like microstructure from the original alpha prime martensite.
- Samples HIPped below the transus showed similar microstructures (although coarser microstructures were formed at the higher HIPping temperatures). Samples HIPped at 1020°C (above the transus) showed significant microstructural coarsening, but otherwise similar microstructures to that seen in samples HIPped below the transus.
- All HIPped samples, including those HIPped above the transus showed very different microstructures from those found in ingot-route samples.
- The lower the HIPping temperature (below the transus, and thus the finer the microstructure) the higher the strength, but the lower the ductility. Samples HIPped at 930°C exhibited a better balance of properties than those HIPped at 880°C and 1020°C.
- Powder samples HIPped at 930°C not only have comparable tensile and fatigue strengths to sample commercially forged at similar temperature, but also exhibit better ductility and higher fracture toughness values.
- The fatigue properties of samples which retained the as-HIPped surface made using a conventional HIPping cycle were downgraded because the Ti-6Al-4V

powder indented the mild steel can resulting in a rough surface. By raising the temperature before applying the pressure, during HIPping the Ti-6Al-4V was softened before compaction, resulting in a smooth surface.

- These smooth as-HIPped samples have better fatigue properties than samples produced by machining or electropolishing conventionally HIPped samples. This ability to improve the fatigue performance of samples containing an as-HIPped surface is clearly very significant in the field of net shape HIPping.
- HIPped samples (with machined surfaces) made using the small powder size fraction showed the lowest ductility and fatigue strength and smoother fracture surfaces than samples made using the larger size fractions, but the tensile strengths were similar for the different powder size fractions.
- These differences have been interpreted in terms of the difference of the size of the unit structure which is much coarser in the samples made using the large size fraction of powders. Further “In-situ” tests will be needed to understand the effect of unit size on the crack behaviour.
- HIPped samples made using complete size fraction powders have better ductility and fatigue property than those made using sieved powders with different size fractions.

References

Bache 1999a: Bache, M. R., *Int. J. Fatigue*, **21**, 1999, p.105.

Bache 1999b: Bache, M. R., and Tasleem, M., *Int. J. Fatigue*, **21**, 1999, p.187.

Bache 2001: Bache, M. R., Evans, W. J., Suddell, B., and Herrouin, F. R. M., *Int. J. Fatigue*, **23**, 2001, p.153.

Bache 2003: Bache, M. R., *Int. J. Fatigue.*, 2003, **25**, p.1079.

Cahn 1991: Cahn, R.W., Haasen, P., and Kramer, E. J., *Materials Science and Technology,* Vol 15*, Processing of Metals and Alloys*, VCH Verlagsgesellschaft, Weinheim, Germany, 1991, p143.

Dellis 1996: Dellis, C., Gallo, P. L., Baccino, R., and Moret, F., in: *Proc. Int. Conf. on 'Hot Isostatic Pressing'*, Materials Park, OH, ASM International, 1996, p.75.

Delo 1999: Delo, D. P. and Piehler, H. R., *Acta mater*., **47**(9), 1999, p.2841.

Gregory 1994: Gregory, J. K., in: *Handbook of Fatigue Crack Propagation in Metallic Structures*, Ed., Carpinteri, A., Elsevier Science, 1994.

Hertzberg 1989: Hertzberg, R. W., *Deformation and Fracture Mechanics of Engineering Materials*, 3rd ed., John Wiley & Son, 1989.

Kelto 1980: Kelto, C., in: *Powder Metallurgy of Titanium alloys*, Eds., Froes, F., and Smugersky, J., American Institute of Mechanical Engineers, Warrendale, PA, 1980, p.5.

Li 1987: Li, W. B., Ashby, M. F., and Easterling, K. E., *Acta. Metall.*, **35** (12), 1987, p.2831.

Long 1999: Long, M., Crooks, R., and Rack, H. J., *Acta Mater.,* **47**, 1999, p.661.

Lütjering 2003: Lütjering, G., Willians, J. C., *Engineering Materials and Processes*: *Titanium*, Springer, Germany, 2003.

Novovic 2004: Novovic, D., Ph.D Thesis., The University of Birmingham, Birmingham, UK, 2004.

Pérez 1995: Pérez, P., González-Carrasco, J. L., Adeva, P., *Materials Science and Engineering*, **A199**, 1995, p. 211.

Raisson 1999: Raisson, G., in: *Hot Isostatic Pressing International Conference 1999,* International Academic Publishing, Beijing, China, 1999, p.390.

Seliverstov 1994: Seliverstov, D., Samarov, V., Goloveshkin, V., Alexandrov, S., and Elkstrom, P., in: *Proc. Conf. on 'Hot Isostatic Pressing'*, eds., Delaey, L. and Tas, H., Amsterdam, Elsevier Science BV., 1994, p.555.

Wagner 1994**:** Wagner, L., and Gregory, J. K., in: *Materials Science Forum*, Dortmund, Germany, **163-165**, 1994, p.159.

Wu 1996: Wu, X., Ph.D Thesis., The University of Birmingham, Birmingham, UK, 1996.

Chapter 5 Microstructure and properties of HIPped samples of BuRTi powder

BuRTi has been developed with the aim of producing an alloy which has a good balance of room temperature ductility, strength and high temperature properties in combination with burn resistance [*Li 1998, Voice 2004*]. Improvements in microstructural stability and room temperature ductility have been achieved by the addition of carbon and by the control of the oxygen level [*Li 1999, Li 2001*]. BuRTi is a strong alloy and requires very high temperatures and/or powerful extrusion or forging facilities. In addition, BuRTi is difficult to machine. In view of these factors near net shape powder metallurgy is potentially a process-route that could reduce the cost of components manufactured from BuRTi. The aim of the present study is to assess the effect of HIPping conditions on microstructure and properties of as-HIPped samples of BuRTi powder so that the properties which could be achieved in near net shape components can be defined.

In the first part of this chapter, powders made from two production methods (gas atomised BuRTi powder, PREP BuRTi powder) were characterised and subsequently used to assess the effect of HIPping processing variables, i.e. temperature, pressure and holding time, on microstructure and properties of HIPped samples made using different powder sources. A detailed fractographic evaluation on fracture surfaces of failed mechanically tested samples has been carried out to reveal the failure mechanism. In the second part of the chapter, the influence of powder particle size on

microstructure and properties has been investigated by HIPping different powder size fractions.

5.1 Microstructure and properties of HIPped BuRTi powder

5.1.1 HIPping of gas atomised BuRTi powder

5.1.1.1 Microstructural examination of original powder

Fig. 5-1 shows the morphology of as-received gas atomised BuRTi powder. Most of the powders are spherical as shown in Fig. 5-1, with a few particles having satellites caused by the collision between particles in flight. Cross sections of a large number of particles were examined by SEM and EBSD. Fig. 5-2 shows the microstructures and matching EBSD analyses of an individual spherical gas atomised BuRTi powder particles. EBSD grain size distribution maps and graphs (Figs. 5-2 (b, c)) were used to characterise the powder particle's grain size, and the range of grain size (3~52 μm) is shown in Fig. 5-2 (c). The individual powder particles are polycrystalline single phase (Figs. 5-2 (a, b, e)). Figs. 5-2 (d, e, f) show the misorientation distribution graph and line profile of misorientation angle *vs.* distance along the line through the powder, and high misorientation angles between the adjacent grains were recorded. Figs. 5-3 (a, b) show the microstructures of another powder particle which has non-spherical shape which contains small grains and some larger grains (such as grains 1 and 2). Uneven grain size distribution can be seen more obviously in the EBSD image and grain size distribution graph, as shown in Figs. 5-3 (c, d). The largest grain which is composed of grains 1 and 2 with similar crystallographic orientations, up to 150 μm, was detected, and a very small change in misorientation angles inside the large grain is shown in misorientation angle analysis through the whole single powder (see Figs. 5-

3 *e*, *f*). EDX analyses were carried out for some individual spherical gas atomised BuRTi powders and the non-spherical powder which has uneven grain size distribution to assess the chemical compositions between the large grains region and other regions, as shown in Fig. 5-4. Lower Cr contents can be detected in large grains (spectra 2 and 3 in Figs. 5-4 (c, d)) compared to other areas in the same powder and areas in spherical powder particle which has even grain size distribution (see Figs. 5-4 (a, b)). Similar chemical compositions in spectra 2 and 3 also show evidence of their belonging to one large grain.

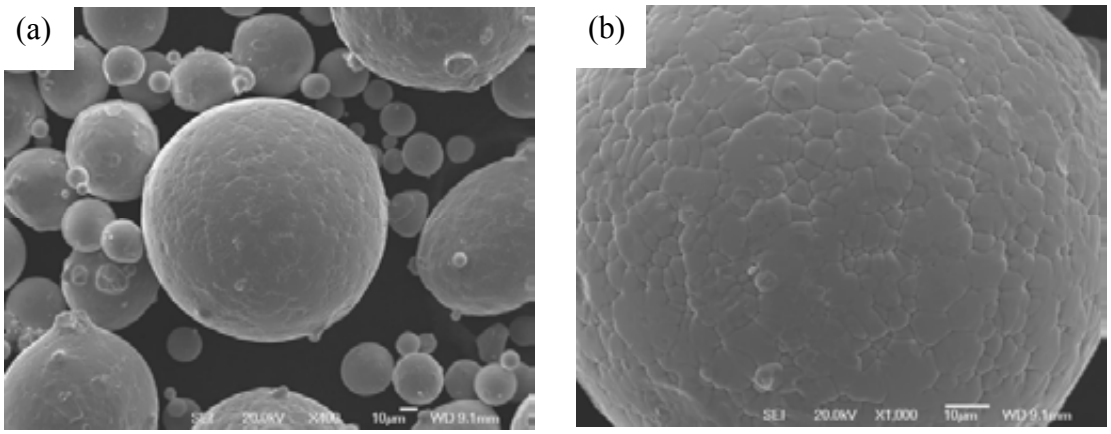

Fig. 5-1 SEM secondary electron micrographs showing the morphology of as-received gas atomised BuRTi powder surfaces at different magnifications: (a, b) spherical BuRTi powder and some satellite particles.

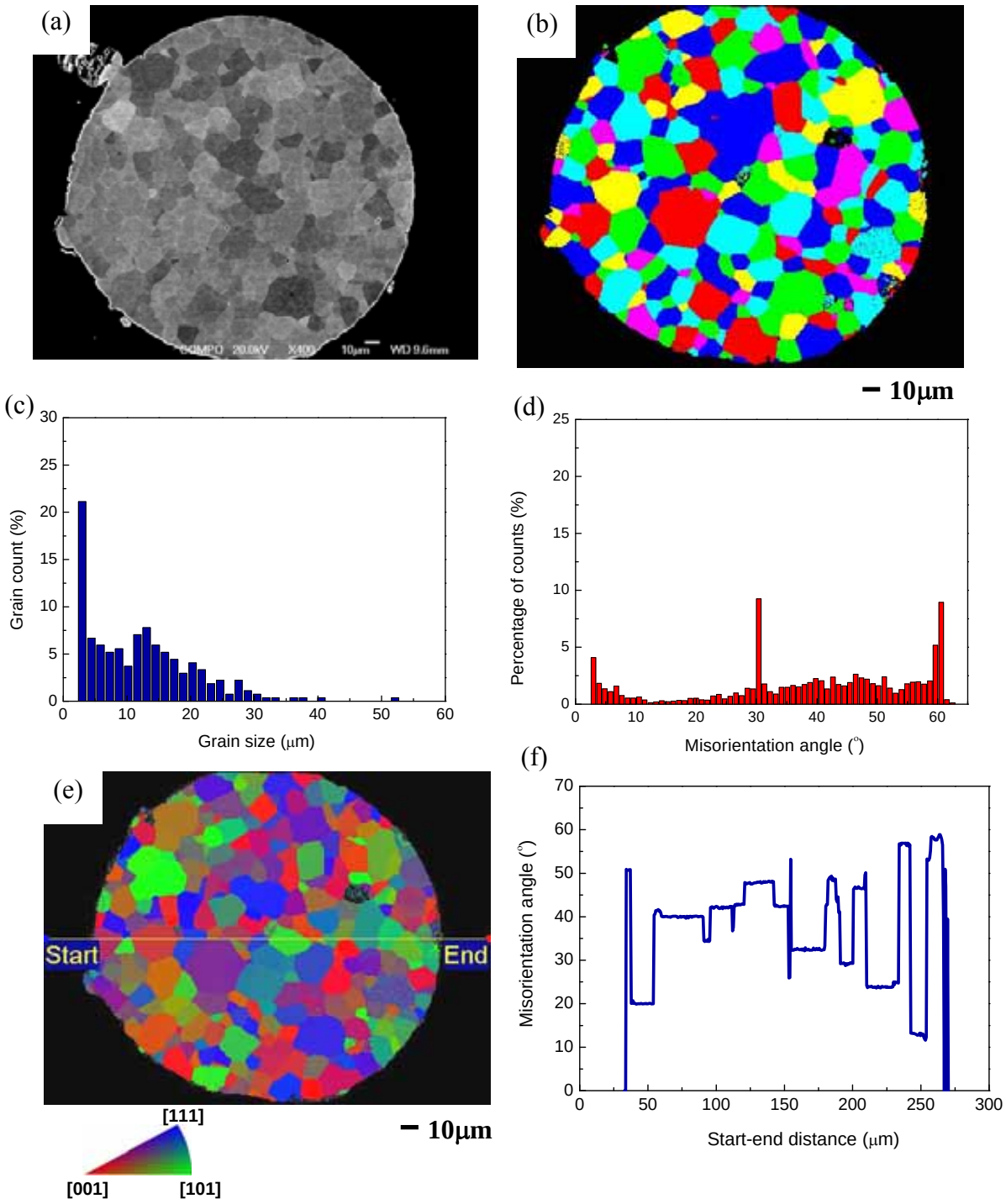

Fig. 5-2 Cross section of an individual spherical gas atomised BuRTi powder of (a) SEM BSE image showing polycrystalline single phase; (b, c) EBSD grain size map and distribution graph; (d) overall misorientation distribution graph; (e, f) EBSD misorientation map and line profile of misorientation angle vs. distance along the cross line showing high misorientation angles across grain boundaries of adjacent grains.

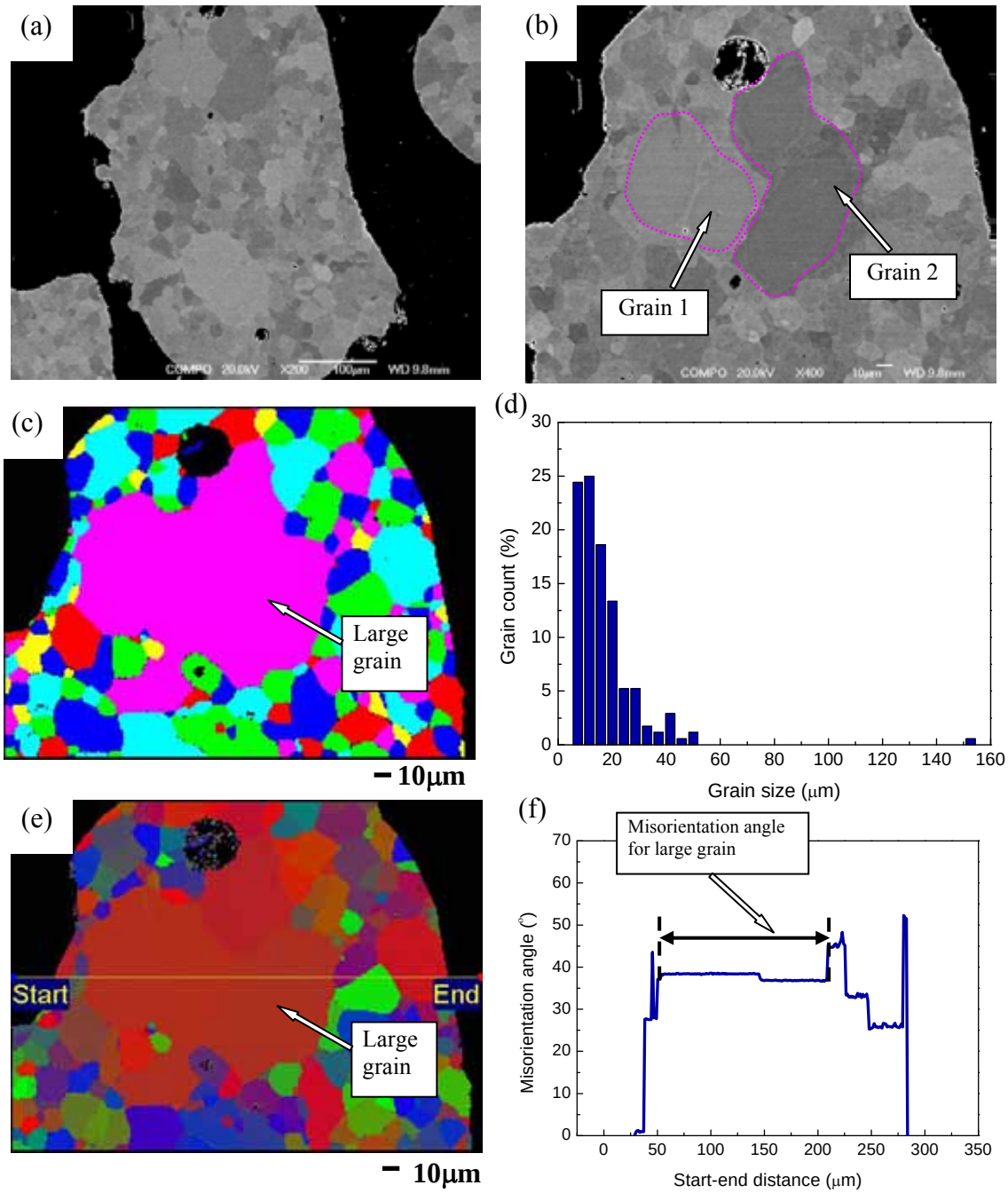

Fig. 5-3 Cross section of an individual non-spherical gas atomised BuRTi powder of (a, b) SEM BSE images at different magnifications showing two large grains; (c, d) EBSD grain size distribution mapping and graph showing that these two grains were counted as a larger grain; (e, f) EBSD misorientation mapping and line profile of misorientation angle vs. distance along the cross line showing these two grains have only a very small misorientation between them so low misorientation angles inside the large grain.

(a)

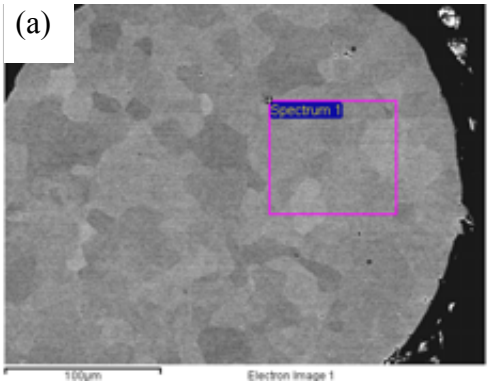

(b)

	Spectrum
V	24.1 ± 0.1
Cr	14.8 ± 0.3
Al	1.9 ± 0.1
Ti	Bal.

∗All results are in weight%, and total counts are around 305000.

(c)

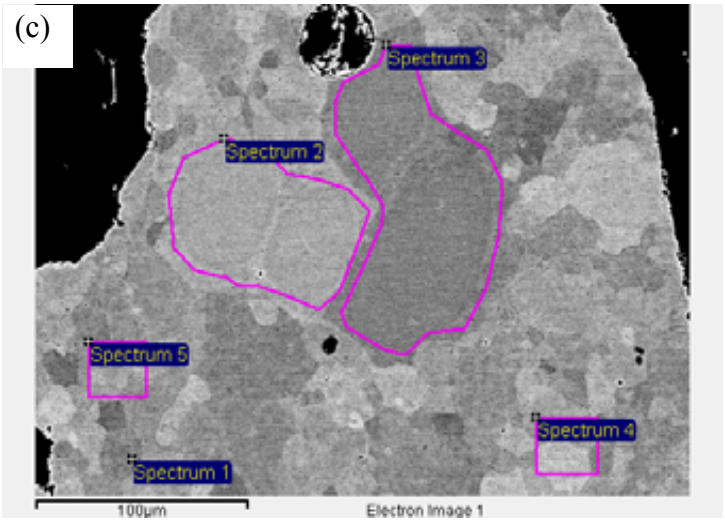

(d)

Spectrum	V	Cr	Al	Ti
Spectrum 1 (point)	23.8 ± 0.3	15.2 ± 0.3	1.8± 0.1	Bal.
Spectrum 2 (large grain area)	25.6 ± 0.4	13.1 ± 0.2	2.1± 0.1	Bal.
Spectrum 3 (large grain area)	25.7 ± 0.4	12.9 ± 0.3	2.2± 0.1	Bal.
Spectrum 4 (other area)	24.5 ± 0.3	14.4 ± 0.3	2.0± 0.1	Bal.
Spectrum 5 (other area)	24.4 ± 0.3	14.6 ± 0.2	2.0 ± 0.1	Bal.

∗All results are in weight%, and total counts for each area are around 317000.

Fig. 5-4 EDX analyses of individual gas atomised BuRTi powders: (a) SEM BSE image of a spherical powder; (b) EDX results; (c) SEM BSE image of a non-spherical powder which has uneven grain size distribution indicating analysed areas; (d) EDX results. The large grains have lower Cr contents than other areas in the same powder and in other spherical powders.

Individual gas atomised particles occasionally showed some porosity, as illustrated in Fig. 5-5. The formation of pores in gas atomised powders is usually associated with shrinkage of the particle during solidification, or from gas entrapment (i.e. Ar, the atomisation gas) during processing [*Rabin 1990*].

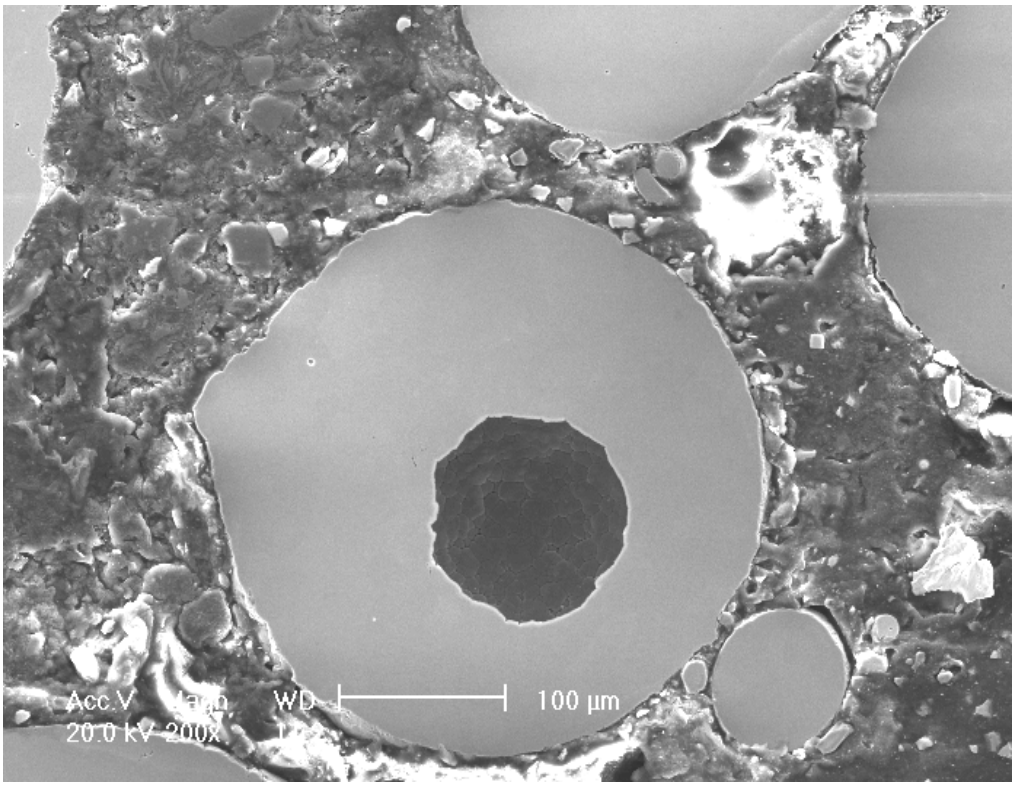

Fig. 5-5 SEM SE image of cross section of an individual gas atomised BuRTi powder (mounted in bakelite) showing the gas bubble in as-received powder.

5.1.1.2 Effect of HIPping parameters (temperature, pressure, holding time) on microstructure

The complete size fraction (50~400 µm) of gas atomised BuRTi powder was HIPped by simultaneously ramping up to the HIPping temperature and pressure, holding the

selected HIPping conditions for a defined time, and slowly cooling down whilst reducing the pressure and temperature in phase. A series of HIPping conditions were used: (i) 900^{o}C, 100MPa, 2h; (ii) 900^{o}C, 100MPa, 4h; (iii) 900^{o}C, 150MPa, 4h; (iv) 950^{o}C, 150MPa, 4h, to assess the effect of the variables of temperature, pressure and time on the microstructures. Figs. 5-6 (a-h) show optical micrographs of these samples which show no obvious differences; in all cases the microstructure was single phase beta at this resolution. At the lower magnification it is possible to identify individual powder particles in all of these HIPped samples; some facetting is apparent with individual particles showing obvious straight edges. The microstructure of extruded BuRTi was also examined and it is clear that the extruded samples have a coarser microstructure than the HIPped samples with bands of carbides visible along the extrusion direction and some carbides on grain boundaries, see Figs. 5-6 (i-j). Some large grains were found randomly in the as-HIPped microstructure (see Fig. 5-7 (a)), which resulted from the original particles with larger grain sizes (see Fig.5-3). EDX analyses were used to assess the chemical compositions of the large grains region and other regions, as shown in Fig. 5-7 (b), and similar results to those of original powder (see Fig.5-4) were obtained (lower Cr contents in area with large grains).

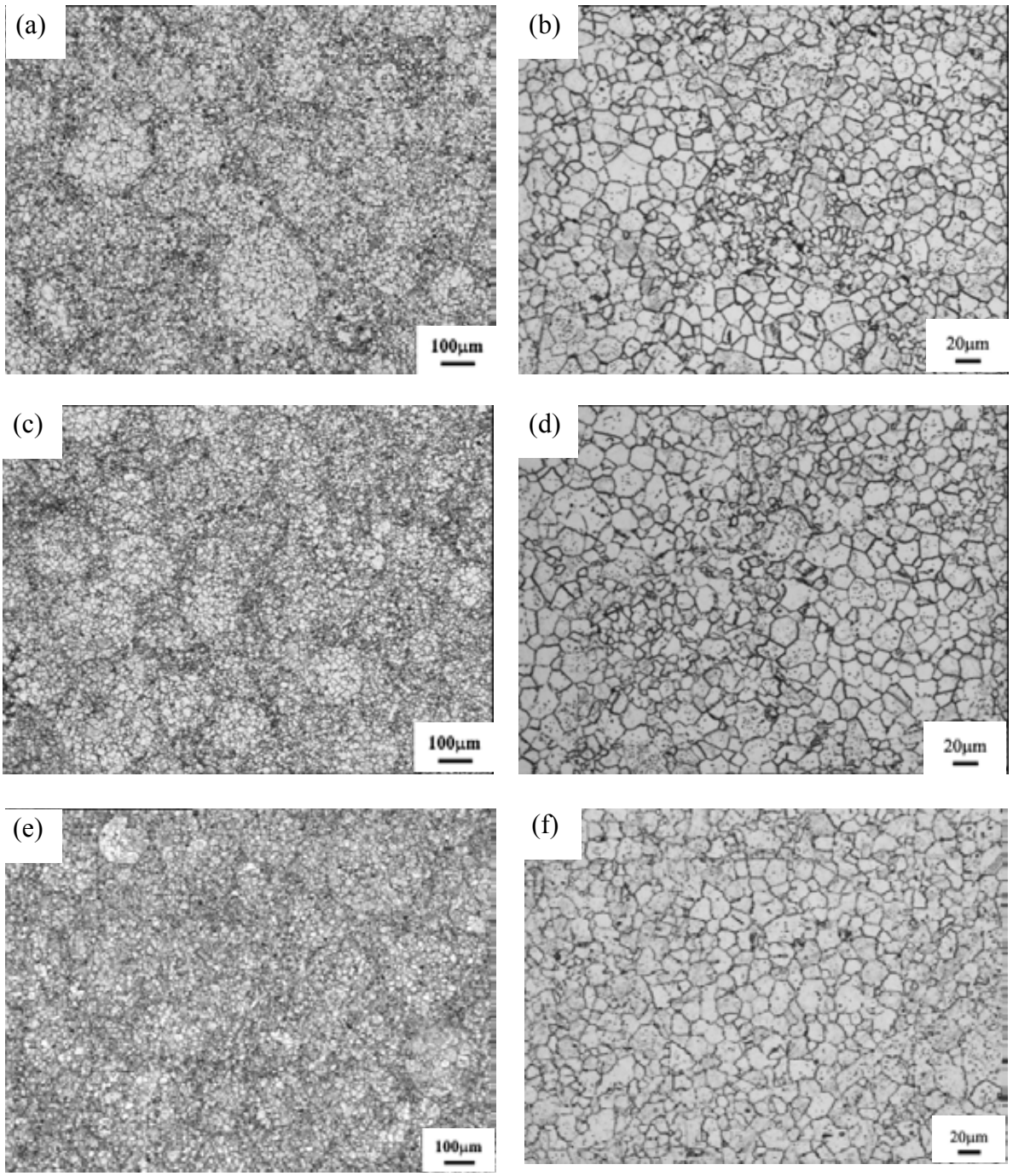
(a)
100μm
(b)
20μm
(c)
100μm
(d)
20μm
(e)
100μm
(f)
20μm

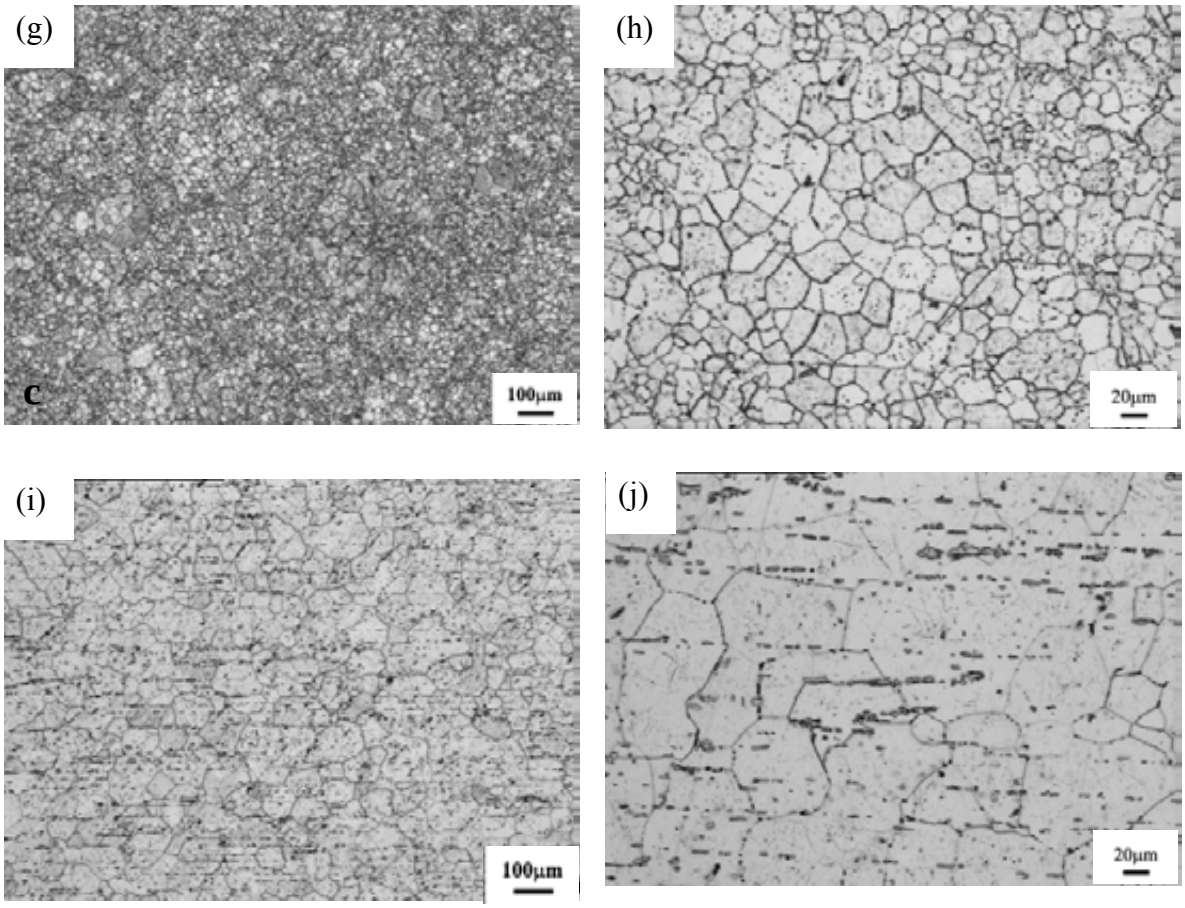

Fig. 5-6 Optical images at different magnifications of HIPped gas atomised BuRTi powder samples at: (a, b) 900^{o}C, 100MPa, 2h; (c, d) 900^{o}C, 100MPa, 4h; (e, f) 900^{o}C, 150MPa, 4h; (g, h) 950^{o}C, 150MPa, 4h; and of (i, j) extruded BuRTi samples showing similar microstructure in HIPped samples for different conditions and coarser microstructure for extruded ones.

(a)

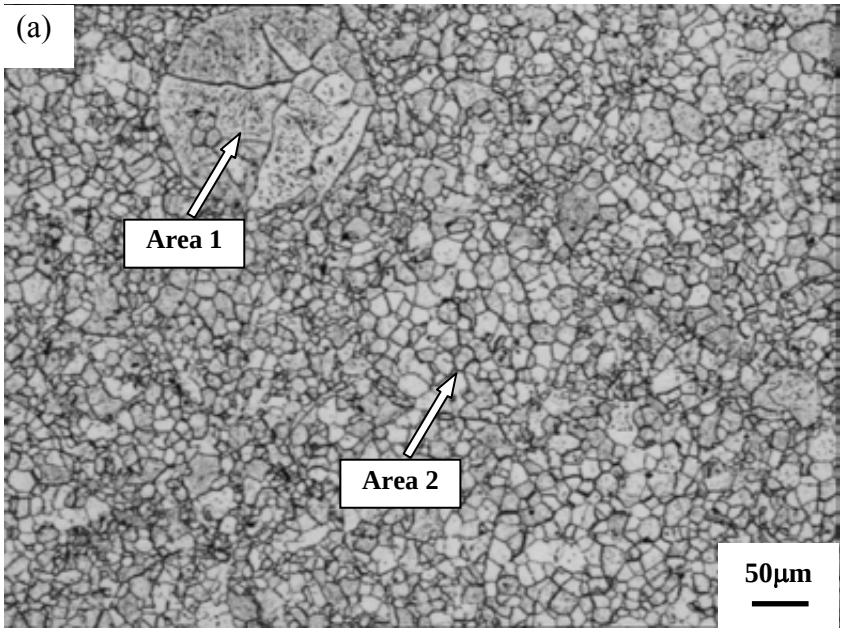

(b)

Area	V	Cr	Al	Ti
1 (containing large grains)	24.2 ± 0.4	12.7 ± 0.3	2.6± 0.1	Bal.
2 (containing fine grains)	24.4 ± 0.3	14.4 ± 0.2	2.2 ± 0.1	Bal.

∗All results are in weight%, and total counts for each area are around 388000.

Fig. 5-7 EDX analyses of HIPped gas atomised BuRTi powder sample at 900^{o}C, 100MPa, 4h: (a) Optical image indicating two analysed areas; (b) EDX results for area with large grain size (Area 1) and area with fine grain size (Area 2). Lower Cr contents can be detected for areas with large grains.

Backscattered electron micrographs and matching EBSD images for samples (ii)-(iv) and for extruded samples are shown in Fig. 5-8. Misorientation distribution and grain size distribution graphs for these samples are illustrated in Figs.5-9, 5-10. It is clear

that HIPped samples have a larger volume fraction of low angle misorientation boundaries than do extruded samples, and the grain sizes of HIPped samples are much finer than that in extruded BuRTi. From the back scattered micrographs, original powder particles can be seen again and at this resolution small carbides, are visible on grain boundaries of the small crystals within the original powder particles. Some original powder particles are particularly obvious when the grain size within them is larger than average as can be seen clearly in the EBSD images. Particles are also visible in the extruded samples and on the basis of earlier work these are carbides visible both in the extruded and in the HIPped powder samples.

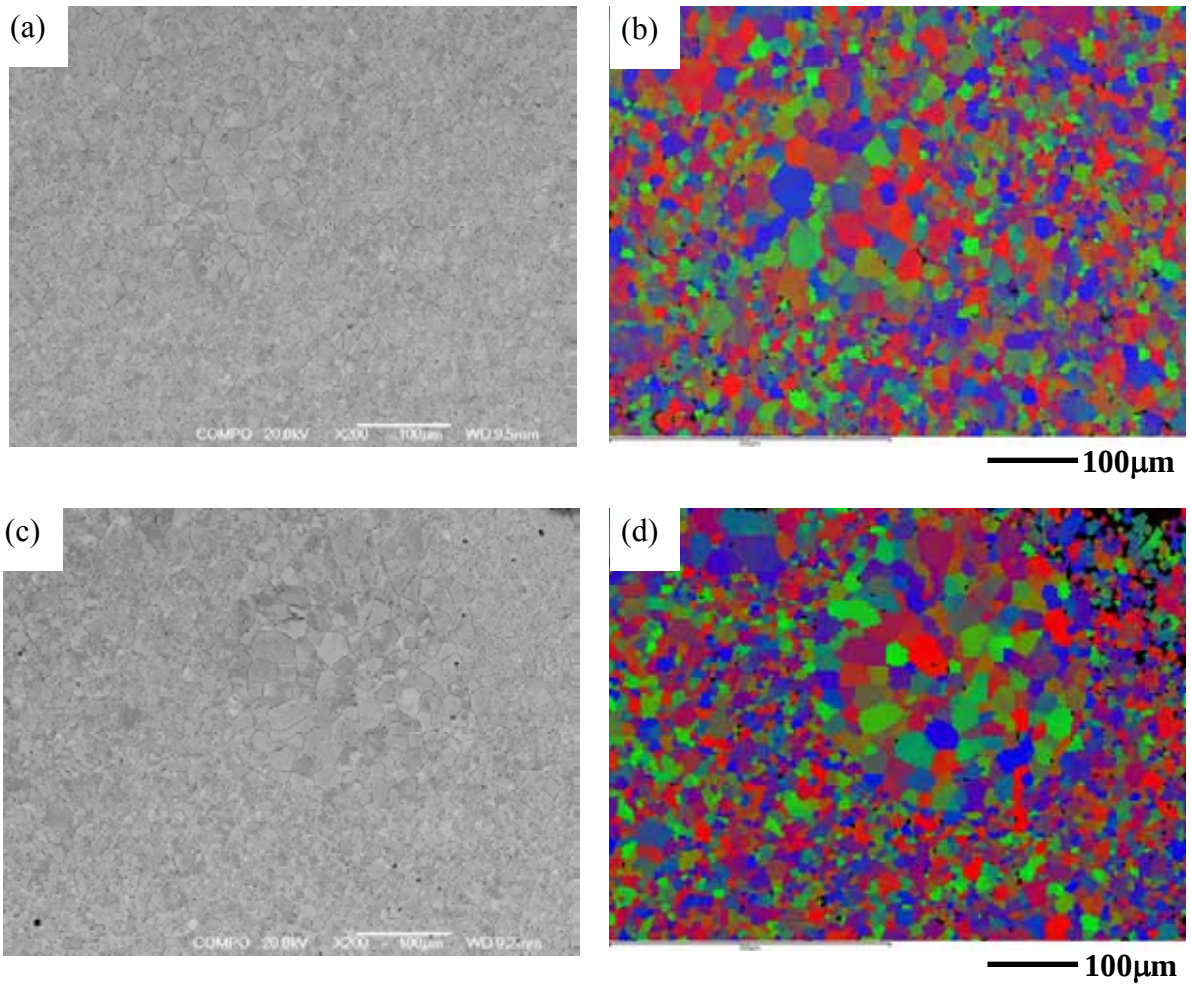

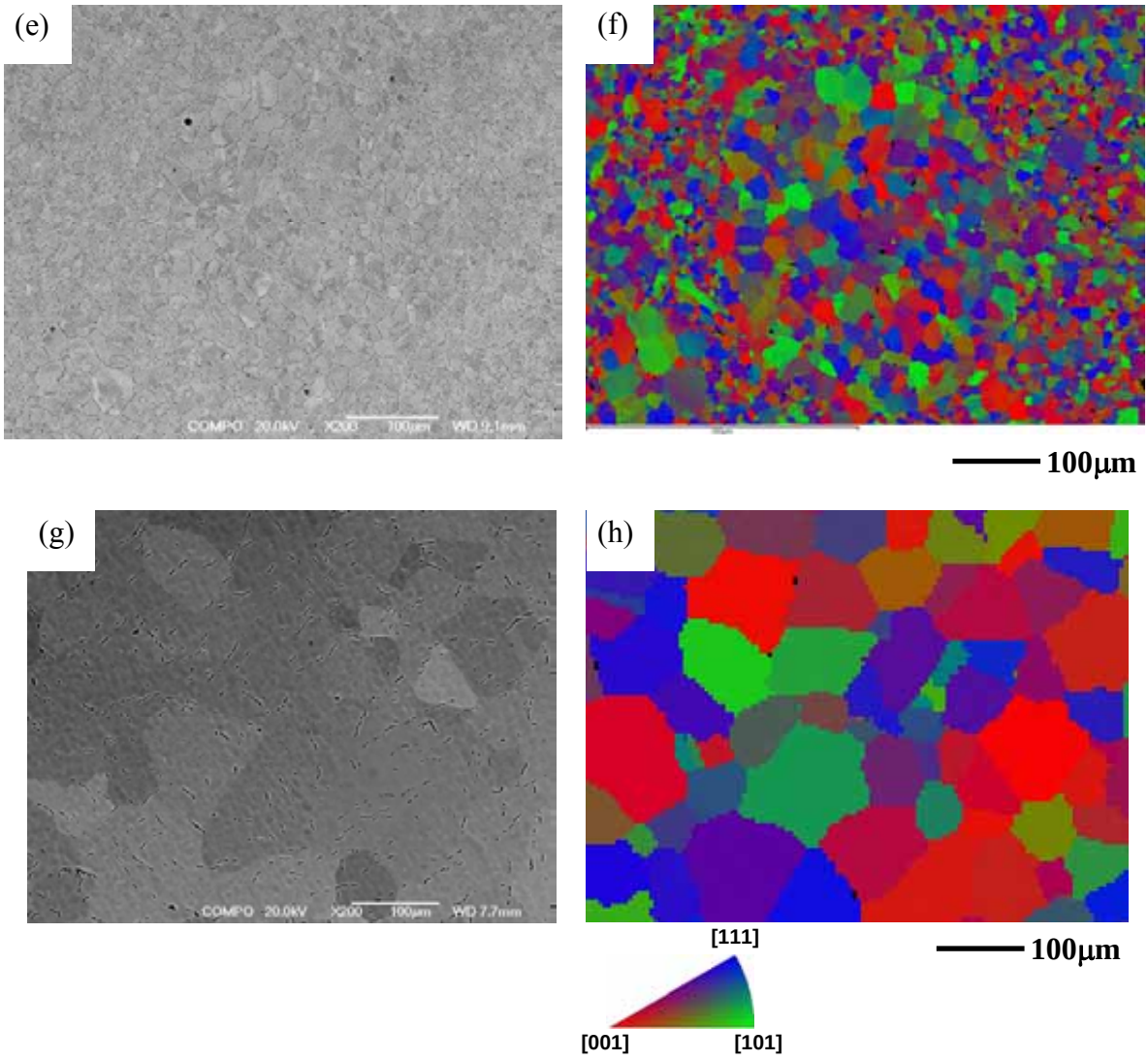

Fig. 5-8 SEM BSE images and matching EBSD misorientation mappings of gas atomised BuRTi powder samples HIPped at: (a, b) 900°C, 100MPa, 2h; (c, d) 900°C, 150MPa, 4h; (e, f) 950°C, 150MPa, 4h; and of (g, h) extruded BuRTi samples. EBSD images of HIPped samples show some original powder particles are obvious when the grain size within them is larger than average.

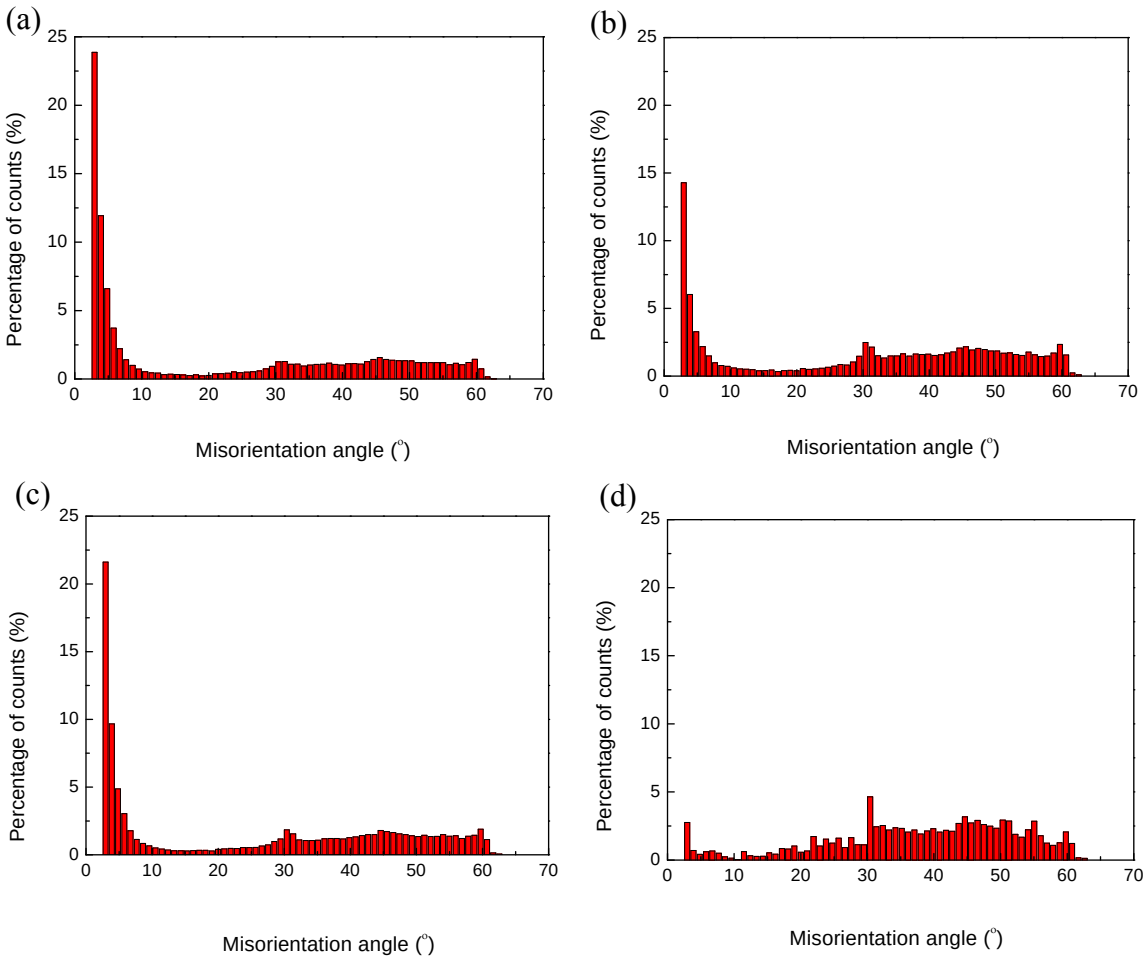

Fig. 5-9 Misorientation distribution graphs of gas atomised BuRTi powder samples HIPped at: (a) 900°C, 100MPa, 2h; (b) 900°C, 150MPa, 4h; (c) 950°C, 150MPa, 4h; and of (d) extruded BuRTi samples. It shows that HIPped samples have a higher volume fraction of low angle misorientation boundaries than do extruded samples.

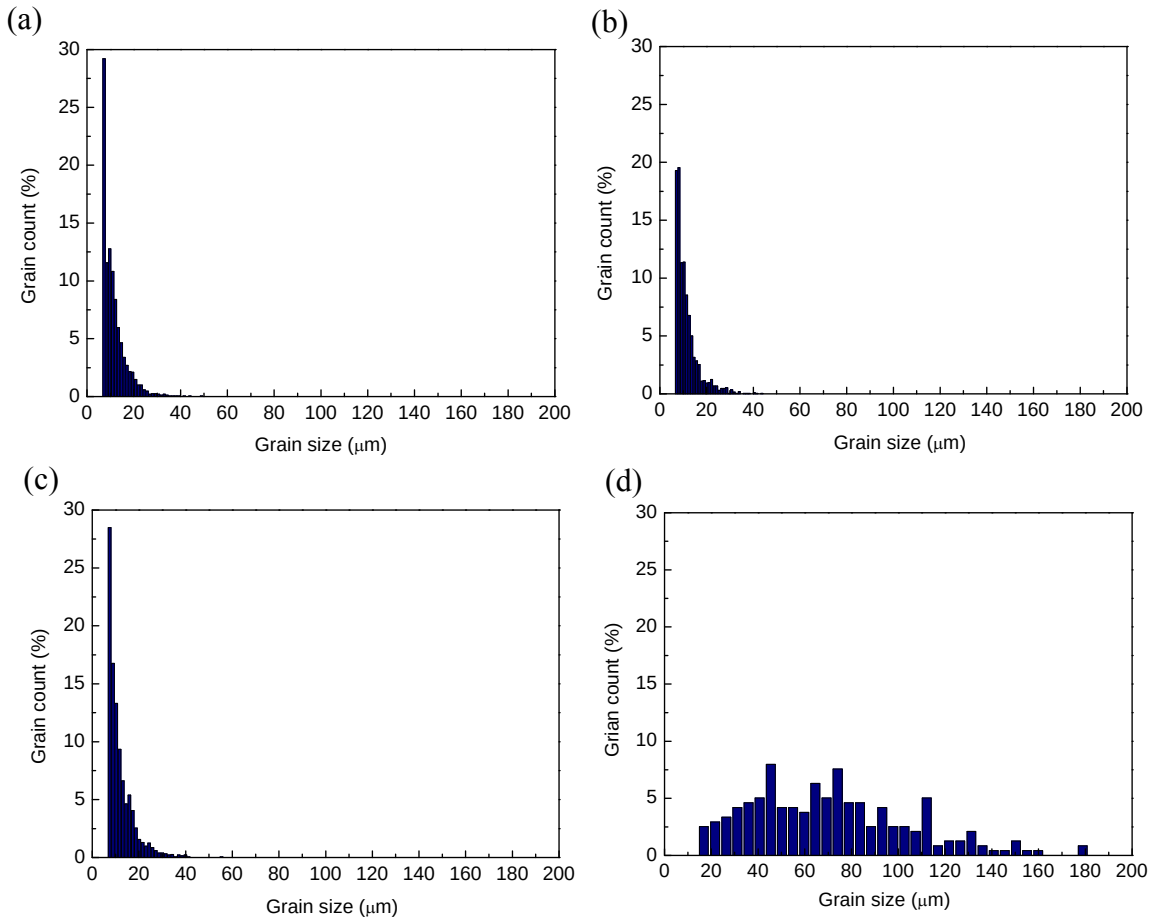

Fig. 5-10 Grain size distribution graphs of gas atomised BuRTi powder samples HIPped at: (a) 900°C, 100MPa, 2h; (b) 900°C, 150MPa, 4h; (c) 950°C, 150MPa, 4h; and of (d) extruded BuRTi samples. These measurements show the finer grain sizes of HIPped samples.

5.1.2 HIPping of PREP BuRTi powder

5.1.2.1 Microstructural examination of original powder

Fig. 5-11 shows SEM secondary electron micrographs of as-received PREP BuRTi powder surfaces, which show different surface morphology from that of gas atomised BuRTi powders with all particles free from satellites. A large number of cross

sections of individual powder particles were examined by SEM and EBSD. As expected the particles were all single phase beta (with some small carbides visible), and both polycrystalline and single crystal particles were observed. Fig. 5-12 shows example of polycrystalline particles (see Figs. 5-12 (a, b)). EBSD grain size distribution map and graph (see Figs. 5-12 (b, c)) show grain sizes in the range 3~54 μm; other samples showed grain sizes up to 80μm. Figs. 5-12 (d, e, f) show the misorientation distribution graph and line profile of misorientation angle *vs.* distance along the line through the powder, and high misorientation angles between the adjacent grains were obtained. Examples of particles which are virtually single crystals of beta are shown in Fig. 5-13. The EBSD grain size distribution map and graph (see Figs. 5-13 (c, d)) show the grain size is same as the powder size, up to 215μm. There is no misorientation angle difference inside the single powder through the examination of EBSD misorientation angle measurement (see Figs. 5-13 (e, f)). The observations on the gas-atomised powder and PREP powder which are polycrystalline show that the average grain size is larger in the PREP powder (see Figs. 5-14 (a, c)). During gas atomisation, powders can solidify quickly owing to heat loss by convection via the argon gas jets. However, the PREP process generally occurs under vacuum or in a low pressure inert gas, which allows more time for powders' solidification and results in coarser grain sizes. The misorientation angles between adjacent grains through both powders were measured and high angle misorientations can be observed predominantly in these powders, as shown in Figs. 5-14 (b, d). Moreover, the overall misorientation distribution of the two powders is similar (see Figs. 5-2 (d), 5-12 (d)).

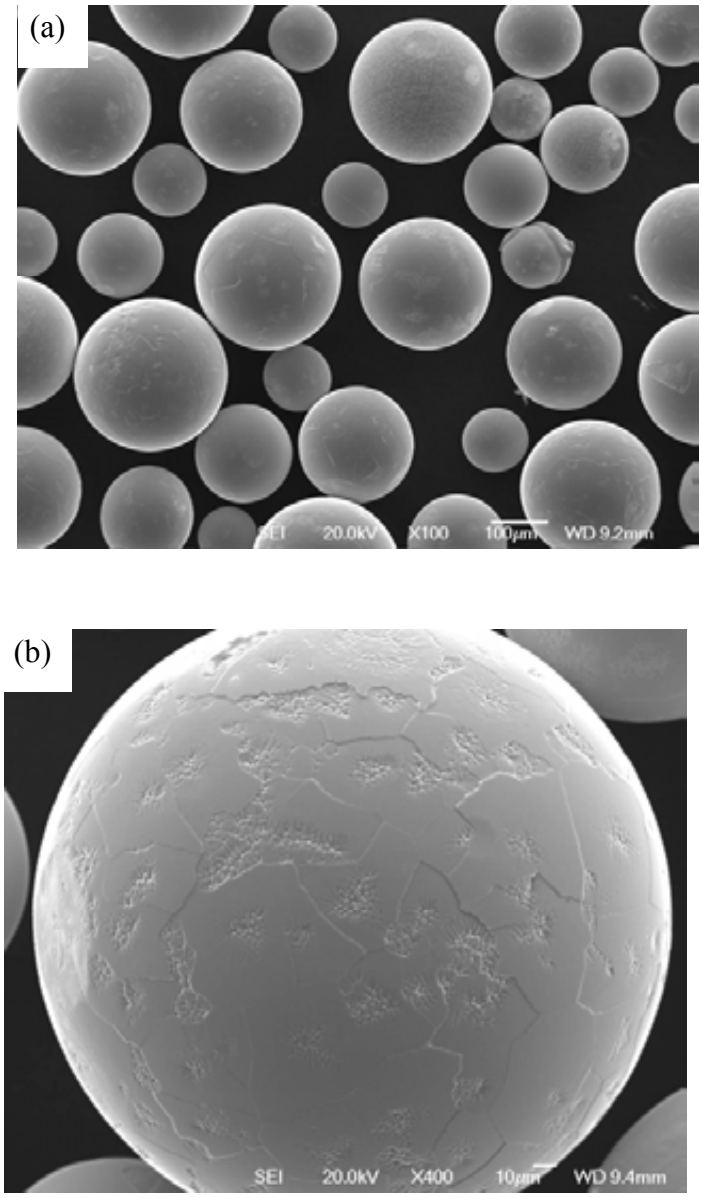

Fig. 5-11 SEM secondary electron micrographs showing the morphology of as-received spherical PREP BuRTi powder surfaces at different magnifications.

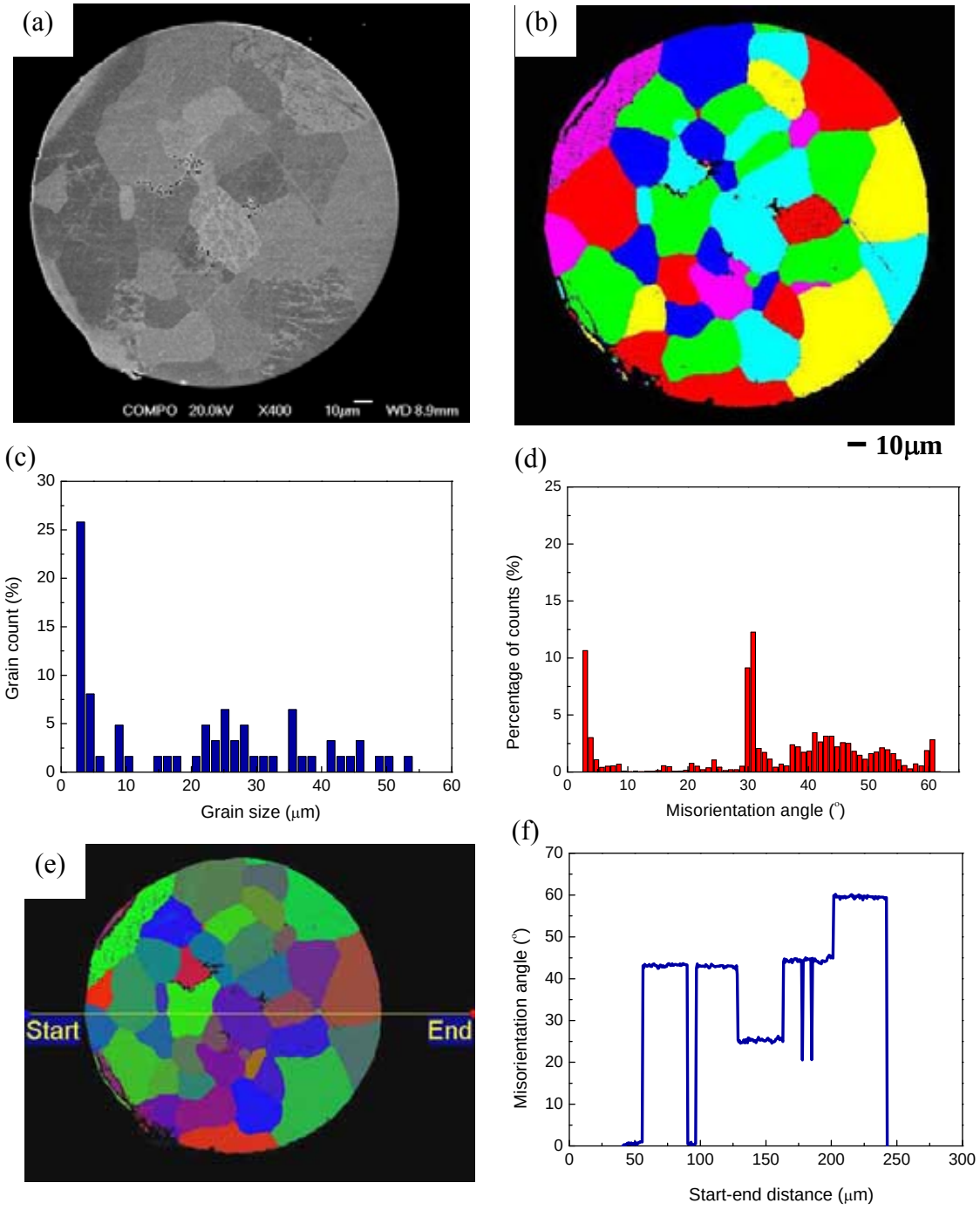

Fig. 5-12 Cross section of an individual PREP BuRTi powder of (a) SEM BSE image showing polycrystalline single phase; (b, c) EBSD grain size map and distribution graph; (d) overall misorientation distribution graph; (e, f) EBSD misorientation map and line profile of misorientation angle vs. distance along the cross line showing high misorientation angles across grain boundaries of adjacent grains.

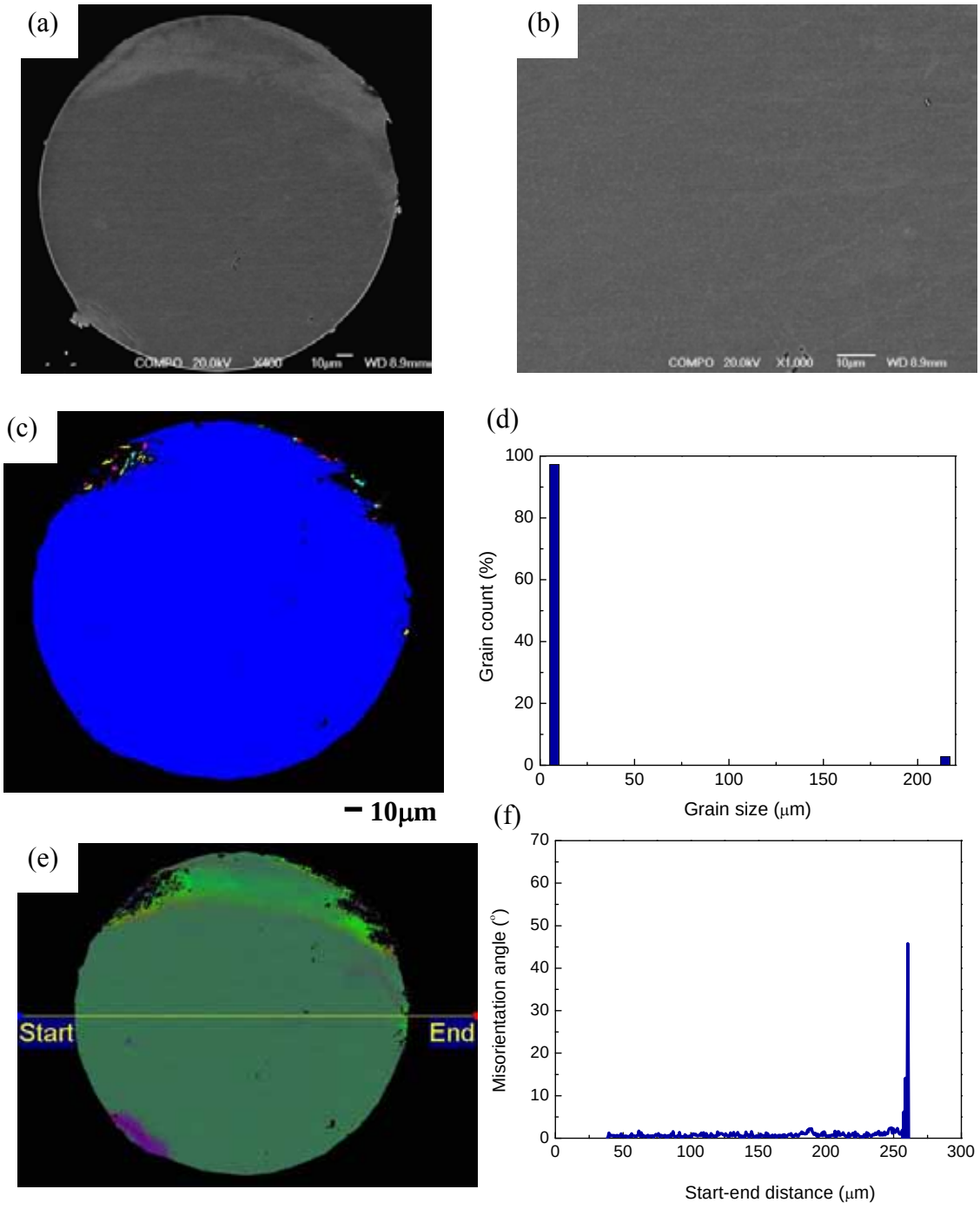

Fig. 5-13 Cross section of an individual PREP BuRTi powder of (a, b) SEM BSE images at different magnifications showing single crystal structure; (c, d) EBSD grain size distribution mapping and graph showing the grain size is same as the powder size, up to 215μm; (e, f) EBSD misorientation mapping and line profile of misorientation angle along the cross line showing no misorientation inside the single powder.

(a)

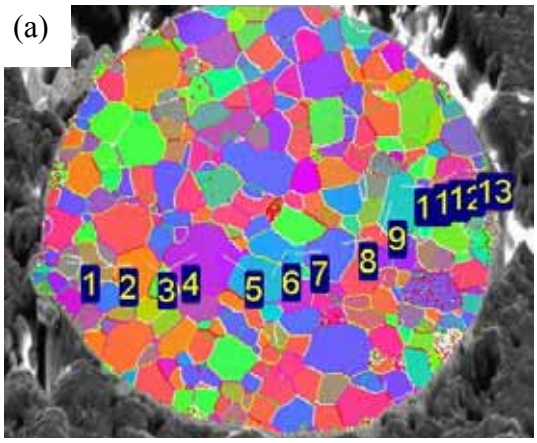

(b)

Line	Angle
1	59.82
2	46.34
3	23.19
4	45.67
5	19.5
6	46.05
7	34.91
8	59.37
9	59.54
10	45.13
11	52.26
12	7.3
13	38.85

(c)

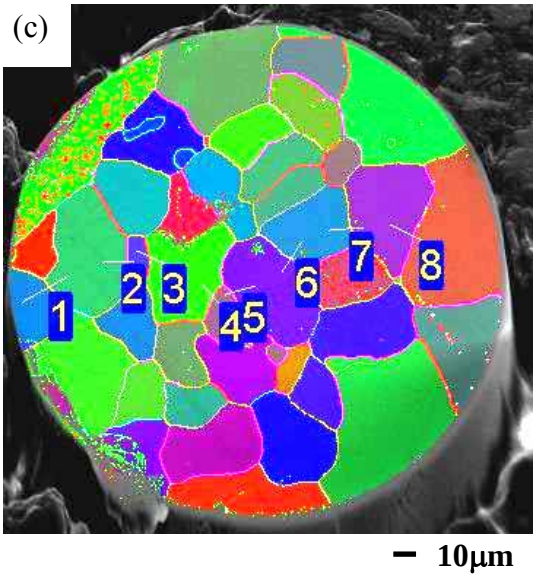

(d)

Line	Angle
1	43.98
2	40.89
3	29.21
4	30.61
5	40.58
6	58.79
7	42.57
8	38.62

Fig. 5-14 (a) EBSD misorientation mapping of gas atomised BuRTi powder; (b) measured gain boundary misorientation angles according to the lines shown in (a); (c) EBSD misorientation mapping of PREP BuRTi powder; (d) measured grain boundary misorientation angles according to the lines shown in c. Larger grains can be observed in the PREP sample, and high misorientation angles between adjacent grains are shown in both powders.

5.1.2.2 Effect of HIPping parameters (temperature, pressure, holding time) on microstructure

The as-received PREP powder (50~400μm) was HIPped by simultaneously ramping up to the HIPping temperature and pressure, holding the selected HIPping conditions for a defined time, and slowly cooling down whilst reducing the pressure and temperature in phase. Samples were HIPped under a series of conditions to assess the effect of the variables, temperature, pressure and time on the as-HIPped microstructures. The conditions used were: (i) 850^{o}C, 100MPa, 2h; (ii) 900^{o}C, 100MPa, 2h; (iii) 900^{o}C, 100MPa, 4h; (iv) 950^{o}C, 150MPa, 2h and (v) 1000^{o}C, 100MPa, 2h. Figs. 5-15 (a-j) show optical micrographs of these samples. As found with gas atomised powders the original particle boundaries can be recognised in the HIPped samples, but in this case most of the prior particles are now clearly polygonal rather than spherical. Some single crystal particles can be seen and as with the polycrystalline particles they are straight-sided polygons. EBSD analyses were carried out on samples for two of the HIPping conditions, (iii) and (iv). SEM BSE images, matching EBSD misorientation maps and misorientation distribution graphs of the samples are shown in Figs. 5-16 (a-f). The large ranges of grain sizes (12~197μm for (iii), 8~176μm for (iv)) can be observed from the grain size distribution graphs (see Figs. 5-16 (g, h)).

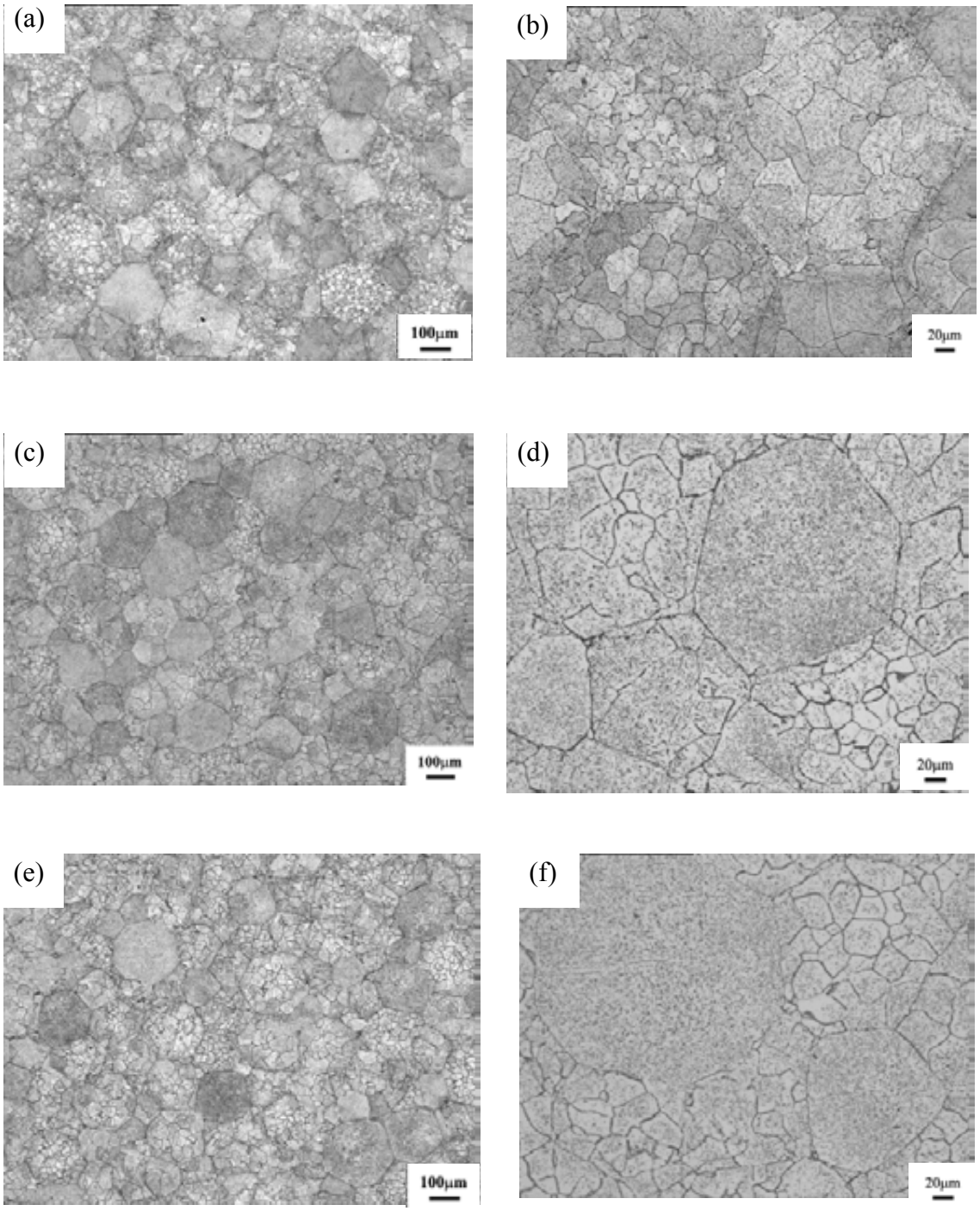
(a)
100μm
(b)
20μm
(c)
100μm
(d)
20μm
(e)
100μm
(f)
20μm

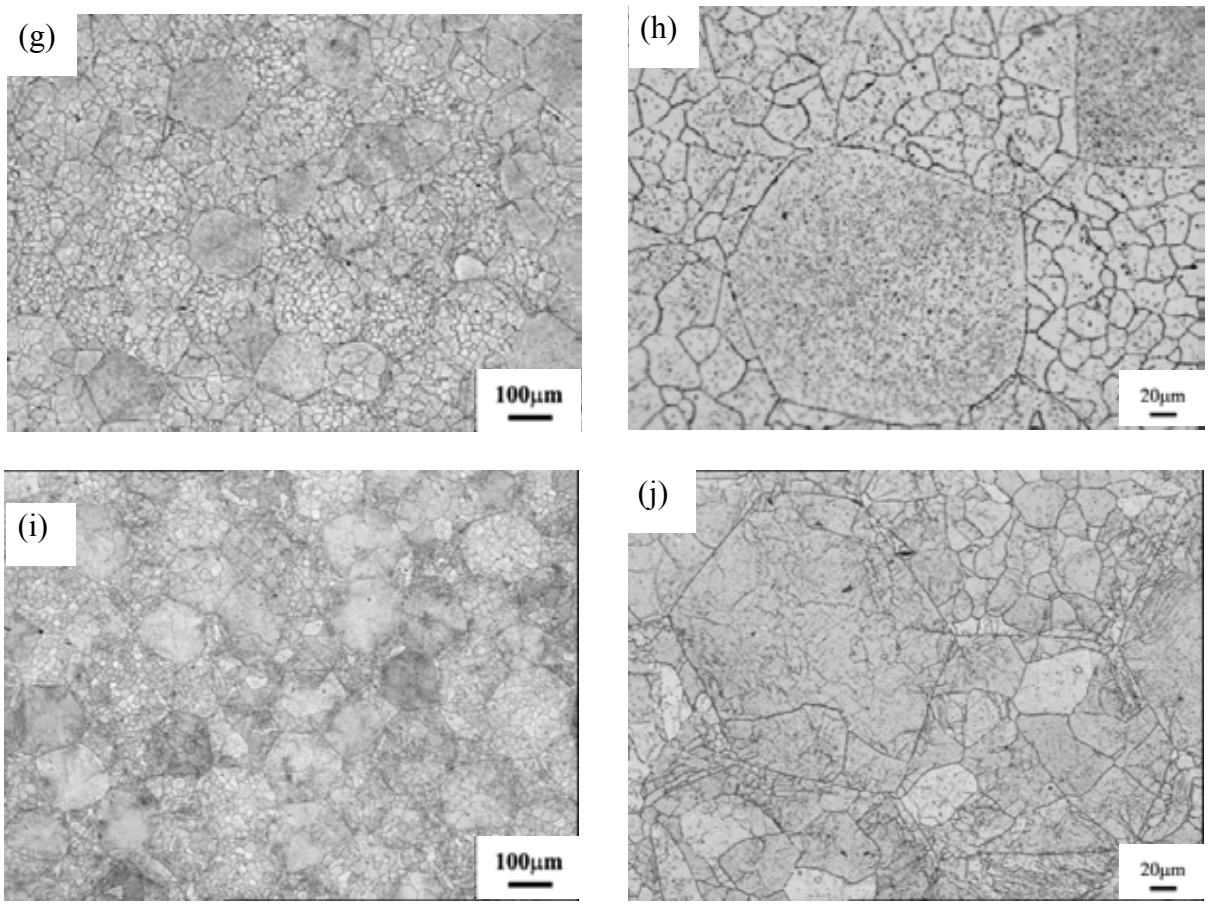

Fig. 5-15 Optical images at different magnifications of PREP BuRTi powder samples HIPped at: (a, b) 850^{o}C, 100MPa, 2h; (c, d) 900^{o}C, 100MPa, 2h; (e, f) 900^{o}C, 100MPa, 4h; (g, h) 950^{o}C, 150MPa, 2h; (i, j) 1000^{o}C, 100MPa, 2h showing a high proportion of large grains up to the individual particle size in the as-HIPped samples under different conditions.

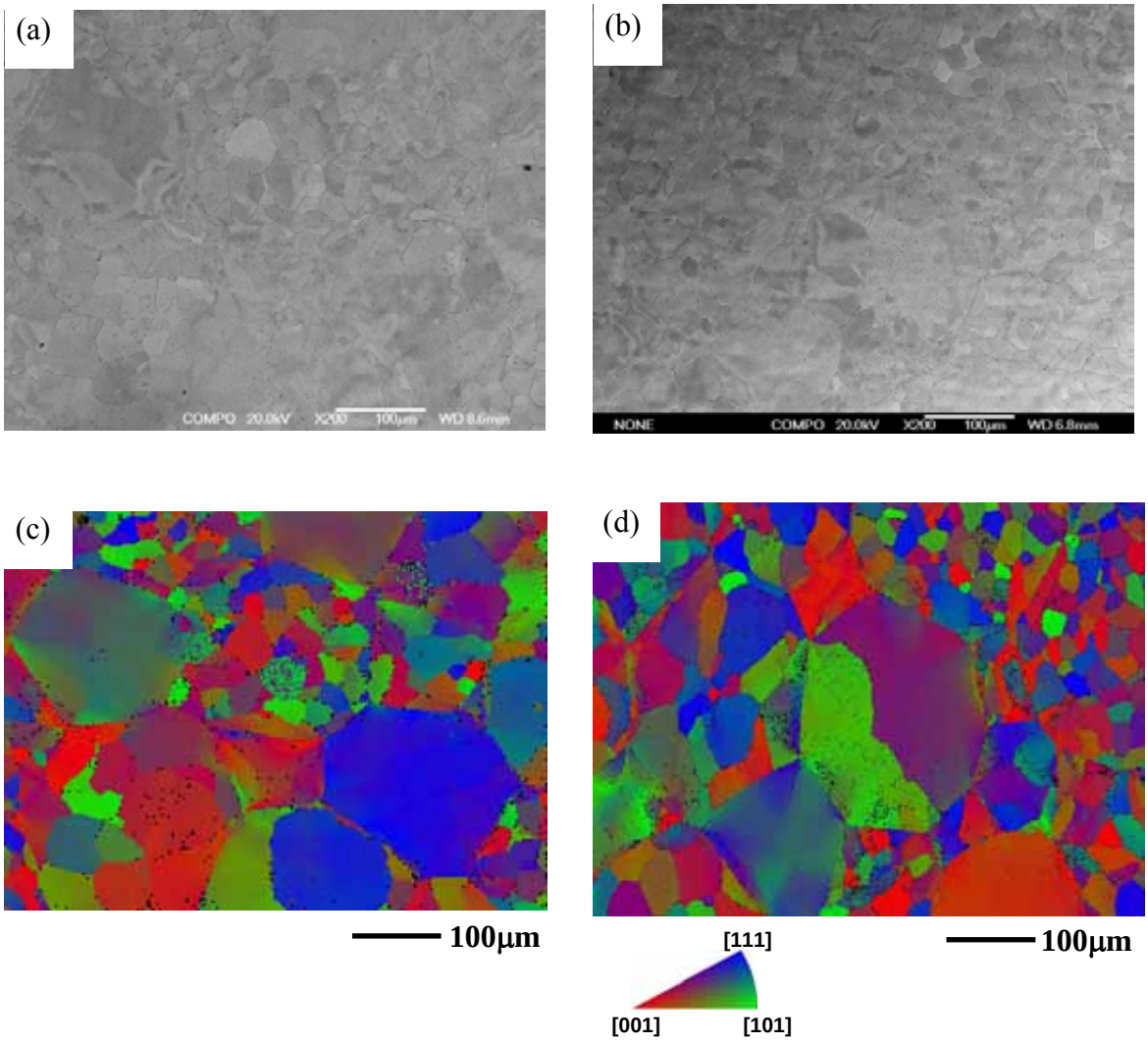
(a)
(b)
(c)
(d)
100μm
100μm
[111]
[001]
[101]
(e)
(f)
Percentage of counts (%)
Misorientation angle (°)
Percentage of counts (%)
Misorientation angle (°)

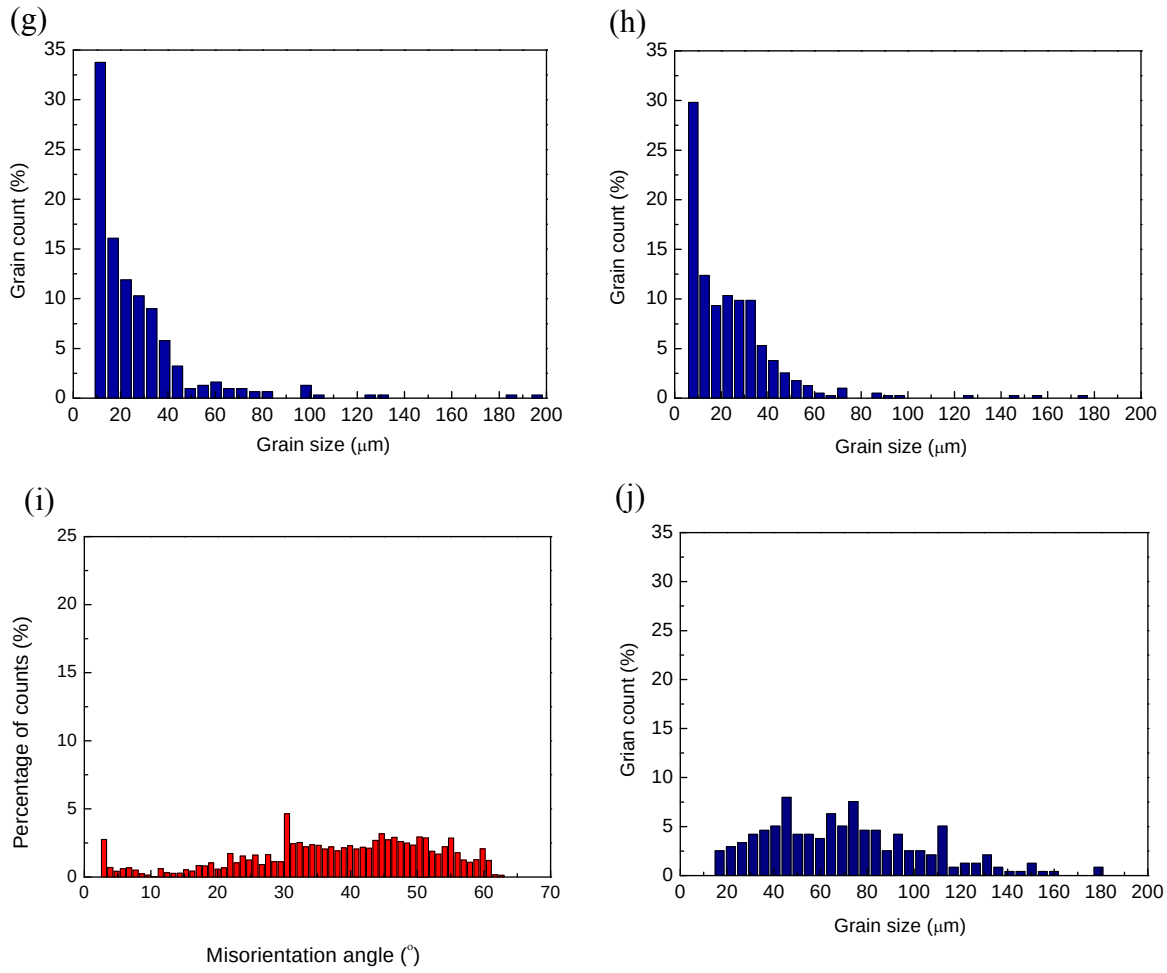

Fig. 5-16 Microstructure and EBSD analysis results of PREP BuRTi powder samples HIPped at (a, c, e, g) 900°C, 100MPa, 2h; (b, d, f, h) 950°C, 150MPa, 2h. Figs. (a, b) are SEM BSE images; Figs. (c, d) are matching EBSD misorientation maps; Figs. (e, f) are misorientation distribution graphs showing similar value; Figs. (g, h) are grain size distribution graphs showing the large ranges of grain sizes. Figs. (i, j) are misorientation distribution and grain size distribution graphs of extruded BuRTi samples showing misorientation and grain size distribution with no obvious peak.

Fig. 5-17 shows EDX spectra of different regions of the sample HIPped at 950°C. The EDX spectrum from single crystal large grain (spectrum 1) is shown in Fig. 5-17 (b); the EDX spectrum from polycrystalline fine grain (spectrum 2) is shown in Fig. 5-17 (c). No obvious difference in chemical compositions can be detected for the particles of such different grain sizes.

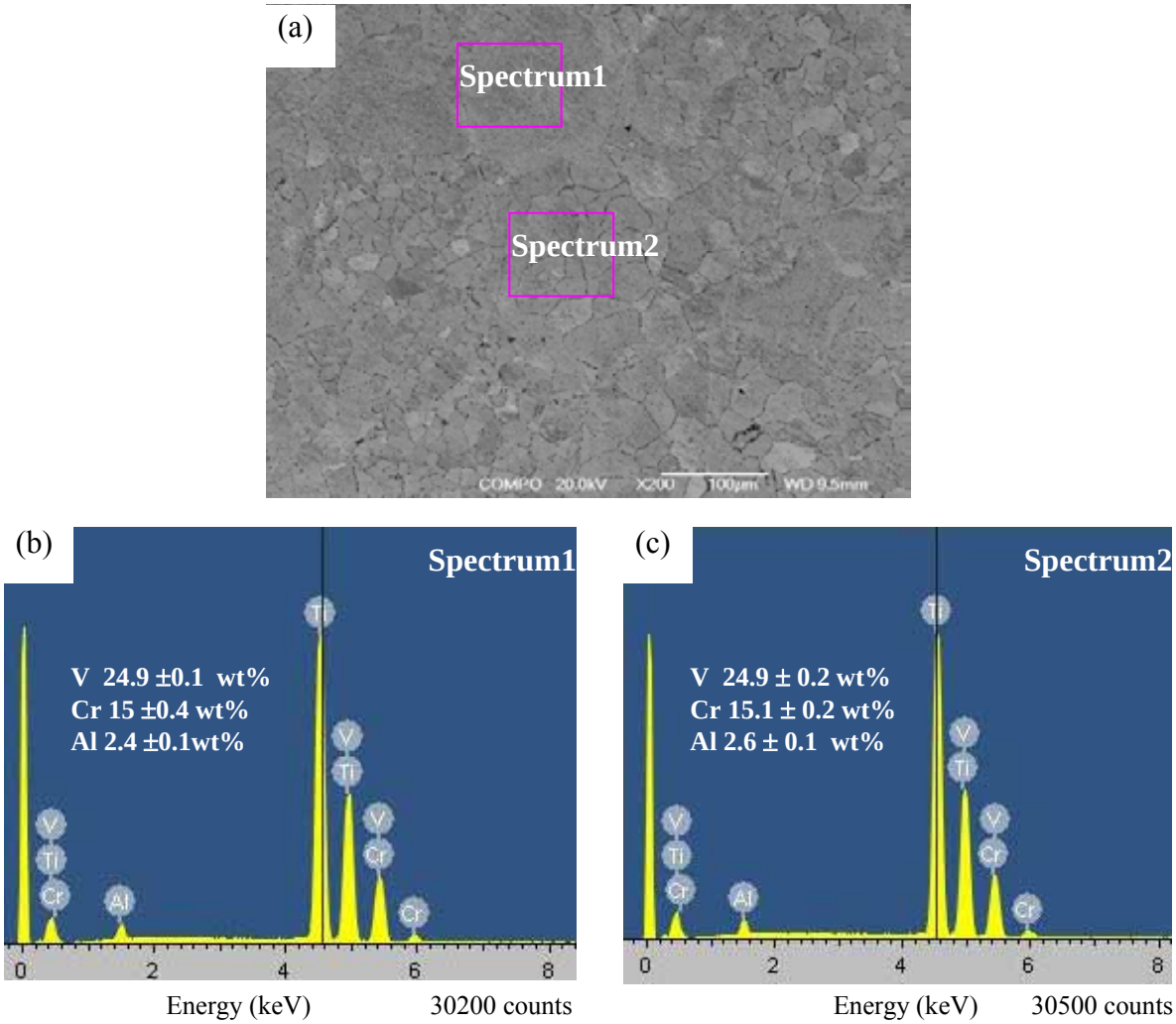

Fig. 5-17 EDX spectra of PREP BuRTi powder samples HIPped at 950°C, 150MPa, 2h: (a) SEM BSE image indicating two analysed regions; (b) EDX spectrum from single crystal large grain (spectrum 1); (c)EDX spectrum from polycrystal fine grain (spectrum 2). No obvious difference in chemical compositions can be detected for different regions.

5.1.3 Heat treatment of HIPped BuRTi samples

Heat treatment experiments were carried out for both gas atomised and PREP HIPped samples in order to assess the microstructural stability of the HIPped samples. Table 5-1 shows the chemical analysis results for gas atomised and PREP as-HIPped samples (HIPped at 900^{o}C, 100MPa, 4h), which are very similar although the PREP samples have higher oxygen contents than the gas atomised samples.

Table 5-1 Chemical analyses of HIPped BuRTi samples made using different powder production methods (unit: wt%)

	C	O	Al	Cr	V	Ti
Gas atomised	0.18	0.077	2.02	15.2	25.4	balance
PREP	0.16	0.15	2.08	15.7	26.6	balance

HIPped samples were heated up to 1050^{o}C and kept at this temperature for 24h, then slowly cooled in the furnace (FC). Optical images of these samples are shown in Fig. 5-18, and SEM BSE images and EBSD results are shown in Fig. 5-19. The maximum grain size for a gas atomised heat treated sample increased to 295 μm, and the carbides also grew so that they are now obvious (see Figs. 5-19 (a, b)). The microstructure and EBSD analyses of a heat treated PREP sample are similar to those of the gas atomised BuRTi sample although the average grain size is larger, up to 330μm (see Figs. 5-19 (d, f)).

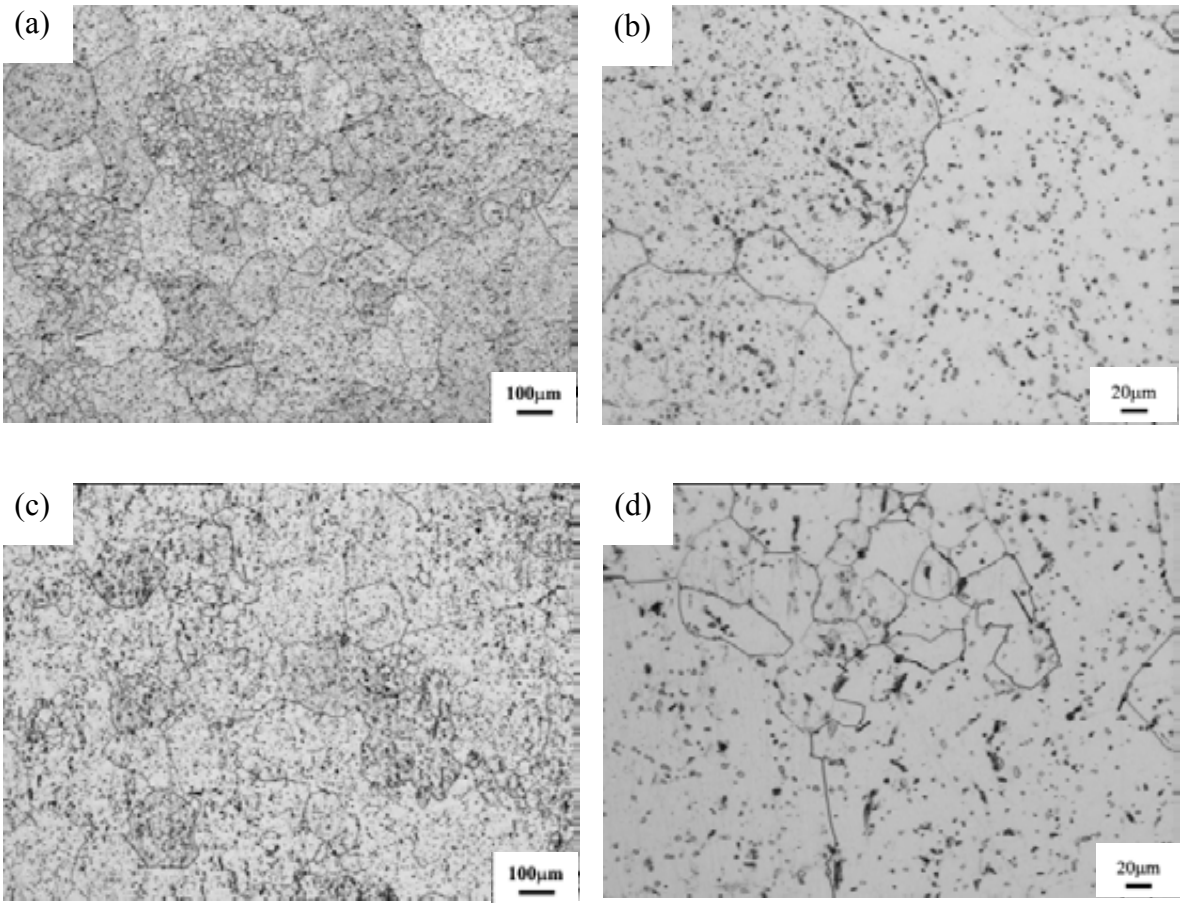

Fig. 5-18 Optical images at different magnifications of samples made using: (a, b) gas atomised BuRTi powder; (c, d) PREP BuRTi powder, and HIPped at 900^{o}C, 100MPa, 4h and heat treated at 1050^{o}C, 24h, furnace cooling (FC) showing coarsened microstructures and grown carbides.

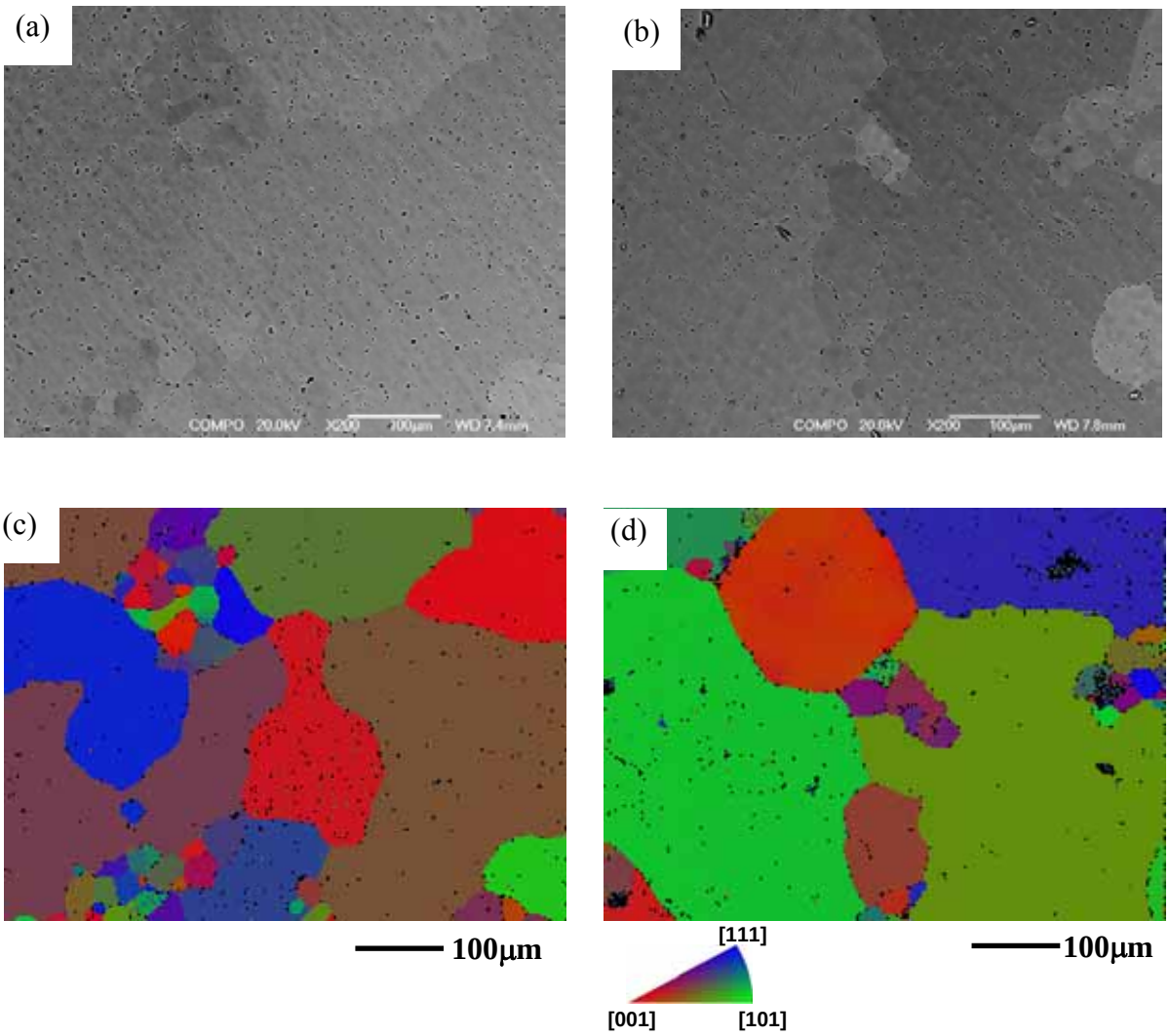
(a)
(b)
(c)
(d)
100μm
100μm
[111]
[001]
[101]
(e)
(f)
Percentage of counts (%)
Misorientation angle (°)
Percentage of counts (%)
Misorientation angle (°)

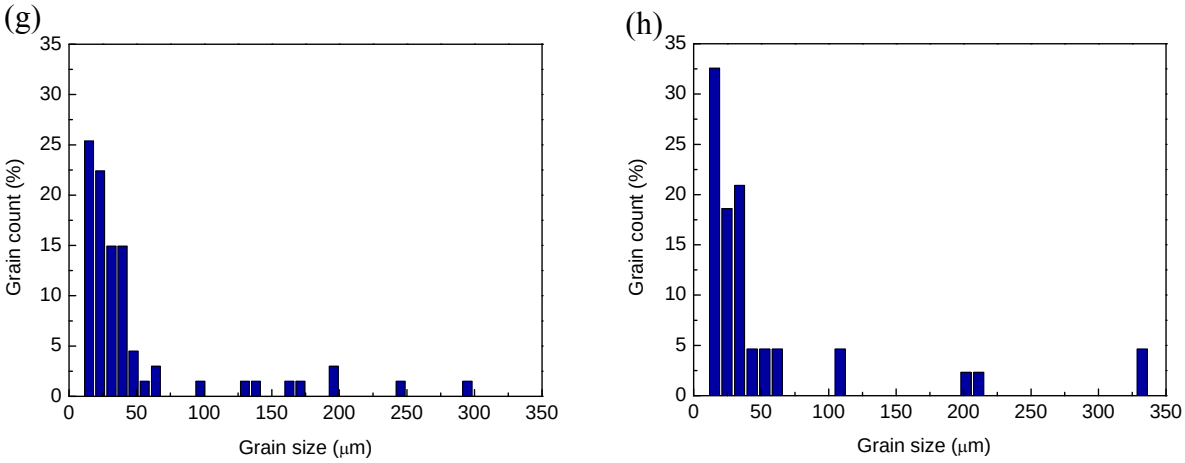

Fig. 5-19 Microstructure and EBSD analysis results of (a, c, e, g) gas atomised BuRTi powder sample; (b, d, f, h) PREP BuRTi powder sample HIPped at 900°C, 100MPa, 4h and heat treated at 1050°C, 24h, furnace cooling (FC). Figs. (a, b) are SEM BSE images; Figs. (c, d) are matching EBSD misorientation maps; Figs. (e, f) are misorientation distribution graphs; Figs. (g, h) are grain size distribution graphs showing coarsened grain sizes.

Tomographic[1] observations of the level of porosity in as-HIPped and in HIPped heat treated gas atomised samples were carried out. The results are shown in Fig. 5-20. Very few pores can be detected in the as-HIPped samples (see Figs. 5-20 (a)) even after heat treatments no significant number of pores can be seen in the gas atomised sample which contains about 0.025vol % porosity as can be seen in Fig. 5-20 (b).

[1] These observations were made by Dr M Preuss using the synchrotron at ESRF.

(a)

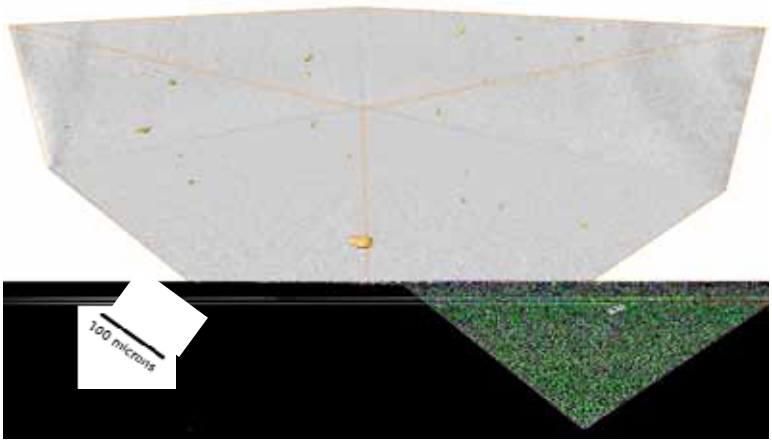

(b)

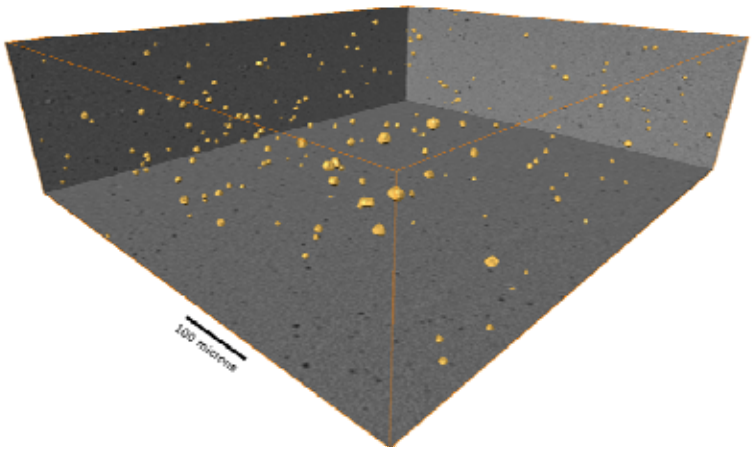

Fig.5-20 Tomographic observation of the porosity in: (a) as-HIPped gas atomised powder sample at 900°C, 100MPa, 4h; (b) gas atomised BuRTi powder HIPped at 900°C, 100MPa, 4h and heat treated at 1050°C, 24h, FC. Very little porosity can be detected in both samples, and 0.025 vol % fraction porosity can be seen in heat treated ones.

5.1.4 Tensile properties and examination of fracture surfaces in samples tested to failure

5.1.4.1 Tensile properties

A summary of tensile properties for different BuRTi samples is given in Table 5-2 and it is clear from this data that overall the as-HIPped powder samples were generally stronger than the extruded samples but they showed either a large scatter in ductility or very low values of ductility down to below 10%. The ductilities of the extruded samples were all about 20% or higher. There was no systematic difference between the samples that were made from gas atomised powder and those made from PREP powder, although the gas-atomised had a slightly lower yield and UTS than the PREP samples HIPped using the same conditions. The HIPped gas atomised sample that was heat treated showed the lowest strength and also showed low ductility.

Table 5-2 Summary of the tensile properties of extruded BuRTi and powder HIPped BuRTi with different conditions

	YS (MPa)	UTS (MPa)	Ductility (%)
Extruded BuRTi	924±13	964±9	26/19/27
Gas atomised BuRTi HIPped at 900°C,100MPa,2h	945±6	1008±5	25/12/10
Gas atomised BuRTi HIPped at 900°C,100MPa,4h	935±11	1013±19	20/11/9
Gas atomised BuRTi HIPped at 900°C,150MPa,4h	970±2	1041±12	23/13/8
Gas atomised BuRTi HIPped at 950°C,150MPa,4h	974±9	1035±8	19/9/8
PREP BuRTi HIPped at 900°C,100MPa,2h	972±7	1040±5	25/24/18
PREP BuRTi HIPped at 900°C,100MPa,4h	996±3	1044±5	9/8/7
PREP BuRTi HIPped at 950°C,150MPa,2h	997±1	1057±13	25//17/15
Gas atomised BuRTi HIPped at 900°C,100MPa,4h + heat treated at1050°C,24h,FC	868±16	902±12	11/12/8

5.1.4.2 Examination of fracture surfaces

The fracture surfaces of the samples which were failed in tension to generate the data shown in Table 5-2 were examined in order to understand the scatter in ductility which characterised the powder HIPped samples. Crack initiations sites were found in all specimens and these are associated with circular regions containing transgranular facets as shown in Fig. 5-21 for gas atomised samples. Similar observations made on PREP samples are shown in Figs. 5-22 (a-d). In addition the PREP samples showed large single facets of about 100μm edge length in regions of

the fracture surfaces (Figs. 5-22 (e, f)). Measurements showed that the lower the ductility, the larger are the circular regions and these data are shown in Table 5-3.

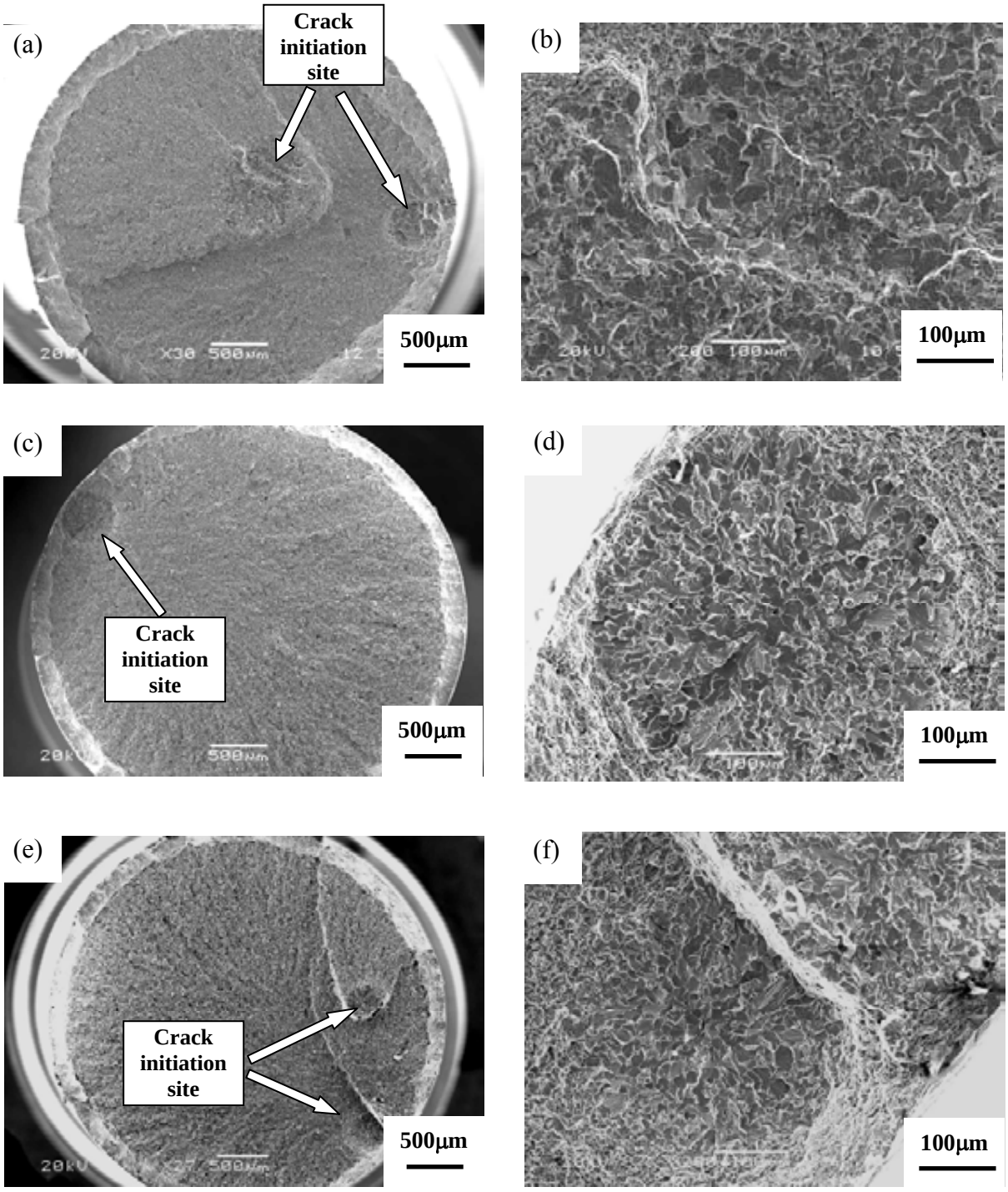

Fig. 5-21 SEM SE images at different magnifications of fracture surfaces in tensile failed gas atomised BuRTi powder samples HIPped at (a, b) 900°C, 100MPa, 2h; (c, d) 900°C, 150MPa, 4h; and (e, f) 950°C, 150MPa, 4h. Large circular regions formed by facets can be seen as the crack initiation sites.

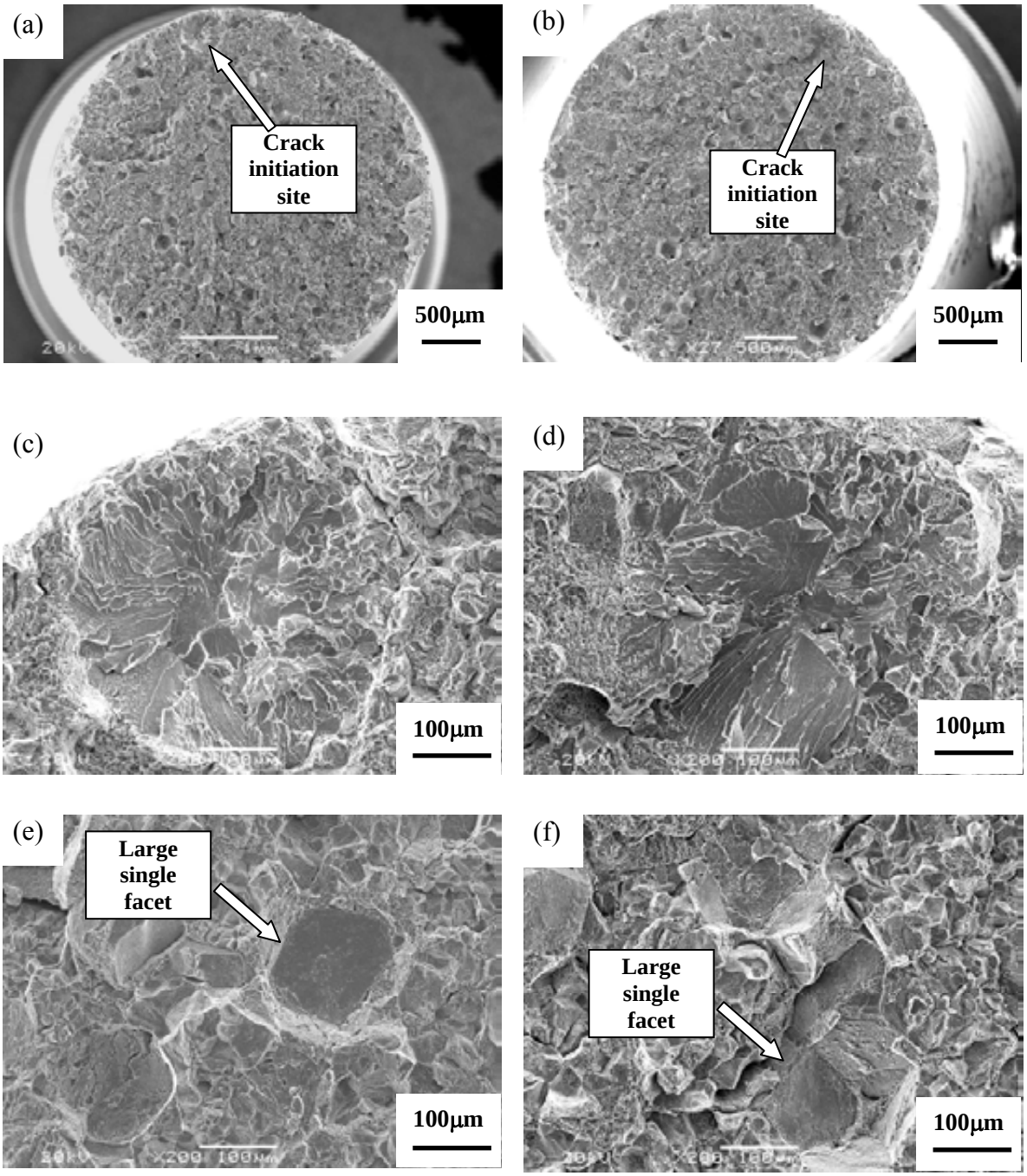

Fig. 5-22 SEM SE images at different magnifications of fracture surfaces in tensile failed PREP BuRTi powder samples HIPped at (a, c, e) 900°C, 100MPa, 2h; (b, d, f) 950°C, 150MPa, 2h. Large circular regions formed by facets can be seen as the crack initiation sites (a, b, c, d). Large single facets about 100μm edge length were also observed on fracture surfaces (e, f).

Table 5-3 Measurements of dimensions of circular regions at crack initiation sites of tensile failed HIPped samples with matching ductility

	Ductility of HIPped samples (%)	Diameter of circular regions at crack initiation sites (μm)
Samples HIPped using gas atomised BuRTi powder	11	450
	19	200
	23	100
Samples HIPped using PREP BuRTi powder	9	400
	18	300
	26	—

Crack initiation sites in extruded samples showed smaller single facets and similar features were observed elsewhere on the fracture surface, as shown in Figs. 5-23 (a, b). The crack initiation sites in the heat treated gas atomised sample showed large facets up to 0.5mm edge length (see Figs. 5-23 (c, d)) associated with the coarsened microstructure.

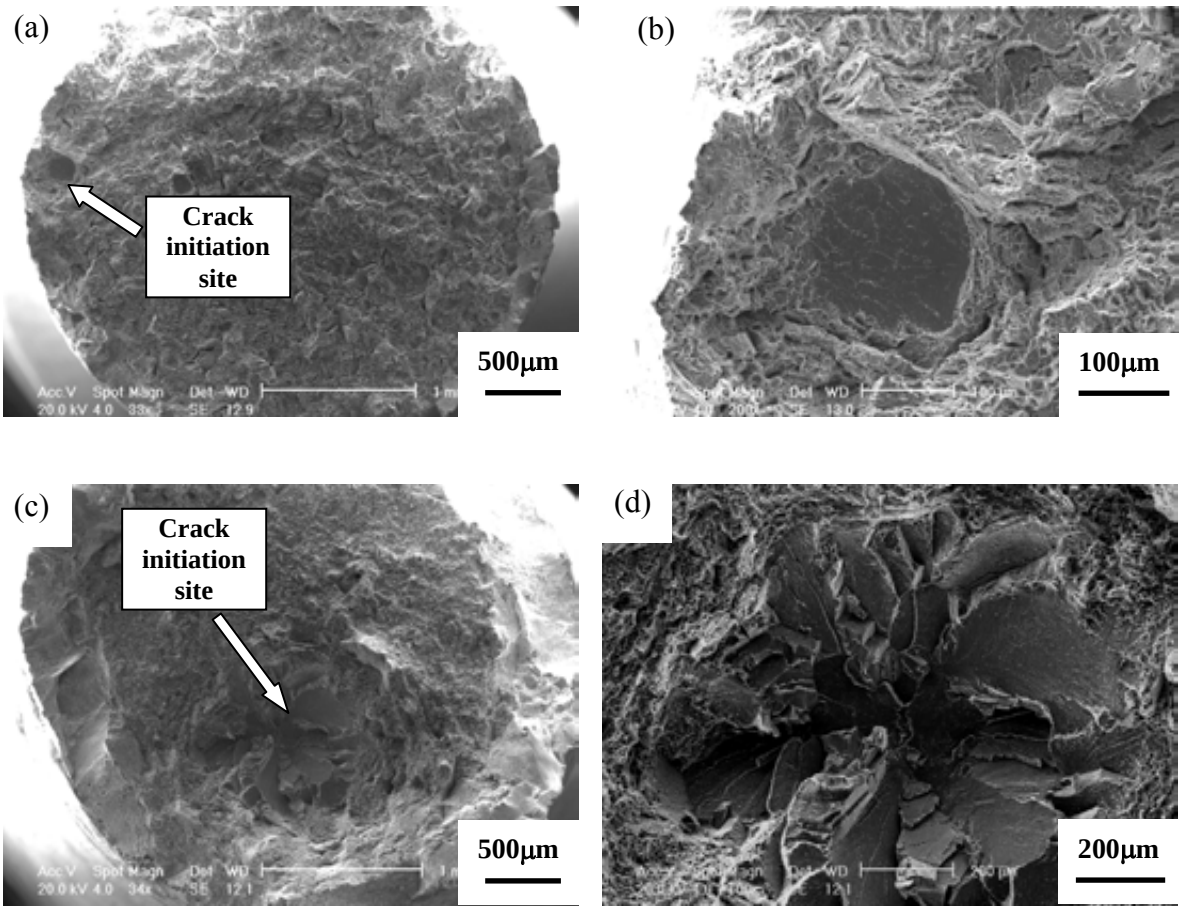

Fig. 5-23 SEM secondary electron images of tensile fracture surfaces in (a, b) extruded BuRTi samples; (c, d) heat treated as-HIPped gas atomised BuRTi powder sample at different magnifications. Crystallographic facets can be seen as the crack initiation sites.

Attempts were made to index the facet surfaces using EBSD observations but the surface were too rough to allow the facets to be observed when the samples were tilted to the required angle of 70° when using EBSD. Some crack initiation sites were therefore sectioned and the misorientations of the grains determined on these sections. Typical results obtained from this approach are shown in Fig. 5-24, but a cross section

may not contain the fracture initiation site and thus no unambiguous information could be obtained using this approach.

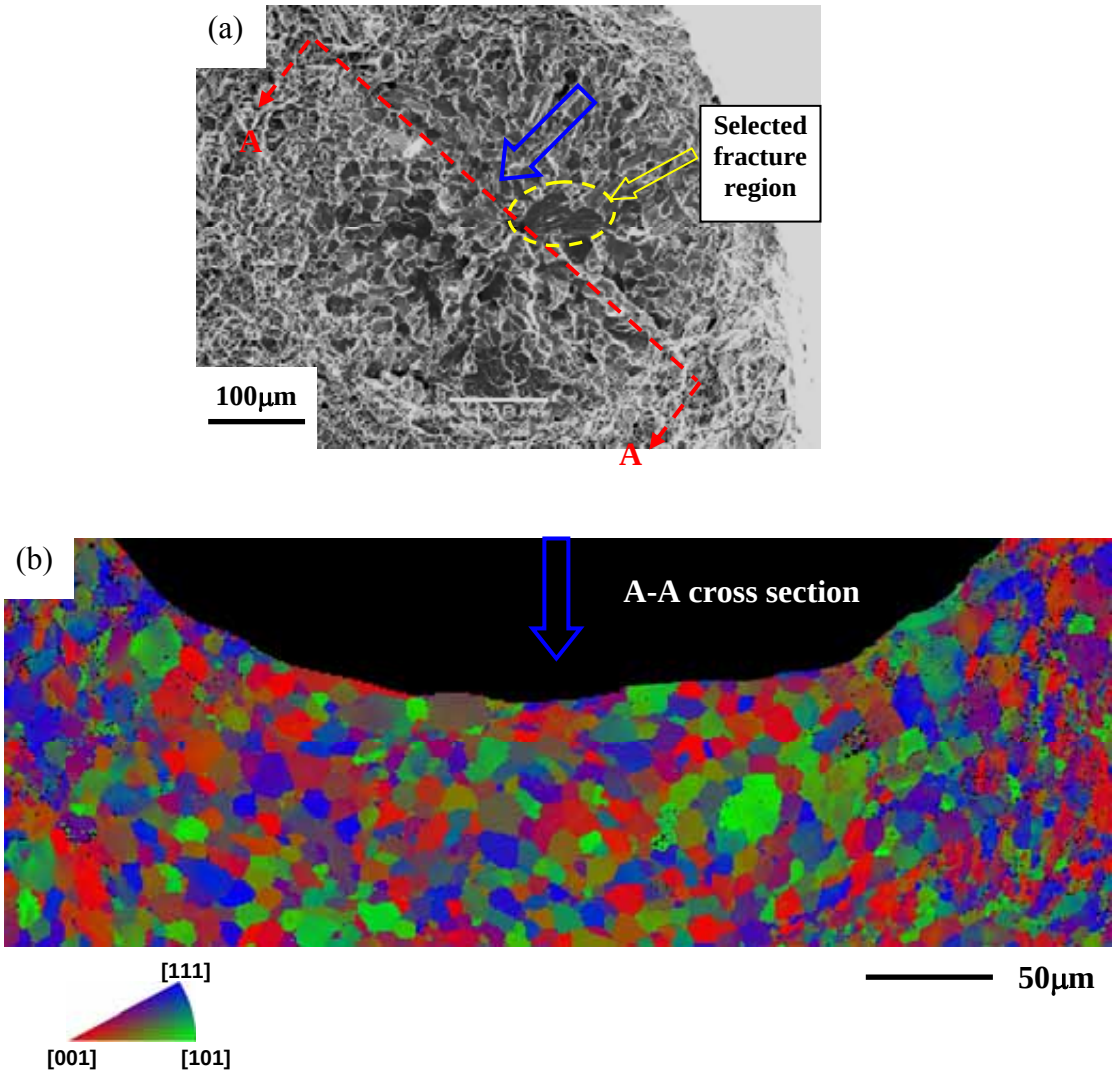

5-24 EBSD analyses of cross section of large circular region in tensile failed as-HIPped gas atomised powder sample with an elongation of 9%: (a) SEM SE image of crack initiation site; (b) EBSD misorientation mapping of A-A cross section showing different crystallographic orientations among the grains on the section.

A second approach has been used[2] in which stereo microscopy is used to define two or more true directions on the fracture site and these are used to determine the fracture plane with respect to the crystal axis and the direction of the applied tensile stress. The observations made are summarised in the pole figures in Fig. 5-25 where the selected fracture region (as shown in Fig. 5-24) was examined for crystallographic orientation determination and the tensile axis is <001>. It is found that the fracture planes in grains 1 and 2 of facet 1 have common {001}, but the pole figures of facets 2 and 3 show different fracture planes, near {101} and {112} respectively.

The origin and significance of these circular regions which appear to lead to failure will be discussed briefly in section 5.1 and in more detail in Chapter 6 since similar observations are reported in section 5.2.2.

[2] This work was done at Ohio State University by J. C. Williams.

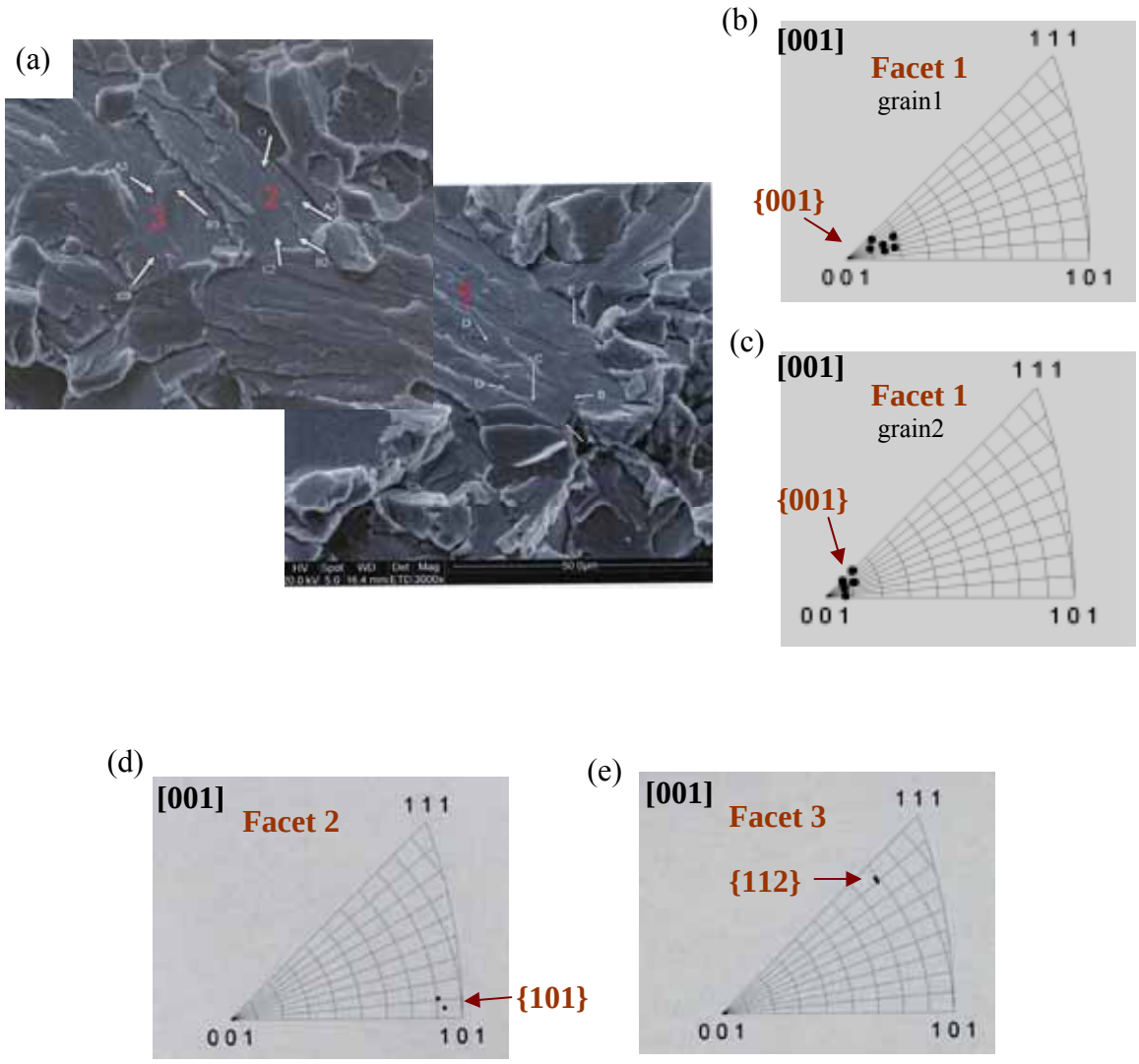

Fig.5-25 Crystallographic orientation determination of a selected fracture region shown in Fig.5-24 and the tensile axis is <001>: (a) SEM SE image of the three facets; (b, c) pole figures of two grains in facet 1 showing they are along the common {001} crystal planes; (d) pole figure of facet 2 showing it is close to the {101} crystal plane; (e) pole figure of facet 3 showing it is close to the {112} crystal plane. The normal of three facets is 16°, 24° and 22° from load axis, respectively.

5.1.5 Fatigue properties and observations of fracture surfaces of fatigued samples

4-point bending fatigue tests were carried out to assess the fatigue properties of as-HIPped gas atomised and PREP powder BuRTi samples. Three sets of samples were chosen to be tested. Fig. 5-26 shows the SN curves for HIPped samples which were machined from HIPped bars and had as-machined surfaces. The gas atomised powder samples HIPped at 900^{o}C, 100MPa, 2h had the highest endurance limit (i.e. a life greater than 10^7 cycles) of 550 MPa. The PREP power samples HIPped at 900^{o}C, 100MPa, 2h had a lower endurance limit of ~400 MPa. The fatigue properties of the PREP power samples HIPped at 950^{o}C, 150MPa, 2h are unexpectedly poor, which failed after between 10^4 and 10^5 cycles at the stress of 400MPa.

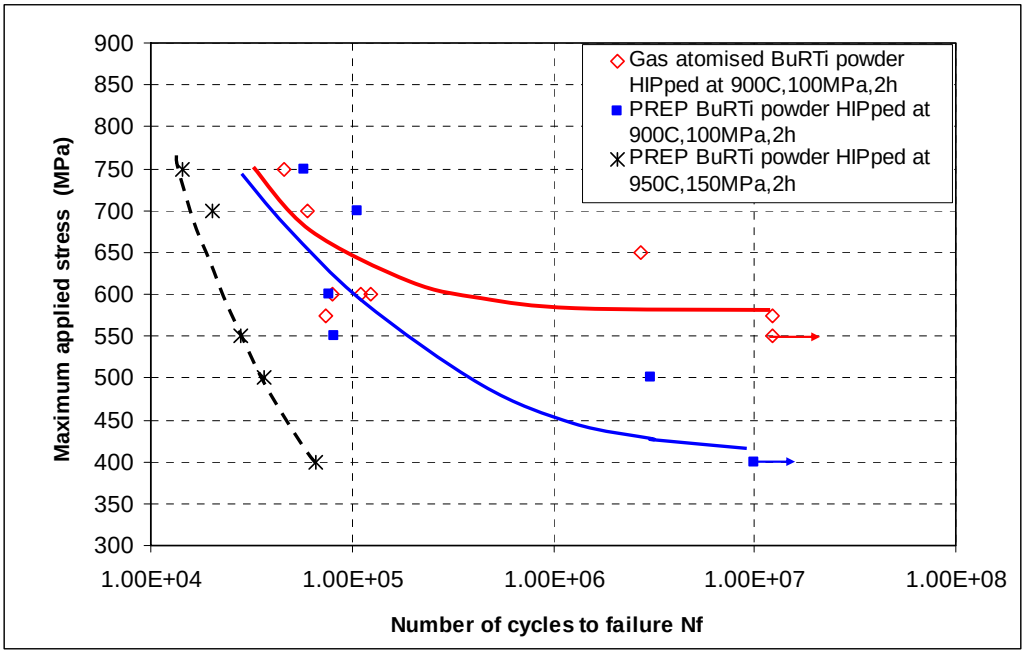

Fig. 5-26 SN fatigue curves for as-HIPped gas atomised and PREP powder BuRTi samples with as-machined surfaces showing highest endurance limit of as-HIPped gas atomised powder samples and poor fatigue properties of PREP powder samples HIPped at 950^{o}C, 150MPa, 2h.

Fig. 5-27 shows fracture surfaces of samples of as-HIPped gas atomised and PREP powder failed in fatigue at the stress levels indicated. Transgranular facets were observed as the crack initiation sites for both samples but the facets in as-HIPped PREP powder samples, which are about 100μm in edge length are notably larger than those in as-HIPped gas atomised powder sample, which are typically below 20μm edge length. EDX analyses were carried out for fracture surfaces of fatigue failed as-HIPped gas atomised samples with short lives, and the result for the sample which was fatigued at a stress level of 600MPa failed after 80500 cycles is shown in Fig. 5-28. A slightly lower Cr content was obtained from the crack initiation site, which

might be associated with the large grains tested in original particles. Further examination for the fracture surface will be needed since EDX results on rough fracture surfaces are inevitably inaccurate, which may account for the low Al analyses in the coarse grained regions, as shown in Fig. 5-28 (b).

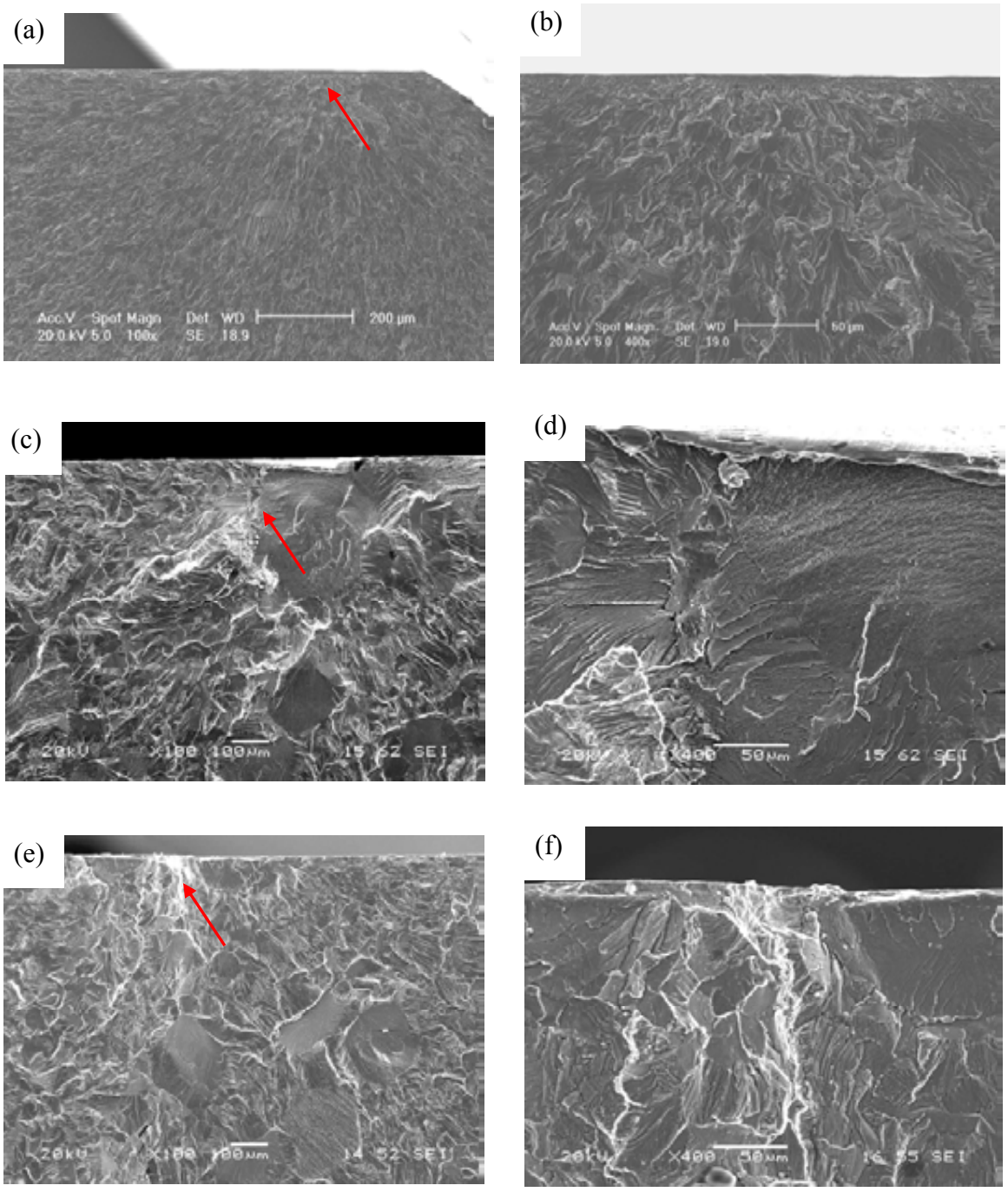

Fig. 5-27 SEM SE images of fracture surfaces in fatigue failed (a, b) gas atomised power sample HIPped at 900°C, 100MPa, 2h (stress=600MPa, cycles=124900); (c, d) PREP power sample HIPped at 900°C, 100MPa, 2h (stress=500MPa, cycles=3052700); (e, f) PREP power samples HIPped at 950°C, 150MPa, 2h (stress=500MPa, cycles=36600). Large single facets were observed in the fracture surfaces of as-HIPped PREP samples. Crack initiation sites are indicated by arrows.

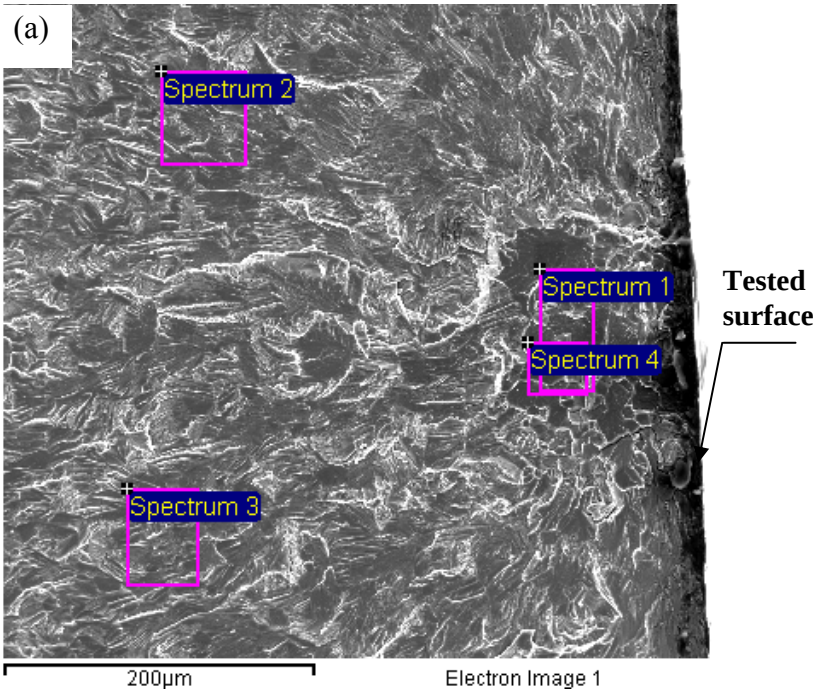

(b)

Spectrum	V	Cr	Al	Ti
Spectrum 1 (crack initiation site)	24.7 ± 0.2	13.5 ± 0.1	1.7± 0.1	Bal.
Spectrum 2 (other area)	24.4 ± 0.2	14.3 ± 0.3	1.9± 0.1	Bal.
Spectrum 3 (other area)	24.6 ± 0.1	14.4 ± 0.1	2.0± 0.1	Bal.
Spectrum 4 (crack initiation site)	24.6 ± 0.3	13.8 ± 0.1	1.8± 0.1	Bal.

Fig. 5-28 EDX analyses of fracture surface in fatigue failed as-HIPped gas atomised BuRTi powder sample (maximum stress=600MPa / number of cycles=80500): (a) SEM SE image indicating analysed areas; (b) EDX results showing that crack initiation sites have slightly lower Cr contents than those of other areas.

5.1.6 Discussion

Before discussing the observations made on gas atomised and PREP powder samples the important observations which will be discussed are listed below.

(i) In the as-HIPped samples, facetted prior particle boundaries are visible in samples made from both powders but the individual powders facet more obviously in HIPped PREP powder.

(ii) The tensile strengths of gas atomised samples are less than those of similarly HIPped PREP samples and the scatter in ductility is similar.

(iii) The fatigue properties of the PREP samples are much lower whereas the fatigue properties of the gas atomised samples are better than those of samples from ingot route.

(iv) The scatter in ductility in powder HIPped samples is associated with large (up to 450μm diameter) circular crack initiation sites, with larger sites associated with lower ductility.

These aspects are discussed in turn below.

(i) Facetting of powders during HIPping.

The observation of facetting of the powder particles during HIPping is a further indication that the majority of the deformation which occurs during densification takes place at prior particle boundaries. In the case of the observations on Ti-6Al-4V the formation of recrystallised equiaxed regions at the prior particle boundaries made any facetting difficult to observe but it did indicate that deformation occurs preferentially at particle boundaries. The fact that this facetting was more obvious in the HIPed PREP BuRTi powder than in the gas atomised powder appears also to be associated with the simpleness of identifying the facets. These are clearly most easily

seen in samples with larger scale microstructure as is apparent by comparing Fig. 5.6 (h) (HIPped at 950^{o}C, 150MPa, 4h) with Fig. 5.6 (f) (HIPped at 900^{o}C, 150MPa, 4h) where only with difficulty can the facetting be seen in Fig. 5.6 (f). On that basis, although the facetting is more obvious in the coarser microstructure in the PREP sample, it does not mean that more deformation occurs in this powder whereas means that it is more easily recognised.

(ii) The tensile strengths of gas atomised samples are less than those of PREP samples but the ductility is similar for identical HIPping conditions.

The yield stress (i.e. the stress corresponding to 0.2% elongation) is significantly higher in the PREP samples than in the gas-atomised for similar HIPping conditions which is not easily understood since the average microstructural unit is larger in the PREP samples. It appears that the presence of a significant number of individual crystals up to about 200μm in diameter does not influence the tensile strength or ductility significantly; they simply act as soft regions and the applied stress is unloaded onto the harder regions. It is possible that the proof stress is influenced by the distribution and sizes of the carbide particles but no accurate measure of any difference is available. As noted in Table 5-3 the ductility of all BuRTi samples appears to be correlated with the size of the circular region which initiates failure and in the case of the heat treated sample with the size of the facetted region – which in fact appears to be roughly circular. This aspect will thus be discussed in chapter 6.

(iii) The fatigue properties of the PREP samples are much lower whereas the fatigue properties of the gas atomised samples are better than those of samples from ingot route. As noted earlier and further discussed below, the poor fatigue properties observed for PREP samples is probably associated with localisation of slip leading to persistent slip bands. This tendency would be aggravated in the samples HIPped at

higher temperatures and the very poor properties of the samples HIPped at 950°C are consistent with this mechanism and the observation of large facets on fatigued samples. Loading under fatigue conditions would continue within the soft region when the stress is reversed leading to persistent slip bands and thus to early failure. Suhr [*Suhr 1988*] reported that a slip band could define the path of the shear crack in the direction of the primary slip system and then develop into fatigue crack growth stages, as shown schematically in Fig. 5-29. A small volume fraction of particles containing larger grains (see Fig. 5-3) in gas atomised powder samples did not show a big effect on the fatigue run out strength but could contribute to the scatter in the fatigue properties.

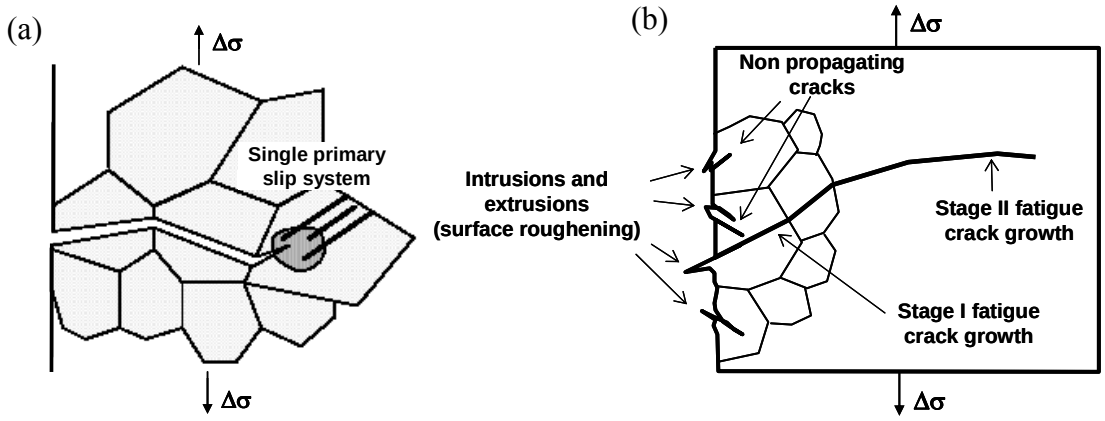

Fig.5-29 Schematic representation of: (a) single primary slip system and (b) fatigue crack growth stages [Suhr 1988].

(iv) The scatter in ductility in powder HIPped samples is associated with large (up to 450μm diameter) circular crack initiation sites, with larger sites associated with lower ductility. Failure in tension was found to be associated with large (over 450μm in diameter) circular crack initiation sites which contained many different cleavage facets (see Section 5.1.4). Measurement on the circular regions shows the dimensions

are sometimes larger than the particle size, which suggests that these sites involve more than one particle (see Section 5.2). Stereographic analysis suggests that the facets on the fracture surface have different fracture planes. Groups of cleavage facets were also observed in the study on mechanical properties of ingot-route BuRTi samples by Novovic [*Novovic 2004*]. The formation of a microcrack, caused by dislocation pile-ups and stress concentrations at defects, can initiate cleavage under high local stresses and propagate throughout a single facet, finally leading to overall failure. She also reported the EBSD evaluation of large faceted areas and indicated that cleavage of multiple adjoining grains occurred if they were orientated preferably for cleavage, leading to the formation of very large cleavage areas within regions. As noted earlier further discussion of this aspect will be discussed in Chapter 6.

5.2 HIPping of individual size fractions of the gas atomised BuRTi powder

This section examines the microstructural characteristics and mechanical properties of gas atomised BuRTi powder samples HIPped at 900C, 100MPa, 2h made using individual size fractions. Two size fractions (small size fraction: 50~150μm, and large size fraction: 250~400μm) were used in this experiment. The microstructure for individual particles was reported in Section 5.1.1 (see Figs. 5-2, 5-3).

5.2.1 Microstructural characterisation

The typical microstructural characteristics of HIPped samples were similar to those of the complete size fraction powder HIPped under the same conditions (as shown in Figs. 5-6 (a, b)), which are composed of single phase beta. Differences can be seen from the optical micrographs for samples made using the two particle size fractions (see Fig. 5-30). The smaller the particle size, the smaller the range of grain size. As mentioned in Section 5.1.1.2, it is possible to identify individual particle boundaries in HIPped samples made using complete particle size fractions. For large size fraction samples, the individual particle boundaries are obvious and some facetting with straight edges (see Figs. 5-30 (c, d)), which is not obvious in small size fraction samples (see Figs. 5-30 (a, b)). Fig. 5-31 shows EBSD misorientation maps and distribution, EBSD grain size maps and distribution of these two size fraction samples. The misorientation distribution is similar, but the difference in grain size distribution is evident. The range of the grain size for small size fraction sample is 5~30μm, and that for large size fraction sample is 7~65μm.

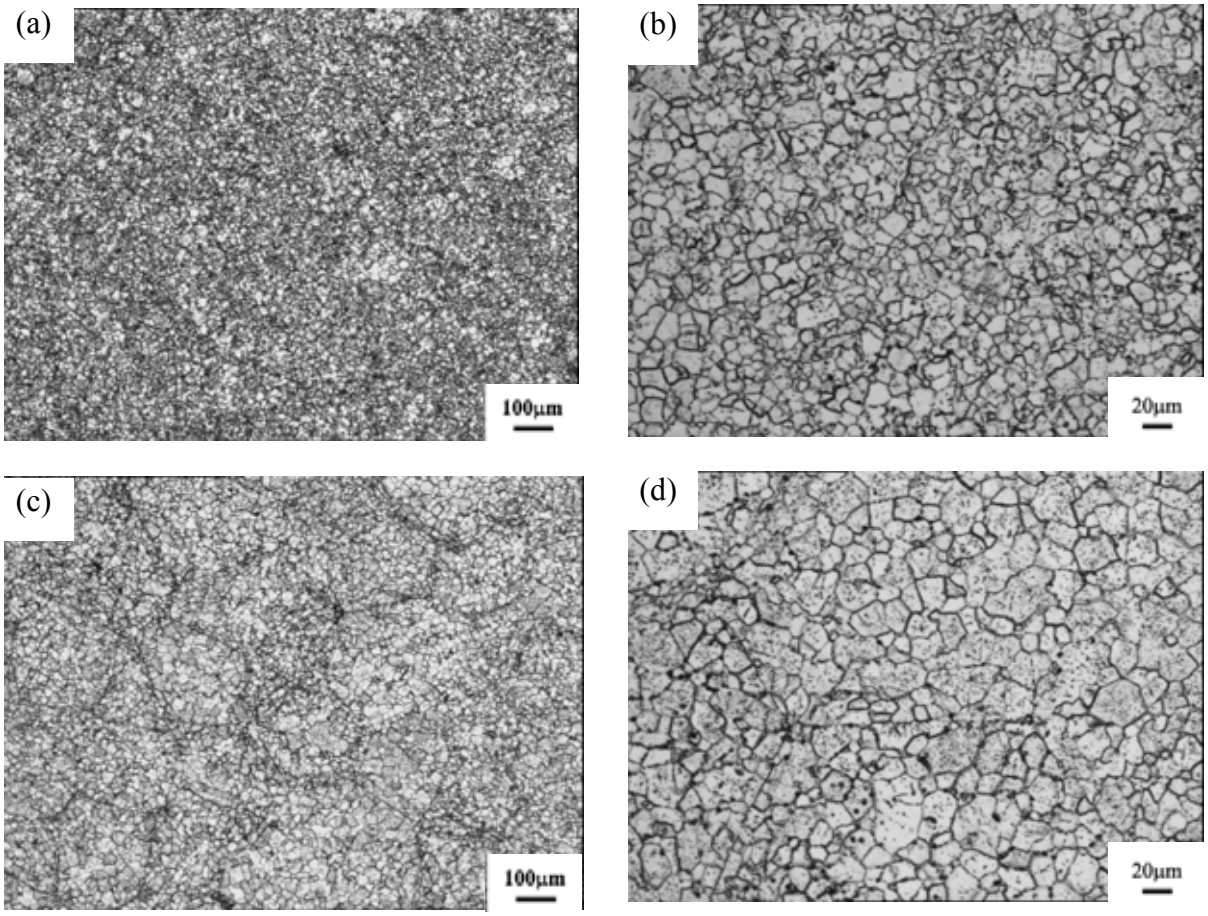

Fig. 5-30 Optical images at different magnifications of gas atomised BuRTi powder samples HIPped at 900°C, 100MPa, 2h made using different particle size fractions: (a, b) 50~150μm; (c, d) 250~400μm showing the different grain sizes.

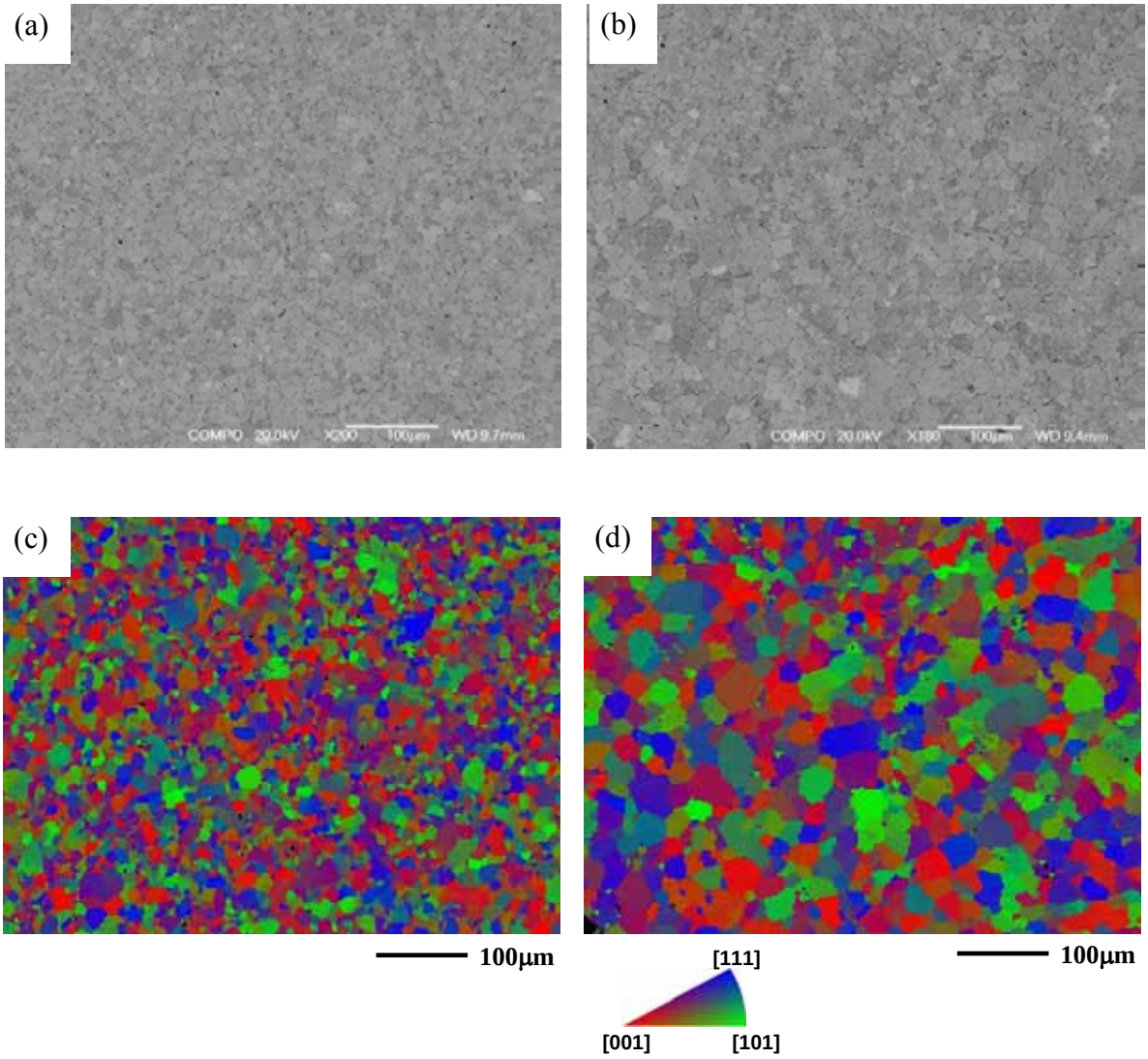
(a)
(b)
(c)
(d)
100μm
[111]
[001]
[101]
100μm
(e)
(f)
Percentage of counts (%)
Misorientation angle (°)
Percentage of counts (%)
Misorientation angle (°)

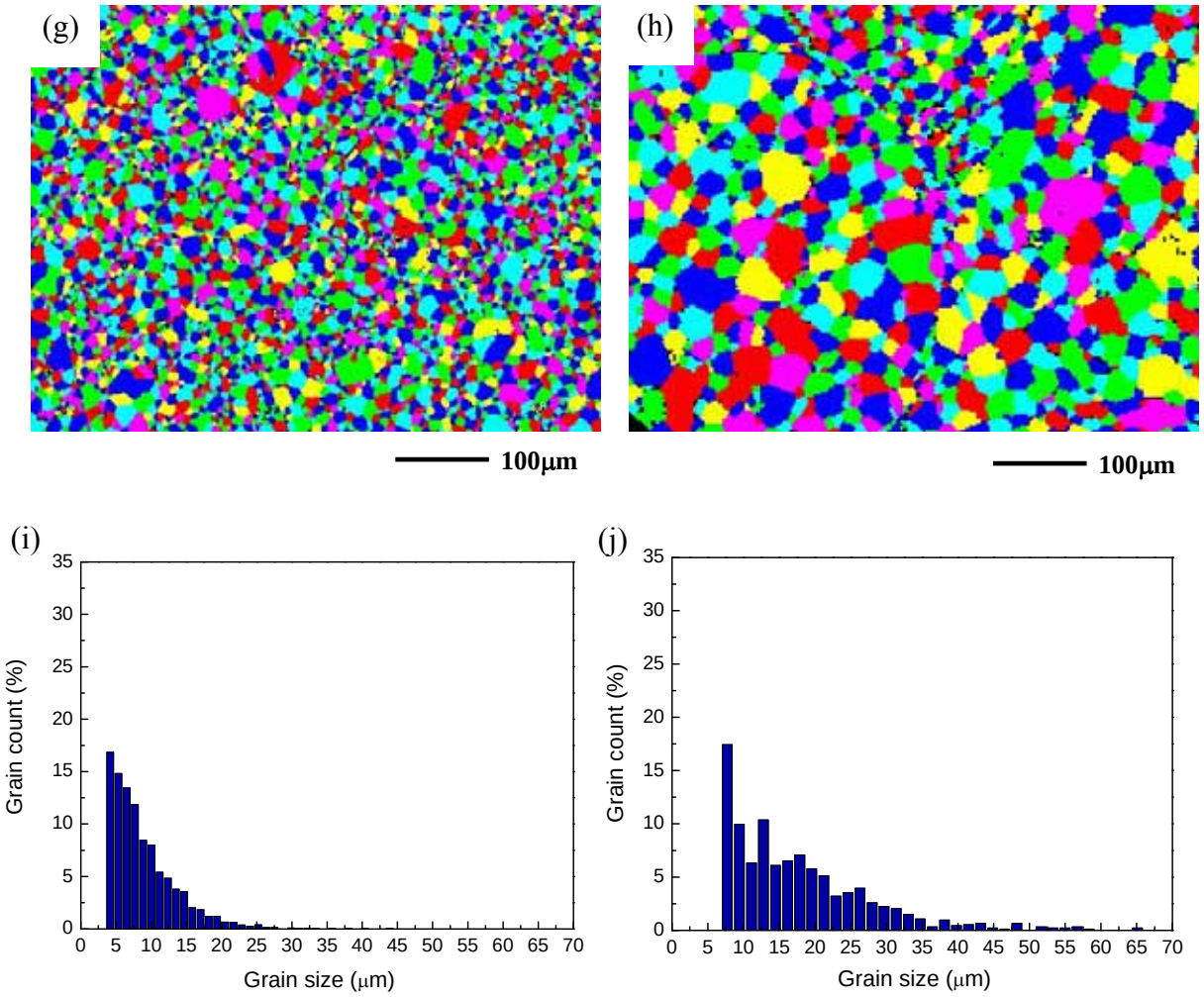

Fig. 5-31 (a, c, e, g, i) gas atomised BuRTi samples HIPped using particle size fraction of 50~150μm; (b, d, f, h, j) samples HIPped using particle size fraction of 250~400μm. (a,b) SEM backscattered electron micrographs; (c,d) EBSD misorientation maps; (e,f) misorientation distribution graphs; (g,h) EBSD grain size distribution maps; (i,j) grain size distribution maps. It shows that the two samples have similar misorientation distribution, but the grain sizes in the sample HIPped using particle size fraction of 250~400μm are coarser than that in the sample HIPped using particle size fraction of 50~150μm.

5.2.2 Influence of particle size on the properties of machined HIPped samples

5.2.2.1 Tensile properties and examination of fracture surfaces in samples tested to failure

Tensile tests of HIPped samples (900°C, 100MPa, 2h) made using two particle size fractions were performed. The tensile data are given in Fig. 5-32 (a) and Table 5-4, respectively. The samples HIPped using small particle size fractions showed slightly higher yield stress and tensile strength than those of samples HIPped using large particle size fractions. However, the larger size fraction had a higher average value of ductility, about 19% than the smaller size fraction, about 8%. A large scatter in ductility is found in both size fractions of HIPped samples. Fig. 5-32 (b) shows a comparison between the tensile properties of HIPped samples using sieved powders and the complete size fraction. It is found that complete size powder HIPped samples have similar strengths to the small particle size fractions HIPped samples and an average value of 16% for elongation. Details can be seen from Table 5-4.

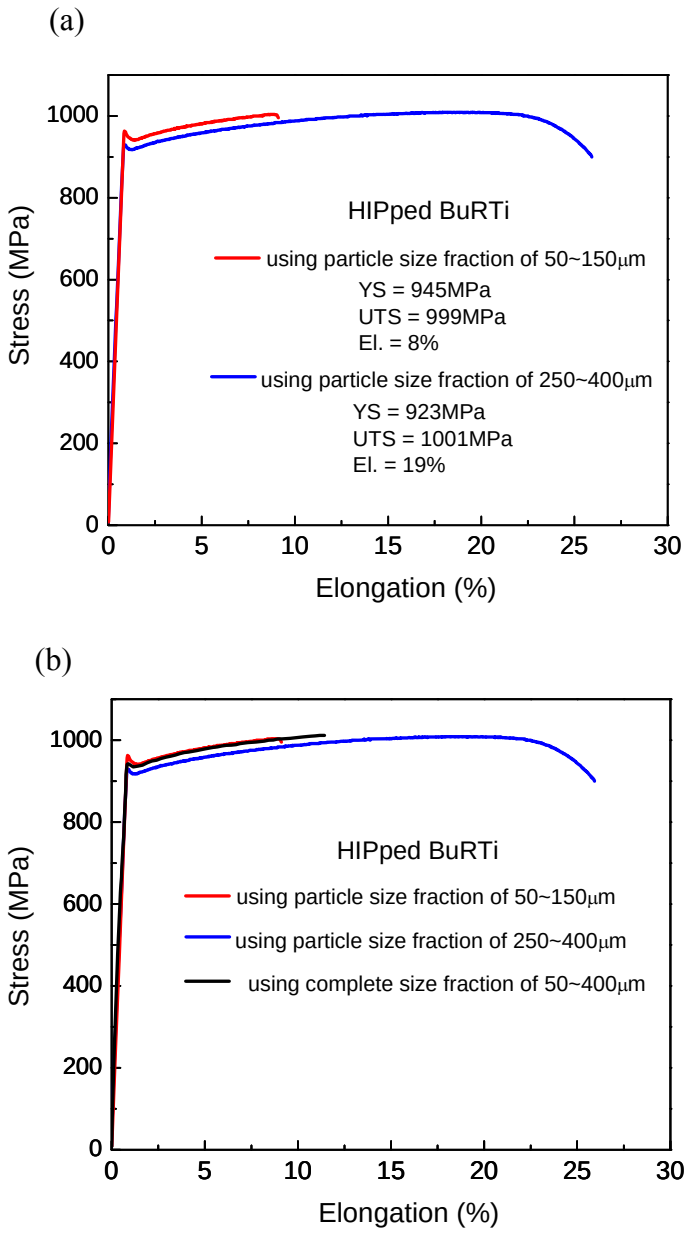

Fig. 5-32 Room temperature tensile properties of gas atomised BuRTi powder samples using (a) sieved powders with different size fractions showing samples HIPped using the particle size fraction of 50~150μm have slightly higher yield stress and tensile strength and lower ductility than those of samples HIPped using the particle size fraction of 250~400μm; (b) sieved powders and complete size fraction showing that the complete size fraction has similar strengths to the small particle size fractions HIPped samples.

Table 5-4 Room temperature tensile properties of HIPped gas-atomised BuRTi powder samples made using different particle size fractions

	YS (MPa)	UTS (MPa)	Ductility (%)
Small size fraction (50~150μm)	945±2/4	999±12/17	13/7/5
Large size fraction (250~400μm)	923±1/2	1001±10/10	26/20/10
As-received size fraction (50~400) μm	945±6	1008±5	25/12/10

Fig. 5-33 shows the fracture surfaces of failed tensile gas atomised powder samples HIPped using two size fractions, and circular regions containing transgranular facets were found to be the crack initiation sites for both samples. Some larger facets can be seen in the circular regions, as indicated by the arrows in Figs. 5-33 (c, d). The relationship between ductility and the dimension of circular region are consistent with Table 5-3 measured for the complete size fraction. The circular region for the small size fraction sample with a ductility of 7% is much larger than that for the large size fraction sample with a ductility of 20%. Some crack initiation sites were also sectioned and the orientations of the grains were determined on these sections. Fig. 5-34 shows the EBSD analyses on a cross section of a large circular region in a sample failed in tension made using particle size fraction of 50~150μm which had an elongation of 5%.

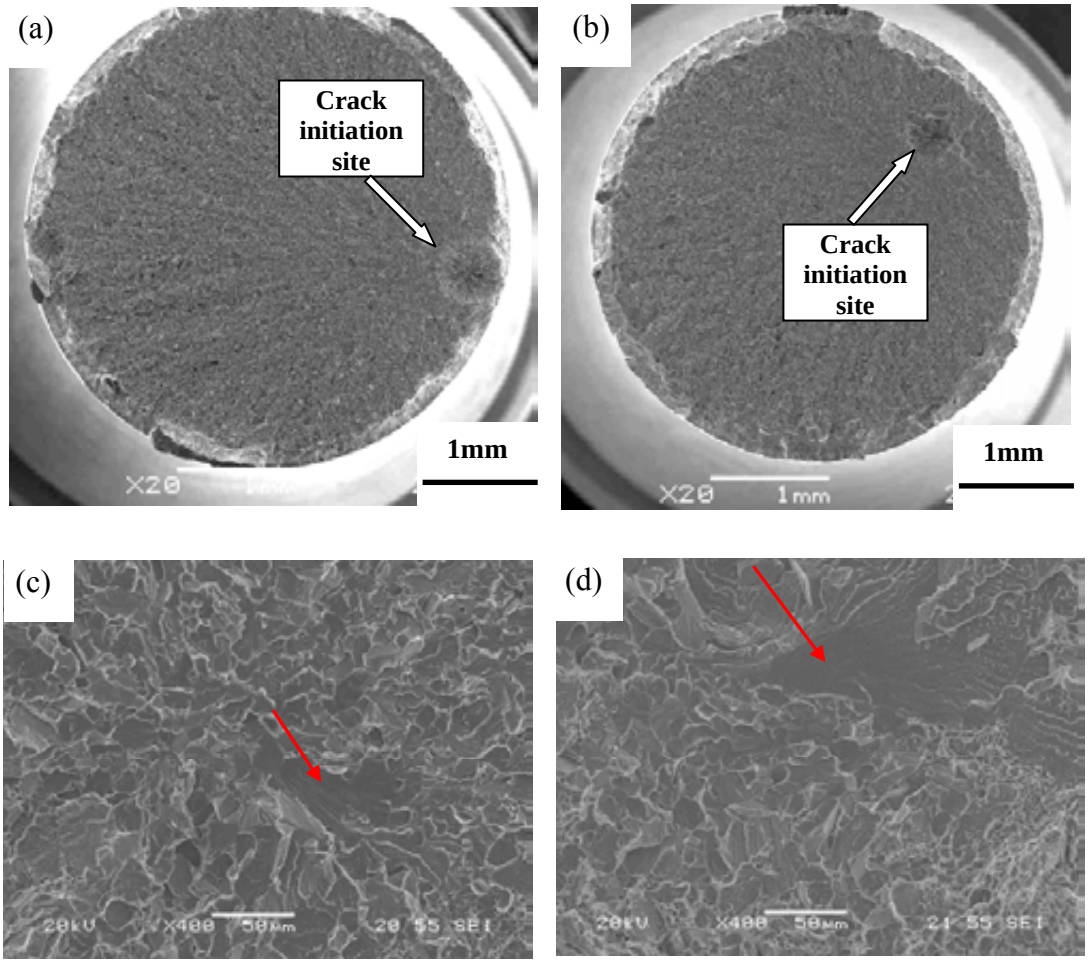

Fig. 5-33 SEM SE images at different magnifications of the fracture surfaces of tensile failed gas atomised BuRTi powder samples HIPped at 900°C, 100MPa, 2h made using: (a, c) particle size fraction of 50~150μm (elongation=7%); (b, d) particle size fraction of 250~400μm (elongation=20%) showing the former has larger circular region associated with lower ductility. The larger facets are indicated by arrows in (c, d).

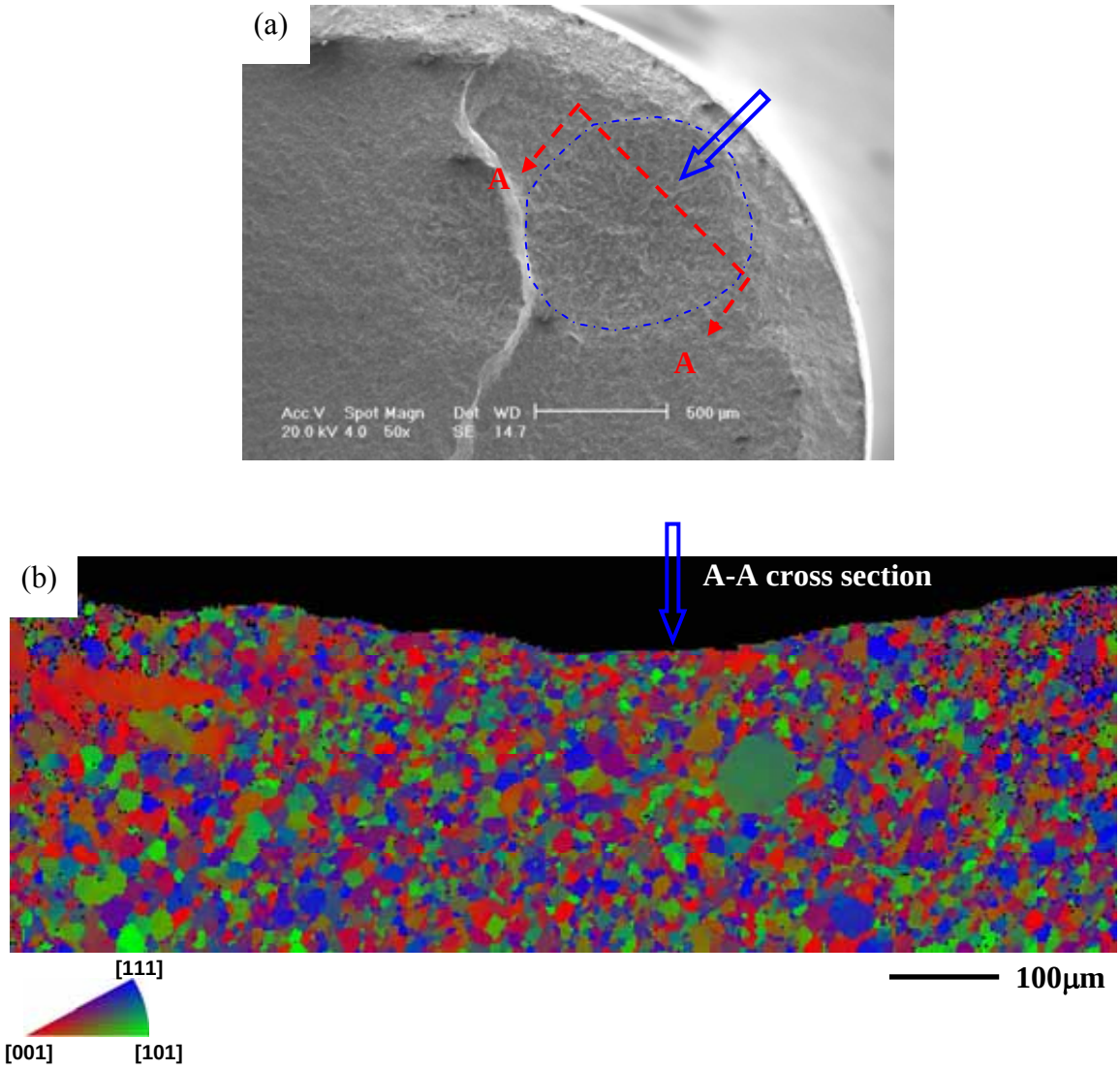

5-34 EBSD analyses of cross section of large circular region in tensile failed as-HIPped gas atomised powder sample made using particle size fraction of 50~150µm with an elongation of 5%: (a) SEM SE image of crack initiation site showing the circular region with a diameter of around 600 µm; (b) EBSD misorientation mapping of A-A cross section showing different crystallographic orientations among the gains on the section.

5.2.2.2 Fatigue properties and observations of fracture surfaces of fatigued samples

Fig. 5-35 (a) shows the SN curve for HIPped gas atomised BuRTi powder samples made using two particle size fractions. A large scatter in the number of cycles to failure at different stress levels was found for both size fraction samples. Under higher stress levels (>600MPa), samples HIPped using two size fractions show similar lives. When the stress amplitudes are lower, they all show a large variation of fatigue lives. The final endurance limit for small size fraction of 50~150μm is about 50 MPa higher than that for large size fraction of 250~400μm. Fig. 5-35 (b) shows a comparison between the fatigue properties of HIPped samples using sieved powders and complete size one. It is found that the complete size powder samples exhibit better fatigue property with a run-out strength of 550 MPa.

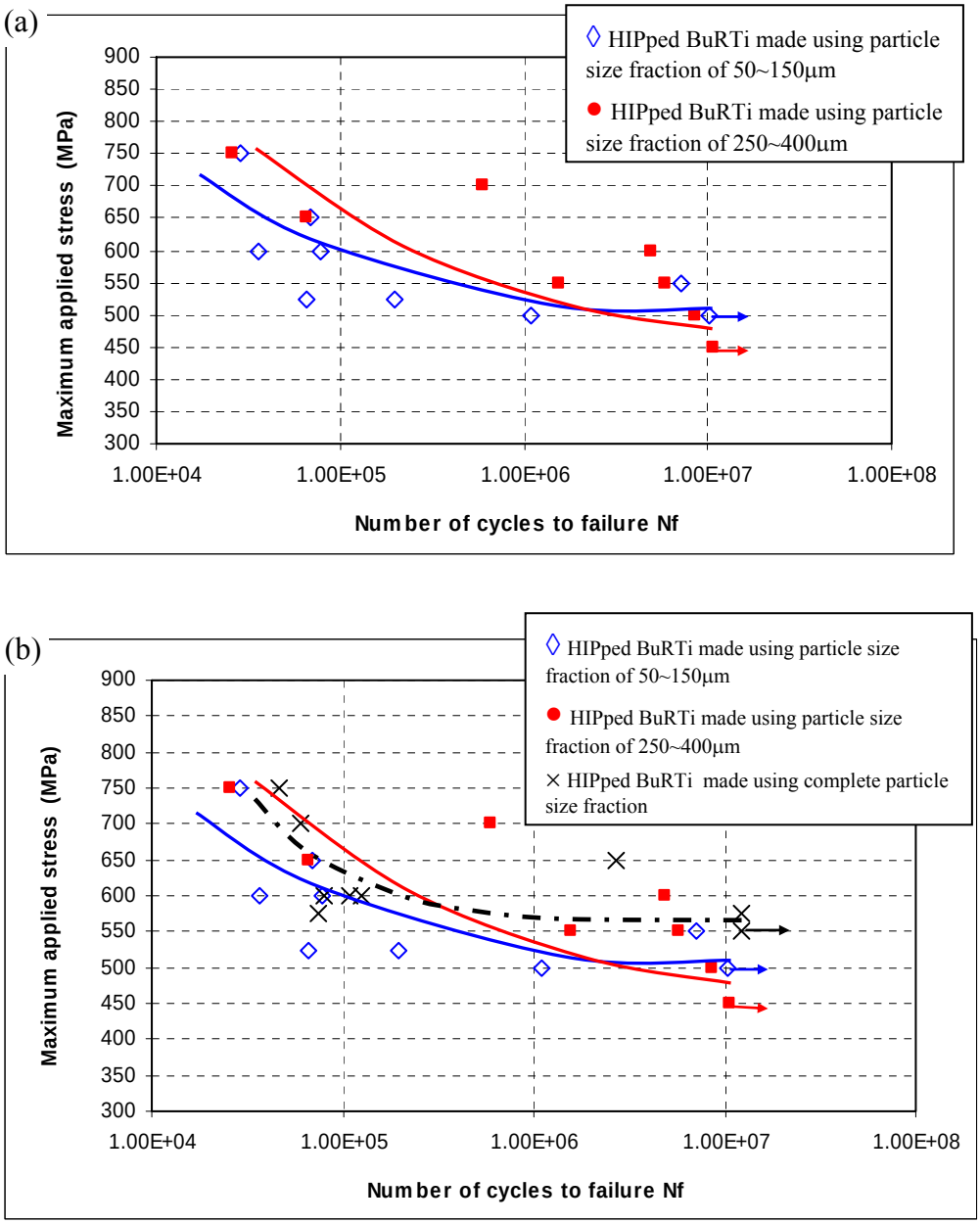

Fig. 5-35 SN fatigue curves for gas atomised BuRTi powder samples HIPped at 900°C, 100MPa, 2h made using (a) sieved powders with different size fractions showing scattered fatigue properties, and samples HIPped using the particle size fraction of 50~150μm have slightly higher endurance limit than that of samples HIPped using the particle size fraction of 250~400μm; (b) sieved powders and complete size fraction one showing slightly higher endurance limit for complete size fraction one.

The fracture surfaces were examined for fatigue failed samples HIPped using two particle size fractions, as shown in Fig. 5-36. Transgranular facets were found at crack initiation sites for both samples (see Figs. 5-36 (b, d)), which shows similar crack initiation resistance for these samples. Fig. 5-37 shows the crack paths of fracture surface cross sections for the samples, and it is clear that the crack path of large size fraction sample is much rougher than that of small size fraction sample, which would contribute to better crack propagation resistance of larger grain sizes in samples HIPped using large particle size fraction.

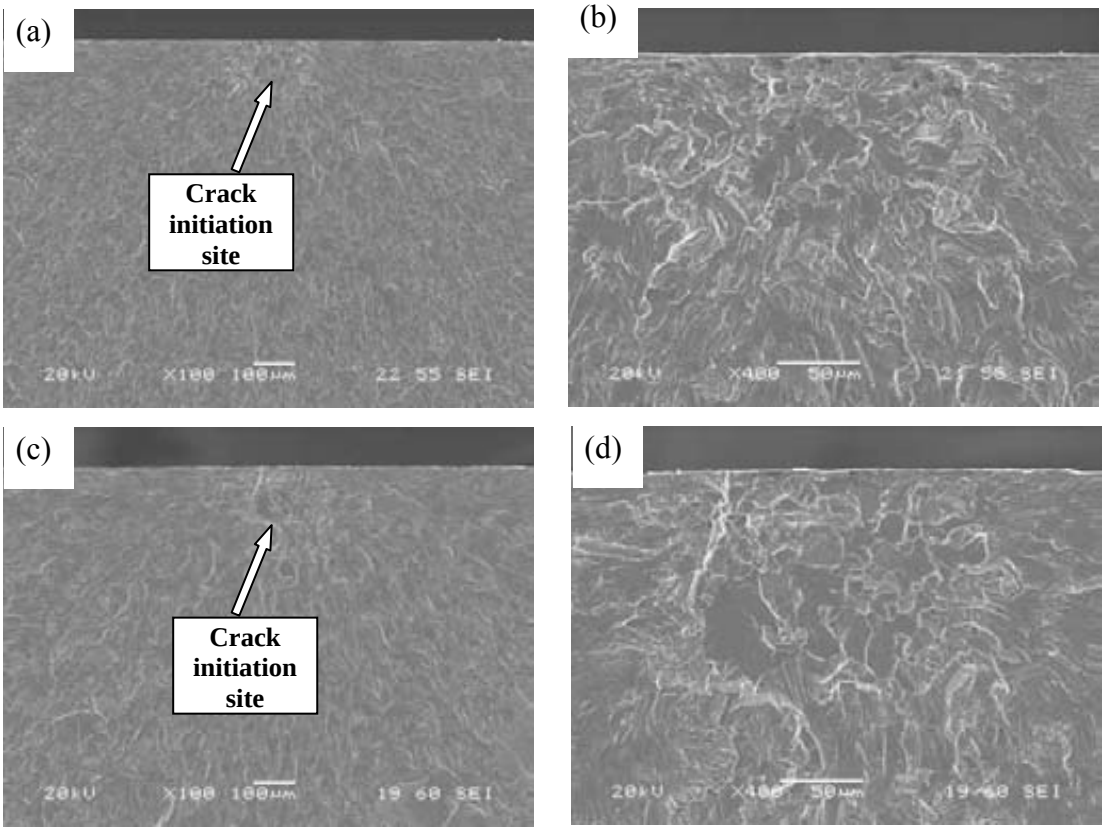

Fig. 5-36 SEM secondary electron micrographs of fracture surfaces of fatigue failed gas atomised BuRTi powder samples HIPped at 900^{o}C, 100MPa, 2h made using: (a, b) particle size fraction of 50~150μm (maximum stress=550MPa / number of cycles=7087800); (c, d) particle size fraction of 250~400μm (maximum stress=470MPa / number of cycles=1549600) showing crack initiation sites at different magnifications.

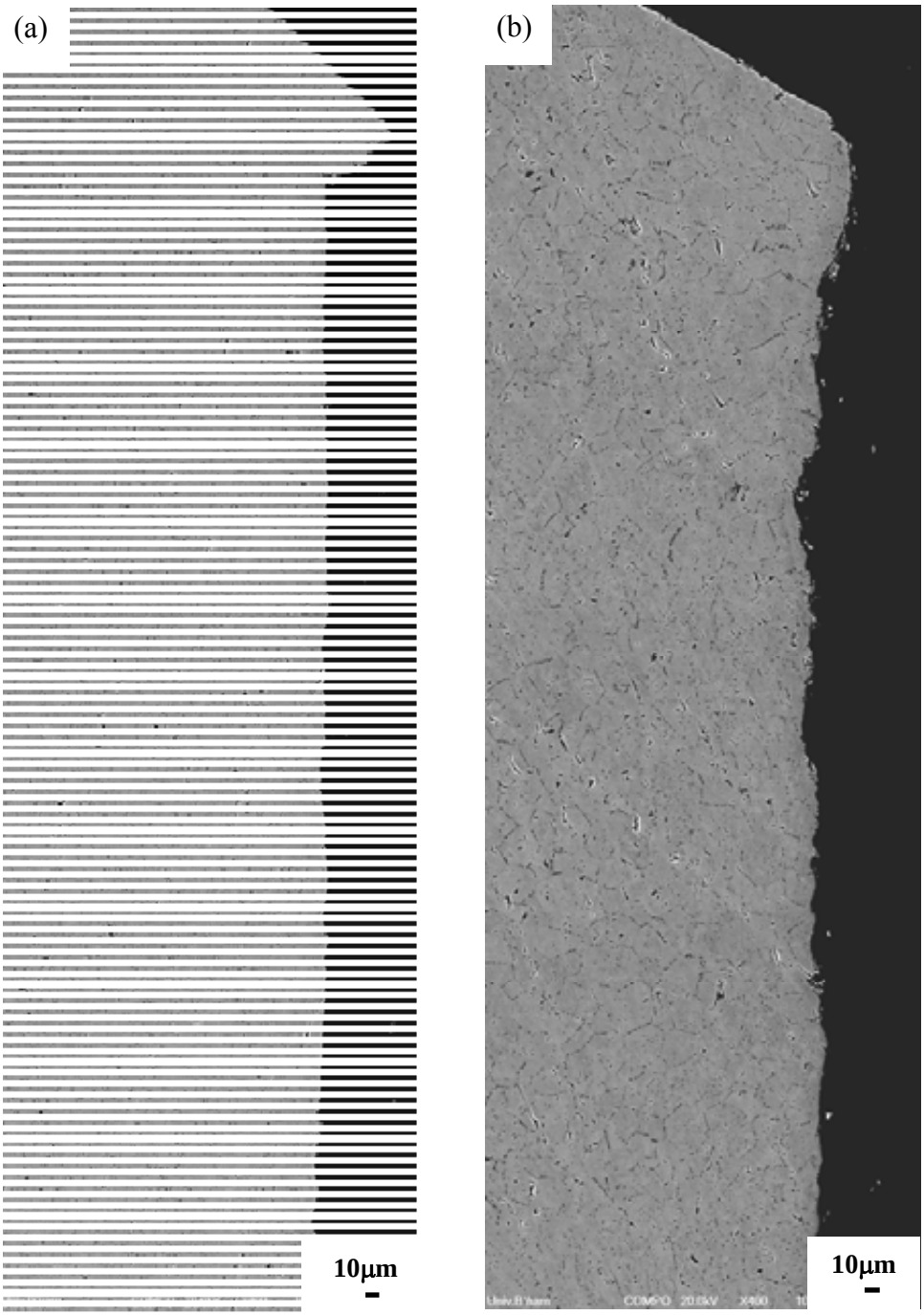

Fig. 5-37 SEM BSE images showing the crack paths of fracture surface cross sections of fatigue failed gas atomised BuRTi powder samples HIPped using: (a) particle size fraction of 50~150μm (maximum stress=550MPa / number of cycles=7087800); (b) particle size fraction of 250~400μm (maximum stress=470MPa / number of cycles=1549600). The crack path of large size fraction is rougher than that of small size fraction.

5.2.3 Discussion

For as-HIPped microstructure of gas atomised BuRTi samples HIPped using different particle size fractions, the grain size is smaller when the particle size fraction is smaller (see Fig. 5-31). The tensile behaviour of the HIPped samples was found to be dependent on the powder particle size of the compacts. Samples obtained with powder of the small particle size have a higher yield stress and tensile strength, as shown in Fig. 5-32 and Table 5-4, respectively. This is attributed to the finer grain size of the compacts with the small particle size. But the small particle size fraction samples have a lower average value of ductility, which is associated with the dimension of circular regions at crack initiation sites. Generally the average values are perhaps not very useful since the large scatter found between different samples (see Table 5-2) makes the comparison between the different size fractions (see Table 5-4) very difficult and the question that has to be addressed is the origin of the scatter in BuRTi powder samples. This will be taken up in Chapter 6. According to the EBSD results for the cross section of crack initiation site in small particle size fraction samples (see Fig. 5-34), it is confirmed that the circular region is not from one single particle since the diameter of the region (around 600 μm) is much larger than the particle size (50~150μm). With respect to the fatigue properties, small particle size fraction samples had a slightly higher run out strength, but the large scatter of fatigue lives under matching stress levels again made the comparison meaningless. The presence of a small proportion of individual particles with larger grains (see Fig. 5-3) in the HIPped samples probably acted as crack initiation sites and could cause the scatter, as discussed in Section 5.1.6.

References

Li 1998 : Li, Y. G., Blenkinsop, P. A., Loretto, M. H. and Walker, N. A., *Acta Mater.*, **46**, 1998, p.5777.

Li 1999: Li, Y. G., Blenkinsop, P. A., Loretto, M. H., Rugg, D. and Voice, W., *Acta Mater.*, **47**, 1999, p.2889.

Li 2001: Li, Y. G., Loretto, M. H., Rugg, D., and Voice, W., *Acta Mater.*, **49**, 2001, p.3011.

Novovic 2004: Novovic, D., Ph.D Thesis., The University of Birmingham, Birmingham, UK, 2004.

Rabin 1990: Rabin, B. H., Smilok, G. R., and Korth, G. E., *Mat. Sci. Eng.,* **A124**, 1990, p1.

Suhr 1988: Suhr, R.W., *The Institute of Metals*, London, 1988, p.226.

Voice 2004: Voice, W., in: *Proceedings of the 10th World Titanium Conference Ti-2003*, Hamburg, Germany, 2004, p.2915.

Chapter 6 General Discussion

In this chapter, the HIPping responses of two alloy powders (Ti-6Al-4V and BuRTi) will be considered together. The aspects which will be discussed are listed below.

1. The microstructures of as atomised powders and their response to HIPping.

2. The influence of experimental variables, powder particle size and HIPping conditions on microstructure and properties of HIPped powders.

6.1 The microstructures of as atomised powders and their response to HIPping

The initial microstructures of the two alloy powders (Ti-6Al-4V and BuRTi) are very different from each other and the microstructures of the two different powders of BuRTi (PREP and gas-atomised) also show important differences. These differences underlie the different responses of these powders to HIPping.

The important differences between the two alloys lie in the facts that BuRTi is single β phase with bcc structure (apart from the presence of a small fraction of carbides) under all cooling conditions. In contrast Ti-6Al-4V is a two phase (α + β) alloy under equilibrium conditions and during rapid cooling (occurring during atomisation) this alloy undergoes a martensitic transformation. The differences between gas-atomised BuRTi and PREP BuRTi are associated with the influence of cooling/solidification conditions on a relatively simple alloy where the main impact is on the presence of a

significantly higher fraction of single crystal particles in the PREP powder than in the gas-atomised powder. The fact that the Ti-6Al-4V powders are martensitic makes an assessment of the grain size within individual powder particles less straightforward but the nature of the martensite within some particles is compatible with some particles having been single beta crystals before they transformed martensitically. It appears however that the grain size within individual powder particles is significantly smaller in PREP Ti-6Al-4V than in PREP BuRTi. These differences should be borne in mind when considering the response to HIPping of the two powders of BuRTi and of the response of PREP BuRTi and PREP Ti-6Al-4V.

It is generally accepted that the dominant mechanisms of densification during HIP are plastic yielding and power-law creep. During the process of densification, powders contact with each other and neck shapes are formed, the geometry of a neck is shown in Fig. 6-1.

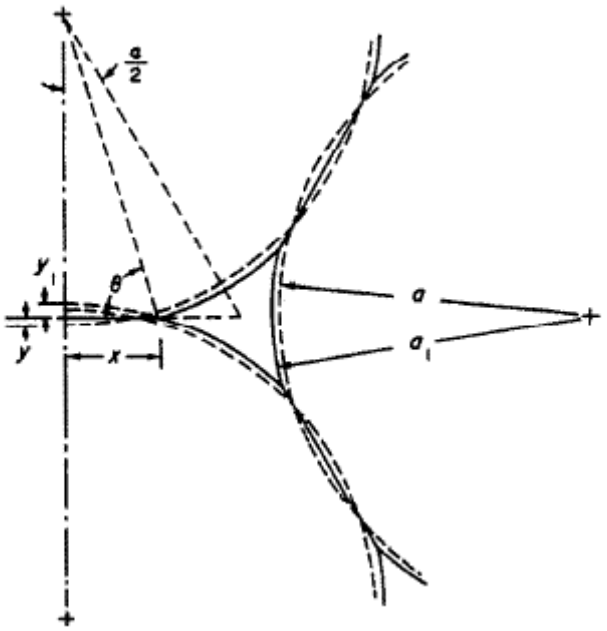

Fig. 6-1 A section through 3 particles during plastic yielding and power-law creep, showing the shape of the pore. Compaction causes the radius of the curvature of the particle surface to increase from a to a_t [*Swinkels 1983*].

Material enters the neck in such a way that the free surface of the particle expands outwards into the pore, remaining a segment of a sphere as it does so. The effective particle radius increases as densification advances, and the pore remains cuspy. Another important aspect is the geometry of the particle packing. During densification, the average number of contacts per particle (the co-ordination number) increases steadily [*Fischmeister 1978*]. At the same time existing contacts grow in area (see Fig.6-1). Both processes cause the effective pressure on a particle contact to decrease during densification. Once full density is reached, the initially spherical particles tend to become polyhedra (i.e. the radius of curvature of the surfaces increases towards infinite). Moreover, due to the simultaneous effects of pressure and temperature, the

HIP process not only “closes” pores, but ideally completely eliminates all trace of powder surfaces by diffusion bonding.

The size-dependent deformation at large-small particle contacts has also been investigated [*Delo 1999*]. The behaviour of a powder particle depends strongly on the relative sizes of neighbouring particles, with smaller particles at large-small particle contacts bearing the vast majority of the deformation. Through examining the effective stress levels in the particles during HIPping process simulation (see Fig. 6-2) it was found that the smaller particle experienced higher stresses than the larger particle causing it to experience more deformation in a fixed time interval relative to the larger particle. The deformation of the smaller particle accommodates the rigid body motion of the larger particles which in turn increases the packing efficiency and relative density.

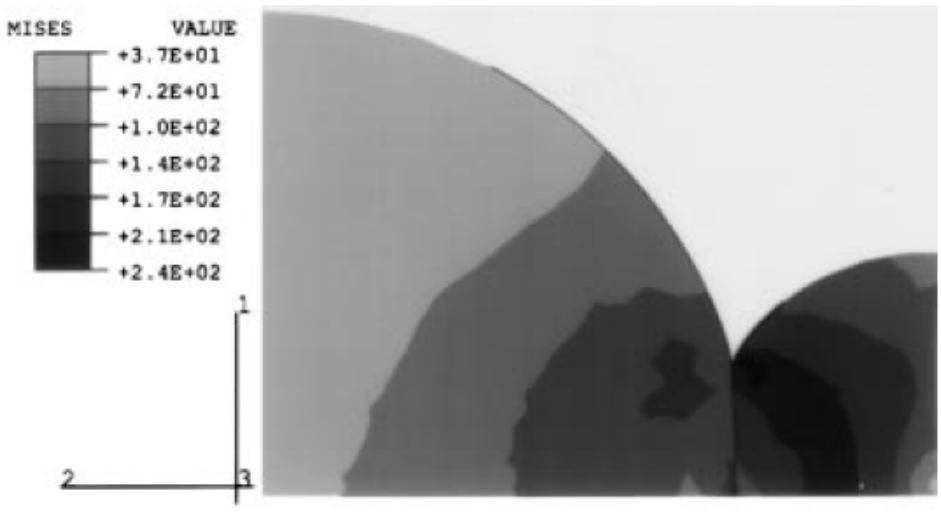

Fig. 6-2 FEM interparticle contact analysis showing relative particle deformation and effective stress levels resulting from contact deformation by plasticity and creep.

Loading is compressive parallel to the 2 direction. Stress units are MPa [*Delo 1999*].

These general descriptions of densification and bonding during HIPping form the basis for understanding the response of the powders used in the present work but the observations made during this work require a more detailed consideration; the response of regions near particle boundaries and the response of the non-equilibrium phase, martensite, in Ti-6Al-4V require further consideration. It is clear that the outer regions of all particles respond differently from the interiors; this differing response is not an aspect that is included in the above description of HIPping, although different stress levels are predicted in the outer and inner regions of particles (see Fig. 6.2), but this difference is clearly a very important aspect which can influence the mechanical properties and microstructure of the HIPped powders. In the case of PREP Ti-6Al-4V the deformation of the outer regions leads to recrystallisation when a reasonably large volume of the particles becomes fine grained with crystals separated by low angle boundaries. The structure of the interiors of HIPped particles are controlled entirely by the decomposition of martensite and as shown by the experiments involving heat treatment without pressure this structure is not obviously changed by HIPping. In BuRTi the powder particles form very obvious facets and become polyhedra during HIPping whilst the misorientations between individual crystals within particles is very significantly reduced, which suggests that the strain and thermal histories during HIPping are such as to cause recrystallisation. These aspects are discussed below.

The stage of HIPping at which polyhedra are formed is not known for certain but it is reasonable to assume that both pressure and temperature are required for the polyhedra to form. PREP BuRTi forms very clear polyhedra when HIPped under all conditions investigated, whereas gas-atomised BuRTi forms fewer and less obvious

polyhedra. It has been suggested in Chapter 5 that this is an apparent rather than a real difference, because smaller grain sizes makes recognition of the facetted volumes less obvious. However it also suggests that the individual particles in PREP powder deform more easily than the particles in gas-atomised powder, so that they reach this low energy configuration more readily. This difference could be associated with the coarser grain size (which implies that dislocation glide rather than grain boundary sliding or climbing in creep is the dominant mechanism of powder particle deformation) and frequency of (weak) single crystal particles in the PREP powder. Polyhedral particles were not as obvious in Ti-6Al-4V (although the presence of an annulus of fine equiaxed crystals makes it more difficult to assess the shapes of the powder particles after HIPping) which suggests that these particles are stronger at the relevant temperature. Although these differences in the formation of polyhedra are obvious they do not appear to lead to any differences which can be correlated with the tensile behaviour of the gas atomised and PREP BuRTi; the tensile strength and ductility for HIPped gas-atomised and PREP BuRTi under similar conditions are very similar. On that basis it is concluded that extensive faceting is not a prerequisite for good bonding and is simply an indication of the ability of a given sample to reach equilibrium during HIPping.

All HIPped gas atomised and PREP BuRTi samples showed large circular regions in the fracture surfaces under tensile testing, with larger sites associated with lower ductility. The mode of failure (large circular regions) in the PREP and gas atomised samples of BuRTi under tensile testing could perhaps imply poor bonding but in view of the tensile properties that is unlikely. All samples showed large circular regions which appear to initiate failure and the size of these regions was larger the lower the

ductility. There is therefore a fundamental problem concerning tensile failure in gas atomised and PREP HIPped BuRTi samples and as will be discussed later, an additional problem with fatigue failure in the PREP samples.

The failure of large circular regions which are significantly larger than the original particle size in both gas atomised and PREP powder samples suggests that there is a common factor which overrides the obvious microstructural differences in these two types of samples. Thus the failure is not associated with the differences between the microstructural units in HIPped PREP and gas-atomised powder (coarser grain size, presence of single crystals) but is associated with a common factor in PREP and gas atomised HIPped powder samples of BuRTi which has a bcc structure. Close examination of the fracture surfaces associated with tensile failure of BuRTi samples (see Fig. 5-33) shows that in general the scale of the individual fracture facets is very close to that of the grain size of the samples (see Fig. 5-31). There is however commonly at least one larger facet within these circular regions (indicated by the arrows in Figs. 5-33 (c, d)) where the failure site is possibly characterised by the larger facet. In fact large facetted regions can also be seen in tensile tested ingot-route BuRTi (see Fig. 5-23) which are within the failure initiation site – although these are not so obviously circular as those in powder HIPped samples.

It is therefore concluded that failure in tension of BuRTi is initiated in an area that is larger than the average grain size and thus may consist of two or more adjacent grains of similar orientation (note that there are more low angle boundaries after HIPping than were present in the atomised powders). Also there is another possibility that the crack initiation could be associated with the large grains present in original particles

(discussed in Chapter 5). Once failure is initiated at stresses close to the UTS the failed area grows rapidly until the whole sample fails. This mode of failure is perhaps associated with this very strong beta alloy which has a high strain rate sensitivity so that as the local strain rate increases the flow stress increases rapidly to reach the fracture stress and thus fracture occurs. When the fracture has propagated a certain distance the imposed strain-rate will decrease as the cross-head takes up the slack, so that the final stage of fracture is ductile in all samples. In the case of powder HIPped samples the local misorientation of adjacent crystals is random (and commonly not large) so the failed region expands symmetrically. In the case of ingot-route samples the grain size is coarser and crystallographic factors may control how the failure spreads, so that it is more irregular. The fact that lower ductility is associated with larger circular regions would on that basis be associated with the size of the initial failure site and its speed of growth.

On the basis of the above discussion it is possible to explain the observed response of powder HIPped BuRTi and it is concluded that whilst properties comparable with ingot-route material can be produced from gas-atomised BuRTi this is not possible with PREP powder because of the tendency to form large single crystals which could cause poor fatigue properties. Examination of fracture surfaces of Ti-6Al-4V samples (see Fig. 4-41) suggests that there are also some facets, on a similar scale to that of alpha and beta with similar orientation (see Fig. 4-39), which act as the fracture initiation sites. These facets may be the origin of the failures - their propagation in a powder-processed sample where there is no obvious texture, is likely to be isotropic, giving rise to circular initiation sites, with subsequent growth focussed on this site. Considering the difference between two-phase microstructure of Ti-6Al-4V and

single beta phase of BuRTi, the morphology of circular sites of two alloys is different. This is what is observed; in BuRTi, obvious river-lines are visible (see Fig 5-33) but are not obvious in the case of Ti-6Al-4V.

6.2 The Influence of experimental variables, powder particle size and HIPping conditions on microstructure and properties of HIPped powders

The variables that have been investigated are HIPping pressure, temperature and holding time. In addition the size fraction used to manufacture samples has been varied in order to establish if this has an influence on properties.

In the case of Ti-6Al-4V it was found that 930°C was the optimum HIPping temperature and the improved HIPping procedure (applying temperature and pressure out of phase) gave optimum properties. Lower temperatures did not allow full bonding and higher temperatures resulted in significant structural coarsening. In the case of BuRTi no obvious property improvement can be achieved for the range of selected HIPping conditions. Any assessment of variables was made difficult

For HIPped PREP Ti-6Al-4V and gas atomised BuRTi samples made using different particle size fractions, a common result was found that the small particle size fraction (50~150μm) samples had lower average values of ductility and smoother fatigue crack paths than did the large particle size fraction (250~400μm) samples. As mentioned in Chapter 4, the equiaxed crystals in HIPped Ti-6Al-4V are formed by

recrystallisation occurring at particle boundaries where the deformation during HIPping is largest. Hence, it is likely that the initiating facet (formed by the structure unit) nucleates at the equiaxed crystals more often than the lath-like structure. The higher volume fraction of equiaxed crystals in the smaller size fraction samples makes the failure more frequent than in the larger size fraction samples. Observations of BuRTi HIPped samples in Chapter 5 show that the original powder particles facet during HIPping, but generally these facets are independent of grain boundaries since they define original powder particle boundaries of polycrystalline particles which have facetted during the high temperature deformation occurring during HIPping. With smaller particles there is an increased possibility that a facet will in fact define a grain boundary and the properties of such a facetted boundary will be very different from that of a facetted boundary which cuts across many grains, examples of which can be seen in Fig. 5-30. It is thus suggested that these facetted grain boundaries could provide the nucleus for failure during tensile testing of these samples – especially if two such facetted grains were in contact; the poorer bonding at boundaries coupled with the possibility of the boundary being a cleavage plane in this single phase beta alloy could thus precipitate failure. The larger scatter in ductility and the low value of ductility in BuRTi, in particular in samples made using the small-sized particle fraction, is thus linked to the increased probability of premature failure via these circular regions. This explanation is consistent with the observation made on HIPped PREP BuRTi samples that large single crystal particles facet and act as failure sites.

In the case of fatigue life in HIPped PREP Ti-6Al-4V samples made using the small particle size fraction exhibited a lower fatigue run out strength which is consistent with the observed smoother crack path leading to smaller crack-deviation. There was

too much scatter in the fatigue life of samples made using gas atomised BuRTi to assess the influence of particle size on fatigue life with any confidence. It is likely that this scatter in fatigue life is associated with the facetting discussed above.

The results are different from those obtained by some researchers. Pérez et al [*Pérez 1995*] studied the influence of the powder particle size on mechanical properties of HIPped Ni_3Al. Their results showed that the material obtained from the smaller size powders exhibited the best mechanical behaviour. They explained that the smaller powder particle sizes produced finer grain sizes in the HIPped samples giving higher yield stress, tensile strength and elongation. Kim et al [*Kim 1993*] also obtained similar relationship between powder particle size and mechanical properties. They studied the influence of HIP parameters on mechanical properties for two particle size ranges of stainless steel powder. They obtained different elongations for different particle size, which showed higher elongation for samples made from smaller particle size. Their explanation for this behaviour is that the contact particle number increases with decreasing powder size. This suggestion implies that failure occurs at prior particle boundaries (which may happen in Ni_3Al) but was not observed in the present work.

Dusczyk et al [*Dusczyk 1990*] suggest that any process involving the use of fine powders is prone to produce intrinsically embrittled alloys. This is because powders have a very high specific surface area and oxide/hydroxide products could be formed on the surface both during the atomisation process and during handling and storage. The presence of a high volume fraction of oxides/hydroxides in PM materials leads to poor ductility and interparticle failure of the alloys. In the case of Ti alloys the oxides

etc would all tend to dissolve during atomisation and in the case of BuRTi the carbides precipitate throughout the matrix and precipitation does not occur at prior particle boundaries to a sufficient extent to influence properties. So the conclusions reached by Dusczyk et al may well apply to many alloys, such as Ni-based but do not apply to Ti alloys although of course if very high oxygen-contents are reached Ti alloys embrittle – but this embrittlement is intrinsic to Ti alloys with high oxygen and is not powder-specific.

The facts that Ti-6Al-4V samples HIPped using the whole size range of powder (50~400 μm) showed similar or better mechanical properties than those of sieved powder samples show the positive effect of relatively wide particle size range on properties in this important alloy.

The aims of this project were to establish the influence of the type and size of powder and the HIPping conditions on the microstructures and associated mechanical properties of two selected Ti alloys because of the potential cost and environmental advantages of net shape HIPping as a manufacturing process. The results have shown that there is a significant influence of the alloy microstructure on the suitability of HIPping as a single-step manufacturing process and of the atomisation process and of the HIPping schedule used. If all of these are optimised it has been shown that net shape HIPping is a process that can yield components with properties which are at least equal to those generated by thermomechanical processing of ingots. This is an important conclusion but the data has shown that an understanding of the microstructures generated through atomisation and HIPping enables the problems met in some alloys such as BuRTi to be understood. It is clear for example that a two

phase alloy such as Ti-6Al-4V, which transforms martensitically during atomisation responds better to HIPping than an alloy such as BuRTi which consists of retained beta after atomisation for reasons made clear in this thesis.

References

Delo 1999: Delo, D. P. and Piehler, H. R., *Acta Mater*., **47**(9), 1999, p.2841.

Dusczyk 1990: Zhuang, L. Z., Majewska-Glabus, I., Veter, R., Buekenhout, L., and Duszczyk, J., in: *Conf. Proc. 4th Int. Conf. Isostatic Pressing,* MPR, Shrewsbury, UK, 1990, p.1.

Fischmeister 1978: Fischmeister., H. F., Arzt, E., and Olsson, R. L., *Powder Metall.,* **21**, 1978, P.179.

Kim 1993: Kim, W., Flinn, J. E., and Byrne, J. G., *Acta. Metall. Mater.,* **41**, 1993, p.49.

Pérez 1995: Pérez, P., González-Carrasco, J. L., Adeva, P., *Materials Science and Engineering*, **A199**, 1995, p. 211.

Swinkels 1983: Swinkels, F. B., Wilkinson, D. S., Arzt, E. and Ashby, M. F. *Acta. Metall*, **31**, 1983, p.1829.

Chapter 7 Conclusions and Future work

This chapter gives the major conclusions drawn from the work reported in this thesis. There have been several issues addressed in this work that need further investigation and recommendations for future work are given below after the main conclusions are listed:

7.1 Conclusions

1. PREP Ti-6Al-4V powder samples HIPped at 930°C ($\alpha + \beta$ phase field) have a better balance of properties (slightly higher tensile strength, better ductility, higher fatigue endurance limit and higher fracture toughness) than those of beta-forged ingot-route samples. These improved properties are associated with a finer microstructural unit size than in beta-forged ingots and to the absence of grain boundary alpha. The properties are also better than those of alpha + beta forged despite the somewhat coarser microstructure in the HIPped samples.
2. The HIPping procedure developed during this work, which produces a smooth surface finish on as-HIPped Ti-6Al-4V, generates fatigue properties which are superior to those of HIPped samples with machined surfaces and superior to those of machined thermomechanically processed samples. This is very significant in the field of net shape HIPping since the as-HIPped surface is retained on the finished components.
3. In the case of HIPping of single phase beta alloy such as BuRTi alloy gas-atomised powder generates a better balance of properties than found in PREP

samples. The tensile strength is comparable for the gas-atomised and PREP samples but the fatigue properties of PREP samples HIPped under some conditions are very poor. This has been attributed to the large fraction of single crystal particles in HIPped PREP BuRTi.

4. The larger scatter in the ductility observed in BuRTi samples than that observed in Ti-6Al-4V is associated with the presence of larger grains in the BuRTi samples, which give rise to a characteristic fracture surface as the crack propagates radially from the initiation site. The tensile strength is not significantly reduced because of these large grains.

7.2 Future work

1. Ti-6Al-4V samples HIPped at 930°C exhibited a better balance of properties than those HIPped either well below the beta transus (about 990°C) at 880°C or well above the transus at 1020°C. Furthermore the lower the HIPping temperature below the beta transus the higher the strength, but the lower the ductility. It would be of interest to investigate the properties of samples HIPped at 960°C-closer to the beta transus than 930°C.
2. The improved HIPping procedure (applying the temperature and pressure out of phase) can produce smoother net shape surfaces of HIPped Ti-6Al-4V samples, which contribute to improved fatigue properties. However this process gave rise to coarser microstructures, presumably because of the increased time at high temperatures. Further work, where time is varied would be of interest in order to identify the optimum HIPping conditions. How the out of phase temperature and pressure affects the grain misorientation at particle boundaries and how such an out of phase temperature and pressure

condition affects mechanical properties are of great importance to the application of net shape HIPping in industry.

3. The effect of powder particle size on properties of HIPped Ti-6Al-4V samples has not been fully interpreted. “In-situ” tests would be needed to observe the behaviour of crack initiation and growth in different size fraction samples to understand the effect on properties.
4. For the HIPping of Ti-6Al-4V, only PREP powders were used. Gas atomisation can produce powders with finer grain sizes than PREP atomisation. Gas atomised Ti-6Al-4V powders are worth HIPping and studying microstructure and resultant properties despite the expected presence of limited porosity.
5. The observed stability of the as-HIPped microstructure of Ti-6Al-4V, when heated to above the beta transus, should be investigated. Both quenching-back experiments and in-situ observations during heating and cooling, using the synchrotron would be of great value in understanding this unexpected observation.
6. The fracture toughness results of HIPped Ti-6Al-4V samples in this work are lower than those obtained in other recent work in the IRC. Thus, future studies are needed to understand the difference.
7. Tomographic observation of the porosity for HIPped PREP BuRTi samples is needed to compare with that of HIPped gas atomised BuRTi samples. In addition work should be carried out to investigate the significance of the observed porosity.

8. BuRTi PREP samples HIPped under different conditions exhibit different fatigue properties although they have similar tensile behaviour. Further work is needed to understand the difference and the large scatter in properties.

9. Fine carbides and grains in HIPped gas atomised BuRTi samples contribute to higher fatigue strength than that of ingot route samples. Since improved fracture toughness would be also expected, further work should be undertaken to assess the fracture toughness properties of HIPped samples.